UNIVERSIDAD DEL PAÍS VASCO
EUSKAL HERRIKO UNIBERSITATEA

FACULTAD DE CIENCIA Y TECNOLOGÍA
ZIENTZIA ETA TEKNOLOGIA FAKULTATEA

DEPARTAMENTO DE QUÍMICA INORGÁNICA
KIMIKA EZORGANIKO SAILA

Low and high voltage stability of Na-ion battery materials: study of structural, transport and interfacial properties

A dissertation submitted to the University of the Basque Country in partial fulfilments of the requirements for the degree of Ph.D

By
Maider Zarrabeitia Ipiña

Thesis advisors:
Dr. Miguel Ángel Muñoz-Márquez
Dr. Montse Casas-Cabanas

Tutor:
Prof. Luis Mª Lezama Diago

Leioa, octubre 2016

Contents

Resumen

La presente tesis doctoral comenzó en Julio del 2013 gracias a la contratación de la doctoranda por el centro de investigación CIC Energigune y la ayuda predoctoral recibida por el Gobierno Vasco (PRE_2013_1_668) en Enero del 2014, así como en los dos años posteriores, bajo la supervisión del Dr. Miguel Ángel Muñoz-Márquez y la Dra. Montse Casas-Cabanas. La tesis ha sido adscrita en el Departamento de Química Inorgánica de la EHU/UPV y realizada en las instalaciones que posee el centro de investigación CIC Enegigune en el Parque Tecnológico de Álava (Miñano, Álava), en el área de Almacenamiento de Energía Electroquímico, grupo de Análisis estructural y de superficie y línea de investigación de ión-sodio. Así como dentro del los proyectos de investigación financiados por el Gobierno Vasco (Etortek10) y el Ministerio de Economía y Competitividad del Gobierno Español (ENE2013-44330-R).
La doctoranda ha realizado una estancia de 6 meses en la Università di Camerino financiada por el CIC Energigune 3 de los 6 meses y por la ayuda recibida por el Gobierno Vasco (Egonlabur, EP_2016_1_0009) otros 3 meses. Además, la doctoranda ha realizado medidas de Difracción de Neutrones en las grandes instalaciones “ISIS Facility” de Didcot, Oxford, y colaborado con el Dr. Neeraj Sharma para llevar a cabo medidas *in-situ* de Difracción de Rayos-X en el sincrotrón de Australia (Australian Synchrotron, Clayton, Australia) y con el Dr. Y. Hu para medidas de Espectroscopia Fotoelectrónica de rayos-X de alta energía en el sincrotrón de Canadá (Canadian Light Source Inc., Saskatoon, Canadá).

El proyecto de tesis aquí expuesto trata sobre del estudio de las propiedades estructurales y de transporte, así como de las interfases, en tres materiales de electrodo de bajo y alto voltaje para baterías de ion-sodio recargables. Las propiedades estudiadas son fundamentales, aunque poco explorados, ya que influyen directamente en la vida útil y seguridad de la batería, la cinética de los procesos redox y el potencial del electrodo. Por ello, el trabajo aquí descrito es de gran importancia.

Principalmente se han utilizados dos técnicas: la Espectroscopia Electroquímica de Impedancia (EIS, en inglés *Electrochemical Impedance Spectroscopy*) y la Espectroscopia Fotoelectrónica de Rayos-X (XPS, en inglés *X-ray Photoelectron Spectroscopy*). La EIS se ha utilizado para el estudio de la evolución de la conductividad electrónica/iónica durante el ciclado relacionándola con las transiciones estructurales y electroquímicas; además también ha sido de gran utilidad para obtener información sobre la estabilidad de la interfase electrodo/ electrolito. Por otro lado, el XPS, ha ayudado a describir la evolución, composición y estabilidad de la interfase electrodo/electrolito tanto en el electrodo negativo como los electrodos positivos. Dichas interfases se conocen como: en el electrodo negativo SEI (en inglés *Solid Electrolyte Interphase*) y en el electrodo positivo SPI (en inglés *Solid Permeable Interphase*). Además, de estas dos técnicas también se han utilizado otras técnicas para la caracterización estructural y morfológica, tales como, difracción de rayos-X y neutrones, microscopia de barrido y resonancia magnética nuclear en estado sólido (más detalle en la sección experimental). En cuanto a los métodos de síntesis llevados a cabo han sido la síntesis en estado sólido y sol-gel.

El proyecto de tesis se presenta en cuatro capítulos que contienen resultados experimentales además de los capítulos de introducción y conclusiones generales. Finalmente, en un anexo se han descrito las técnicas experimentales utilizadas.

Capítulo 1: Introducción

En el capítulo 1 se proporciona una visión sobre el estado actual de la demanda energética y la gran cantidad de gases contaminantes que se están liberando debido al uso de combustibles fósiles para generar energía. Por ello, las instituciones se han puesto manos a la obra y están llevando a cabo reformas para incrementar el uso de energías renovales y así reducir dichos gases. Sin embargo, este tipo de energías son intermitentes por lo que es necesario el uso de sistemas de almacenamiento energético. Hoy en día entre los más utilizados están los sistemas hidroeléctricos y de aire comprimido. Sin embargo estos tienen una gran desventaja puesto que están limitados geográficamente, por ello se necesita otro tipo de sistema de almacenamiento, como podrían ser las baterías; que almacenan la energía eléctrica en energía química y la liberan cuando la demanda lo requiere. Entre las baterías se pueden encontrar las de plomo acido, níquel-cadmio, níquel metal hidruro, baterías de flujo, sodio-azufre y litio-ion. Todas ellas tienen algunos inconvenientes para aplicaciones estacionarias: o no son aconsejables medio ambientalmente o son costosas. Por todo ello, hoy en día la investigación se está centrando en nuevas baterías más baratas y medio ambientalmente más respetuosas.

A pesar de que las baterías de ion-Li están poco a poco posicionándose como las baterías de referencia en electrónica portátil, electrónica de potencia, transporte y almacenamiento estacionario. Las baterías de ion-Na se están convirtiendo en una alternativa atractiva por su bajo coste debido a la abundancia del Na, su distribución geográfica y su fácil procesamiento. Además, es posible utilizar en ambos electrodos colectores de corriente de Al en lugar de Cu (en electrodo negativo de las baterías ion-Li es necesario utilizar Cu debió a que el Al forma aleaciones con Li) que los hace aun más baratas. Las baterías de ion-Na funcionan de manera similar a las baterías de ion-Li, a través del movimiento de iones de un electrodo a otro mediante reacciones redox que circulan por el electrolito. Lo que ocurre es que los electrolitos más utilizados están basados en una sal que contiene iones de sodio y uno o varios solventes orgánicos. Como materiales de intercalación se emplean materiales con un voltaje bajo en el electrodo negativo y alto en el electrodo positivo para obtener la mayor diferencia de voltaje posible y así una mayor densidad energética. Sin embargo, estos voltajes de trabajo conllevan a la descomposición del electrolito formando una interfase entre el electrodo y el electrolito debido a que la batería trabaja fuera de la ventana de estabilidad del electrolito. Como se ha mencionando anteriormente a esta interfase se le denomina SEI o SPI deponiendo de si se forma en el electrodo negativo o en el positivo respectivamente. En ambos casos se trata de una capa insoluble de productos derivados de la descomposición (reducción/oxidación) de la sal y los solventes que componen el electrolito. Idealmente, ambas interfases, SEI y SPI, actúan como un electrolito sólido y son fundamentales para el buen funcionamiento de la batería.

Por otro lado, las propiedades de transporte de los materiales de intercalación pueden influir en las propiedades electroquímicas, afectando de manera significativa en el empobrecimiento o mejora de la capacidad, su estabilidad, etc.

Es por todo ello que en este proyecto de tesis se han estudiado materiales de bajo y alto voltaje para determinar e identificar las propiedades de transporte e interfase. El material de bajo voltaje estudiado es el $Na_2Ti_3O_7$ y los material de alto voltaje: el P2-$Na_{2/3}[Fe_{1/2}Mn_{1/2}]O_2$ y el $Na_4Co_3(PO_4)_2P_2O_7$.

En este capítulo, además del estado energético y las propiedades de los tipos de baterías, se recogen las propiedades de los materiales que se han estudiado. Por un lado el $Na_2Ti_3O_7$ cuyo voltaje de inserción de Na es 0.3 V *vs.* Na^+/Na con una buena capacidad teórica (178 mAh/g), y por otro lado los cátodos, P2-$Na_{2/3}[Fe_{1/2}Mn_{1/2}]O_2$, que es uno de los candidatos más prometedores debido a su bajo coste y su gran densidad energética con un voltaje de corte alto (4.25 V vs. Na^+/Na) y $Na_4Co_3(PO_4)_2P_2O_7$, que es el cátodo con mayor voltaje de inserción de Na hasta ahora reportado (4.5 V *vs*. Na^+/Na).

Por último el capítulo recoge una comparación entre las interfases formadas en las baterías de ion-Li y en las baterías de ion-Na, así como un resumen de los estudios realizados hasta la fechas acerca de las interfases formadas en las baterías de ion-Na. La mayor diferencia está en la composición, grosor y estabilidad. Mientras que las interfases de las baterías de ion-Li están compuestas mayormente por compuestos orgánicos, con un espesor >20 nm y son estables durante el ciclado, en de las baterías de ion-Na están formadas por compuestos inorgánicos, con un espesor cerca de unos 5 nm y normalmente demuestran un comportamiento inestable.

Capítulo 2: $Na_2Ti_3O_7$ como material anódico para baterías de ión-Na: influencia de los parámetros de síntesis en las propiedades electroquímicas y estabilidad en ambiente húmedo y agua

En el capítulo 2 se recoge el estudio realizado para mejorar las propiedades electroquímicas del electrodo negativo $Na_2Ti_3O_7$; ya que a pesar de sus interesantes propiedades electroquímicas interesantes la retención de la capacidad inicialmente reportada era baja. Primero, se han estudiado los efectos de los parámetros de síntesis, tales como el precursor de Na, la atmosfera durante el proceso de enfriamiento y el efecto de recubrir el material con carbón. Posteriormente la estabilidad en un atmosfera húmeda y su efecto cuando se utilizan aglutinantes acuosos como el Na-CMC para la preparación del electrodo, ya que permite la utilización de materiales menos costosos y medio ambientalmente favorables.

La retención de la capacidad ha sido mejorada mediante la erradicación de Na_2CO_3 residual proveniente del precursor, evitando la corrosión de la superficie y recubriendo el material activo con carbón. Además se ha observado que el $Na_2Ti_3O_7$ muestra reactividad cuando se expone a un ambiente húmedo formando el compuesto $Na_{2-x}H_xTi_3O_7$ mediante el intercambio iónico que prácticamente no influye en las propiedades electroquímicas.

Capítulo 3: $Na_2Ti_3O_7$ como material anódico para baterías de ión-Na: propiedades de transporte y el estudio de la SEI

El capitulo 3 está enfocado en el estudio de las propiedades electrónicas/iónicas y de la composición, estabilidad y evolución de la SEI formada en electrodo negativo $Na_2Ti_3O_7$ durante el ciclado. Estas propiedades han sido investigadas en dos tipos de muestras: no recubierta y recubierta con carbón. Las propiedades electrónicas/iónicas y la estabilidad de la SEI han sido determinadas mediante la técnica EIS. La composición, evolución así como la estabilidad de la SEI han sido investigadas mediante la técnica XPS, combinado el estudio convencional de XPS con la determinación del parámetro *Auger* y análisis de perfiles de profundidad mediante bombardeando con iones Ar para la muestra no recubierta con carbón, y con XPS de alta energía para la muestra recubierta con carbón. Finalmente, con la muestra recubierta con carbón se ha montado una batería completa utilizando como contraelectrodo $NaFePO_4$ y poder así observar las diferencias y la influencia del sodio metálico cuando se utiliza como contraelectrodo.

El estudio ha demostrado que el $Na_2Ti_3O_7$ sufre una transición de aislante a conductor durante la inserción de Na^+. La SEI formada en los electrodos estudiados es de unos pocos nanómetros de grosor, mayormente formada por compuestos inorgánicos y parcialmente inestables, siendo la muestra recubierta de carbón la que exhibe mayor grosor y estabilidad. Además se ha observado que el aglutinante utilizado PVdF y la sal del electrolito ($NaClO_4$) se descomponen espontáneamente antes de empezar el ciclado, dando lugar a la formación de NaF y NaCl. Por último, la interfase formada en el $Na_2Ti_3O_7$ en una celda completa es más estable que la obtenida en una media celda, y la descomposición del electrolito no empieza nada mas montar la celda al contario que ocurre en una celda con Na metálico.

Capítulo 4: P2-$Na_{2/3}[Fe_{1/2}Mn_{1/2}]O_2$ como material catódico para baterías de ión-Na: propiedades electroquímicas y de transporte y el estudio de la SPI

El capítulo 4, está centrado en el estudio de las propiedades de transporte y de la SPI en uno de los cátodo más prometedores: P2-$Na_{2/3}[Fe_{1/2}Mn_{1/2}]O_2$. Primero, el material se ha caracterizado estructural, morfológica y electroquímicamente, estudiando el impacto del electrolito y la ventana de voltaje en las propiedades electroquímicas mediante medidas galvanostaticas y de impedancia. La técnica EIS además ha sido empleada para determinar y entender los motivos de la degradación de la capacidad que sufre este cátodo, pudiendo relacionarlo con las transiciones estructurales durante la inserción y extracción de Na. Por último se ha estudiado las propiedades de la SPI mediante las técnicas EIS y XPS, demostrando que la degradación de la capacidad del P2-$Na_{2/3}[Fe_{1/2}Mn_{1/2}]O_2$ está relacionada con el incremento de la resistencia electrónica debido a la transición estructural que sufre de P2 a OP4 a altos voltajes. En cuanto a la SPI está mayormente compuesta por compuestos inorgánicos, derivados de la descomposición espontanea del aglutinante (PVdF) y de la sal; en este caso $NaPF_6$; así como de los solventes, al igual que ocurre en el electrodo negativo anteriormente estudiado. Durante el ciclado una capa fina (menor que la SEI) y no homogénea de Na_2CO_3, recubre los productos derivados del aglutinante y la sal.

Capítulo 5: $Na_4Co_3(PO_4)_2P_2O_7$ como material catódico para baterías de ión-Na: propiedades electroquímicas y de transporte y el estudio de la SPI

El capítulo 5 recoge el estudio realizado en el cátodo con mayor voltaje de extracción/inserción de Na reportado hasta la fecha: el $Na_4Co_3(PO_4)_2P_2O_7$ (cuyo voltaje promedio es de 4.5 V). Al igual con en el otro cátodo, primero se ha caracterizado estructural, morfológica y electroquímicamente. En este caso además se han investigado los cambios estructurales mediante difracción de rayos X *in-situ*. Posteriormente se ha estudiado las propiedades de transporte médiate la técnica EIS así como la estabilidad de la SPI. Y por último la composición, evolución y estabilidad de SPI mediante la técina XPS utilizando dos fuentes de rayos-X: Mg K_α y Ag L_α.

El estudio ha revelado que el recubrimiento con nanotubos de carbón del $Na_4Co_3(PO_4)_2P_2O_7$ mejora las propiedades electroquímicas con una retención prácticamente del 100% después de 100 ciclos. Las medidas *in-situ* de difracción de rayos-X muestran que la evolución durante el ciclado es muy similar al la del compuesto isoestructural $Na_4Mn_3(PO_4)_2P_2O_7$. En cuanto a las medidas realizadas para determinar las propiedades de transporte, demuestran que la SPI es estable durante los dos primeros ciclos y que en el segundo ciclo un proceso nuevo tiene lugar; posiblemente originado por le los cambios que sufre la superficie de los nanotubos que rodean el material activo. Por último, la SPI formada es prácticamente igual que la creada en el P2-$Na_{2/3}[Fe_{1/2}Mn_{1/2}]O_2$, con la diferencia que debido a un mayor voltaje de trabajo la sal no solo se descompone dando lugar a la formación de compuesto fosfatos sino también fluorofosfatos. Además, la SPI es prácticamente estable (tal y como se ha visto por EIS), manteniendo las propiedades electroquímicas y demostrando así la posibilidad de emplear materiales catódicos de alto voltaje en las NIBs.

Capítulo 6: Conclusiones generales

En el capítulo 6 se recogen las conclusiones más relevantes obtenidas en el proyecto de tesis, comparando los resultados entre ellos así como con los resultados reportados para las baterías de ion-Li.

Anexo: Técnicas experimentales

Por último, en el anexo se han recogido las técnicas experimentales utilizadas a lo largo de la investigación; las cuales se han dividido en dos grupos principales: técnicas de caracterización físico-química y técnicas de caracterización electroquímica. El primer grupo a su vez ha sido dividido en 4 grupos dependiendo del tipo de técnica utilizada: técnicas de difracción (de rayos-X (XRD), de neutrones (ND), electrones (ED) y laser), microscopia electrónica (de barrido (SEM) y de transmisión (TEM)), técnicas espectroscópicas (de infrarrojo-transformada de Fourier (FTIR), resonancia magnética nuclear en estado sólido (ssNMR), espectroscopia de emisión óptica (ICP), análisis elemental y espectroscopia fotoelectrónica de rayos-X (XPS)) y análisis térmico (análisis termogravimétrico (TGA)), detallando los fundamentos teóricos, equipos empleados y las condiciones de medida. El segundo grupo describe los fundamentos principales de las técnicas de caracterización electroquímica: voltametría cíclica (CV), estudio galvanostático y espectroscopia electroquímica de impedancia (EIS). A su vez se detalla el proceso de preparación de los electrodos y el montaje de las celdas.

Abstract

Na-ion batteries (NIBs) are becoming an attractive alternative to Li-ion batteries because of their low cost owing to sodium abundance, geographical distribution and ease of processing. Moreover, cheaper current collectors made of Al instead of Cu can be used in both electrodes. Most of the recent works in NIBs have been focussed on the study of new electrode materials and their structural evolution upon cycling; however, not many works have investigated interfacial and transport properties. Their properties have a direct influence on the cycle life and safety of the battery, the kinetics of redox processes and electrode potential, and therefore its study is of outmost importance.

In this work, the structural, transport and interfacial properties of three selected low and high voltage electrode materials has been studied. On the one hand, electrochemical impedance spectroscopy (EIS) has been applied to study the evolution of the electronic/ionic conductivity upon cycling, coupled to structural changes, and its impact on the electrochemical properties. On the other hand, the electrode/electrolyte interphase properties (known as Solid Electrolyte Interphase -SEI- on the negative side and Solid Permeable Interphase -SPI- on the positive) have been studied with X-ray photoelectron spectroscopy (XPS).Our work focus is on the negative electrode $Na_2Ti_3O_7$, whose capacity retention was enhanced by suppressing residual Na_2CO_3 from synthesis precursors and avoiding its formation by surface corrosion, and by C-coating the material. $Na_2Ti_3O_{7,}$ has also been shown to react with moisture to form $Na_{2-x}H_xTi_3O_7$ compounds by ion exchange, with no major impact in the electrochemical properties, and to exhibit a reversible insulator to conductor transition during Na^+ insertion as revealed EIS. The SEI layer composition and stability was also investigated for uncoated and coated $Na_2Ti_3O_7$ in a half-cell and the results obtained show that both interphases are a few nanometers-thick, mainly formed by inorganic compounds and partially unstable (more ticker and stable in coated sample).The coated $Na_2Ti_3O_7$ also was tested in a full-cell, showing a higher stability at OCV state, since the SEI layer formation is almost negligible due to the PVdF and $NaClO_4$ salt decomposition reactions were not observed.

The second part of this work focuses on cathode materials. In P2-$Na_{2/3}[Fe_{1/2}Mn_{1/2}]O_2$ (average voltage 2.75 V) it has been shown that one of the reasons of capacity fading is linked to the increase of bulk electronic resistance due to the structural transition from P2 to OP4. It has also been shown that a very thin, discontinuous and stable SPI layer mainly composed by inorganic species is formed when cycled up to 4.25 V. On the other hand, the SPI layer formed on $Na_4Co_3(PO_4)_2P_2O_7$, which is the highest voltage cathode material reported to date (average voltage of 4.5 V), is also composed by inorganic compounds, with a partial dissolution of $NaCO_3R$ upon Na^+ insertion. However, this SPI layer was almost stable not leveraging on the electrochemical performance and showing the possibility to employ high voltage cathode materials in NIBs.

1 Introduction

1.1. Overview of energy demand

The International Energy Outlook 2016 (IEO2016) by the U.S. Energy Information Administration (EIA) has been presented that the total world energy consumption rises from 549 quadrillion Btu in 2012 to 815 quadrillion Btu in 2040, an increases of 48%. However, the renewable energies are the fastest growing energy source increasing by average of 2.6%/years between 2012 and 2040. Since the policy preferences for lower carbon energy options are reinforced by the tendency in cost of oil and natural gas. Even through, the consumption of fossil fuels still account with 78% of energy use in 2040 [1, 2].

The energy consumption has also continuously grown during the 20th century in the Basque Country reaching the maximum value in 2007 (around 20.612 GW·h) although, in the last years the demand has slightly decreased reaching 16.335 GW·h in 2014 (**Figure 1.1a**) [3]. One of the main problems of the high energy demand is that around 80% of this energy comes from oil, natural gas and carbon (**Figure 1.1b**), which release greenhouse gases emissions and are one of the primary factors responsible of global warming [4]. From 1990 the emissions of these gases were above 20 millions of tons of dioxide equivalents per year only in the Basque country (**Figure 1.1c**). Nevertheless, in the last years the emissions of these gases have slightly decreased [5] since EVE (*Ente Vasco de la Energía*), the Basque Country institution of energy, started applying a strategy with the purpose to reduce in a 40% this kind of emissions by 2030. In order to achieve this goal, EVE institution started to implement more clean energy sources such as renewable energies, with the objective to reach 22% of the total energy produced by renewable energies by 2030 which in 2014 represented only 7% of the total energy sources [4].

The main problem of renewable energies is that its production is not constant; therefore to smooth out the intermittency of renewable energy production, low-cost electrical energy storage (EES) systems will be required. EESs are considered key enablers of the future grid, since play an important role in the process of shifting electric energy from peak to off-peak periods, storing the electrical energy when it can be produced and releasing at peak times when it is more necessary. Nowadays, EESs only contribute to 10% of the installed generation capacity in Europe, where hydroelectric pumped storage are the most used technologies. There are many other EESs devices such as compressed air storage, flywheels and different kind of rechargeable batteries (Pb-acid, Ni-Cd, Ni-MH, redox flow, Na-S and Li-ion) which can be competitive depending on the requirements of the

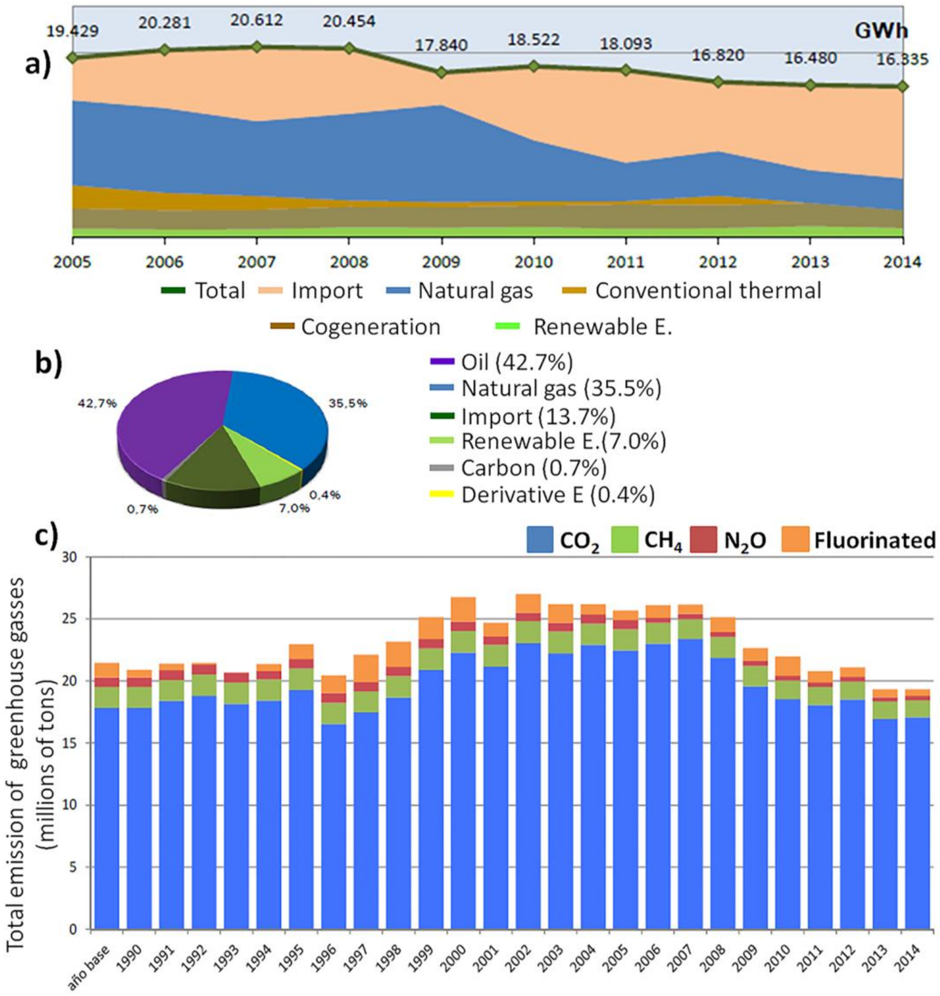

Figure 1.1: a) Energy consumption from 2005 to 2014, **b)** energy sources in 2014 and **c)** total emission of greenhouse gases from 1990 to 2014 (emissions are expressed in millions tons of dioxide equivalents). These data corresponds to the Basque Country autonomous community [3, 4, 5].

application markets [6]. For stationary applications rechargeable batteries can probably be the most efficient devices since can store electricity in chemicals and reversibly release it according to the demand, while hydroelectric pumped and compressed air energy storage are limited by geographic requirements. In **Table 1.1** the characteristic properties of hydro pumped, compressed air storage and some of the most relevant commercial batteries are collected.

Table 1.1: Comparison of potential EES systems [6, 7].

Type	OCV (V)	Specific energy (Wh/kg)	Operating temperature (°C)	Discharge time	Cycle life (cycles)	Energy efficiency (%)
PH				up to 8 h	30*	70 - 80
CA				0.1 - 15 h	30*	60 - 79
Pb-A	2.1	24 - 40	-40 - 60	up to 8 h	1000	50 - 75
Ni-Cd	1.35	30 - 45	-10 - 45	up to 4 h	2000	55 - 70
Ni-MH	1.35	63 - 75	-30 - 65	up to 4 h	2000	75 - 80
VRF	1.4	10 - 20	10 - 40	4 - 12 h	3000	70 - 85
Na-S	2.1	150 - 240	300 - 350	up to 4 h	4000	75 - 90
Li-Co	3 - 4	155	-25 - 40	up to 4 h	1000	94 - 99
Li-LFP	1.7	50 - 70	-25 - 40	up to 4 h	4000	94 - 99

* Cycle life in years.

PH: pumped hydro, CA: compressed air storage, Pb-A: Lead-acid, Ni-Cd: Nickel-cadmium, Ni-MH: Nickel-metal hybrid, VRF: Vanadium redox flow, Na-S: Sodium-sulfur, Li-Co: Li-ion, graphite as anode and $LiCoO_2$ as cathode, Li-LFP: Li-ion $Li_4Ti_5O_{12}$ as anode and $LiFePO_4$ as cathode.

1.2. Rechargeable batteries: a potential technology

Rechargeable batteries are devices that convert reversibly the chemical energy into electric energy by electrochemical oxidation/reduction reactions. The stored energy density depends on the average voltage between two active materials (cathode/positive electrode and anode/negative electrode) and their specific capacity. During the charge process the positive active material (cathode) is oxidized, releasing electrons which are transferred to the negative electrode (anode) through an electric circuit and reducing the negative active material. During the discharge process electrons follow the opposite behaviour and the negative active material is oxidized while the positive active material is reduced. Additionally, both electrodes are separated by the electrolyte which can behave as a simple medium for internal ion flow between positive and negative electrodes or as active participant in the electrochemical reaction [8].

1.2.1. Lead-acid batteries (Pb-acid)

Pb-acid batteries were invented by Gaston Planté in 1860 and nowadays are still the most sold batteries, around 70% of all secondary batteries [8]. These batteries are used in stationary applications, automotive industry, communication devices, and power sources for mining and material handling equipment. In **Table 1.2** the advantages and disadvantages of this technology are collected.

Table 1.2: Advantages and disadvantages of Pb-acid batteries.

Advantages	Disadvantages
Low-cost	Limited energy density (30-40 Wh/kg)
Variety of sizes and designs (from smaller than 1 Ah to thousand Ah)	Long-term storage in discharged conditions can lead to irreversible polarization
Good high rate performance	Difficult to manufacture in a small sizes
Large working temperature range	Explosion hazard due to hydrogen evolution (only in some designs)
Efficient (over 70%)	Sb and As devices can be a healthy hazard
High cell voltage (>2.0 V)	Thermal runaway
Good float service	
Good charge retention for intermittent charge app.	
Available in maintenance-free designs	
Cell components are easily recycled	

Pb-acid batteries are constituted at charged state by a lead (II) dioxide metallic lead (PbO_2) as the active material of the positive electrode and porous structure metallic lead (Pd(m)) with a high surface area as negative electrode material. At the discharged state both electrodes are made of lead (II) sulphate ($PbSO_4$), being the process reversible. The electrolyte is a sulphuric acid solution (H_2SO_4) typically about 37 wt.% acid in fully charged conditions [8]. The charge and discharge processes are mentioned below:

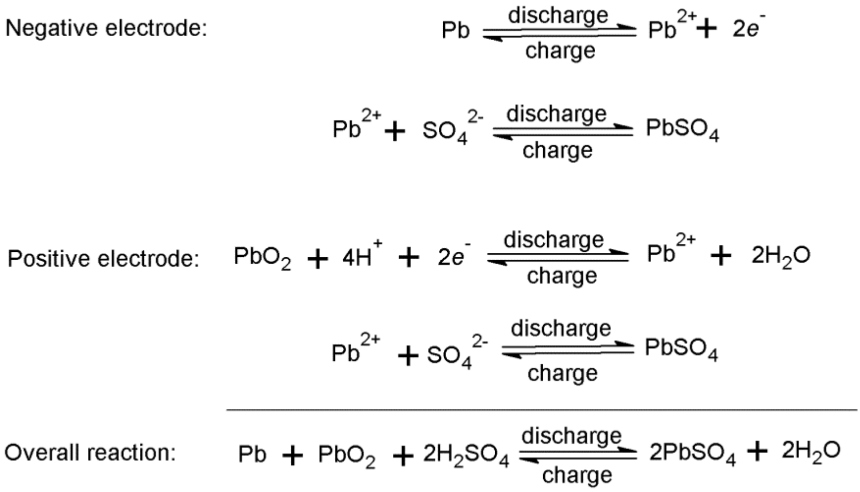

1.2.2. Nickel-cadmium batteries (Ni-Cd)

The Ni-Cd batteries was invented by Waldemar Jungner in 1899 but until 1960 was not commercialized in large volume. There are several configurations of Ni-Cd batteries where the oldest configuration is the pocket-plate Ni-Cd battery. This configuration is employed in a number of applications such as railroad services, switchgear operation, telecommunications, uninterruptible power supplies (UPSs), energy lighting and also for military and space industry. Later, during the 1940s the sintered-plate configuration was developed which the main difference between these two configurations is that, in the pocket type, the active material is embedded within perforated steel pockets while in the sintered type the active material has sintered structure surrounding the grid. Moreover, the latter type is thinner than the pocket-type and has lower internal resistance that gives superior high rate and low temperature performance. This configuration is used in high power applications. Further development was a smaller design called sealed Ni-Cd battery. This battery incorporates specific design features to prevent a build-up of pressure in the battery caused by gassing during overcharge. This property gives the opportunity to use this battery in a variety of applications from lightweight portable power to high rate and high capacity power devices. In the following table (**Table 1.3**) the benefits and drawbacks are collected.

Table 1.3: Benefits and drawbacks of Ni-Cd batteries.

Type	Benefits	Drawbacks
Pocket-plate	Long cycle life	Low energy density
	Rugged and reliable	Higher cost than Pb-acid batteries
	Good charge retention	Contains Cd which is toxic
	Excellent long term storage	Memory effect
	Low maintenance	
	Flat discharge profile	
Sintered-plate	Higher energy density	Even higher cost
	Superior high rate and low temperature performance	
Sealed Ni-Cd	No maintenance required	More expensive than others Ni-Cd type batteries
	Long shelf cycle life	Poor charge retention
	Rapid recharge capability	Better performance at higher temperature
	Safety vent system	Lower capacity
	Low internal impedance	

Ni-Cd batteries use a basic aqueous electrolyte, typically KOH, for its higher conductance, Ni oxyhydroxide (NiOOH) as positive electrode and Cd as negative electrode, where the battery is manufactured in discharge state but it is sold in charge state [8]. The reactions during battery operation are illustrated below:

Negative electrode:

$$\mathrm{Cd} + 2\mathrm{OH}^- \xrightleftharpoons[\text{charge}]{\text{discharge}} \mathrm{Cd(OH)_2} + 2e^-$$

Positive electrode:

$$2\mathrm{NiO(OH)} + 2\mathrm{H_2O} + 2e^- \xrightleftharpoons[\text{charge}]{\text{discharge}} 2\mathrm{Ni(OH)_2} + 2\mathrm{OH}^-$$

Overall reaction:

$$2\mathrm{NiO(OH)} + \mathrm{Cd} + 2\mathrm{H_2O} \xrightleftharpoons[\text{charge}]{\text{discharge}} 2\mathrm{Ni(OH)_2} + \mathrm{Cd(OH)_2}$$

1.2.3. Nickel-metal hybrid batteries (Ni-MH)

Ni-MH batteries were studied in the 1960 as a derivative of Ni-Cd batteries, due to the environmental benefits, higher energy, lower pressure and low-cost. More advantages as well as the disadvantage are collected in **Table 1.4**. From their commercialization in 1989 for portable PCs, nowadays remains in the market which is one of the important rechargeable battery system for hybrid vehicles, industrial standby applications including energy storage for Telecom, UPSs and distributed generation applications and in many consumer applications for example digital camera, cell phone, etc..

Table 1.4: Advantages and disadvantages of Ni-MH batteries.

Advantages	Disadvantages
Higher energy density and specific energy than Pb-acid and Ni-Cd batteries	Higher cost than Pb-acid batteries
Good high temperature performance	Lower specific energy and specific power compared to Li-ion batteries
High rate capability	Bigger size due to the pumps
Good charge retention	Decreased performance at low temperature
Long cycle life	
Rapid recharge capability	
Long shelf life	
Sealed maintenance-free design	
Safe	

As Ni-Cd batteries the Ni-MH batteries use a basic aqueous electrolyte and β-NiOOH as positive electrode while the employed negative electrode is more environmental friendly: metal hybrid (MH) such as ZrNi, Ti_2Ni, $LaNi_5$ or $TiNi_2$. The reactions during cell performance are illustrated below:

$$\text{Negative electrode:} \quad MH + OH^- \underset{\text{charge}}{\overset{\text{discharge}}{\rightleftharpoons}} M + H_2O + e^-$$

$$\text{Positive electrode:} \quad B\text{-}NiOOH + H_2O + e^- \underset{\text{charge}}{\overset{\text{discharge}}{\rightleftharpoons}} Ni(OH)_2 + OH^-$$

$$\text{Overall reaction:} \quad MH + B\text{-}NiOOH \underset{\text{charge}}{\overset{\text{discharge}}{\rightleftharpoons}} M + Ni(OH)_2$$

1.2.4. Redox flow batteries

Redox flow batteries were originated in 1960 when the zinc/ chlorine (Zn/Cl) hydrate battery was developed. However, since 1970s, a huge variety of redox flow systems have been investigated such as, iron/ chromium (Fe/Cr), vanadium/ bromine (V/Br), bromine/ polysulfide (Br/PSB), zinc/ cerium (Zn/Ce), zinc/ bromine (Zn/Br) and all vanadium. The two latter redox flow batteries are the most advanced and mainly are used as stationary EESs. The all vanadium system is the most interesting redox flow battery due to the fact that is composed by a single cationic element. Hence the crossover of vanadium ion through the membrane during long term cycling is less deleterious than in the other redox flow systems [9]. In **Table 1.5** are collected the general advantages and disadvantages of this vanadium redox flow battery.

Table 1.5: Advantages and disadvantages of vanadium redox flow battery [7, 9].

Advantages	Disadvantages
High efficient (70 - 85%)	Low to medium energy density
Simple electrode reaction	Require more parts (such as pumps)
Less electrolyte degradation	Bigger size due to the pumps
No high temperature are required	Few field applications
No morphological change	Flow management

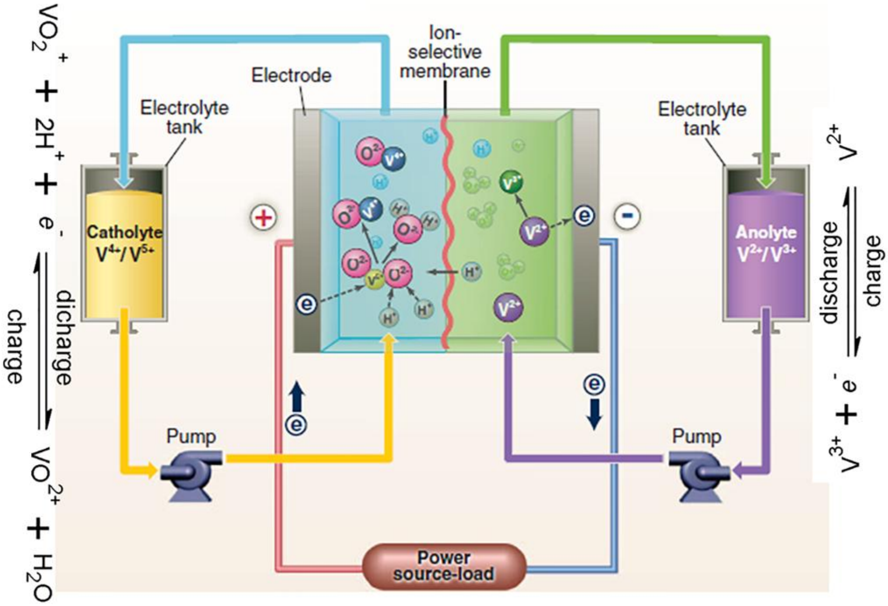

Figure 1.2: Schematic of an all vanadium redox flow battery and related redox reactions. Modified from [9].

The all vanadium system is constituted of an ion selective membrane which separates the positive catholyte (V^{4+}/V^{5+}) and the negative anolyte (V^{2+}/V^{3+}). These redox species are liquid and are stored in different tanks. The catholyte and anolyte are pumped by different hoses until arrive to the cell stack where electrons transfer reactions take place [7, 9]. Charge/discharge reactions and the schematic illustration of the battery are shown in **Figure 1.2**.

1.2.5. Sodium-sulfur batteries (Na-S)

Na–S batteries have been commercialized since 1970s [10] but this technology can be traced back to the 1960s when the ceramic electrolyte sodium β–alumina ($NaAl_{11}O_{17}$) was discovered by Ford company. This material exhibits high ionic conductivity for Na^+ at moderate temperatures, around 270 - 310 ^{o}C and low electronic conductivity [9]. However, Na-S batteries have several drawbacks also (**Table 1.6**).

Table 1.6: Advantages and disadvantages of Na-S batteries [10].

Advantages	Disadvantages
High efficient (89 - 92%)	Higher working temperature than other batteries
High energy density	Highly reactive molten electrode materials
Long cycle life	Corrosion problem because of polysulphides
Chemical and thermal stability	
Low-cost and maintenance requirements	

The β-alumina ceramic electrolyte is placed between two molten electrodes (Na and S as anode and cathode, respectively). During the discharge Na is oxidized at the ceramic electrolyte interface. The resulting Na^+ migrates through the β-alumina electrolyte to the cathode side to react with S that is reduced forming Na_2S_5. Although initially two liquid phases are formed since Na_2S_5 is immiscible with S. During the charge Na_2S_5 are oxidized and, when the Na content falls below Na_2S_5 stoichiometry, the two immiscible phases reappear (**Figure 1.3**). It is possible to form S onto or near the electrolyte increasing the cell resistance and limiting the amount of charge, finally affecting the cycle life of the battery [8, 9].

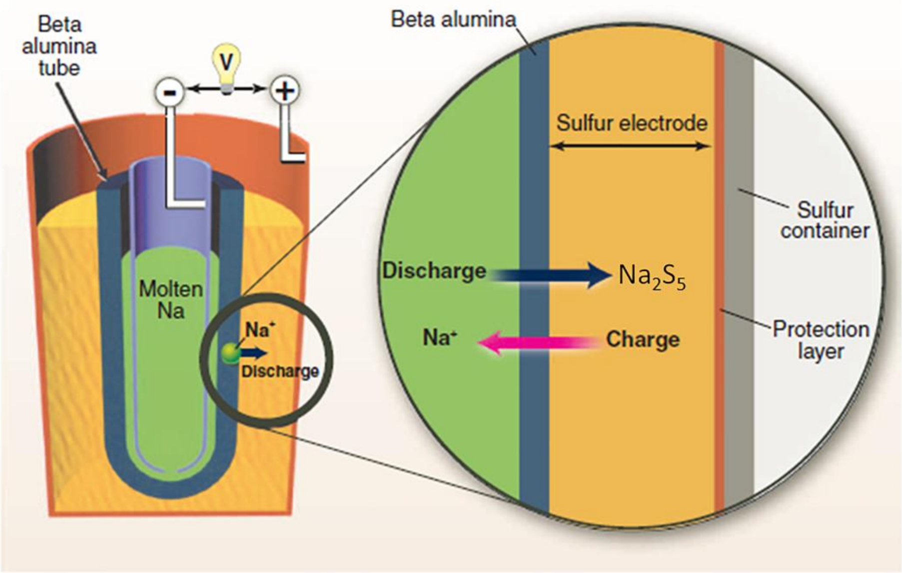

Figure 1.3: Schematic of a Na-S battery and related redox reactions. The figure is modified from [9].

1.2.6. Li-ion batteries (LIBs)

LIBs were first commercialized by Sony Corporation in 1991 [11] and quickly became a competitive technology in terms of energy and power density for EESs applications thanks to the low molecular weight of Li (M = 6.94 g/mol) and small ionic radius of Li^+ (0.96 Å) which enables fast diffusion and low redox potential (-3.04 V *vs.* standard hydrogen electrode (SHE)). In the **Table 1.7** below, the general advantages and disadvantages of this competitive technology are gathered which can vary depending onf electrode composition. Most commercial LIBs work via Li-ion intercalation, with Li^+ migration across the electrolyte located between two host structures (positive and negative electrodes) (**Figure 1.4**). This mechanism is at the origin of the rocking chair appellation of these batteries since the Li^+ "rocks" back and forth between the positive and negative electrode during the cycling.

Table 1.7: General advantages and disadvantages of LIBs [8].

Advantages	Disadvantages
Long cycle and low shelf life	Moderate initial cost
High columbic and energy efficiency	Capacity loss and potential thermal runway when overcharged
Broad temperature range operation	
No maintenance required	
Rapid charge capability	
High rate and power discharge capability	
No memory effect	

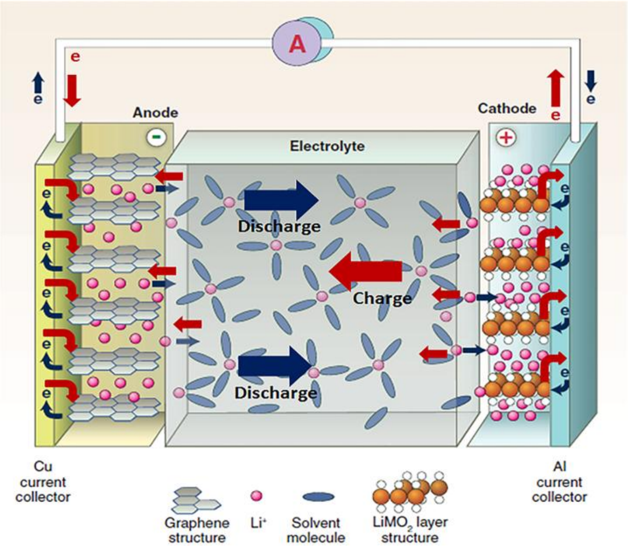

Figure 1.4: Schematic of a LIB and its intercalation mechanism. Modified from [9].

The electrolyte can be liquid, as is the case of most commercial batteries, or solid. Liquid electrolytes consist of Li salts, such as $LiPF_6$, $LiBF_4$ or $LiClO_4$ in an organic solvent, for example ethylene carbonate (EC), propylene carbonate (PC), dimethyl carbonate (DMC), diethyl carbonate (DEC) or mixtures of them. Solid electrolytes are typically based in polyethylene glycol (PEO) polymer [8].

Three main families are found for cathode materials: layered oxides, spinel structure and polyanionic compounds (**Figure 1.5**), all with a high operating potentials which result in high energy storage devices [12]. The first commercial cathode material is $LiCoO_2$ layered oxide (LCO) which was firstly proposed as Li^+ intercalation material by Goodenough in 1980 [13]. LCO is a very attractive cathode material for its high theoretical specific capacity (274 mAh/g), high theoretical volumetric capacity (1363 mAh/cm^3), low self-discharge, high discharge voltage and good cycling performance. However, it exhibits some drawbacks such as high-cost, low thermal stability and fast capacity fade at high current. Therefore, one of the strategies in order to avoid these hassles is to replace the Co by other transition metals for example Ni, Mn or mixtures of both (NCM, aka NMC) and/or by doping with Mg or Al (NCA). Nevertheless, all of them show advantages and disadvantages. Moreover, the spinel $LiMn_2O_4$ is beneficial in terms of abundance, low cost and environmentally friendly material. However; it also exhibits insufficient long cyclability because of the irreversible side reactions with electrolyte, oxygen loss from delithiated state, Mn dissolution and formation of tetragonal $Li_2Mn_2O_4$ at the surface at high C rates. Finally, amidst the polyanionic compounds, the most representative is $LiFePO_4$ (LFP) which shows a more stable structure (olivine) and good thermal stability, as well as high power capability, safety and low cost. The weaknesses are the lower average voltage (3.4 *vs.* Li^+/Li)

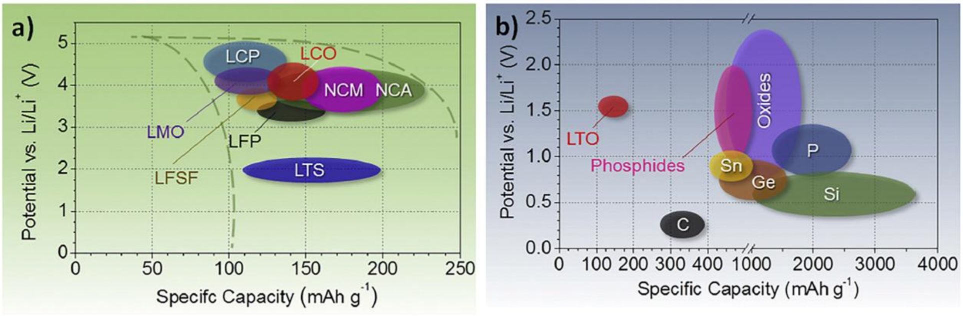

Figure 1.5: Potential (*vs.* Li^+/Li) *vs.* specific capacity of some relevant **a)** cathode and **b)** anode materials for LIBs. (LCO: $LiCoO_2$; NCM, aka NMC: $LiNi_xCo_yMn_zO_2$, NCA: $LiNi_{0.8}Co_{0.15}Al_{0.05}O_2$, LMO: $LiMn_2O_4$, LFP: $LiFePO_4$, LCP: $LiCoPO_4$, LSFS: $LiFeSO_4F$, LTS: $LiTiS_2$ and LTO: $Li_4Ti_5O_{12}$) [12].

and low electrical and ionic conductivity. However, the latter drawback can be reduced by C-coating.

Carbon-based compounds are the best option among anode materials due to their low-cost, abundant availability, low potential, high Li^+ diffusivity and high electrical conductivity. The most commonly used anode material is graphite, but non-graphitic carbons such as soft carbons and hard carbons (HC) are also employed. Another commercial anode material is $Li_4Ti_5O_{12}$ (LTO) which, although exhibits lower Li^+ diffusivity and electrical conductivity, it has higher thermal stability, high rate, volumetric capacity (zero strain intercalation mechanism, 0.2%) and long cycle life ideal for lower energy but high power applications. The higher Li^+ intercalation potential (1.55 V *vs.* Li^+/Li) would though that is a disadvantage, however, this allows to avoid the formation of the SEI layer which can be beneficial for longer cycle life of the battery [12].

Additionally, electrodes are typically composed of a certain amount of conductive additive (carbon) to increase the electrical conductivity since most materials exhibit low electrical conductivity, and a binder (polyvinylidene fluoride, PVDF and sodium carboxymethylcellulose, Na-CMC among the most used) which allows obtaining a better connectivity between the all components that form the electrode. The electrode composite is casted as a thin film on Al and Cu foils which work as current collectors for cathode and anode, respectively [8].

The main application of LIBs is in the portable electronic market and power tools equipments. However, they are penetrating in the vehicle market and are the technology of choice for the next generation of hybrid electric vehicles (HEVs). In order to achieve the required autonomy of HEVs, research is now focused on new electrode materials with higher voltage and/or specific capacities which will result in higher energy density batteries. Additionally, due to their high energy efficiency compared with other technologies, are also used as stationary EESs. However, the limited availability of Li, the cost of used material as cathode (for example in LCO the cost of Co (10 - 25 USD/lb) is the major contribution factor of the total price of the battery [14]); and the need to use Cu as current collector in the anode side (1.80 $\$/m^2$) increase the total cost off the battery. It is thus necessary to find cheaper alternative materials for stationary applications where the cost is the most important requirement.

1.3. Na-ion batteries (NIBs): alternative technology for stationary applications

NIBs are becoming one of the most promising low-cost alternatives technologies for stationary applications for its advantages: abundance of Na precursor, Na evenly distributed in the earth and possibility to use Al current collectors (0.80 $/m^2) in both electrodes since Al does not alloy with Na at low voltage. Moreover, Na is chemically similar to Li (**Table 1.8**) [15, 16] and the acquired knowledge in LIBs can be employed in this new technology which is in the research step.

However, NIBs in general exhibit lower electrochemical performance than LIBs, since the larger size of Na^+ results in significant differences in the host structure of the intercalated and deintercalated materials [17], as well as in the volumetric capacity. Moreover the reduction of voltage (0.33 V *vs*. SHE) becomes in lower energy density. Finally the different surface passivation process can influences on the electrochemical properties. Although, this differences are more significant when compared metallic Li and Na electrode while the variances become smaller and not as pronounced when compared between intercalated materials as electrode. For example, the theoretical capacity of $LiCoO_2$ and $NaCoO_2$ is reduced only 14% in the Na compound compared to Li one. Furthermore the volumetric capacity is also reduced since the difference in molar volume decrease from 18 Å^3 in the case when metallic Li and Na are compared to 5 Å^3 taking into account the difference between $LiCoO_2$ and $NaCoO_2$ [18]. Since, the final technology will be based on intercalated and deintercalated materials and not in metallic Li or Na electrode the energy loss is significantly reduced. Even so, the energy density, electrochemical performance and cost of NIBs are necessary to improve in order to become competitive future technology for stationary application.

Table 1.8: Comparison of some Li and Na characteristics [15, 16].

Characteristics	Li	Na
Abundance	20 mg/kg	$23.6\cdot10^3$ mg/kg
Distribution	70% South America	Everywhere
Price for carbonate	4.11 - 4.49 €/kg[a]	0.07 - 0.37 €/kg[b]
Ion radius	0.69 Å	0.98 Å
Atomic weight	6.9 g/mol	23 g/mol
Voltage *vs.* SHE	- 3.0 V	- 2.7 V
A-O coordination	Octahedral or tetrahedral	Octahedral or prismatic
Melting point	180.5 °C	97.7 °C

[a] Battery grade: 99.9% [b] Purity: 98.8 - 99.2% min.

The principle of operation of NIBs is similar to that of LIBs [19], and due to the similar chemistry many Li analogues have been proposed as cathode materials for NIBs. However, when it comes to anodes, the “Li-analogue” approach is less effective. A short description of the main electrode materials under study is given below, focusing in detail in the intercalation materials for NIBs studied in this thesis: $Na_2Ti_3O_7$ anode material and P2-$Na_{0.66}[Fe_{1/2}Mn_{1/2}]O_2$, $NaFePO_4$ and $Na_4Co_3(PO_4)_2P_2O_7$ cathode materials.

1.3.1. Anode materials

One of the most significant challenges in NIBs field is to find suitable and safe anode materials able to deliver a stable capacity without the risks of operating at low voltages [20]. Indeed, as in LIBs, metallic Na cannot be employed as the negative electrode due to its high reactivity with the commonly used organic electrolyte [21] and dendrite formation which can lead to short circuits in battery [22]. The most relevant anode materials are gathered in **Figure 1.6** according to their voltage and gravimetric capacity, and their energy density was calculated *vs.* P2-$Na_{2/3}[Fe_{1/2}Mn_{1/2}]O_2$ as cathode material.

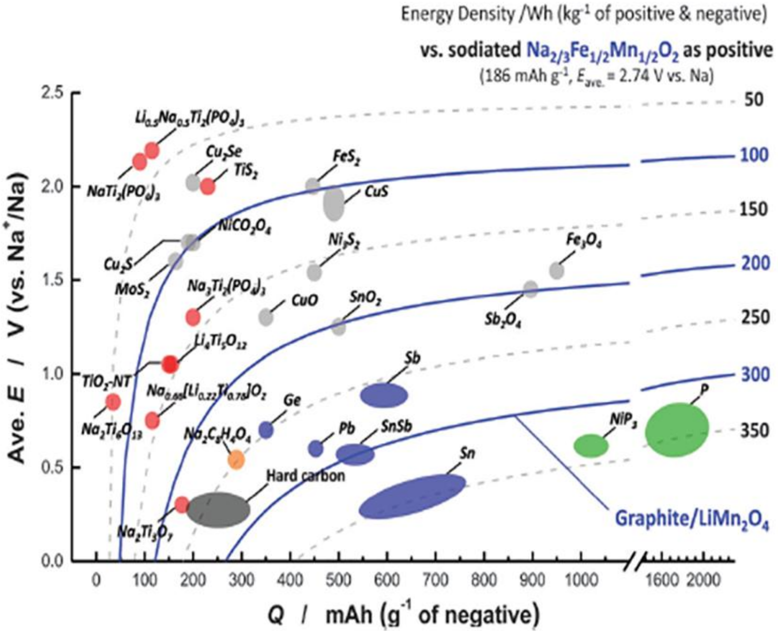

Figure 1.6: Average voltage and energy density *vs.* gravimetric capacity of reported anode material for NIBs: carbons (black), titanium-based (red), organic based (orange) and phosphorous (green) compounds, oxides and sulphides (gray) and alloys (blue). The energy density has been calculated *vs.* P2-$Na_{2/3}[Fe_{1/2}Mn_{1/2}]O_2$ [20].

1.3.1.1. Carbons

One of the most employed anodes for NIBs is the HC and its electrochemical performance depends on the synthesis conditions such as carbon source and carbonization temperature. The reaction voltage is close to 0 V *vs.* Na^+/Na and hence at high current density represents a safety hazard because of the possible Na plating [18]. The reversible Na^+ insertion/ extraction into HC was firstly reported by Stevens *et al*. where they prepared a HC by carbonization of glucose at 1000 °C with a high reversible capacity of ~ 300 mAh/g in the voltage range of 1.2 - 0.1 V *vs.* Na^+/Na for more than 100 cycles at low C rate of C/80 (5 mA/g). However, several improvements have been performed in recent years and when sucrose is carbonized at 1300 °C a reversible capacity of 200 mAh/g is observed with a 90% of Coulombic efficiency at higher C rate, more precisely at 0.1C [18]. Moreover, as regards the Na^+ insertion/extraction mechanisms the HC not react via an intercalation mechanism but by porous filling of the disordered carbon layers, although the mechanisms is still controversial [23, 24].

Furthermore, graphite, which is the most common Li-ion anode material, is able to insert only a very limited amount of Na^+ (NaC_{70}) [25]. Nevertheless, the recent investigation shows the possibility to insert Na^+ in expanded graphite. The interlayer distance between the graphene layers is directly correlated with the reversible capacity, the optimal spacing being 4.3 Å and resulting in 280 mAh/g at 20 mA/g [26]. Jache *et al.* have also demonstrated the possibility of co-intercalating Na^+ in graphite with a $Na(dyglyme)_2C_{20}$ stoichiometry, which leads close to 100 mAh/g for 1000 cycles [27]. Nevertheless, their performance is still far from that of LIBs.

1.3.1.2. Titanium-based compounds

Titanium-based oxides represent a promising family of anode materials because of their low cost, low toxicity, easiness of preparation and safety also at high current density [28]. There is a wide variety of reported compounds which can reversibly insert Na^+ (see **Table 1.9**) such as binary oxides (several TiO_2 polymorphs), ternary oxides with general formula $A_xTi_nO_{2n+1}$ or $A_xTi_nO_{2n+2}$ that crystallize in layered or tunnel structures, quaternary oxides and NASCION type structures.

Table 1.9: Some characteristic of the most studied Ti-based compounds as negative electrode for NIBs.

Material	Cap. 1st dis. (mAh/g)	1st irrev. Cap. (mAh/g)	Average V (V)	Cap. reten. at 20th cycle*	Rate	Structure
Anatase [29]	650	405	0.3	92%	0.1C	Tunnel
Rutile[30]	400	275	~ 0.7	+40%[a]	0.15C	Tunnel
β-TiO_2[31]	430	245	~ 0.75	59%	0.1C	Tunnel
$H_2Ti_3O_7$[32]	135	60	1.3	6%	0.1C	Layered
$Na_2Ti_6O_{13}$[33]	65	23	0.83	90%[b]	0.2C	Tunnel
O3-$NaTiO_2$[34]	168	16	0.9	99%	0.1C	Layered
N-$Na_2Ti_7O_{15}$[35]	550	300	0.55 - 0.3	76%[b]	0.1 A/g	Tunnel
$NaTi_3O_6(OH)\cdot 2H_2O$[36]	275	125	0.3	--	30 mA/g	Layered
T-$Na_4Ti_5O_{12}$[37]	65	40	~ 0.5	--	0.05C	Tunnel
M-$Na_4Ti_5O_{12}$[38]	137	67	~ 1.0	80%	0.05C	Layered
$Li_4Ti_5O_{12}$[39]	170	30	0.91	99%	0.1C	Tunnel
$Na_2Ti_4O_9$[40]	530	410	0.8	~ 60%	12 mA/g	Tunnel
$Na_2Ti_3O_7$[41]	351	192	0.3	90%	0.1C	Layered
$Na_1[FeTi]O_4$[42]	330	149	1.2	--	0.1C	Tunnel
$Na_{4/3}[FeTi]O_4$[42]	275	155	1.2	-	0.1C	Tunnel
$Na_{2.65}Ti_{3.35}Fe_{0.65}O_9$/C [43]	380	205	0.5	74%	40 mA/g	Tunnel
$NaTi_2(PO_4)_3$[44]	160	--	2.1	--	0.1C	Tunnel

* Capacity retention has been determined taking into account the 1st charge capacity.

[a] The capacity increases in the first 15 cycles due to side reactions.

[b] Capacity retention of the 50th cycle.

Among binary oxides the most promising TiO_2 polymorphs until nowadays is C-coated anatase TiO_2 nanoparticles (~ 11 nm) which reaches 227 mAh/g at 0.1C and at higher current density (10C) more than the half of the capacity is keep it (134 mAh/g) [29]. Amongst ternary oxides, several compounds have been reported in the last years inspired in the 80s work of Maazas *et al*. [45] (see **Table 1.9**). The most studied ternary Ti-based compound are the tunnel structure $Na_2Ti_6O_{13}$ and the layered structure $Na_2Ti_3O_7$. $Na_2Ti_6O_{13}$ only intercalate 1 Na^+ at 0.83 V *vs.* Na^+/Na, resulting in a capacity of 40 mAh/g at 0.1C but is able to deliver 25 mAh/g at very high current density of 20C over 5000 cycles [33]. While $Na_2Ti_3O_7$ is one of the most promising Ti-based oxides because has the lowest voltage ever reported at 0.3 V *vs.* Na^+/Na, which inserts additionally 2 Na^+, and good specific capacity close to 178 mAh/g [46]. Interestingly, the Na^+ insertion voltage is 1.3 V lower than in the Li analogue ($Li_2Ti_3O_7$) and this has been attributed to the larger radius of Na^+ that destabilizes the sodiated material and the lower polarizing character of Na^+ than Li which produce the expansion of the sodiated cell volume in contrary to in $Li_4Ti_3O_7$ [47]. However, these promising characteristics are hindered since $Na_2Ti_3O_7$ exhibits a poor capacity retention where in the best experimentally results it delivers a reversible capacity of 150 mAh/g at the 20th cycle at 0.1C [41]. Hence it is necessary to improve the capacity retention. Finally, NASICON type structure $NaTi_2(PO_4)_3$ [48] also can be a good candidate, since although reversibly deintercalate/intercalate 2 Na^+ at 2.1 V *vs*. Na^+/Na which is quite high voltage plateau to use as anode, is possible to avoid the organic electrolyte decomposition that can be beneficial for a long-term cycle life or it is also possible to use as anode in aqueous media [49]. Moreover, recently Senguttuvan *et al.* discovered that the Ti^{+3}/Ti^{2+} redox pair is also accessible at lower voltage which opens the doors to use as low voltage anode material [44].

1.3.2. Cathode materials

A great variety of compounds are studied as possible cathode materials for NIBs but can be roughly grouped in three main families: layered oxides, polyanionic compounds and Prussian blue analogues (**Figure 1.7**), where each family presents its own advantages and disadvantages [50].

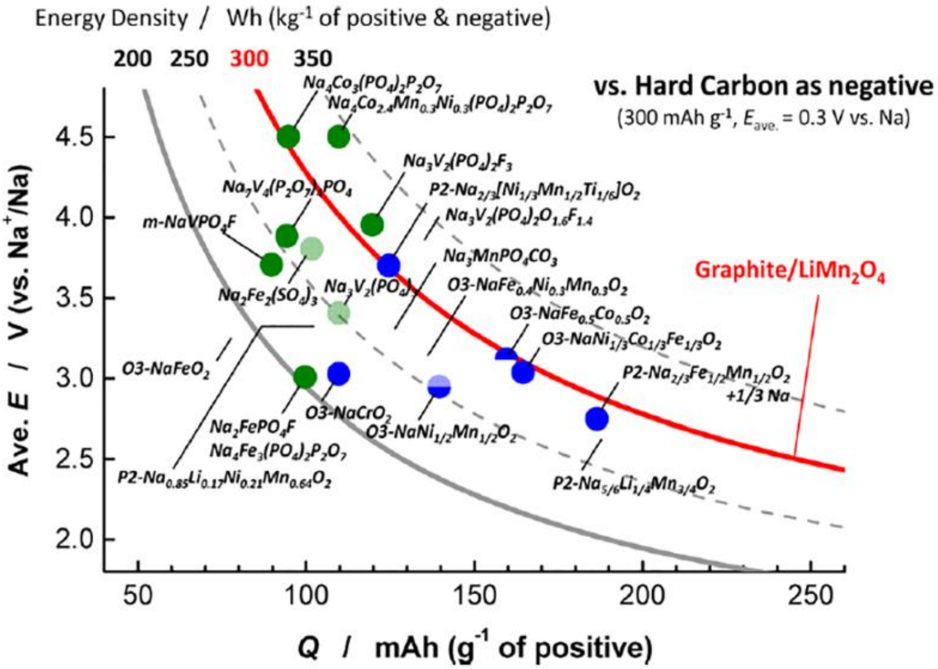

Figure 1.7: Average voltage and energy density *vs.* gravimetric capacity of reported cathode materials for NIBs: layered oxides (blue) and polyanionic compounds (green). The energy density has been calculated *vs.* HC [18].

1.3.2.1. Layered oxides

Layered oxides are considered as the most promising cathode material for NIBs due to their higher capacity compared with other cathode compounds. Moreover, most of them are composed by earth abundant T_Ms (T_M= one or more transition metal) and hence are low-cost compounds. Although, most of them are air sensitive which would be a drawback for low-cost applications [51]. The general formula of layered oxides is $Na_xT_MO_2$ and they crystallize in several layered type structures depending on the alkaline atom position (octahedral (O), tetrahedral (T) or prismatic (P)) and on the oxygen position in the hexagonal sheets (A, B or C). Hence, taking into account these two aspects, the possible structures types are: octahedral ABCABC (O3-type), tetrahedral ABAB (T1-type) and prismatic ABBA (P2-type) or ABBCCA (P3-type) [52]. Most cathode materials studied so far crystallize in O3-type (**Figure 1.8a**) or P2-type (**Figure 1.8b**) and most of them are based on Mn and Fe due to their abundance in the earth.

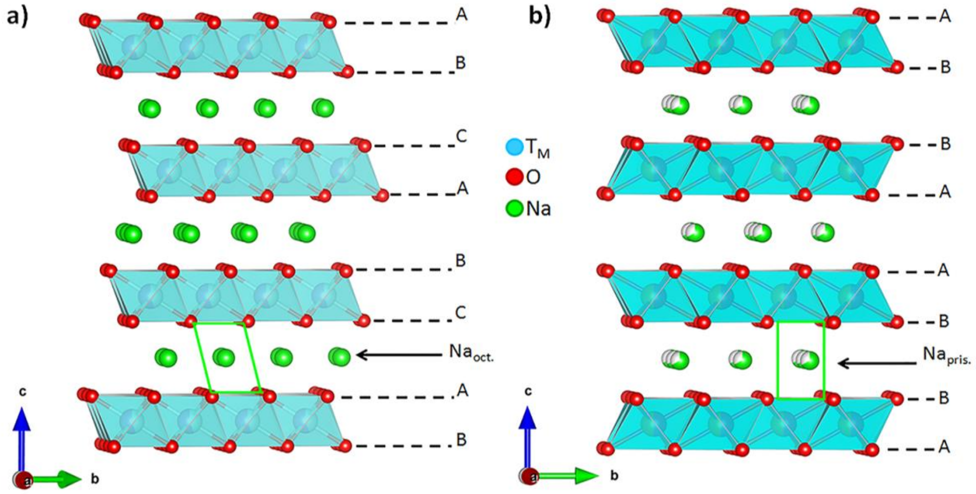

Figure 1.8: Structures of **a)** O3-$Na_xT_MO_2$ and **b)** P2-$Na_XT_MO_2$ The symbols A, B and C represent the three different oxygen layers.

P2-$Na_{2/3}[Fe_{1/2}Mn_{1/2}]O_2$ is a promising layered oxide in terms of cost and energy density. This material, made from earth abundant elements, delivers a high reversible capacity (190 mAh/g) when is cycled in the voltage range 1.5 - 4.3 V *vs.* Na^+/Na (average voltage of 2.75 V) and has a comparable energy density (520 Wh/kg) to that of LIBs cathode material LFP (530 Wh/kg) considering metallic Na or Li respectively as anode, which at the moment is not a commercial option. The P2-type compound shows higher capacities but also higher irreversibility in the first cycle (50 mAh/g) than O3-type [53, 54].Moreover, the capacity retention (84% at 15th cycle) [53] of P2-$Na_{2/3}[Fe_{1/2}Mn_{1/2}]O_2$ should be enhance and one of the reason of that capacity degradation might be the phase transition from P2 to OP4 (BACBBCAB) [55].

A few approaches have been followed in the recent years to decreases the irreversibility of the 1st cycle due to the Na deficiency of the initial material as well as to improve the cyclability. Singh *et al.* added 5 wt.% of NaN_3 to improve the 1st cycle irreversibility [56] while Zhang *et al.* mixed with metallic Na [57]. On the other hand, the most common strategy to improve cyclability has been to partially replace Mn by other electrochemically active or inactive elements such us, Ti^{4+} [58], Ni^{2+}[59, 60], Mg^{2+} [61, 62] or Li^+ [63] which in general exhibit better capacity retention, higher potential voltage and/or better structural stability. Another procedure to enhance the capacity retention is by alternative synthesis route for example by sol-gel method [64] or using $NH_3.H_2O$ as chelating agent [65]. However, the most useful approach has been shown when the high cut-off voltage was controlled, being the main hypothesis of the capacity loss the structural transitions. Although the reason of that improvement is not clear and is not corroborated yet [60, 64, 65, 66].

1.3.2.2. Polyanionic compounds

Another studied family of cathode materials for NIBs are polyanionic compounds [15] where several phosphate, pyrophosphates, fluorophosphates, sulfates and combinations of them have been reported as possible cathode material [16, 50]. Although in general the polyanions exhibit lower specific capacity than layered oxides, they provide good specific capacity at low and high current density, good thermal stability and very good long cycle life due to their stable framework during Na^+ deintercalation/intercalation processes [50].

$NaFePO_4$ (NFP) olivine type is a well known cathode material since is the Na analogue to olivine type LFP, which is a low cost and safe alternative to the most used LCO [12]. Olivine NFP operates around 3.0 V *vs*. Na^+/Na and has a high theoretical specific capacity (154 mAh/g) and high theoretical energy density of 446 W/kg *vs*. metallic Na (which is not a commercial option due to the safety hazard). Experimentally it reaches 80% of the theoretical capacity at low rate (125 mAh/g, 0.04C) which has been attributed to the poor electronic and ionic conductivity of the formed $FePO_4$ [67], despite the theoretical calculations suggest that good Na^+ mobility [68]. It has been shown that the mechanism of NFP is different than that of LFP, since NFP exhibits a $Na_{0.7}FePO_4$ intermediate phase [69, 70]. However, the disadvantage is that the olivine type should be synthesized via LFP delithiation since maricite NFP is more thermodynamically stable. The latter, contrary to the common believe of poor electrochemical activity [71, 72], has been recently shown to deliver 142 mAh/g at 0.05C when nanosized, which is 92% of the theoretical capacity, and a good capacity retention of 95% over 200 cycles [73].

Pyrophosphates ($NaT_MP_2O_7/Na_2T_MP_2O_7$) represent another family of polyanionic compounds that have been proposed as cathode materials for their stable 3D $(P_2O_7)^{4-}$ framework, rich chemistry, ease of synthesis, good Na^+ mobility and multiple available sites for it. Several compositions have been synthesized such as, $NaFeP_2O_7$, $NaTiP_2O_7$, $NaVP_2O_7$, $Na_2FeP_2O_7$, $Na_2MnP_2O_7$, $Na_2CoP_2O_7$, $Na_2CuP_2O_7$ and $Na_2VOP_2O_7$ [74]. However to the best of our knowledge, most of them have not been tested as electrode for NIBs yet. The studied compounds are the 3D structure triclinic-$Na_2FeP_2O_7$ [75, 76] and (P1) $Na_2MnP_2O_7$ [77], and layered orthorhombic

$Na_2CoP_2O_7$ [78] with 2D channels for Na^+ mobility. The three compounds exhibit the T_M^{3+}/T_M^{2+} plateau around 3.0 V *vs.* Na^+/Na (expect the Mn compound, at 3.6 V) and reach a capacity around 80 - 90 mAh/g at low current C rate of 0.05C. Their theoretical specific capacities close to 100 mAh/g and experimental ones are quite close, however, further optimization should be carried out.

New approach to enhance the theoretical capacity and the average voltage of the pyrophosphate is by combining with phosphate groups. Several compounds have been reported in the last three years, $Na_4Fe_3(PO_4)_2(P_2O_7)$ [79], $Na_4Co_3(PO_4)_2(P_2O_7)$ [80], $Na_4Co_{2.4}Mn_{0.3}Ni_{0.3}(PO_4)_2(P_2O_7)$ [81], $Na_4Mn_3(PO_4)_2(P_2O_7)$ [82] and $Na_4Ni_3(PO_4)_2(P_2O_7)$ [83]. These compounds are formed by PO_4^{3-} and $P_2O_7^{4-}$ groups which crystallize in an orthorhombic non-centrosymmetric space group, $Pn2_1a$. $[T_{M3}P_2O_{13}]$ blocks are in parallel to *bc* plane (**Figure 1.9a**) building up $[T_MO_6]$ octahedra and $[PO_4]$ tetrahedral which they are sharing corner along *a* direction (**Figure 1.9b**). This 3D structure gives a good polyhedral connectivity and produces 3D large tunnels along three main crystallographic directions ([100], [010], [001]). Na^+ are accommodated within these tunnels, where there are four symmetrically distinguishable Na sites. Two of them formed by NaO_7 polyhedra and NaO_6 octahedra along *a* and the other two Na formed by NaO_6 octahedra on the *b-c* plane [84, 85].

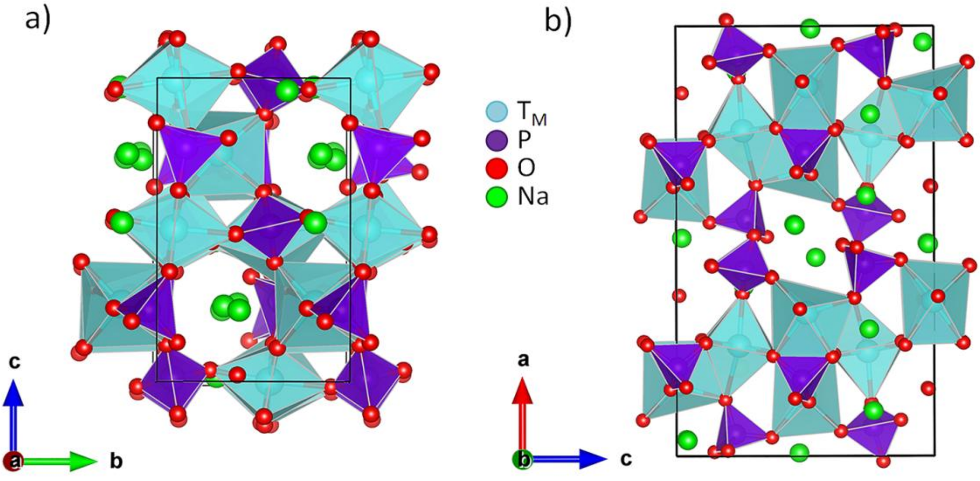

Figure 1.9: Structure of $Na_4T_{M3}(PO_4)_2P_2O_7$ (T_M = Co, Fe, Mn, Ni) along **a)** *a* and **b)** *b*

The polyanions which are formed by PO_4^{3-} and $P_2O_7^{4-}$ groups not only provide higher theoretical capacity than the compounds with only $P_2O_7^{4-}$ groups, additionally the redox potential is increased than that of phosphate and pyrophosphate compounds with only one of each group. **Figure 1.7** shows the energy density of some cathode for NIBs taking into account as anode HC, and the cell HC *vs.* $Na_4Co_{3-x}T_{Mx}(PO_4)_2(P_2O_7)$ (T_M=Mn, Ni) delivers similar energy density (300 Wh/kg) than Graphite *vs.* $LiMn_2O_4$. Moreover, these PO_4^{3-} and $P_2O_7^{4-}$ mixed polyanions present low activation energy and good Na^+ diffusion coefficient; therefore they are very good cathode candidates for high rate applications. Furthermore, they suffer low volume change during cycling [86] which is very important for a good long-term cycle life of the batteries. **Table 1.10** shows some differences of electrochemical properties of the PO_4^{3-} and $P_2O_7^{4-}$ mixed polyanions studied as cathode material.

Table 1.10: Some characteristic of the studied PO_4^{3-} and $P_2O_7^{4-}$ mixed polyanions $Na_4T_{M3}(PO_4)_2P_2O_7$ as cathode for NIBs.

Parameters	T_M=Fe [79]	T_M=Co [80]	T_M=$Co_{2.4}Mn_{0.3}Ni_{0.3}$ [81]	T_M=Mn [82]	T_M=Ni[a] [83]
Theoretical cap. (mAh/g)	129	127	129	129	129
Cap. 1st charge (mAh/g)	~ 105	130	150	90	
1st irrev. cap. (mAh/g)	~ 5	30	60	~ 5	
Exp. cap. (mAh/g)	100	95	90	~ 85	25
Average V (V)	3.2	4.5	~ 4.4	3.84	~ 3.1
Cap. reten at 15th the cycle*	99.9%	99.9%	--	94%	99.9%
C-rate	0.05C	0.2C	0.2C	0.2C	40C
Energy density (Wh/kg)	320	428	396	327	77.5

* Cap. reten. has been determinate taking into account the 1st insertion capacity.

[a] It has not been tested as cathode for NIBs but for hybrid supercapacitor, using 2 M NaOH solution, Pt foil and Ag/AgCl as electrolyte, counter and reference electrode, respectively.

1.3.3. Electrolyte

The choice of the electrolyte will affect to the cycle life, electrochemical performance, capacity values, rate capability, capacity retention and safety among others parameters of the battery [87]. A good electrolyte should fulfil several properties such as:

1. Lack of reactivity or at least stable passivation reactions during the cycling with other components of the battery: electrode, current collectors, separator, cell container, etc.

2. Electrochemical stability in a wide voltage range. Since most electrode materials operate outside the electrolyte electrochemical stability window (ESW) and stable, homogeneous, ionic conductor and electronic insulator electrode/electrolyte interphase should be formed, known as Solid Electrolyte Interphase (SEI) in the anode side and Solid Permeable Interphase (SPI) in the cathode side.

3. Thermal stability in typical operation temperatures ($- 10\ ^{o}C \leq T \leq 60\ ^{o}C$).

4. High ionic conductivity since Na^+ should go from one electrode to the other during the electrochemical reaction.

5. Absence of electronic conductivity since electrons must go through the external electric circuit from one electrode to the other.

6. Low toxicity and low-cost, which these aspects are much more important in NIBs than in LIBs.

The knowledge acquired for LIBs electrolytes is being implemented for NIBs and hence, the most commonly used electrolytes for NIBs are the analogue organic electrolytes to those of LIBs, which consist of an inorganic salt dissolved in an organic solvent or a mixture of two or more of them. However, the differences in the chemistry of Li^+ and Na^+, for example the radius, Lewis acidity, cation-anion interaction and the solvation degree, make the direct transfer from LIBs to NIBs more difficult than expected.

On the one hand, the salts influence mainly in the chemical and electrochemical stability. Indeed, the anion part of the salt limits the upper voltage since is the first to oxidize, while the lower limit voltage is limited mostly for the solvent reduction. On the other hand, the solvent controls more the thermal stability and ion mobility which is approximately inversely proportional to electrolyte viscosity [87].

Na-salts in general show higher melting point and thermal stability than Li-salts which is an advantage in terms of safety. The most used salts for NIBs are $NaClO_4$ and $NaPF_6$ followed by NaTFSI and NaFSI however, all of them exhibit different drawbacks. $NaClO_4$ is not safe, the ClO_4^- anion is strongly oxidant and $NaClO_4$ is hygroscopic being difficult to dry [88]. $NaPF_6$ is easier to dry nevertheless, PF_6^-

suffers hydrolysis reaction forming PF_5, POF_3 and HF. NaTFSI and NaFSI have lower upper limit voltages (not higher than 3.3 - 3.5 V) due to the anion ($TFSI^-$ or FSI^-) and corrode the Al current collector [19].

Organic solvents should have high dielectric constant (ε >15) for an easy salt dissociation, long liquid range and low viscosity as well as good ionic conductivity. Because all these parameters are necessary, a mixture of solvents is normally used as in LIBs, such as EC:PC, EC:DMC, EC:DEC, etc. [87]. It should be taken into account that for a good formation of the SEI, even SPI layer, and stability of electrode materials the mixture of solvent is fundamental. For example, in LIBs graphite does not combine well with only PC-based electrolyte since PC intercalates together with Li^+ between the graphite planes causing graphite exfoliation and capacity lose, that issue is solved by the addition of EC [12] (in NIBs this issue is not important since the Na^+ cannot intercalate into graphite [25]). Furthermore, the addition of a 3rd component in a small amount, usually less than 5 wt.%, can modify the SEI layer properties forming a more stable layer. Theses additives have lower LUMO (lowest unoccupied molecular orbital energies) than organic solvents and hence increase the lower voltage limit [87]. The most used additive in NIBs is fluoroethylene carbonate (FEC) [89, 90, 91].

Several of these organic liquid electrolytes have been investigated by various groups. Ponrouch *et al.* found that $NaClO_4$ or $NaPF_6$ in EC:PC (50:50 wt.%) solvent mixtures is the best choice for HC [92]. Latter they studied that adding 10 wt.% of DMC in this mixture shows better ionic conductivity and lower viscosity, resulting in a better capacities and rate capability [93]. On the other hand, Zhao *et al*. report better capacity retention with $NaClO_4$ EC:DMC (50:50 vol.%) electrolyte for HC [94]. FEC additive has also been studied and some discrepancies have been reported. While Komaba *et al*. identified that the FEC improves the irreversibility of the HC [89], Ponrouch *et al*. showed that an additive-free electrolyte resulted in lower irreversibility and better capacity stability [95].

Therefore, the electrolyte study in detail has been performed mainly using HC as anode and to the best of our knowledge never has been tested with other anode material. However during this year several electrolyte studies have been reported for example using sodium Prussian Blue as cathode [96]. Nevertheless, contradictory results have been obtained using even similar electrode compounds which show the high importance of the electrolyte as well as the combinations between the electrodes and its. And hence, is necessary more work as regard the electrolyte and its behaviour to fully characterize each system.

1.4. Solid Electrolyte Interphase and Solid Permeable Interphase

As already mentioned, the electrolyte reduction/oxidation is usually expected since normally the working voltage range of the active materials used as electrodes is outside the electrolyte ESW. The ESW is defined by the LUMO and the highest occupied molecular orbital (HOMO) of the electrolyte. Therefore the SEI layer will be formed when the anode electrochemical potential (μ_A) is outside of the electrolyte ESW and electrolyte will be reduced. Analogously, the oxidation of the electrolyte occurs when the cathode electrochemical potential (μ_C) is not inside the ESW of the electrolyte and a SPI layer will be formed. Hence, the formation of a homogeneous and stable passivation SEI layer in the anode or SPI layer in the cathode will be needed to widen the ESW while avoiding further electron transfer between the electrode and electrolyte and the continuous electrolyte reduction/oxidation [97].

Since the SEI layer model was described for the first time by Peled in 1979 [98, 99], many investigations have been carried out on the study of the morphology, composition, properties and electrochemical behaviour of this layer as well as of SPI in LIBs performing several changes on the proposed model of Peled [100, 101, 102, 103, 104, 105, 106]. However, there are not any direct proofs that veracity the described models. The SEI and SPI layer usually are formed along the 1st discharge (for negative electrode) or charge (for positive electrode) cycle due to electrolyte decomposition. This is normally more significant in the negative electrode than in the positive because most cathode materials work inside the electrolyte ESW although some oxidation reactions occur above 3.0 - 3.5 V [107]. These interphases formation are one of the main responsible factors for the 1st irreversible capacity, and involves the loss of a certain amount of the electrolyte. Nevertheless, the formation of the interphase (SEI and SPI) is necessary since will protect the electrolyte against further decomposition (if it is stable upon cycling) in the following cycles. Furthermore their properties determine the safety, power capability, morphology of Li deposits, shelf life and cycle life of the battery. It was proposed that the SEI layer of LIBs is divided in two main parts one close to the electrode formed by inorganic compounds; and another one closer to the electrolyte, whose main components are organic species and which are the main component in the overall SEI layer. Moreover, the thickness in general is between >20 nm. While the thickness of the SPI layer was estimated to a few nanometers with a similar composition as SEI layer. Although the electrode/electrolyte interphase properties (morphology, composition and thickness) vary depends on the electrochemical configuration (electrode and electrolyte) [105, 106, 108].

The ESW of some Na-based organic liquid electrolytes such as $NaClO_4$, $NaPF_6$ and $NaCF_3SO_3$ dissolved in EC:DMC has been reported to be around ~ 1.0 to 4.5 - 5.0 V *vs.* Na^+/Na (0.3 V higher than Li-based organic electrolytes) (**Figure 1.10**). Although the electrolyte EWS range depends on the mixture of solvent and salt as well as in the material used to determinate the stability. Since some side reduction and oxidation reactions already occur below 1.0 V and above 3.0 V, respectively as in Li-based electrolytes due to the electrolyte ESW strongly depends on the used working electrode and current collector [109]. Therefore several discrepancies can be found in the literature suggesting that the electrolyte ESW range is expected to vary depending on the electrochemical system.

Despite the composition and stability of the SEI and SPI layer of Na-material have a important role few works have been reported and most of them in the last two years, such as, HCs [119, 110], Sb [111, 112], Cu_2Sb thin films [113], SnSb/C nanofibres [114] and $Na_2Ti_3O_7$ [115]. The most studied SEI layer for NIBs is onto HC anode material. The first study was reported by Komaba *et al.* which analysed the SEI by scanning electronic microscopy (SEM), transmission electronic microscopy (TEM), X-ray photoelectron spectroscopy (XPS) and time-of-flight secondary ion mass spectroscopy (TOF-SIMS). The experiments concluded that the SEI morphology and composition of NIBs differs from LIBs. SEM images shown dispersed sub-micrometer particles onto the electrode surface where the particles were larger and unevenly distributed. TEM experiments revealed a rough and non-uniform SEI layer onto HC. Moreover, XPS spectra and TOF-SIM confirmed that the SEI formed in the Na-based battery is mainly composed by inorganic compounds, with a thickness around 5 - 10 nm (much thinner than in LIBs) as determined by Ar^+ etching [119].

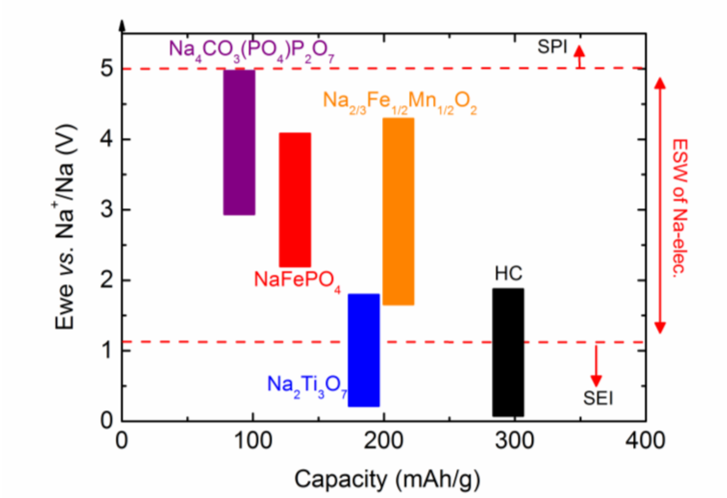

Figure 1.10: Ewe *vs.* capacity of the studied electrode materials in this thesis related with the "theoretically" EWS of 0.5 M $NaPF_6$ EC: DMC electrolyte.

Bodenes *et al*. studied the comparison of the SEI layer formed onto Sb anode for Na ion and Li-ion battery by XPS. The formed SEI layer using PVdF as binder was found to be quite similar. Nevertheless, more differences have been found when Na-CMC was used as binder. As Komaba *et al*. observed, more inorganic compounds have been found in NIBs, while in LIBs the SEI was mainly formed by hydrocarbons. Again, the Li-ion cells exhibited a much thicker SEI layer than the Na-ion cell [111]. Recently, Darwiche *et al*. reported that using 1 M $NaClO_4$ in PC as electrolyte a stable SEI layer was formed composed mainly by Na_2CO_3 [112].

SEI formation when Cu_2Sb thin film was used as anode has also been investigated by XPS. As already has been shown for HC and Sb the composition of SEI layer consisted mainly in carbonates ($Na_{2-x}CO_3R_x$) with some minor quantities of ether, and the formed layer was not stable. They suggest that the reason of this instability was due to the material contraction associated with Na^+ extraction [113]. However, SnSb porous carbon nanofibres were found to form a stable SEI layer *vs.* Na^+/Na but the main reason has been attributed to the fact that the FEC additive was used and would suppress the decomposition of the electrolyte, improving the quality of the SEI and stabilizing it during cycling [114].

Another anode material studied has been $Na_2Ti_3O_7$ which formed an unstable SEI layer, although the study has been carried out by *ex-situ* HRTEM and Fourier Transform Infrared Spectroscopy (FTIR) and not with XPS, which gives more information regarding its surface composition [115].

Finally only one work has been recently published with regards to the study of the SPI layer onto a Na-based cathode. The used cathode material has been the P2-$Na_x[Co_{2/3}Mn_{2/9}Ni_{1/9}]_2$ and the formed SPI was thinner and quite stable comparing to the SEI layer. However, some small changes in composition and thickness have been observed during the cycling. The composition consisted mainly in inorganic compounds (primarily Na_2CO_3) and $NaPF_6$ salt decomposition products where phosphate has been found at low potential (lower than 3.7 V) while at high potential, above 4.25 V fluorophosphates has been detected in majority [116].

Hence the formation of a homogeneous and stable SEI and SPI interphase in NIBs is less favourable than for LIBs [20] due to the fact that the Na^+ has higher chemical reactivity and lower Lewis acidity than Li^+. Additionally, the Na^+ intercalation material has higher reactivity than Li^+ material and the formed products during the electrolyte decomposition have higher solubility in the organic electrolyte, for example Na_2CO_3 [87. 117, 118]. Thus, the nature and properties of the SEI and SPI such as, composition, thickness and stability during cycling are expected to be different for NIBs. The SEI layer of NIBs has been reported to be mainly formed by inorganic compounds and with a thickness close to 10 nm in contrast to the thicker layer of LIBs which mainly is formed by organic species [87, 106,119].

1.5. Aim of this doctoral thesis

The aim of this doctoral thesis is to study the transport properties linked to their structural transitions upon cycling and the composition and stability of the electrode/electrolyte interphase for low and high voltage Na-ion materials. At the beginning of this thesis, in 2012, for the best of our knowledge there were not works focussed on the transport properties of Na-based material and there was only Komaba *et a*l. work regarding the composition and stability of the SEI layer on HC. $Na_2Ti_3O_7$ had just been reported as promising anode for NIBs and was chosen for the first part of this study since is the oxide electrode with the lowest voltage ever reported (at 0.3 V *vs.* Na^+/Na) and leads a specific capacity close to 178 mAh/g. However, its promising electrochemical properties are hindered by a continuous capacity fading. **Chapter 2** deals with the origin of the capacity fading and several strategies are provided to enhance the electrochemical properties, such as synthesis parameters, C-coating and water soluble binder. Once the electrochemical properties were improved the transport properties and the formed SEI layer were studied by Electrochemical Impedance spectroscopy (EIS) (transport properties even SEI layer stability) and X-ray photoelectron spectroscopy (XPS) (**chapter 3**). Moreover, due to the high reactivity of metallic Na the SEI layer properties (composition, evolution, stability) were studied not only in a half-cell, also in full-cell using $NaFePO_4$ as counter electrode (**chapter 3**). Finally, due to the lack information in the cathode electrode/electrolyte interphase (SPI) (the first report corresponds to 2016) and also on the transport properties we have studied the electronic/ionic conductivity and the SPI layer formed onto two promising high cut-off voltage cathode materials for NIBs: P2-$Na_{2/3}[Fe_{1/2}Mn_{1/2}]O_2$ (**chapter 4**) and $Na_4Co_3(PO_4)_2P_2O_7$ (**chapter 5**). The layered oxide has been chosen for its high energy density (520 Wh/kg *vs*. Na) and low-cost, and the polyanionic compounds because it has the highest Na^+ intercalation/deintercalation voltage (average voltage at 4.5 V) reported up to date.

1.6. References

[1] International Energy Outlook 2016, U.S. Energy Information Administration, EIA, July 2016, http://www.eia.gov/forecasts/ieo/

[2] World Energy Outlook 2015, Energy Information Administration, EIA, July 2016, http://www.worldenergyoutlook.org/

[3] Euskadi Energia 2014. Energia datuak, Datos energéticos, EVE, Ente Vasco de la Energía, June 2016, http://www.eve.eus

[4] Estrategia energética de Euskadi 2025, EVE, Ente Vasco de la Energía, June 2016, http://www.eve.eus

[5] Inventario de emisiones de gases de efecto invernadero. Comunidad autónoma del País Vasco, ©Ihobe S.A, June 2016, http://www.ihobe.net

[6] Z. Yang, J. Zhang, M.C.W. Kintner-Meyer, X. Lu, D. Choi, J.P. Lemmon, J. Liu, Electrochemical energy storage for green grid, Chem. Rev. 111 (2011) 3577-3616.

[7] M. Skyllas-Kazacos, M.H. Chakrabarti, S.A. Hajimolana, F.S. Mjalli, M. Saleem, Progress in flow battery research and development, J. Electrochem. Soc. 158 2011 R55-R79.

[8] T.B. Reddy, D. Linden, Linden´s handbook of batteries, 4th ed., Mc Graw Hill Companies, Inc., United State of America, 2011.

[9] B. Dunn, H. Kamath, J.M. Tarascon, Electrical energy storage for the grid: a battery of choices, Science, 334 (2011) 928-935.

[10] J. Sudworth, R. Tilley, The sodium sulfur battery, Chapman and Hall Ltd., London 1985.

[11] http://www.sonyenergy-devices.co.jp/en/keyword/ (acceded June 2016).

[12] N. Nitta, F. Wu, J.T. Lee, G. Yushin, Li-ion battery materials: present and future, Mater. Todays 18 (2015) 252-264.

[13] K. Mizushima, P.C. Jones, P.J. Wiseman, J.B. Goodenough, Li_xCoO_2 (0<x<1): a new cathode material for batteries of high energy density, Mat. Res. Bull. 15 (1980) 783-789.

[14] P.A. Nelson, K.G. Gallagher, I. Bloom, D.W. Dees, Modeling the performance and cost of lithium-ion batteries for electric-drive vehicles, Electrochemical Energy Storage Theme, Chemical Sciences and Engineering division, Argonne National Laboratory, September 2011.

[15] V. Palomares, P. Serras, I. Villaluenga, K.B. Hueso, J. Carretero-González, T. Rojo, Na-ion batteries, recent advances and present challenges to become low cost energy storage systems, Energy Environ. Sci. 5 (2012) 5884-5901.

[16] H. Pan, Y.S. Hu, L. Chen, Room-temperature, stationary sodium-ion batteries for large-scale electric energy storage, Energy Environ. Sci. 6 (2013) 2338-2360.

[17] J. Wook Choi, D. Aurbach, Promise and reality of post-lithium-ion batteries with high energy densities, Nature Rev. 1 (2016) 1-16.

[18] N. Yabuuchi, K. Kubota, M. Dahbi, S. Komaba, Research development on sodium-ion batteries, Chem. Rev. 114 (2014) 11636-11682.

---

[19] D. Kundu, E. Talaie, D.V. Duffort, L.F. Nazar, The emerging chemistry of sodium ion batteries for electrochemical energy storage, Angew. Chem. Int. Ed. 54 (2015) 3431-3448.

[20] M. Dahbi, N. Yabuuchi, K. Kubota, K. Tokiwa, S. Komaba, Negative electrodes for Na-ion batteries, Phys. Chem. Chem. Phys. 16 (2014) 15007-15028.

[21] D.I. Iermakova, R. Dugas, M.R. Palacín, A. Ponrouch, On the comparative stability of Li and Na metal anode interfaces in conventional alkyl carbonate electrolytes, J. Electrochem. Soc. 162 (2015) A7060-A7066.

[22] M.J. Jäckle, A. GroB, Microscopic properties of lithium, sodium and magnesium battery anode material related to possible dendrite growth, J. Chem. Phys. 141 (2014) 17410-1-17410-7.

[23] D. A. Stevens, J. R. Dahn, High capacity anode materials for rechargeable sodium-ion batteries, J. Electrochem. Soc. 147 (2000) 1271–1273.

[24] C. Bommier, T.W. Surta, M. Dolgos, X. Ji, New mechanistic insights on Na-ion storage in nongraphitizable carbon, Nano Lett. 15 (2015) 5888-5892.

[25] M.M. Doeff, Y. Ma, S.J. Visco, L.C. De Jonghe, Electrochemical insertion of sodium into carbon, J. Electrochem. Soc. 140 (1993) L169-L170.

[26] Y. Wen, K. He, Y. Zhu, F. Han, Y. Xu, I. Matsuda, Y. Ishii, J. Cumings, C. Wang, Expanded graphite as superior anode for sodium-ion batteries, Nat. Commun. 5 (2014) 4033-4042.

[27] B. Jache, P. Adelhelm, Use of graphite as a highly reversible electrode with superior cycle life for sodium-ion batteries by making use of co-intercalation phenomena, Angew. Chem. 126 (2014) 10333-10337.

[28] M.M. Doeff, J. Cabana, M. Shirpour; Titanate anodes for sodium ion batteries, J. Inorg. Organomet. Polym. 24 (2014) 5-14.

[29] M.N. Tahie, B. Oschman, D. Buchhloz, X. Dou, I. Lieberwirth, M. Panthöfer, W. Tremel, R. Zentel, S. Passerini, Extraodinary performance of carbon-coated anatase TiO_2 as sodium-ion anode, Adv. Energy Mater. 6 (2016) 1501489-9.

[30] H. Usui, S. Yoshioka, K. Wasada, M. Sihimizu, H. Sakaguchi, Nb-doped rutile TiO_2: a potential anode material for Na-ion battery, ACS Appl. Mater. Interfaces, 7 (2015) 6567-6573.

[31] L. Wu, D. Bresser, D. Buchholz, S. Passerini, Nanocrystaline TiO_2(B) as anode material for sodium-ion batteries, J. Electrochem. Soc. 162 (2015) A3052-A3058.

[32] A. Eguía-Barrio, E. Castillo-Martínez, M. Zarrabeitia, M.A Muñoz-Márquez, M. Casas-Cabanas, T. Rojo, Structure of $H_2Ti_3O_7$ and its evolution during sodium insertion as anode for Na ion batteries, Phys. Chem. Chem. Phys 17 (2015) 6988-6994.

[33] A. Rudola, K. Saravanan, S. Devaraj, H. Gong, P. Balaya, $Na_2Ti_6O_{13}$: a potential anode for grid-storage sodium-ion batteries, Chem. Comm. 49 (2013) 7451-7453.

[34] D. Wu, X. Li, B. Xu, N. Twu, L. Liu, G. Ceder, $NaTiO_2$: a layered anode material for sodium-ion batteries, Energy Environ. Sci. 8 (2015) 195-202.

[35] H. Li, H. Fei, X. Liu, J. Yang, M. Wei, In-situ synthesis of $Na_2Ti_7O_{15}$ nanotubes on Ti net substrate as a high performance anode for Na-ion batteries, Chem. Comm. 51 (2015) 9298-9300.

[36] M. Shirpour, J. Cabana, M. Doeff, New materials based on layered sodium titanate for dual electrochemical Na and Li intercalation systems, Energy Environ. Sci. 6 (2013) 2538-2547.

[37] S.H. Woo, Y. Park, W.Y Choi, N.S Choi, S. Nam, B. Park, K.T. Lee, Trigonal $Na_4Ti_5O_{12}$ phase as an intercalation host for rechargeable batteries, J. Electrochem. Soc. 159 (2012) A2016-A2023.

[38] P.J.P Naeyaert, M. Avdeev, N. Sharma, H.B. Yahia, C.D. Ling, Synthetic, structural and electrochemical study of monoclinic $Na_4Ti_5O_{12}$ as sodium-ion battery anode material, Chem. Mater. 26 (2014) 7067-7072.

[39] Y. Sun, L. Zhao, H. Pan, X. Lu, L. Gu, Y.S. Hu, H. Li, M. Armand, Y. Ikuhara, L. Chen, X. Huang, Direct atomic-scale confirmation of three-phase storage mechanism in $Li_4Ti_5O_{12}$ anodes for room-temperature sodium-ion batteries, Nat. Commun. 4 (2013) 1870-1880.

[40] K. Kataoka, J. Akimoto, Synthesis and electrochemical sodium and lithium insertion properties of sodium titanium oxide with the tunnel type structure, J. Power Sources 305 (2016) 151-155.

[41] M. Zarrabeitia, E. Castillo-Martínez, J.M. López Del Amo, A. Eguía-Barrio, M.A. Muñoz-Márquez, T. Rojo, Identification of the critical synthesis parameters for enhanced cycling stability of Na-ion anode material $Na_2Ti_3O_7$, Acta Mater. 104 (2016) 125-130.

[42] J. Wang, B. Qiu, X. He, T. Ristahus, H. Liu, M.C. Stan, S. Schulze, Y. Xia, Z. Liu, M. Winter, J. Li, Low-cost orthorhombic $Na_x[FeTi]O_4$ (x=1 and 4/3) compounds as anode materials for sodium-ion batteries, Chem. Mater. 27 (2015) 4374-4379.

[43] M. Xu, J.K. Hou, Y.B. Niu, G.N. Li, Y.T Li, C.M. Li, Exploration of $Na_{2.65}Ti_{3.65}Fe_{0.65}O_9$ as anode materials for Na-ion batteries, Chem. Commun. 51 (2015) 3227-3230.

[44] P. Senguttuvan, G. Rousse, M. E. Arroyo Y De Dompablo, H. Vezin, J.M. Tarascon, M.R. Palacín, Low-potential sodium insertion in a NASICON-type structure through the Ti(III)/Ti(II) redox couple, J. Am. Chem. Soc. 135 (2013) 3897–3903.

[45] A. Maazaz, C. Delmas, P. Hagenmuller, A study of the Na_xTiO_2 system by electrochemical deintercalation, J. Inclusion Phenom. 1 (1983) 45-51.

[46] P. Senguttuvan, G. Rousse, V. Seznec, J.M. Tarascon, M.R. Palacín, $Na_2Ti_3O_7$: lowest voltage ever reported oxide insertion electrode for sodium ion batteries, Chem. Mater. 23 (2011) 4109-4111.

[47] G. Rousse, M.E. Arroyo Y De Dompablo, P. Senguttuvan, A. Ponrouch, J.M. Tarascon, M.R. Palacín, Rationalization of intercalation potential and redox mechanism for $A_2Ti_3O_7$ (A = Li, Na), Chem. Mater. 25 (2013) 4946-4959.

[48] C. Delmas, F. Cherkaoui, A. Nadiri and P. Hagenmuller, A nasicon-type phase as intercalation electrode: $NaTi_2(PO_4)_3$, Mat. Res. Bull. 22 (1987) 631-639.

[49] A.J. Fernández-Ropero, D. Saurel, B. Acebedo, T. Rojo, M. Casas-Cabanas, Electrochemical characterization of $NaFePO_4$ as positive electrode in aqueous sodium-ion batteries, J. Power Sources 291 (2015) 40-45.

---

[50] V. Palomares, M. Casas-Cabanas, E. Castillo-Martínez, M.H. Han, T. Rojo, Update on Na-based battery materials. A growing research path, Energy Environ. Sci. 6 (2013) 2312-2337.

[51] M.H. Han, E. Gonzalo, G. Singh, T. Rojo, A comprehensive review of sodium layered oxides: powerful cathodes for Na-ion batteries, Energy Environ. Sci. 8 (2015) 81-102.

[52] C. Delmas, C. Fouassier, P. Hagenmuller, Structural classification and properties of the layered oxides, Physica B&C 99 (1980) 81-85.

[53] N. Yabuuchi, M. Kajiyama, J. Iwatate, H. Nishikawa, S. Hitomi, R. Okuyama, R. Usui, Y. Yamada, S. Komaba, P2-type $Na_x[Fe_{1/2}Mn_{1/2}]O_2$ made from earth-abundant elements for rechargeable Na batteries, Nat. Mater. 11 (2012) 512-517.

[54] K. Kubota, S. Komaba, Review-practical issues and future perspective for Na-ion batteries, J. Electrochem. Soc. 162 (2015) A2538-A2550.

[55] G. Singh, J.M. López del Amo, M. Galceran, S. Pérez-Villar, T. Rojo, Structural evolution during sodium deintercalation/intercation in $Na_{2/3}[Fe_{1/2}Mn_{1/2}]O_2$, J. Mater. Chem. A 3 (2015) 6954-6961.

[56] G. Singh, B. Acebedo, M. Casas-Cabanas, D. Shanmukaraj, M. Armand, T. Rojo, An approach to overcome first cycle irreversible capacity in P2-$Na_{2/3}[Fe_{1/2}Mn_{1/2}]O_2$, Electrochem. Commun. 37 (2013) 61-63.

[57] B. Zhang, R. Dugas, G. Rousse, P. Rozier, A.M. Abakumov, J.M. Tarascon, Insertion compounds and composites made by ball milling for advanced sodium ion batteries, Nat. Commun. 7 (2016) 10308.

[58] M.H. Han, E. Gonzalo, N. Sharma, J.M. López del Amo, M. Armand, M. Avdeev, J.J. Saiz Gariotaonandia, T. Rojo, High-performance P2-phase $Na_{2/3}Mn_{0.8}Fe_{0.1}Ti_{0.1}O_2$ cathode material for ambient-temperature sodium-ion batteries; Chem. Mater. 28 (2016) 106-116.

[59] H. Yoshida, N. Yabuuchi, K. Kubota, I. Ikeuchi, A. Garsuch, M. Schulz-Dobrick, S. Komaba, P2-type $Na_{2/3}Ni_{1/3}Mn_{2/3-x}Ti_xO_2$ as new positive electrode for higher energy Na-ion batteries, Chem. Comm. 50 (2014) 3677-3680.

[60] E. Talaie, V. Duffort, H.L. Smith, B. Fultz, L.F. Nazar, Structure of the high voltage phase of layered P2-$Na_{2/3-z}[Mn_{1/2}Fe_{1/2}]O_2$ and the positive effect of Ni substitution on its stability, Energy Environ. Sci. 8 (2015) 2512-2523.

[61] J. Billaud, G. Singh, A. R. Armstrong, E. Gonzalo, V. Roddatis, M. Armand, T. Rojo, P. G. Bruce, $Na_{0.67}Mn_{1-x}Mg_xO_2$ ($0 \leq x \leq 0.2$): a high capacity cathode for sodium-ion batteries Energy Environ. Sci. 7 (2014) 1387–1391.

[62] N. Sharma, N. Tapia-Ruiz, G. Singh, A.R. Armstrong, J.C. Pramudita, H.E.A. Brand, J. Billaud, P.G. Bruce, T. Rojo, Rate dependent performance related to crystal structure evolution of $Na_{0.67}Mn_{0.8}Mg_{0.2}O_2$ in a sodium-ion battery, Chem. Mater. 27 (2015) 6976-6986.

[63] N. Yabuuchi, R. Hara, M. Kajiyama, K. Kubota, T. Ishigaki, A. Hoshikawa, S. Komaba, New O2/P2-type Li-excess layered manganese oxides as promising multi-functions electrode material for rechargeable Li/Na batteries, Adv. Energy Mater. 4 (2014), 1301453-23.

[64] J. Xu, S.L. Chou, J.L. Wang, H.K. Liu, S.X. Dou, Layered P2-$Na_{0.66}Fe_{0.5}Mn_{0.5}O_2$ cathode material for rechargeable sodium-ion batteries, Chem. Electro. Chem. 1 (2014) 371-374.

[65] Y. Bai, L. Zhao, C. Wu, H. Li, Y. Li, F. Wu, Enhanced sodium ion storage behavior of P2-type $Na_{2/3}Fe_{1/2}Mn_{1/2}O_2$ synthesized via a chelating agent assisted route, ACS Appl. Mater. Interfaces 8 (2016) 2857-2865.

[66] B. Mortemard de Boisse, D. Carlier, M. Guignard, L. Bourgeois, C. Delmas, P2-$Na_xMn_{1/2}Fe_{1/2}O_2$ phase used as positive electrode in Na batteries: structural changes induced by the electrochemical (de)intercalation process, Inorg. Chem. 53 (2014) 111977-11205.

[67] S.M. Oh, S.T. Myung, J. Hassoun, B. Scrosati, Y.K. Sun, Reversible $NaFePO_4$ electrode for sodium secondary batteries, Electrochem. Commun. 22 (2012) 149-152.

[68] R. Tripathi, S.M. Wood, M.S. Islam, L.F. Nazar, Na-ion mobility in layered Na_2FePO_4F and olivine $Na[Fe,Mn]PO_4$, Energy Environ. Sci. 6 (2013) 2257-2264.

[69] M. Casas-Cabanas, V.V. Roddatis, D. Saurel, P. Kubiak, J. Carretero-González, V. Palomares, P. Serras, T. Rojo, Crystal chemistry of Na insertion/deinsertion in $FePO_4$-$NaFePO_4$, J. Mater. Chem. 22 (2012) 17421–17423.

[70] M. Galceran, D. Saurel, B. Acebedo, V.V. Roddatis, E. Martin, T. Rojo, M. Casas-Cabanas, The mechanism of $NaFePO_4$ (de)sodiation determined by in situ X-ray diffraction, Phys. Chem. Chem. Phys. 16 (2014) 8837–8842.

[71] A. Sune, F.R. Beckd, D. Haynes, J.A. Poston Jr., S.R. Narayanan, P.N. Kumta, A. Manivannan, Synthesis, characterization, and electrochemical studies of chemically synthesized $NaFePO_4$, Mater. Sci. Eng. B 177 (2012) 1729-1733.

[72] P.P. Prosini, C. Cento, A. Masci, M. Carewska, Sodium extraction from sodium iron phosphate with a maricite structure, Solid State Ionics. 263 (2014) 1-8.

[73] J. Kim, D.H. Seo, H. Kim, I. Park, J.K. Yoo, S.K. Jung, Y.U. Park, W.A. Goddard III, K. Kang, Unexpected discovery of low-cost maricite $NaFePO_4$ as a high-performance electrode for Na-ion batteries, Energy Environ. Sci. 8 (2015) 540-545.

[74] P. Barpanda, S. Nishimura, A. Yamada, High-voltage pyrophosphate cathodes, Adv. Energy Mater. 2 (2012) 841–859.

[75] P. Barpanda, G. Liu, C.D. Ling, M. Tamaru, M. Avdeev, S.C. Chung, Y. Yamada, A. Yamada, $Na_2FeP_2O_7$: a safe cathode for rechargeable sodium-ion batteries, Chem. Mater. 25 (2013) 3480–3487.

[76] H. Kim, R.A. Shakoor, C. Park, S.Y. Lim, J.S. Kim, Y.N. Jo, W. Cho, K. Miyasaka, R. Kahraman, Y. Jung, J.W. Choi, Na2FeP2O7 A promising iron-based pyrophosphate cathode for sodium rechargeable batteries: a combined experimental and theoretical study, Adv. Funct. Mater. 23 (2013) 1147-1155.

[77] P. Barpanda, T. Ye, M. Avdeev, S.C. Chung, A. Yamada, A new polymorph of $Na_2MnP_2O_7$ as a 3.6 V cathode material for sodium-ion batteries, J. Mater. Chem. A 1 (2013) 4194–4197.

[78] P. Barpanda, J. Lu, T. Ye, M. Kajiyama, S.C. Chung, N. Yabuuchi, S. Komaba, A. Yamada, A layer-structured $Na_2CoP_2O_7$ pyrophosphate cathode for sodium-ion batteries RSC Adv. 3 (2013) 3, 3857–3860.

[79] H. Kim, I. Park, D.H. Seo, S. Lee, S.W. Kim, W.J. Kwon, Y.U. Park, C.S, Kim, S. Jeon, K. Kang, New iron-based mixed-polyanion cathodes for lithium and sodium rechargeable batteries: combined first principles calculations and experimental study, J. Am. Chem. Soc. 134 (2012) 10369-10372.

[80] M. Nose, H. Nakayama, K. Nobuhara, H. Yamaguchi, S. Nakanishi, H. Iba, $Na_4Co_3(PO_4)_2P_2O_7$: a novel storage material for sodium-ion batteries, J. Power Sources 234 (2013) 175-179.

[81] M. Nose, S. Shiotani, H. Nakayama, K. Nobuhara, S. Nakanishi, H. Iba; $Na_4Co_{2.4}Mn_{0.3}Ni_{0.3}(PO_4)_2P_2O_7$: high potential and high capacity electrode material for sodium-ion batteries, Electrochem. Comun. 34 (2013) 266-269.

[82] H. Kim, G. Yoon, I. Park, K.Y. Park, B. Lee, J. Kim, Y.U. Park, S.K. Jung, H.D. Lim, D. Ahn, S. Lee, K. Kang, Anomalous Jahn-Teller behavior in a manganese-based mixed-phosphate cathode for sodium ion batteries, Energy Environ. Sci. 8 (2015) 3325-3335.

[83] B. Senthilkumar, G. Ananya, P. Ashok, S. Ramaprabhu, Synthesis of carbon coated nano-$Na_4Ni_3(PO_4)_2P_2O_7$ as a novel cathode material for hybrid supercapacitors, Electrochim. Acta 169 (2015) 447-455.

[84] F. Sanz, C. Parada, U. Amador, M.A. Monge, C. Ruiz Valero, $Na_4Co_3(PO_4)_2P_2O_7$, a new sodium cobalt phosphate containing a three-dimensional system of large intersecting tunnels, J. Solid State Chem. 123 (1996) 129-139.

[85] F. Sanz, C. Parada, J.M. Rojo, C. Ruiz-Valero, Synthesis, structure, characterization, magnetic properties and ionic conductivity of $Na_4M_3(PO_4)_2P_2O_7$ (MnII=Mn, Co, Ni), Chem. Mater. 13 (2001) 1334-1340.

[86] S.M. Wood, C. Eames, E. Kendrick, M.S. Islam, Sodium ion diffusion and voltage trends in phosphates $Na_4M_3(PO_4)_2P_2O_7$ (M= Fe, Mn, Co, Ni) for possible high-rate cathodes, J. Phys. Chem. C 119 (2015) 15935-15941.

[87] A. Ponrouch, D. Monti, A. Boschin, B. Steen, P. Johansson, M.R. Palacín, Non-aqueous electrolytes for sodium-ion batteries, J. Mater. Chem. A 3 (2015) 22-42.

[88] D.J. Devlin, P.J. Herlery, Thermal decomposition and dehydration of sodium perchlorate monohydrate, React. Solids 3 (1987) 75-84.

[89] S. Komaba, T. Ishikawa, N. Yabuuchi, W. Murata, A. Ito, Y. Ohsawa, Fluorinated ethylene carbonate as electrolyte additive for rechargeable Na batteries, ACS Appl. Mater. Interfaces 3 (2011) 4165–4168.

[90] S. Komaba, Y. Matsuura, T. Ishikawa, N. Yabuuchi, W. Murata, S. Kuze, Redox reaction of Sn-polyacrylate electrodes in aprotic Na cell, Electrochem. Commun. 21 (2012) 65-68.

[91] M. Dahbi, T. Nakano, T. Ishikawa, K. Kubota, M. Fukunishi, S. Shibahara, J.Y. Son, Y.T. Cui, H. Oji, S. Komaba, Sodium carboxymethyl cellulose as a potential binder for hard-carbon negative electrodes in sodium-ion batteries, Electrochem. Commun. 21 (2012) 65-68.

[92] A. Ponrouch, E. Marchante, M. Courty, J.M. Tarascon, M.R. Palacín, In search an optimized electrolyte for Na-ion batteries, Energy Environ. Sci. 5 (2012) 8572-8583.

---

[93] A. Ponrouch, R. Dedryvère, D. Monti, A.E. Demet, J.M.A. Mba, L. Croguennec, C. Masquelier, P. Johansson, M.R. Palacín, Towards high energy density sodium ion batteries through electrolytes optimization, Energy Envion. Sci 6 (2013) 2361-2369.

[94] J. Zhao, L. Zhao, K. Chihara, S. Okada, J. Yamaki, S. Matsumoto, S. Kuze, K. Nakane, Electrochemical and thermal properties of hard carbon-type anodes for Na-ion batteries, J. Power Sources 244 (2013) 752–757.

[95] A. Ponrouch, A.R. Goñi, M.R. Palacín, High capacity hard carbon anodes for sodium ion batteries in additive free electrolyte, Electrochem. Commun. 27 (2013) 85-88.

[96] M.Jose Piernas-Muñoz, E. Castillo-Martínez, J.L. Gómez-Cámer, T. Rojo, Optimizing the electrolyte and binder composition for sodium Prusian Blue, $Na_{1-x}Fe_{x+(1/3)}(CN)_6{\cdot}yH_2O$, as cathode in sodium ion batteries, Electrochim. Acta 10 (2016) 123-130.

[97] J.B. Goodenough, Y Kim, Challenges for rechargeable Li batteries, Chem. Mater. 22 (2010) 587-603.

[98] E. Peled, The electrochemical behavior of alkali and alkaline earth metals in nonaqueous battery systems the solid electrolyte interphase mode, J. Electrochem. Soc. 126 (1979) 2047-2051.

[99] E. Peled, D. Golodnitsky, G. Ardel. Advanced model for solid electrolyte intherphase electrode in liquid and polymer electrolytes, J. Electrochem. Soc. 144 (1997) L208-L210.

[100] D. Aurbach, Review of selected electrode-solution interactions which determine the performance of Li and Li ion batteries, J. Power Sources 89 (2000) 206-218.

[101] R.I.R. Blyth, H. Buqa, F.P. Netzer, M.G. Ramsey, J.O. Besenhard, P. Golob, M. Winter, XPS studies of graphite electrode materials for lithium ion batteries, Appl. Surf. Sci. 167 (2000) 99-106.

[102] A.M. Andersson, D.P. Abraham, R. Haasch, S. MacLaren, J. Liu, K. Amine, Surface characterization of electrodes from high power lithium-ion batteries, J. Electrochem. Soc. 149 (2002) A1358-A1369.

[103] A.M. Andersson, A. Henningson, H. Siegbahn, U. Jansson, K. Edtröm, Electrochemically lithiated graphite characterized by photoelectron spectroscopy, J. Power, Sources 119-121 (2003) 522-527.

[104] K. Edström, T. Gustafsson, J.O. Thomas, The cathode-electrolyte interface in the Li-ion battery, Electrochim. Acta 50 (2004) 397-403.

[105] S. Malmgren, K. Ciosek, M. Hahlin, T. Gustafsson, M. Gorgoi, H. Rensmo, Comparing anode and cathode electrode/electrolyte interface composition and morphology using soft and hard X-ray photoelectron spectroscopy, Electrochim. Acta 97 (2013) 23-32.

[106] M. Nie, J. Demeaux, B.T. Young, D.R. Heskett, Y. Chen, A. Bose, J.C. Woicik, B.L. Lucht, Effect of vinylene carbonate and fluoroethylene carbonate on SEI formation on graphitic anodes in Li-ion batteries, J. Electrochem. Soc. 162 (2015) A7008-A7014.

---

[107] P. Georén, G. Lindbergh, On the use of voltammetric methods to determine electrochemical stability limits for lithium battery electrolytes, J. Power Sources 124 (2003) 213-220.

[108] P.B. Balbuena, Y. Wang, Lithium-ion batteries. Solid-Electrolyte Interphase, 1st ed., Imperial College Press, London, 2004.

[109] A. Bhide, J. Hofmann, A.K. Dürr, J. Janek, P. Adelhelm, Electrochemical stability of non-aqueous electrolytes for sodium-ion batteries and their compability with $Na_{0.7}CoO_2$; Phys. Chem. Chem. Phys. 16 (2014) 1987-1998.

[110] A. Ponrouch, R. Dedryvère, D. Monti, A.E. Demet, J.M. Ateba Mba, L. Croguennec, C. Masquelier, P. Johansson, M.R. Palacín, Towards high energy density sodium ion batteries through electrolyte optimization, Energy Environ. Sci. 6 (2013) 2361-2369.

[111] L. Bodenes, A. Darwiche, L. Monconduit, H. Martinez, The solid electrolyte interphase a key parameter of the high performance of Sb in sodium-ion batteries: comparative X-ray photoelectron spectroscopy study of Sb/Na-ion and Sb/Li-ion batteries, J. Power Sources 273 (2015) 14-24.

[112] A. Darwiche, L. Bodenes, L. Madec, L. Monconduit, Impact of the salts and solvents on the SEI formation in Sb/Na batteries: An XPS analysis, Electrochim. Acta 207 (2016) 284-292.

[113] L. Baggetto, E. Allcorn, A. Manthiram, G.M. Veith, Cu_2Sb thin films as anode for Na-ion batteries, Electrochem. Commun. 27 (2013) 168-171.

[114] L. Ji, M. Gu, Y. Shao, X. Li, M.H. Engelhard, B. W. Arey, W. Wang, Z. Nie, J. Xiao, C. Wang, J.G. Zhang, J. Liu, Controlling SEI formation on SnSb-porous carbon nanofibers for improves Na ion storage, Adv. Mater. 26 (2014) 2901-2908.

[115] H. Pan, X. Lu, X. Yu, Y.S. Hu, H. Li, X.Q. Yang, L. Chen, Sodium storage and transport properties in layered $Na_2Ti_3O_7$ for room-temperature sodium-ion batteries, Adv. Energy Mater. 3 (2013) 1186-1194.

[116] S. Doubaji, B. Philippe, I. Saadoune, M. Gorgoi, T. Gustafsson, A. Solhy, M. Valvo, H. Rensmo, K. Edström, Passivation layer and cathodic redox reactions in sodium-ion batteries probed by HAXPES, Chem. Sus. Chem. 9 (2016) 97-108.

[117] X. Xia, J.R. Dahn, Study of the reactivity of Na/Hard Carbon with different solvents and electrolytes, J. Electrochem. Soc. 159 (2012) A515-A519.

[118] A. Darwiche, C. Marino, M.T. Sougrati, B. Fraisse, L. Stievano, L. Monconduit, Better cycling performances of bulk Sb in Na-ion batteries compared to Li-ion systems: an unexpected electrochemical mechanism, J. Am. Chem. Soc. 134 (2012) 20805-20811.

[119] S. Komaba, W. Murata, T Ishikawa, N. Yabuuchi, T. Ozeki, T. Nakayama, A. Ogata, K. Gotoh, K. Fujiwara, Electrochemical Na insertion and Solid Electrolyte Interphase for Hard-Carbon electrodes and application to Na-ion batteries, Adv. Funct. Mater. 21 (2011) 3859-3867.

2

$Na_2Ti_3O_7$ as anode material for NIBs: influence of the synthesis parameters on the electrochemical properties and moisture and water stability

In this chapter, motivated by the technological interest of $Na_2Ti_3O_7$ as anode material for NIBs, several aspects have been studied in order to improve its electrochemical performance. Firstly, the effects of synthesis conditions, such as the choice of Na precursor, the atmosphere used during the cooling process and the effect of C-coating have been correlated with the electrochemical performance of $Na_2Ti_3O_7$. Secondly, the moisture and water stability of this compound have been investigated and the effect of using a water-based solution for electrode preparation, which allows for the use of low-cost and environmental friendly binders like sodium carboxymethylcellulose (Na-CMC), has been evaluated.

2.1. Introduction

Titanium-based oxides represent a promising family of anode materials because of their low-cost, low toxicity and easiness of preparation [1]. Among them, $Na_2Ti_3O_7$ is one of the most interesting in terms of low voltage and good capacity. [2]. However, the promising electrochemical properties of $Na_2Ti_3O_7$ are hindered by a continuous capacity fading [3, 4]. Pan *et al*. studied the impact of the electrolyte and binder in order to improve the poor capacity retention. The best value was obtained using 1 M NaFSI in PC as electrolyte and sodium alginate (NaAlg) as binder; however the capacity fades from ~ 190mAh/g to 80 mAh/g at the 20th cycle and at the 60th cycle decreases to 60 mAh/g at 0.1C rate [3]. While Rudola *et al*. increases the retention by synthesizing the $Na_2Ti_3O_7$ with NaOH as Na precursor instead of Na_2CO_3 and optimizing the electrode preparation by ball milling. The obtained 1st Na extraction capacity is close to 180 mAh/g and was reduced to 150 mAh/g afer 20th cycle at 0.1C rate [4]. Therefore, the capacity retention ranges is from 42% [3] to 80% [4] at the 20th cycle. Only by C-coating was significantly improved showing retention of 82% at the 20th cycle and 65% after 100 cycles [5]. Although, the underlying reason for this poor retention still remains unclear, one of the hypotheses is the self relaxation of $Na_4Ti_3O_7$ and therefore in a recent work first-principles calculations and *in-situ* XRD experiments have been carried out in order to investigated this assumption. The first-principles calculations showed the reversibility of the $Na_4Ti_3O_7$ structure during cycling and the XRD experiments the complete reversibility of the Na^+ insertion reaction since no structural damage is detected after 50 cycles [6].

On the other hand, it is already known that $Na_2Ti_3O_7$ and $H_2Ti_3O_7$ form a complete solid solution of the form $Na_{2-x}H_xTi_3O_7$ ($0 \leq x \leq 2$) [7, 8, 9] but its detailed structural characterization, as well as the effect of moisture exposure in the electrochemical properties of $Na_2Ti_3O_7$ have not been previously reported. Although during the course of this work a partial ion exchange of Na^+ by H^+ in $Na_2Ti_3O_7$ was detected since an extra plateau was observed at 1.3 V. However, it has not been investigated in detail [6]. As regards the structural and electrochemical characterization of $H_2Ti_3O_7$, it was performed in 2015 [10]. The stability of $Na_2Ti_3O_7$ in water and the structural characterization of the resulting compounds is extremely relevant since will determine the storage and electrode preparation conditions, which are going to have an impact in both the environmental footprint and final cost of NIBs.

$Na_2Ti_3O_7$ structure consists of zigzag layers of edge-sharing [TiO_6] octahedra (**Figure 2.1a**), stacked along the *a* cell axis resulting in AA [TiO_6] layer stacking sequence and $P2_1/m$ monoclinic space group [11]. Two types of Na^+ (Na1 and Na2) are located in the interlayer space at 2*e* Wyckoff sites. On the other hand, the structure of $H_2Ti_3O_7$ is slightly different since it is indexed with the monoclinic *C2/m* space group. The layers are displaced by *b/2* due to the formation of O-H bonds, which leads to a doubling of the unit cell and AB [TiO_6] layer stacking sequence (**Figure 2.1b**) [8]. Two types of H^+ at 4*i* Wyckoff positions have been reported by Kataoka *et al.* from neutron diffraction data [12]. However, Eguía-Barrio *et al.* recently reported an extra type of H^+ at 2*a* Wyckoff position for $H_2Ti_3O_7$, and therefore three types of H^+ can be found in the structure [10].

Moreover, the structural characterization of mixed $Na_{2-x}H_xTi_3O_7$ ($0<x<2$) compositions is still controversial. Indeed, Izawa *et al.* used a primitive unit cell and the same space group as $Na_2Ti_3O_7$ ($P2_1/m$) to index a compound described as $Na_{1.43}H_{0.57}Ti_3O_7$ (**Figure 2.1a**) [7]. On the other hand, Feist *et al.* described the structure of $Na_{0.8}H_{1.2}Ti_3O_7$ with the same layer stacking as $H_2Ti_3O_7$ (**Figure 2.1b**), and therefore a $C2/m$ unit cell [8]. Mori *et al.* investigated the structure of the whole $Na_{2-x}H_xTi_3O_7$ ($0\leq x\leq 2$) series by first-principles calculations [9], concluding that compositions between $0\leq x\leq 0.75$ would present an AA stacking like $Na_2Ti_3O_7$ (**Figure 2.1a**), while the phase in the range $1\leq x\leq 2$ would crystallize in AB stacking sequence

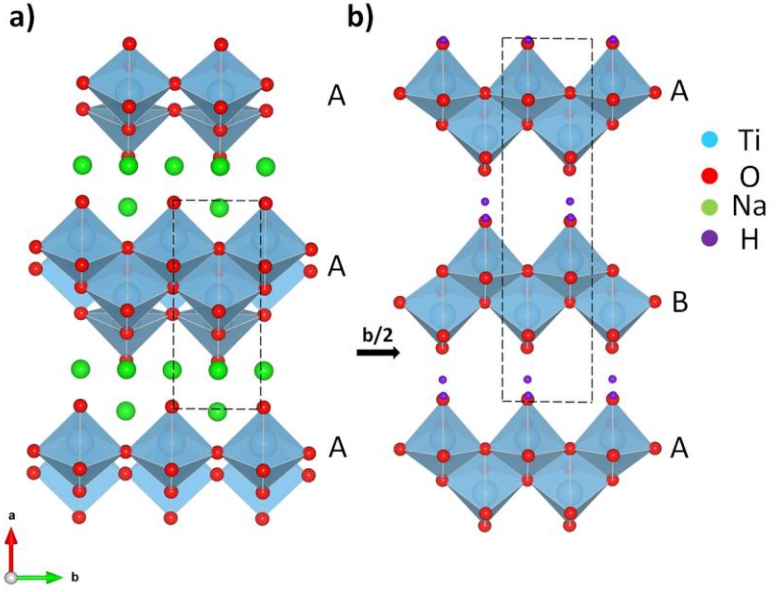

Figure 2.1: Structures of **a)** $Na_2Ti_3O_7$ with AA [TiO_6] layer stacking and **b)** $H_2Ti_3O_7$ with AB [TiO_6] layer stacking along *a*.

as $H_2Ti_3O_7$ (**Figure 2.1b**). Still, the theoretical results of Mori *et al.* have not been experimentally validated and the exact positions of Na^+ and H^+ in $Na_{2-x}H_xTi_3O_7$ are not known yet.

2.2. Influence of the synthesis parameters on the electrochemical properties

2.2.1. Synthesis of $Na_2Ti_3O_7$

$Na_2Ti_3O_7$ was synthesized by solid state method mixing TiO_2 anatase and either $Na_2CO_3{\cdot}H_2O$ or NaOH as Na precursors. In the case of $Na_2CO_3{\cdot}H_2O$, a 5% excess was used to avoid the formation of $Na_2Ti_6O_{13}$ as secondary phase and the mixture was heated up to 800 ^oC for 24 h [13]. On the other hand, TiO_2 anatase and NaOH were blended in stoichiometric amount and heated up to 750 ^oC for 20 h [4]. The synthesis was always carried out in air, but two different cooling atmospheres were tested: air and Ar (in this case the atmosphere was changed to Ar when cooling started and was maintained until room temperature was reached, then the sample was transferred to an Ar-filled glove box without any contact with the atmosphere). By combining the different precursors ($Na_2CO_3{\cdot}H_2O$ *vs.* NaOH) and the cooling atmosphere (air *vs.* Ar) four samples were obtained: **NTO-CO-Air** and **NTO-CO-Ar** for the samples prepared from $Na_2CO_3{\cdot}H_2O$ cooled in air and Ar, respectively and **NTO-OH-Air** and **NTO-OH-Ar** for those prepared from NaOH.

2.2.2. Influence of the Na precursor

2.2.2.1. Structural and morphological characterization

2.2.2.1.1. Powder X-ray Diffraction (PXRD)

The PXRD patterns of both **NTO-CO-Air** and **NTO-OH-Air** samples are refined by the Rietveld method taking as starting parameters those of PDF file 01-072-0148 (**Figure 2.2**). The refined parameters have been the zero and scale factor, cell and profile parameters, atomic position and isotropic displacement parameters (B_{iso}). The B_{iso} values of the same atom have been constrained. The cell parameters, listed in **Table 2.1** are similar for both samples and agree with previously reported data [11]. The list of refined atomic positions, occupancies and B_{iso} are also similar for both samples (**Table 2.2** and **Table 2.3**). Therefore, from a structural point of view, there are not significant differences when $Na_2Ti_3O_7$ is synthesized using the two different Na precursors.

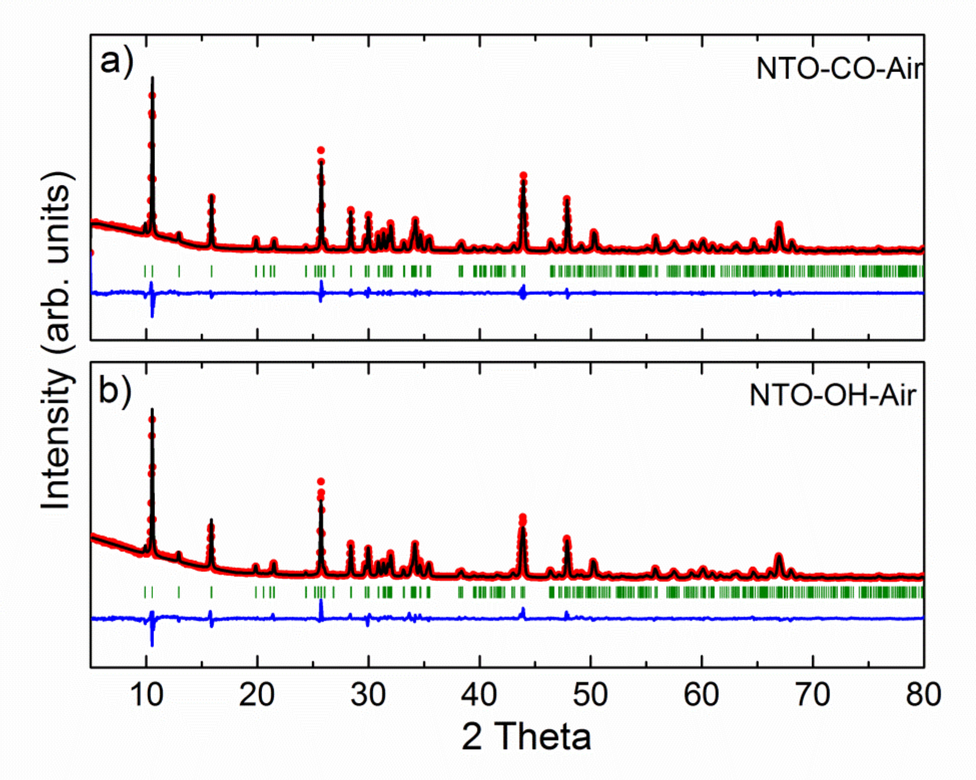

Figure 2.2: Rietveld refined PXRD data of **a) NTO-CO-Air** and **b) NTO-OH-Air**. Observed (red points), calculated (black line), difference (blue line) and Bragg reflections (green vertical bars).

Table 2.1: The atomic positions of **NTO-CO-Air** and **NTO-OH-Air** ($P2_1/m$) determined by Rietveld method from PXRD data at room temperature.

Sample	*a* (Å)	*b* (Å)	*c* (Å)	*β* (º)
NTO-CO-Air	8.5695(3)	3.8002(1)	9.1278(3)	101.598(3)
NTO-OH-Air	8.5768(6)	3.7978(2)	9.1278(5)	101.582(5)

Table 2.2: The atomic positions, isotropic displacement parameters (B_{iso}), occupancies (SOF) and reliability factors of **NTO-CO-Air** ($P2_1/m$) determined by Rietveld method from PXRD data at room temperature.

Atomic position, B_{iso} and SOF

Atom	Wyckoff	SOF	*x* (Å)	*y* (Å)	*z* (Å)	B_{iso} (Å^2)
Ti1	2*e*	1.0	0.0287(5)	0.25	0.2801(5)	1.6(1)
Ti2	2*e*	1.0	0.2512(5)	0.25	0.6769(5)	1.6(1)
Ti3	2*e*	1.0	0.1490(6)	0.25	0.9853(5)	1.6(1)
O1	2*e*	1.0	0.268(2)	0.25	0.188(2)	0.2(1)
O2	2*e*	1.0	0.158(2)	0.25	0.465(2)	0.2(1)
O3	2*e*	1.0	0.438(2)	0.25	0.651(2)	0.2(1)
O4	2*e*	1.0	0.329(2)	0.25	0.907(1)	0.2(1)
O5	2*e*	1.0	0.013(2)	0.25	0.747(1)	0.2(1)
O6	2*e*	1.0	0.799(2)	0.25	0.324(1)	0.2(1)
O7	2*e*	1.0	0.920(2)	0.25	0.043(2)	0.2(1)
Na1	2*e*	1.0	0.672(9)	0.25	0.592(1)	1.3(1)
Na2	2*e*	1.0	0.501(1)	0.25	0.155(1)	1.3(1)

Reliability factors

χ^2	R_p	R_{wp}	R_e	R_F
5.77	14.6	16.1	6.83	4.77

Table 2.3: The atomic positions, isotropic displacement parameters (B_{iso}), occupancies (SOF) and reliability factors of **NTO-OH-Air** ($P2_1/m$) determined by Rietveld method from PXRD data at room temperature.

Atomic position, B_{iso} and SOF

Atom	Wyckoff	SOF	*x* (Å)	*y* (Å)	*z* (Å)	B_{iso} (Å^2)
Ti1	2*e*	1.0	0.0314(7)	0.25	0.2816(7)	1.5(2)
Ti2	2*e*	1.0	0.2524(6)	0.25	0.6773(7)	1.5(2)
Ti3	2*e*	1.0	0.1509(8)	0.25	0.9837(7)	1.5(2)
O1	2*e*	1.0	0.228(2)	0.25	0.184(2)	0.1(2)
O2	2*e*	1.0	0.157(2)	0.25	0.472(2)	0.1(2)
O3	2*e*	1.0	0.436(2)	0.25	0.649(2)	0.1(2)
O4	2*e*	1.0	0.342(2)	0.25	0.902(2)	0.1(2)
O5	2*e*	1.0	0.010(2)	0.25	0.740(2)	0.1(2)
O6	2*e*	1.0	0.784(2)	0.25	0.328(2)	0.1(2)
O7	2*e*	1.0	0.924(2)	0.25	0.042(2)	0.1(2)
Na1	2*e*	1.0	0.671(1)	0.25	0.595(1)	1.4(2)
Na2	2*e*	1.0	0.500(1)	0.25	0.152(1)	1.4(2)

Reliability factors

χ^2	R_p	R_{wp}	R_e	R_F
7.38	19.1	19.4	7.14	6.48

2.2.2.1.2. Scanning Electron Microscopy (SEM)

From SEM analysis it can be concluded that both samples crystallize as platelets of micrometric size (**Figure 2.3a** and **Figure 2.3b**). Additionally, the laser diffractometer experiment shows that the particle size distribution is heterogeneous since 50% of particles have a size of 20 µm or smaller while 90% of them have 40 µm or even lower size in both cases (**Figure 2.3c**). Thus, the Na precursor neither affects the morphology or the particle size of $Na_2Ti_3O_7$.

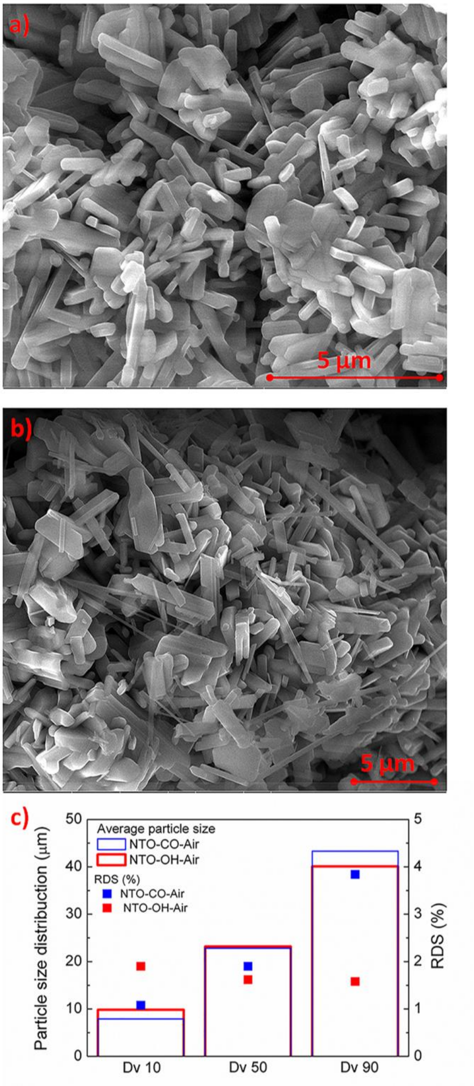

Figure 2.3: SEM images of **a)** **NTO-CO-Air** and **b)** **NTO-OH-Air**. **c)** Particle size distribution obtained by laser diffraction (points RDS%).

2.2.2.1.3. ^{23}Na solid-state Nuclear Magnetic Resonance (ssNMR)

Solid-state NMR can provide very accurate structural descriptions of materials and can detect small amounts of amorphous impurities or secondary phases not observed by PXRD. The ^{23}Na-ssNMR spectrum of **NTO-CO-Air** is shown in **Figure 2.4a** and two main signals centred at 3 ppm and -18 ppm are observed. These signals have been fitted using the Dmfit software [14] and the result of the fit (red line in **Figure 2.4a**) is shown superimposed to the experimental data (black line in **Figure 2.4a**). While the signal at 3 ppm is rather narrow, the signal centred at -18 ppm is clearly characterized by a second order quadrupolar broadening, typically observed for nuclei with spin quantum numbers higher than 1 (I_{Na}= 3/2). The differences observed between these two signals are in agreement with the dissimilarities in the local symmetries of the two Na^+ positions (Na1 and Na2) found in $Na_2Ti_3O_7$ [11]. High symmetric sites like in the case of Na2 result in reduced or even negligible quadrupolar broadenings and therefore the narrow signal at 3 ppm is attributed to this site while Na1 are assigned to the peak centered at -18 ppm, which is located at low symmetric sites (inset **Figure 2.4a**). The relative population of Na^+ in sites 1 and 2, calculated from the integration of the two main signals, is very close to 1:1 in agreement with the site multiplicities of the two Na^+ in $Na_2Ti_3O_7$ (**Table 2.2**). The small signal at 5.6 ppm is observed in all samples independently of the Na precursor and the atmosphere used in the cooling process, and therefore can be ascribed to a small impurity not detected by PXRD which does not contribute to the differences in the electrochemical performance. It is interesting to notice that the fit of the spectrum of **NTO-CO-Air** failed to reproduce the broad component observed between 0 to ~ -15 ppm (see the enlarged zone in **Figure 2.4a**). Since the synthesis of the material is performed using $Na_2CO_3{\cdot}H_2O$ as Na precursor, the spectrum of a reference sample of $Na_2CO_3{\cdot}H_2O$ has been recorded and is shown in **Figure 2.4b**. Comparing these two spectra (**Figure 2.4a** *vs.* **Figure 2.4b**) it is clear that the shape and chemical shift of $Na_2CO_3{\cdot}H_2O$ can account for this broad component in **NTO-CO-Air** sample. The lack of quadrupolar features for this component in the **NTO-CO-Air** spectrum can be explained by the amorphous character of the Na_2CO_3 (in agreement with the PXRD pattern since it is not detected).

The ^{23}Na-ssNMR spectrum of **NTO-OH-Air** is shown in **Figure 2.4c**. This spectrum is characterized by the same main signals observed for **NTO-CO-Air**, indicating that the local symmetries of the Na^+ populations in both samples are not influenced by the Na precursor used in the synthesis. Measurable differences are only observed in the amount of Na_2CO_3 in both samples. It is clear that some unreacted Na_2CO_3

remaining in **NTO-CO-Air** can explain its presence, while in the case of **NTO-OH-Air** its presence is more intriguing.

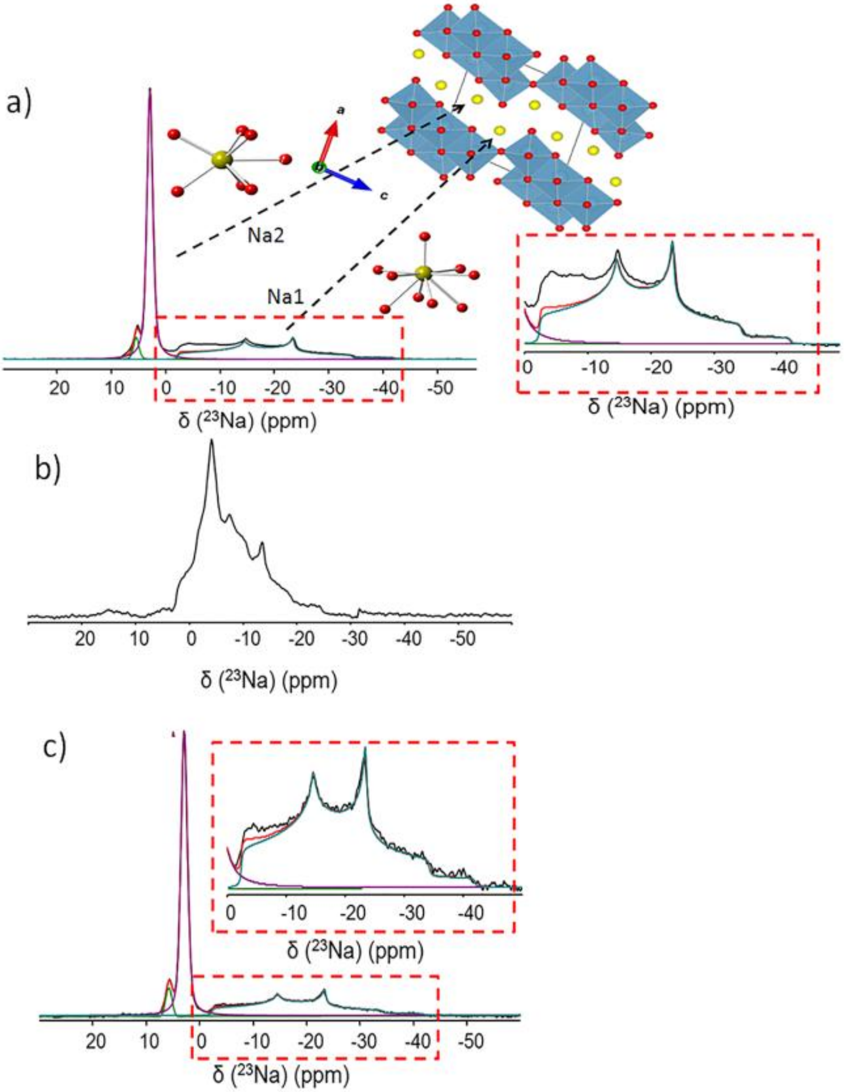

Figure 2.4: ^{23}Na-ssNMR spectra of **a)** **NTO-CO-Air**, **b)** a reference sample$Na_2CO_3 \cdot H_2O$ and **c)** **NTO-OH-Air**. Inset **a)** $Na_2Ti_3O_7$ structure and local environment of Na1 and Na2; and the zone between 0 and -40 ppm is enlarged. Observed (black line), calculated (red line), Na1 (dark cyan line), Na2 (purple line) and impurity (green line).

2.2.2.1.4. Fourier Transform Infrared Spectroscopy (FTIR)

Infrared spectra (**Figure 2.5**) confirm the presence of Na_2CO_3 in both samples since the stretching frequencies of the carbonyl group at 1445 cm^{-1} are observed, in addition to the bending and stretching vibrations of Ti-O bonds at low wavelengths (940 - 460 cm^{-1}) [15].

In order to remove Na_2CO_3, which could influence on the electrochemical performance, the as-prepared **NTO-CO-Air** sample has been rinsed in water as has been previously done with $LiNi_{0.83}Co_{0.15}Al_{0.02}O_2$ lithium layered oxide [16]. The infrared spectrum (**Figure 2.6**) shows that the treatment used is able to partially remove Na_2CO_3 since the stretching frequency of the carbonyl group at 1445 cm^{-1} is reduced [15].

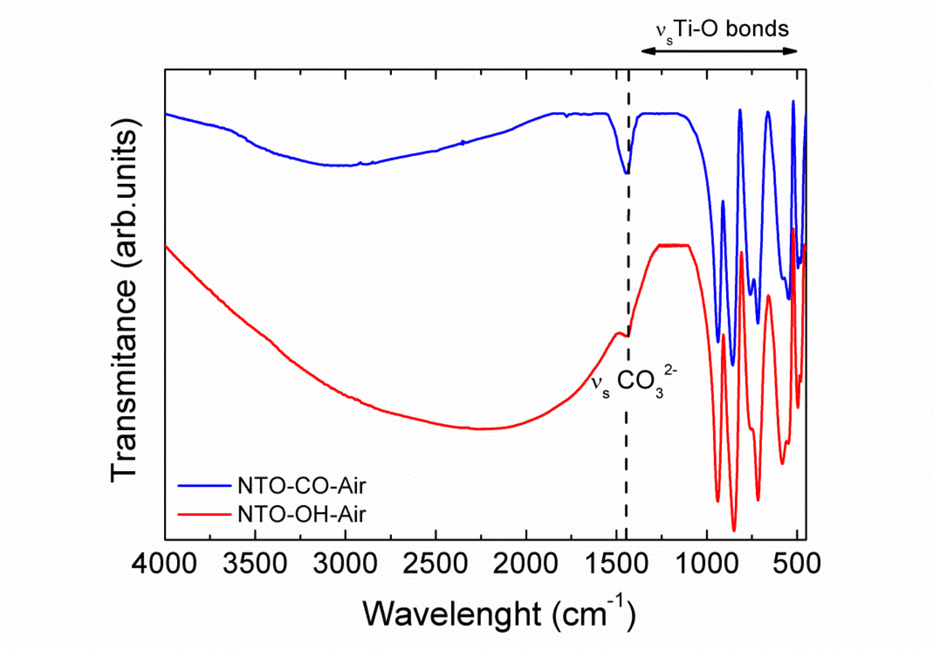

Figure 2.5: FTIR spectra from 4000cm^{-1} to 500 cm^{-1} of **NTO-CO-Air** (blue) and **NTO-OH-Air** (red)

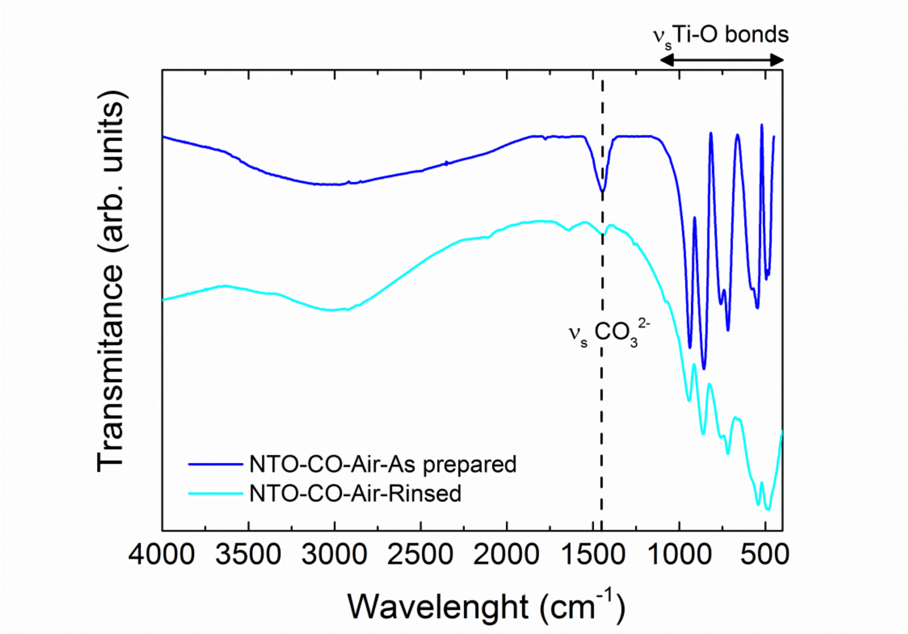

Figure 2.6: FTIR spectra from 4000 cm^{-1} to 500 cm^{-1} of **NTO-CO-Air**-as prepared (blue) and **NTO-CO-Air**-rinsed (cyan

2.2.2.1.5. Powder Neutron Diffraction (PND)

Duffort *et al*. have recently proposed from neutron diffraction Fourier difference maps that CO_3^{2-} could be inserted in the tetrahedral sites of the T_MO_2 layer of P2-$Na_{0.67}Fe_{0.5}Mn_{0.5}O_2$ layered oxide when is exposed to air [17]. In order to confirm or discard this hypothesis PND data has been collected for **NTO-CO-Air** sample, with a wavelength λ = 1.28 Å, at ILL (Grenoble, France). In **Figure 2.7** the Rietveld refinement of the PND pattern is shown, where zero and scale factor, cell and profile parameters, atomic position and B_{iso} factors (for the same atom the B_{iso} have been constrained) have been refined (**Table 2.4**). The inset of **Figure 2.7** the Fourier difference map is represented from which it can be concluded that the structure contains no carbon, since carbon has a positive nuclear scattering (6.6511 fm) [18] and would appear as positive intensity.

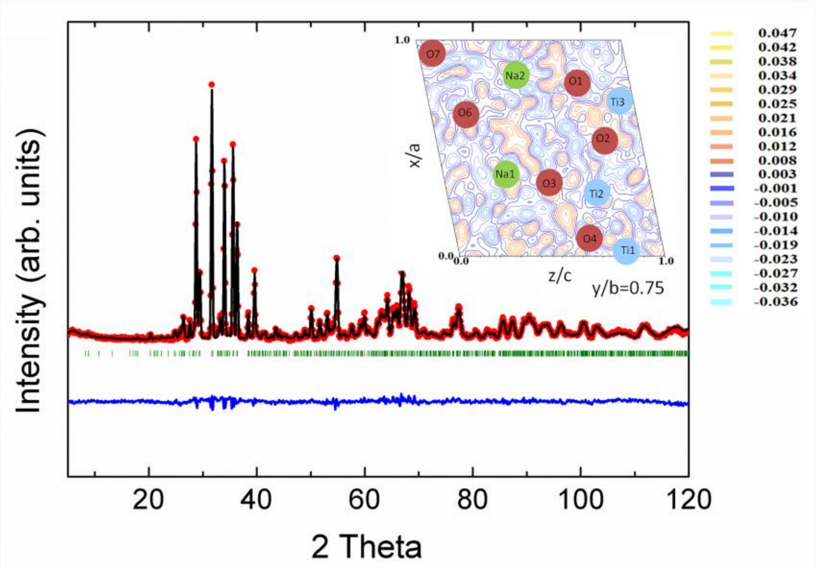

Figure 2.7: Rietveld refined PND pattern of **NTO-CO-Air** collected at λ = 1.28 Å. Observed (red points), calculated (black line), difference (blue line) and Bragg positions (green vertical bars). The inset shows the difference Fourier maps at b = 0.75, in which orange lines and blue lines indicate positive and negative nuclear scattering, respectively.

Table 2.4: The refined cell parameters, atomic positions, isotropic displacement parameters (Biso), occupancies (SOF) and reliability factors of **NTO-CO-Air** ($P2_1/m$) determined by Rietveld method from PND data at room temperature.

Cell parameter

a (Å)	*b* (Å)	*c* (Å)	*β* (º)
8.5675(9)	3.8029(3)	9.1309(9)	101.594(6)

Atomic position, B_{iso} and SOF

Atom	Wyckoff	SOF	*x* (Å)	*y* (Å)	*z* (Å)	*Biso* ($Å^2$)
Ti1	2*e*	1.0	0.030(4)	0.25	0.278(4)	0.4(2)
Ti2	2*e*	1.0	0.249(5)	0.25	0.678(4)	0.4(2)
Ti3	2*e*	1.0	0.146(5)	0.25	0.987(5)	0.4(2)
O1	2*e*	1.0	0.221(3)	0.25	0.189(3)	0.64(9)
O2	2*e*	1.0	0.143(2)	0.25	0.459(2)	0.64(9)
O3	2*e*	1.0	0.441(3)	0.25	0.648(3)	0.64(9)
O4	2*e*	1.0	0.322(3)	0.25	0.911(3)	0.64(9)
O5	2*e*	1.0	0.016(2)	0.25	0.753(3)	0.64(9)
O6	2*e*	1.0	0.804(2)	0.25	0.318(1)	0.64(9)
O7	2*e*	1.0	0.915(2)	0.25	0.044(2)	0.64(9)
Na1	2*e*	1.0	0.677(4)	0.25	0.590(4)	0.8(5)
Na2	2*e*	1.0	0.502(4)	0.25	0.160(4)	0.8(5)

Reliability factors

χ^2	R_p	R_{wp}	R_e	R_F
3.17	12.0	11.9	6.72	5.06

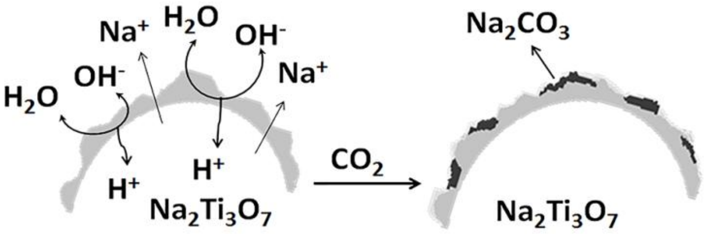

Figure 2.8: Schematic reaction of $Na_2Ti_3O_7$ with atmospheric H_2O.

Since the insertion of CO_3^{2-} into the structure can be excluded in this case; the most plausible explanation to explain the presence of Na_2CO_3 in both samples is that Na_2CO_3 is formed at the surface of $Na_2Ti_3O_7$ particles by the interaction of $Na_2Ti_3O_7$ particles with atmospheric water by Na^+/H^+ exchange. The exchanged Na^+ would then react with OH^- groups which in turn would further react with atmospheric CO_2 to form Na_2CO_3 (**Figure 2.8**).

Similar processes have been observed previously for layered oxide materials, such us, $LiNi_{0.83-0.8}Co_{0.15}Al_{0.02-0.05}O_2$ [19, 20] and $NaNi_{1/3}Mn_{1/3}Co_{1/3}O_2$ [21] cathode materials for LIBs and NIBs, respectively and in $Li_{0.34}La_{0.55}TiO_3$ [22] ceramic electrolyte for LIBs, for which in all cases their electrochemical performance is impoverished.

2.2.2.2. Electrochemical characterization

Electrochemical study were carried out with laminate electrodes prepared with a 70:20:10 ($Na_2Ti_3O_7$:carbon Super C65:PVdF) in half-cells using Na disks as counter electrode and 1 M $NaClO_4$ in EC:PC as electrolyte. All tests were performed at 0.1C rate in the voltage window of 0.05 - 1.6 V *vs.* Na^+/Na.

The voltage profile of the first two cycles of **NTO-CO-Air** and **NTO-OH-Air** samples at 0.1C is similar (**Figure 2.9**). As expected, the reversible Na^+ insertion occurs throughout a long plateau at 0.3 V *vs.* Na^+/Na, the irreversible plateau at 0.7 V being due to both the reaction of Na^+ with carbon Super C65, which is used to increase the conductivity [2], and SEI layer formation, since electrolyte reduction is expected to occur because of the low working voltage of $Na_2Ti_3O_7$.

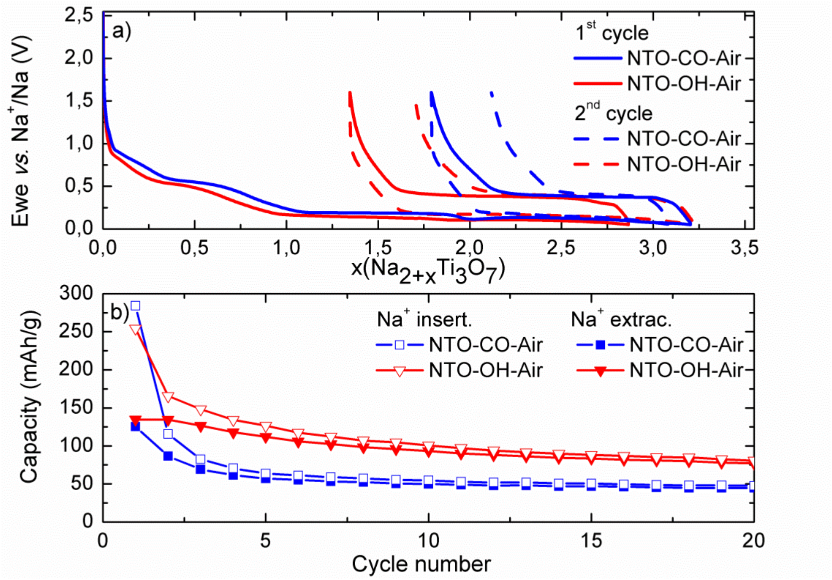

Figure 2.9: a) Voltage *vs.* inserted Na$^+$ ($Na_{2+x}Ti_3O_7$) corresponding to the 1st and 2nd cycles and **b)** Na$^+$ insertion and extraction capacity *vs.* cycle number of **NTO-CO-Air** (blue) and **NTO-OH-Air** (red).

Table 2.5: Capacity values and capacity retention at 20th cycle of **NTO-CO-Air** and **NTO-OH-Air** at 0.1C over voltage window 0.05 - 1.6 V *vs.* Na$^+$/Na.

Parameters	**NTO-CO-Air**	**NTO-OH-Air**
1st Na$^+$ insertion capacity (mAh/g)	284	254
1st Irreversible. capacity (mAh/g)	159	119
Capacity retention at 20th cycle	35%	57%

Despite the 1st Na$^+$ insertion capacity of **NTO-CO-Air** is larger than that of **NTO-OH-Air**, the irreversible capacity in the 1st cycle is also larger. In fact, the 1st Na$^+$ extraction capacity of both samples is similar (around 130 mAh/g). Moreover, the capacity of **NTO-CO-Air** severely fades and decays abruptly after the first 5 cycles while **NTO-OH-Air** presents slightly better capacity retention and fades more smoothly reaching 57% in the 20th cycle (values are collected in **Table 2.5**). The Coulombic efficiency after 5 cycles of both is not 100%, for **NTO-CO-Air** 94% while **NTO-OH-Air** 96%. These lower values suggest that the electrolyte is reducing and forming a SEI layer.

This improvement in the 1st reversible capacity and capacity retention using NaOH as Na precursor is in agreement with data presented by Rudola *et al.* [4]; although its origin was not discussed. Furthermore, the structural (c.f. **Figure 2.2**) and morphology (c.f. **Figure 2.3**) study shows that both samples are similar, and do not suggest any particular reason of that improvement. However, ^{23}Na-ssNMR (c.f. **Figure 2.4**) and FITR (c.f. **Figure 2.5**) show that both samples exhibit Na_2CO_3 which is formed by the interaction of the active material with the atmospheric water and CO_2, although **NTO-CO-Air** has a higher amount than **NTO-OH-Air**. The presence of Na_2CO_3 could have a negative impact in the stability of the SEI layer (whose formation is expected because Na^+ insertion in $Na_2Ti_3O_7$ occurs at low voltage), and therefore in capacity retention, since exhibits a high solubility in the commonly used organic electrolyte. Moreover, Na_2CO_3 could act as a catalyst for electrolyte reduction which can additionally create a safety problem [23].

The capacity retention of the **NTO-CO-Air** sample once rinsed in water to remove the Na_2CO_3 has substantially improved, 54% *vs.* 35% at 20th cycle, and now is close to **NTO-OH-Air**, with a sharp fading in the first few cycles (**Figure 2.10**). Although this approach is not enough to avoid capacity fading these results are in agreement with the fact that Na_2CO_3 is involved in the poor capacity retention of $Na_2Ti_3O_7$.

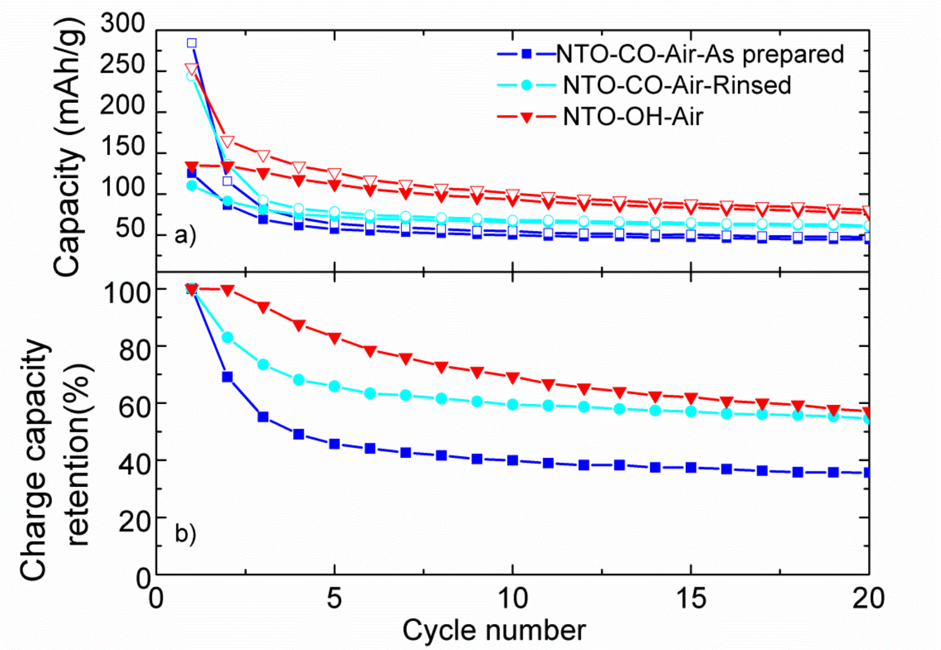

Figure 2.10: a) Capacity of Na^+ insertion (empty marks) and extraction (fill marks) *vs.* cycle number and **b)** charge capacity retention (taking into account the 1st Na extraction capacity) of **NTO-CO-Air**-As prepared (blue), **NTO-CO-Air**-Rinsed (cyan) and **NTO-OH-Air** (red).

2.2.3. Influence of the cooling atmosphere

Since the strategy to suppress Na_2CO_3 by washing with water is not satisfactory, another approach has been explored. It consists in avoiding any contact with the atmosphere by carrying out the cooling process under an inert and dry Ar atmosphere (samples **NTO-CO-Ar** and **NTO-OH-Ar**). Once the cooling process is finished the powder has been transferred to an Ar-filled glove box without any contact with the atmosphere and has never been exposed to air.

2.2.3.1. Structural characterization

2.2.3.1.1. Powder X-ray Diffraction (PXRD)

The PXRD patterns are refined by Rietveld method (**Figure 2.11**), refining zero and scale factor, cell and profile parameters, atomic positions and the overall isotropic displacement parameters (B_{ove}). The refined cell parameters, B_{ove}, atomic positions and reliability factors of these two samples are collected in **Table 2.6** and **Table 2.7** where they do not exhibit any significant differences compared with the samples cooled in Air (**Table 2.1**), indicating that the structure of the obtained materials is the same.

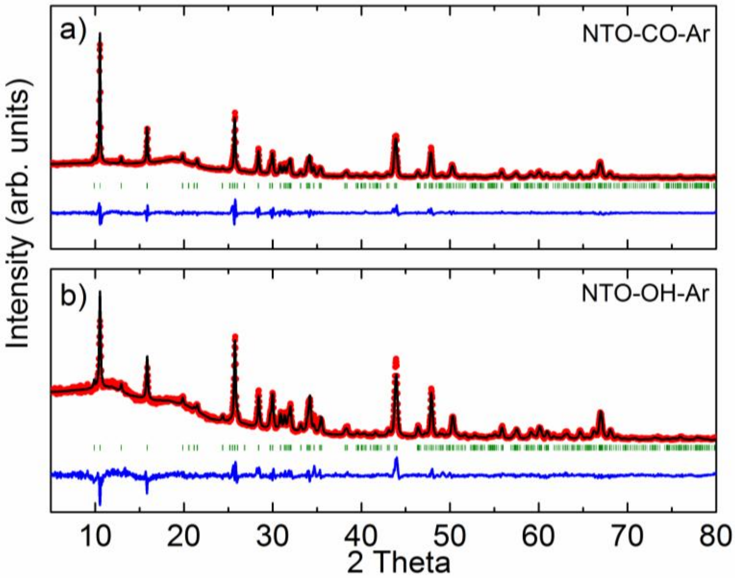

Figure 2.11: Rietveld refined PXRD data of **a) NTO-CO-Ar** and **b) NTO-OH-Ar**. Observed (red points), calculated (black line), difference (blue line) and Bragg reflections (green vertical bars).

Table 2.6: The refined cell parameters, atomic positions, overall isotropic displacements parameter (B_{ove}), occupancies (SOF) and reliability factors of **NTO-CO-Ar** ($P2_1/m$) determined by Rietveld method from PXRD data at room temperature.

Cell parameter and B_{ove}

a (Å)	*b* (Å)	*c* (Å)	*β* (º)	B_{ove} (Å^2)
8.5780(8)	3.8016(2)	9.1315(7)	101.601(7)	0.3(2)

Atomic position and SOF

Atom	Wyckoff	SOF	*x* (Å)	*y* (Å)	*z* (Å)
Ti1	2*e*	1.0	0.029(2)	0.25	0.280(2)
Ti2	2*e*	1.0	0.249(2)	0.25	0.677(2)
Ti3	2*e*	1.0	0.147(2)	0.25	0.986(2)
O1	2*e*	1.0	0.229(7)	0.25	0.192(6)
O2	2*e*	1.0	0.151(7)	0.25	0.462(6)
O3	2*e*	1.0	0.440(6)	0.25	0.654(6)
O4	2*e*	1.0	0.333(7)	0.25	0.902(6)
O5	2*e*	1.0	0.013(7)	0.25	0.743(5)
O6	2*e*	1.0	0.801(7)	0.25	0.326(5)
O7	2*e*	1.0	0.921(7)	0.25	0.039(7)
Na1	2*e*	1.0	0.674(4)	0.25	0.590(4)
Na2	2*e*	1.0	0.500(4)	0.25	0.154(4)

Reliability factors

χ^2	R_p	R_{wp}	R_e	R_F
6.04	21.1	21.2	8.73	4.31

Table 2.7: The refined cell parameters, atomic positions, overall isotropic displacements (B_{ove}), occupancies (SOF) and reliability factors of **NTO-OH-Ar** ($P2_1/m$) determined by Rietveld method from PXRD data at room temperature.

Cell parameter and B_{ove}

a (Å)	*b* (Å)	*c* (Å)	*β* (º)	B_{ove} (Å^2)
8.571(1)	3.7981(1)	9.126(1)	101.592(9)	0.1(3)

Atomic position and SOF

Atom	Wyckoff	SOF	*x* (Å)	*y* (Å)	*z* (Å)
Ti1	2*e*	1.0	0.031(3)	0.25	0.283(2)
Ti2	2*e*	1.0	0.249(2)	0.25	0.680(3)
Ti3	2*e*	1.0	0.156(3)	0.25	0.986(3)
O1	2*e*	1.0	0.237(9)	0.25	0.196(9)
O2	2*e*	1.0	0.192(8)	0.25	0.472(8)
O3	2*e*	1.0	0.454(9)	0.25	0.658(9)
O4	2*e*	1.0	0.355(9)	0.25	0.918(8)
O5	2*e*	1.0	0.016(8)	0.25	0.737(8)
O6	2*e*	1.0	0.776(9)	0.25	0.321(7)
O7	2*e*	1.0	0.914(9)	0.25	0.042(9)
Na1	2*e*	1.0	0.658(5)	0.25	0.587(5)
Na2	2*e*	1.0	0.489(6)	0.25	0.145(6)

Reliability factors				
χ^2	R_p	R_{wp}	R_e	R_F
4.26	27.6	24.4	11.9	7.87

2.2.3.1.2. ^{23}Na solid-state Nuclear Magnetic Resonance (ssNMR)

In order to verify if this approach is successful to suppress the Na_2CO_3 formed by surface corrosion, ^{23}Na-ssNMR has been carried out. The ^{23}Na-ssNMR spectra of **NTO-CO-Ar** and **NTO-OH-Ar** are shown in **Figure 2.12**. Both spectra can be satisfactorily simulated considering the same main ^{23}Na signals used for the fits of **NTO-CO-Air** and **NTO-OH-Air** shown in **Figure 2.4**. This indicates that there is no influence of the cooling atmosphere used during synthesis on the structure of $Na_2Ti_3O_7$ as confirmed by PXRD. However, the cooling atmosphere has a clear impact on the relative amount of Na_2CO_3 (0 to ~ -15 ppm) present in these samples. While a significant amount of Na_2CO_3 is still observed in **NTO-CO-Ar** (**Figure 2.12a**), although less than in **NTO-CO-Air**, because some unreacted Na precursor remains in the material, the amount found in **NTO-OH-Ar** (**Figure 2.12b**) it is negligible and therefore this is a successful approach to suppress surface corrosion.

2.2.3.1.3. Fourier Transform Infrared Spectroscopy (FTIR)

Additionally, FTIR experiments have been done in **NTO-CO-Ar** and **NTO-OH-Ar** sample. **NTO-CO-Ar** spectrum exhibits the stretching frequency of the carbonyl group (1445 cm^{-1}) while **NTO-OH-Ar** does not show this band (**Error! Reference source not found.**), therefore the FTIR results are in agreement with ^{23}Na-ssNMR. Moreover, both samples have a typical bending and stretching vibrations bands of Ti-O bonds at low wavelengths (940 - 460 cm^{-1}) [15]. Hence, the control of the cooling atmosphere clearly allows preventing the formation of Na_2CO_3.

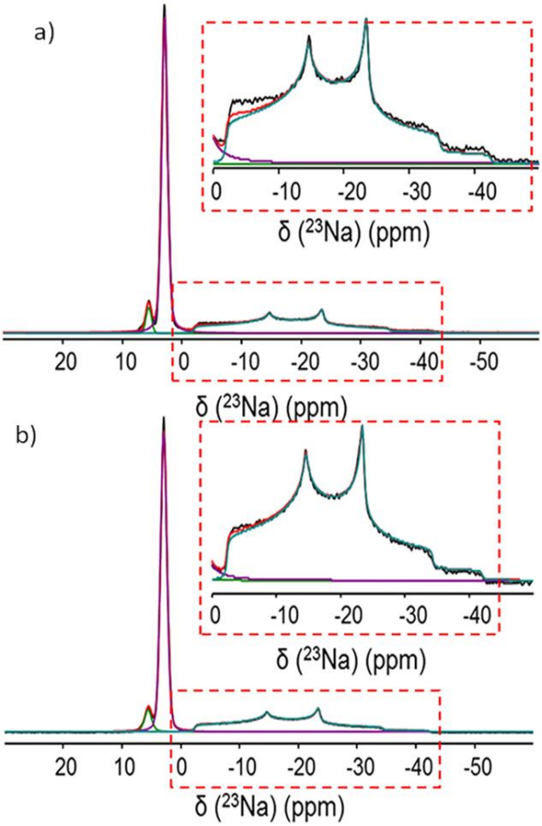

Figure 2.12: ^{23}Na-ssNRM spectra a) **NTO-CO-Ar** and b) **NTO-OH-Ar**. Observed (black line), calculated (red line), Na1 (dark cyan line), Na2 (purple line) and impurity (green line)

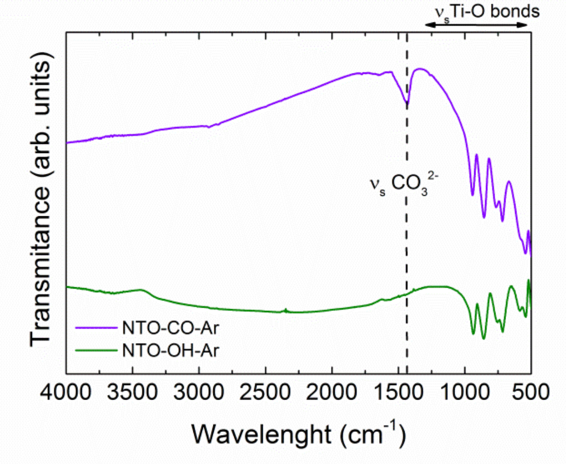

Figure 2.13: FTIRspectra from 4000 cm^{-1} to 500 cm^{-1} of **NTO-CO-Ar** (violet, top) and **NTO-OH-Ar** (green bottom).

2.2.3.2. Electrochemical characterization

The electrochemical performance of the samples cooled in Ar atmosphere were carried out in the same conditions as air cooled samples. **Figure 2.14** shows a comparison of the 1st,2nd, 8th, 50th and 100th Na^+ insertion and extraction profiles at 0.1C for the four samples: **NTO-CO-Air**, **NTO-OH-Air**, **NTO-CO-Ar** and **NTO-OH-Ar** (in **Table 2.8** some significant values are collected). Regarding the 1st Na^+ insertion capacity, which is higher than the theoretical capacity (178 mAh/g) due to the SEI layer formation that occurs below 0.9 V *vs.* Na^+/Na [24], the sample **NTO-OH-Ar** has lower 1st capacity than the others and higher reversibility. This indicates that the reduction of the electrolyte occurs in a lesser extent and a more stable SEI layer is formed. No improvement is observed between **NTO7-CO-Air** and **NTO-CO-Ar** samples since, despite the cooling atmosphere has been changed; residual Na_2CO_3 are still present in the samples. On the other hand, despite the insertion/extraction capacity in the 1st cycles is larger for the **NTO-OH-Air** sample, the same capacity is already obtained for **NTO-OH-Ar** sample in the 8th cycle and, more importantly, the capacity retention after 100 cycles is almost doubled; confirming that the "free" Na_2CO_3 sample shows better electrochemical performance.

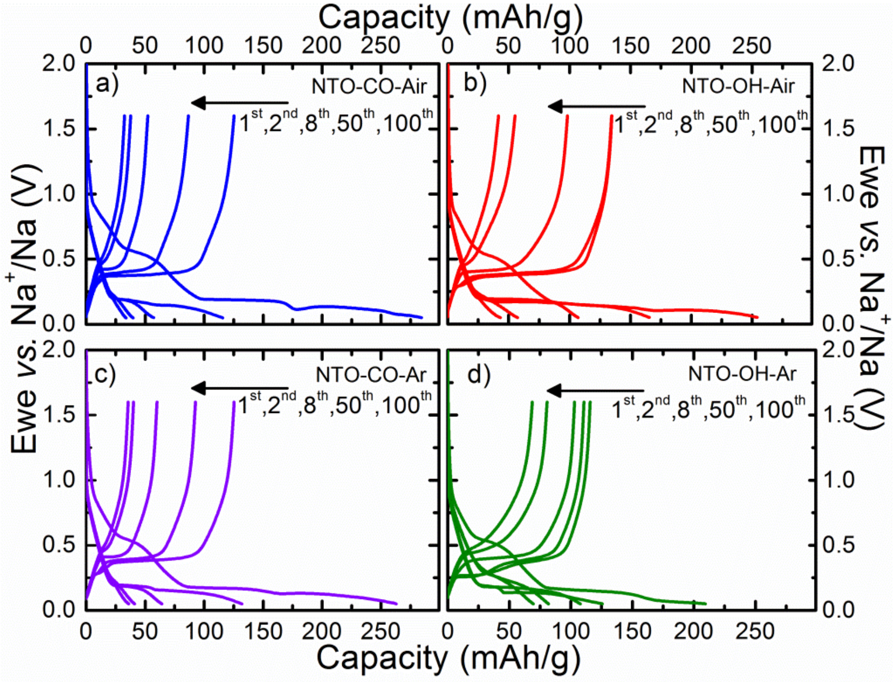

Figure 2.14: Voltage-capacity curves of **a) NTO-CO-Air** (blue), **b) NTO-OH-Air** (red), **c) NTO-CO-Ar** (violet) and **d) NTO-OH-Ar** (green).

Table 2.8: Capacity values and capacity retention obtained of the 20th and 100th cycles of **NTO-CO-Air**, **NTO-OH-Air**, **NTO-CO-Ar** and **NTO-OH-Ar** at 0.1C over voltage window 0.05 - 1.6 V *vs.* Na^+/Na.

Parameters	**NTO-CO-Air**	**NTO-OH-Air**	**NTO-CO-Ar**	**NTO-OH-Ar**
1st Na^+ insert. capacity (mAh/g)	284	254	263	209
1st Irreversible. capacity (mAh/g)	159	120	137	94
Capacity retention at 20th cycle	35%	57%	39%	85%
Capacity retention at 100th cycle	26%	31%	28%	59%

2.2.4. Influence of the C-coating

In order to further improve the capacity of sample **NTO-OH-Ar** a C-coating has been performed. In this case phthalocyanine (Ph) was used as carbon precursor in a 1:1 weight ratio and the mixture was pyrolyzed at 700 °C during 5 h under Ar atmosphere (sample **NTO-OH-Ar-C**) [25].

2.2.4.1. Structural and morphological characterization

2.2.4.1.1. Powder X-ray Diffraction (PXRD)

PXRD data were collected to check that the C-coating treatment does not affect the structure of $Na_2Ti_3O_7$. **Figure 2.15** shows the Le Bail refinement of the coated **NTO-OH-Ar-C** sample where zero factor, cell and profile parameters have been refined, as well as the PXRD pattern of the carbon precursor Ph. The obtained X^2 value has been 4.19 and the cell parameters are collected in **Table 2.9**, which are similar to those of the uncoated **NTO-OH-Ar** sample, suggest that the treatment done for the C-coating does not give rise to any structural change.

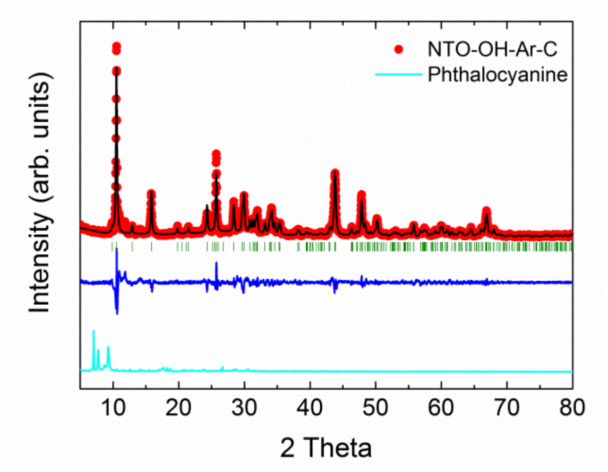

Figure 2.15: PXRD pattern of **NTO-OH-Ar-C** (black) refined by Le Bail method and the carbon precursor Ph (cyan).

Table 2.9: Comparison of the cell parameters of uncoated **NTO-OH-Ar** and coated **NTO-OH-Ar-C** samples ($P2_1/m$)

Sample	*a* (Å)	*b* (Å)	*c* (Å)	*β* (º)
NTO-OH-Ar	8.571(1)	3.7981(1)	9.126(1)	101.592(9)
NTO-OH-Ar-C	8.577(1)	3.7983(5)	9.136(1)	101.58(1)

2.2.4.1.2. Thermogravimetic analysis (TGA)

Thermogravimetic analysis was done to determine the amount of carbon of the C-coated sample in order to take it into account later in the electrochemical characterization. The carbon amount determined by TGA is 12 wt.%. (**Figure 2.16**).

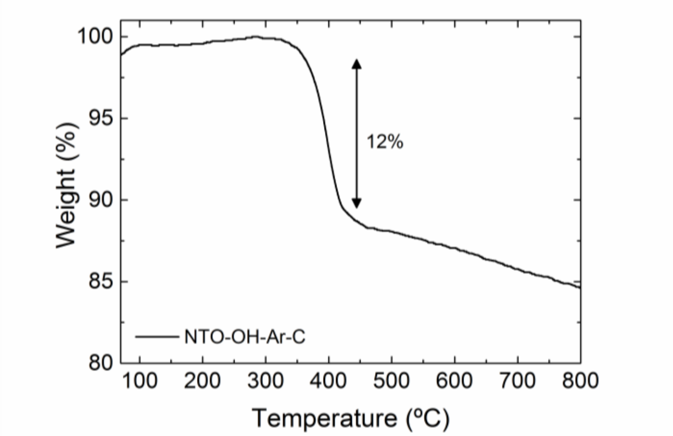

Figure 2.16: TGA analysis under air atmosphere heated up to 800 ^{o}C of **NTO-OH-Ar-C** (black).

2.2.4.1.3. Transmission Electron Microscopy (TEM)

The homogeneity and thickness of the C-coating was analysed by TEM (**Figure 2.17**). The measured thickness of the C-coating is around 6.0 nm and completely covers the $Na_2Ti_3O_7$ surface homogenously, except for some small isolated aggregates as those that can be observed in **Figure 2.17a**.

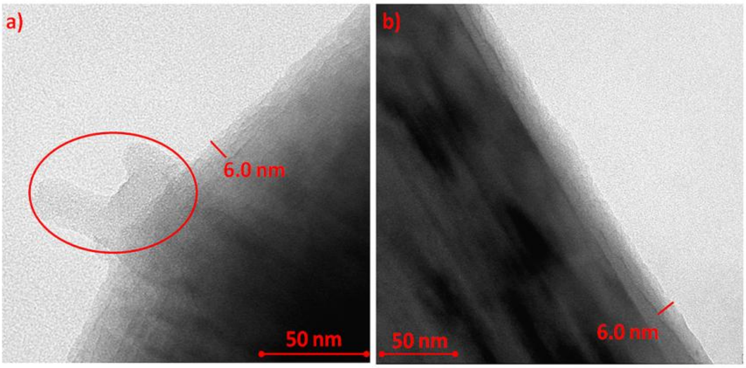

Figure 2.17: TEM images **a)** and **b)** of **NTO-OH-Ar-C**.

2.2.4.2. Electrochemical characterization

NTO-OH-Ar-C sample exhibits larger irreversible capacity than **NTO-OH-Ar** in the 1st cycles (**Figure 2.28a**). This value is similar to that observed by Xu *et al*. in C-coated $Na_2Ti_3O_7$ [26] and can be explained by the porous texture of the carbon, which results in a larger surface area and therefore a larger amount of SEI layer. However, the C-coated sample presents considerable higher capacities (**Figure 2.28b)** ranging from 166 mAh/g (1st cycle), close to the theoretical value (178 mAh/g), to 125 mAh/g (100th cycle). Additionally, the capacity retention is still further improved since a 78% of charge capacity is retained instead of 59% for the uncoated sample **NTO-OH-Ar** (**Figure 2.28c**; **Table 2.10** shows the significant values). This improvement can be correlated with the fact that the C-coating covers the surface of $Na_2Ti_3O_7$ particles suppressing direct interaction with the electrolyte, which can influence on the SEI layer composition and stability. This will be further discussed in **chapter 3**, and characterized with EIS and XPS experiments.

In order to evaluate the impact of the C-coating on the kinetics of Na^+ insertion/extraction, a rate capability test has been carried out at 0.1C, 0.2C, 0.5C, 1C, 2C and 5C (**Figure 2.28d**). As expected, the capacity decreases, from 149 mAh/g at 0.1C to 51 mAh/g at 5C, losing around 66% of the initial capacity. A similar behaviour was shown by Rudola *et al*. where they reported a 60% of capacity loss for the same rates. This is because Na^+ do not have enough time to intercalate into the structure at high current density. However, the C-coated sample slightly increases its capacity after the rate capability tests since, while Rudola *et al*. recovered the 93% of the initial capacity after tested at high currents, **NTO-OH-Ar-C** sample gets back almost its initial capacity (>97%).

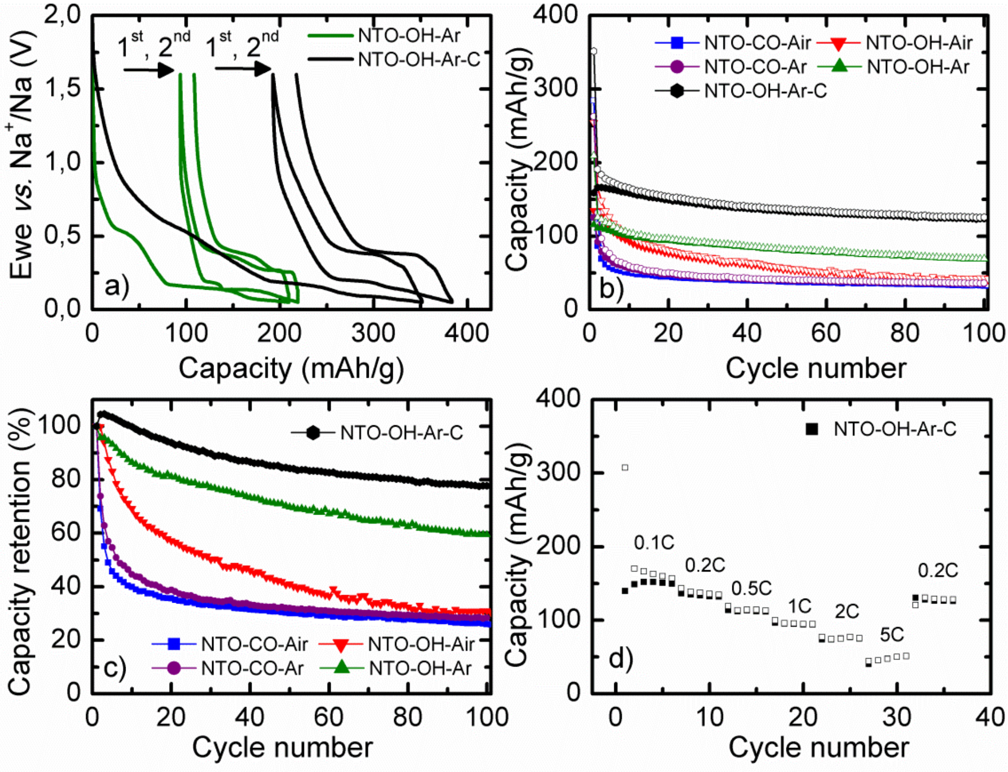

Figure 2.18: a) Voltage *vs.* capacity of the 1st and 2nd cycles of **NTO-OH-Ar** (green) and **NTO-OH-Ar-C** (black). **b)** Capacity and **c)** capacity retention *vs.* cycle number (taking into account as reference the 1st Na^+ extraction capacity of each). **NTO-CO-Air** (blue), **NTO-OH-Air** (red), **NTO-CO-Ar** (violet), **NTO-OH-Ar** (green) and **NTO-OH-Ar-C** (black). **d)** Rate capability at 0.1C, 0.2C, 0.5C, 1C, 2C and 5C of **NTO-OH-Ar-C**.

Table 2.10: Capacity values and capacity retention obtained of the 20th and 100th cycles of **NTO-CO-Air**, **NTO-OH-Air**, **NTO-CO-Ar**, **NTO-OH-Ar** and **NTO-OH-Ar-C** at 0.1C over voltage window 0.05 - 1.6 V *vs.* Na^+/Na

Parameters	**NTO-CO-Air**	**NTO-OH-Air**	**NTO-CO-Ar**	**NTO-OH-Ar**	**NTO-OH-Ar-C**
1st Na^+ insert. capacity (mAh/g)	284	254	263	209	352
1st Irreversible. capacity (mAh/g)	159	120	137	94	192
Capacity retention at 20th cycle	35%	57%	39%	85%	94%
Capacity retention at 100th cycle	26%	31%	28%	59%	78%

As conclusion, the surface corrosion and subsequent Na_2CO_3 formation can be avoided by using NaOH as Na precursor and cooling in Ar atmosphere, leading to better electrochemical performance. Moreover, capacity retention can be significantly enhanced with a C-coating, and the best capacity retention reported for $Na_2Ti_3O_7$ up to date has been obtained.

2.3. Moisture stability

As has been shown in the **section 2.2.**, $Na_2Ti_3O_7$ shows a high reactivity when exposed to air during the cooling process. This section focusses on the moisture stability of $Na_2Ti_3O_7$ so as to find out if it can be stored in air, which will have an impact in the final cost of battery.

A fresh batch of **NTO-CO-Air** was exposed to a saturated moisture environment to accelerate possible transformations by placing the material in a desiccator with a beaker full of water at room temperature and the evolution of the material was followed by collecting a PXRD pattern every week for a total of eight weeks. These are shown in **Figure 2.19**, together with that of the fresh **NTO-CO-Air** sample and an **HTO** sample prepared as reference (in both cases the Le Bail refinement shows the purity of the phases). The PXRD patterns of **NTO-CO-Air** and **HTO** are similar and mainly differ in the position of the diffraction peaks owing to their different cell parameters and the doubling of the unit cell along *a* axis (more details in **section 2.1.**). The evolution of the PXRD pattern of the exposed **NTO-CO-Air** sample exhibits a progressive shift of the diffraction peaks (100) and (101) towards higher 2 Theta values and the appearance of new reflections which are indexed as (202), (310) and (003) reflections of a *C2/m* unit cell similar to that of **HTO** sample. This evolution therefore indicates the progressive transformation into $H_2Ti_3O_7$ by the exchange of

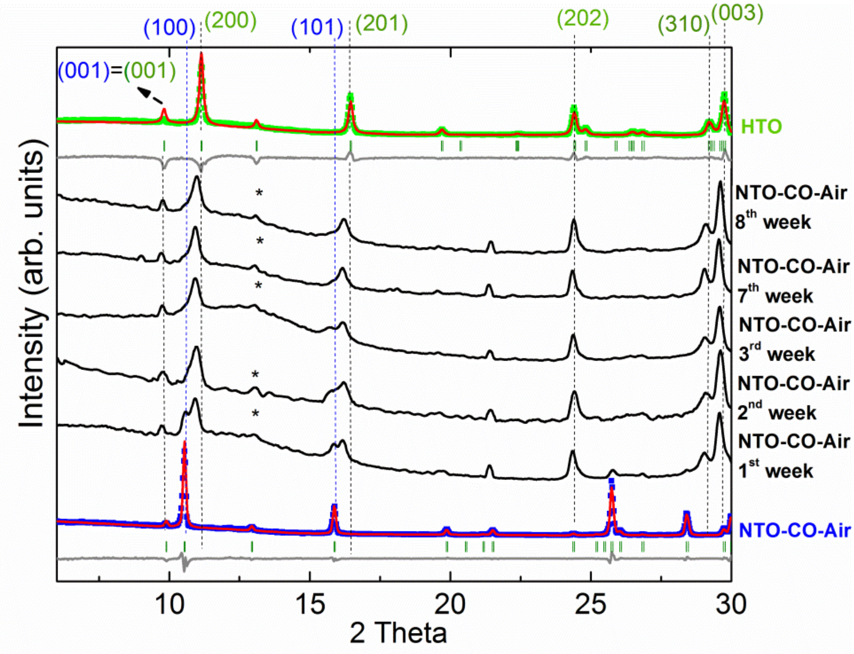

Figure 2.19: PXRD data of as prepared **NTO-CO-Air** (bottom), after humid air exposure during eight weeks and **HTO** sample (top). Le Bail refinements of **NTO-CO-Air** and **HTO** samples are shown. Observed (points), calculated (solid line), difference (gray line) and Bragg reflections (green vertical bars). *Sample holder.

Na^+ by H^+ through the formation of intermediate compositions of the $Na_{2-x}H_xTi_3O_7$ (0<x<2) solid solution. The transformation is partial since the initial phase $Na_2Ti_3O_7$ is still found in all patterns ((001) peak remains in all patterns) and involves a structural modification. From the intensity ratios it can be estimated that after one week the amount of $Na_2Ti_3O_7$ is still considerable, while almost disappears in the following weeks. During the evolution process, a widening of diffraction peaks is also detected which can be related to the formation of smaller domains, microstrains or stacking faults due to the shift of the $[TiO_6]$ layer along *b* axis. Although all patterns are indexed using *C*2/*m* space group and therefore with a doubling of the unit cell the amount of Na^+ in the main phase can be roughly estimated assuming a linear evolution of the *a* cell parameter following Vegard's law and using the value of the subcell (**Table 2.11**). It is found that more than half of Na^+ have already been exchanged in part of the sample during the 1st week, the transformation continues to progress in the following weeks and a composition close to $Na_{0.5}H_{1.5}Ti_3O_7$ is obtained after the 8th week never achieved the complete transformation to $H_2Ti_3O_7$ under these conditions. Interestingly, $Na_{0.5}H_{1.5}Ti_3O_7$ has been found to be one of the most stable compositions in the work of Mori *et al.* [9].

Table 2.11: Space group, cell parameter evolution and volume per formula unit (values in brackets correspond to the equivalent volume in a supercell 2*abc* to allow for comparison between $Na_2Ti_3O_7$ and $H_2Ti_3O_7$ type structures) of air exposed samples compared to end member compositions and corresponding Na^+ amount estimated by Vegard's law using *a* cell parameter evolution.

Sample	Space Group	*a* (Å)	*b* (Å)	*c* (Å)	*β* (º)	Volume per formula unit (Å^3)	Na^+ amount*
NTO	$P2_1/m$	8.5657(2)	3.79836(7)	9.1231(2)	101.601(2)	291.4 (582.8)	2.0
NHTO-H_2O	$C2/m$	16.440(3)	3.7419(6)	9.249(2)	101.85(2)	557.3	0.80
NTO-1st week	$C2/m$	16.419(9)	3.741(2)	9.207(4)	101.87(6)	553.4	0.70
	$P2_1/m^†$	8.550(2)	3.7744(9)	9.137(2)	101.30(2)	289.1 (578.2)	
NTO-2nd week	$C2/m$	16.369(5)	3.733(1)	9.231(3)	102.101(3)	551.5	0.60
	$P2_1/m^†$	8.551(2)	3.7729(7)	9.132(2)	101.17(1)	298.0 (578)	
NHTO-HCl	$C2/m$	16.369(3)	3.7498(7)	9.268(1)	103.14(1)	5540.	0.60
NTO-3rd week	$C2/m$	16.36(1)	3.735(3)	9.243(7)	101.99(5)	552.5	0.55
	$P2_1/m^†$	8.554(3)	3.773(2)	9.139(3)	101.17(3)	289.3 (578.6)	
NTO-7th week	$C2/m$	16.35(2)	3.736(5)	9.27(1)	102.13(1)	553.8	0.55
	$P2_1/m^†$	8.541(4)	3.785(2)	9.137(2)	101.37(4)	289.6 (579.2)	
NTO-8th week	$C2/m$	16.33(1)	3.73(2)	9.237(8)	102.18(6)	551.0	0.50
	$P2_1/m^†$	8.533(4)	3.784(1)	9.127(4)	101.47(4)	288.8 (577.6)	
HTO	$C2/m$	16.0243(1)	3.74973(5)	9.1888(2)	101.4384(2)	542.3	0.0

*Vegard´s law, † $Na_2Ti_3O_7$

The value of *a* parameter in the air exposed samples is larger with respect to that of HTO. This can be explained by the fact that the distance between [TiO_6] layers (*a* axis corresponds to the layer stacking direction) should be larger in Na containing samples. On the other hand, the *b* cell parameter in all cases is similar to that of HTO. The limited amount of sample recovered did not allow determining the *c* cell parameter with accuracy and therefore, no clear trend is observed. The fact that the value of *c* parameter is higher than that of HTO can be due to the larger distortion of [TiO_6] octahedra when Na^+ is present, as will be discussed later. The volume of $Na_2Ti_3O_7$ (582.8 Å^3) is much higher than that of $H_2Ti_3O_7$ (542.3 Å^3) due to the fact that in $H_2Ti_3O_7$ the interlayer distance is reduced owing to the lower ionic radius of H^+ and H bonds. While air exposed samples show higher volume per unit cell by the fact that Na^+ remains in the interlayer distance.

In summary, $Na_2Ti_3O_7$ must be stored in a dry atmosphere and must be handled with care to avoid its transformation into $Na_{2-x}H_xTi_3O_7$ ($0<x\leq2$) unless the transformation is not detrimental to the electrochemical properties of the material and, in that case, can even be processed in aqueous solution.

2.4. Water stability

Na-CMC has already been proposed by several groups as an environmentally friendly and low-cost replacement of PVdF binder [27, 28, 29, 30, 31]. Indeed, Na-CMC can be dissolved in water and organic solvents, such as NMP, can be suppressed from the electrode fabrication process, which enormously reduces the cost of the final battery. However, the transformation of $Na_2Ti_3O_7$ into $Na_{2-x}H_xTi_3O_7$ ($0<x\leq2$) is expected to be enhanced in water. This has been explored in this section and is detailed below.

2.4.1. Synthesis of $Na_{2-x}H_xTi_3O_7$ ($0<x\leq2$)

Two $Na_{2-x}H_xTi_3O_7$ ($0<x<2$) samples were prepared by ionic exchange. The first was prepared by soaking **NTO-CO-Air** in distilled water and refluxing at 60 ^oC for 1 day (**NHTO-H_2O**), while for the second **NTO-CO-Air** was soaked in a 0.1 M HCl solution at room temperature for 1 h (**NHTO-HCl**). $H_2Ti_3O_7$ (**HTO**) was also prepared by ion exchange by soaking **NTO-CO-Air** in excess HCl 0.1 M and refluxing at 60 ^oC for 3 days. After the ion exchange reaction the samples were filtered and washed with distilled water and dried under vacuum overnight at 60 ^oC.

2.4.2. Structural, morphological and chemical characterization

2.4.2.1. Powder X-ray Diffraction (PXRD)

From the PXRD pattern of **NHTO-HCl** sample it can be concluded that this sample is pure, while **NHTO-H_2O** sample shows a small amount of $Na_2Ti_6O_{13}$ as impurity. This compound must has been formed during the ion exchange treatment since the same $Na_2Ti_3O_7$ batch is used for both ionic exchange processes (**Figure 2.20**). The PXRD of **NHTO-H_2O** sample shows a shoulder at low 2 Theta values that corresponds to the sample holder since a small amount of powder is used for the measurement. By comparing the cell parameters of these two samples obtained by Le Bail refinement, where the parameters refined have been zero factor and cell and profile parameters, with those resulting from **NTO-CO-Air** exposed in humid air (**Table 2.11**). It can be concluded that **NHTO-H_2O** is richer in Na^+ than **NHTO-HCl**,

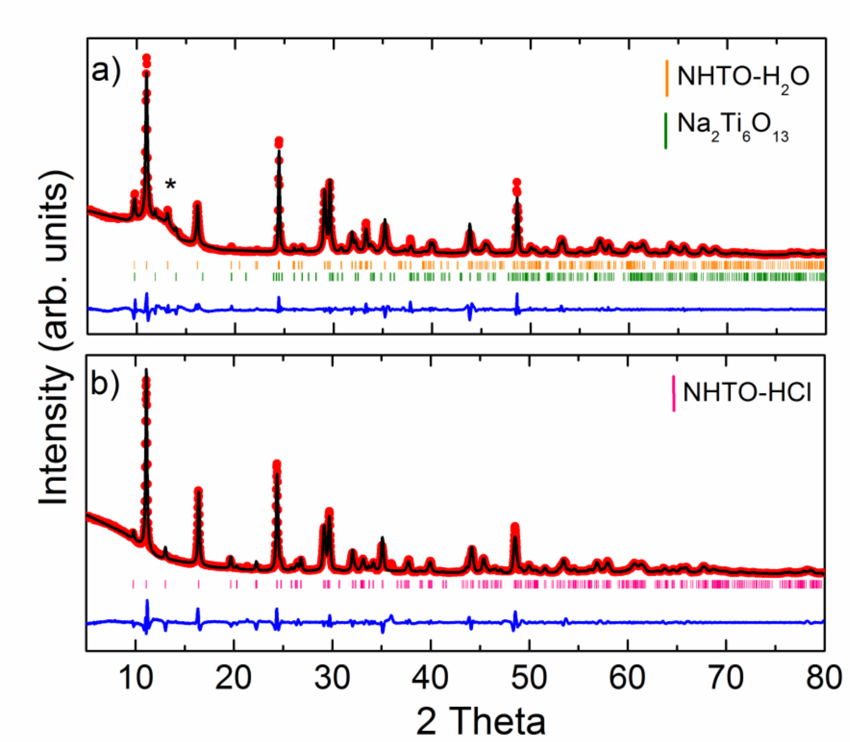

Figure 2.20: Le Bail refinement of PXRD **a)** **NHTO-H_2O** (orange vertical bars), $Na_2Ti_6O_{13}$ impurity (green vertical bars) and **b)** **NHTO-HCl** (pink vertical bar) samples. Observed (red points), calculated (black line) and difference (blue line). *Sample holder.

whose composition would be close to that obtained for the samples exposed to humid air between the 2nd and 3rd week.

The fact that no remaining $Na_2Ti_3O_7$ is found in any of the two samples enabled further chemical and structural characterization.

2.4.2.2. Scanning Electron Microscopy (SEM)

The morphology of the solid solution $Na_{2-x}H_xTi_3O_7$ ($0 \leq x \leq 2$) remains invariable in the studied compositional range. All samples crystallize as platelets of micrometric size (**Figure 2.21**), but the particles of **NHTO-H_2O** show cracks (**Figure 2.21b**, the highlighted particles in red), probably due to exfoliation when the ion exchange process is longer.

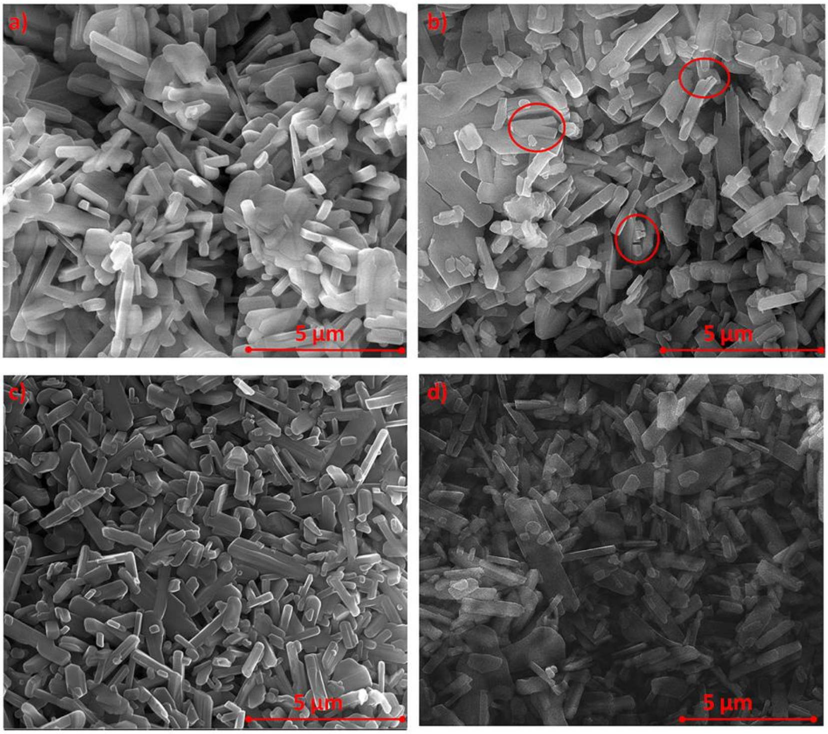

Figure 2.21: SEM images of **a) NTO-CO-Air**, **b) NHTO-H_2O**, **c) NHTO-HCl** and **d) HTO**.

2.4.2.3. Electron Diffraction (ED)

Since the space group of the two end members is different and the indexation of the intermediate compositions of $Na_{2-x}H_xTi_3O_7$ (0<x<2) solid solution is unclear ED data were recorded for **NHTO-H_2O** and **NHTO-HCl** in order to determinate the space group. **Figure 2.22a** and **Figure 2.22b** show the pattern corresponding to [001] zone axis, which is the one most frequently found for both samples. In both cases a lattice centering is observed and therefore a C-centred unit cell must be used to describe the structure. According to the reconstruction of the reciprocal space it can be concluded that both samples are isostructural to $H_2Ti_3O_7$ with *C*2/*m* space group. In the [001] zone axis, streaks along *a** are also observed which result from disorder in the stacking direction. This disorder along *a** is indicative of the existence of stacking faults that result from the gliding of [TiO_6] layers as the structure evolves from AA [TiO_6] layer stacking sequence (S.G: $P2_1/m$) into an AB stacking sequence (S.G: *C*2/*m*). Moreover this disorder might also partially contribute to the broadening of the PXRD peaks (c.f. **Figure 2.19**) most probably because of some residual local AA motifs remain in the structure. The evidence of

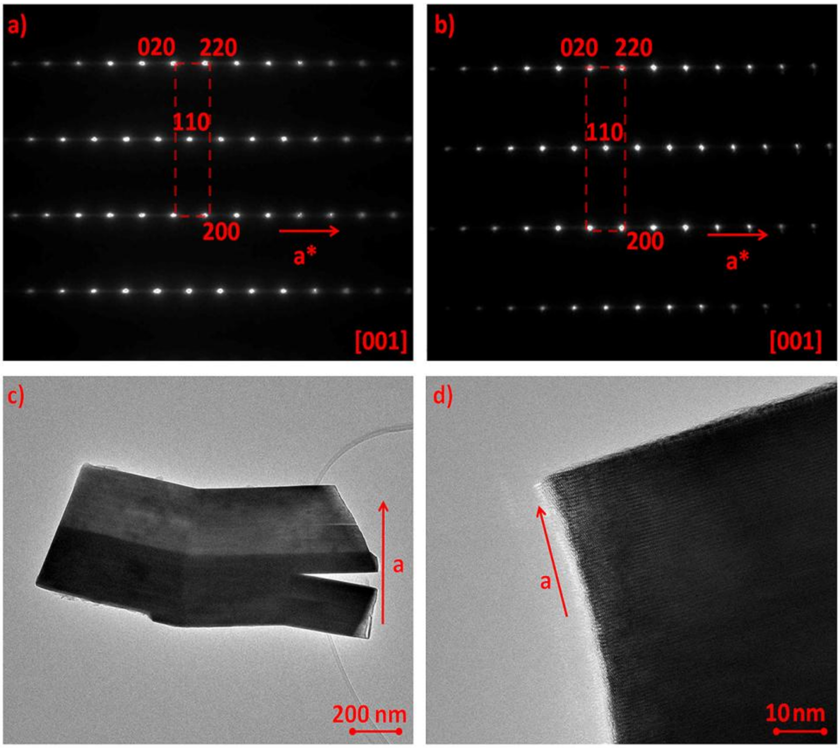

Figure 2.22: ED patterns of [001] zone axis of **a)** **NHTO-H_2O** and **b)** **NHTO-HCl** samples. HTEM images of **NHTO-H_2O** **c)** showing the exfoliation of the particles and **d)** the staking direction of [TiO_6] layer along *a*.

exfoliation already observed by SEM image (**Figure 2.21b**) along the stacking direction is shown in some particles of the **NHTO-H_2O** sample (**Figure 2.22c**) while are not observed in the **NHTO-HCl**, most probably because the duration of the ion exchange treatment in the first one is considerably longer. **Figure 2.22d** shows a high resolution TEM image (HTEM) of the staking direction along *a* of **NHTO-H_2O** sample.

2.4.2.4. Chemical analysis

To determine the exact amount of H^+ and Na^+ in the prepared $Na_{2-x}H_xTi_3O_7$ (0<x<2) compounds TGA and ICP-OES were respectively used, and the obtained results are summarized in **Table 2.12**. From TGA analysis the amount of H^+ can be determined from the weight loss corresponding to the release of water when the sample is heated. The weight loss at 100 ^oC corresponds to the absorbed water on the surface while at 350 ^oC is related with structural water. A weight loss of 2.39% and

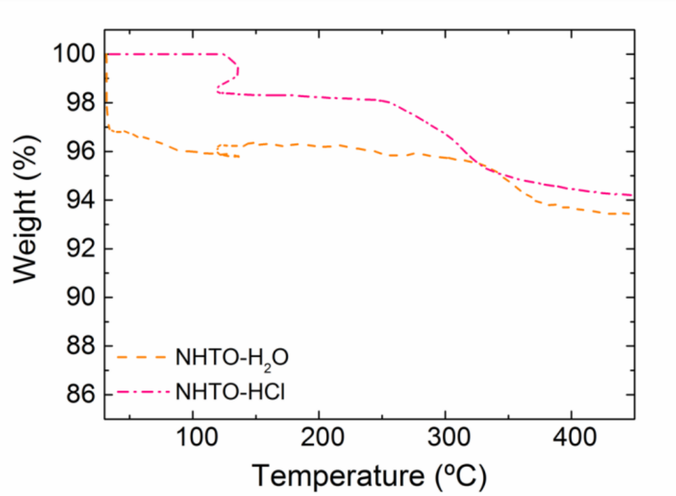

Figure 2.23. TGA analysis in air atmosphere heated up until 800 °C of **NHTO-H_2O** (orange) and **NHTO-HCl** (pink).

4.00% is observed for **NHTO-H_2O** and **NHTO-HCl**, respectively (**Figure 2.23**) which corresponds to 0.8 and 1.4 H^+ per formula unit.

To determine the amount of Na^+, ICP-OES analyses were used after digestion of both samples in HCl aqueous solution, resulting in 1.3 and 0.60 Na^+ per formula unit.

Ion beam analysis (IBA) techniques have been done at the *Centro Nacional de Aceleradores* (CNA, Sevilla) to verify the amount of H^+ and Na^+ since these techniques are more accurate and a full analysis of the composition (H^+, Na^+, Ti and O) can be performed. For this analysis, two pellets of **NHTO-H_2O** and **NHTO-HCl** have been prepared and the Na^+, Ti and O content are determined by Rutherford backscattering spectrometry (RBS). The determination of the H^+ concentration has been done by elastic recoil detection analysis (ERDA), since RBS is not suited for the determination of H^+ concentration. As can be seen in **Table 2.12**, the TGA and ICP-OES results are in very good agreement with the RBS and ERDA analysis.

Table 2.12: H^+ and Na^+ content of **NHTO-H_2O** and **NHTO-HCl** obtained from TGA, ICP-OES, RBS and ERDA analysis.

	NHTO-H_2O				**NHTO-HCl**			
	H^+	Na^+	Ti	O	H^+	Na^+	Ti	O
TGA	0.8				1.4			
ICP-OES		1.3				0.6		
ERDA/RBS	0.7(2)	1.3(2)	2.2(2)	6.4(5)	1.4(2)	0.6(2)	2.3(2)	7.0(5)

Therefore, we can unambiguously determine the composition of the **NHTO-H_2O** to be $Na_{1.3}H_{0.7}Ti_3O_7$, while that of the **NHTO-HCl** is $Na_{0.6}H_{1.4}Ti_3O_7$. As expected, the sample prepared in acidic solution contains more H^+, even though the duration of the treatment was shorter.

2.4.2.5. ^{23}Na and ^{1}H solid-state Nuclear Magnetic Resonance (ssNMR)

The ^{23}Na-ssNMR spectrum of **NHTO-H_2O** is shown in **Figure 2.24a**. The spectrum corresponds to the superposition of a number of ^{23}Na-NMR signals that are not resolved in a simple 1D spectrum due to the quadrupolar character of ^{23}Na (I_{Na} = 3/2). The second order quadrupolar broadening of the signals is normally large and precludes high resolution 1D experiments [32]. Nevertheless, the individual components of 1D spectrum can be resolved by Multiple Quantum Magic Angle Spinning (MQMAS) experiment [33], since in a 2D experiment multiple- and single-quantum coherences are correlated in the presence of MAS. The ^{23}Na-MQMAS spectrum of **NHTO-H_2O** is shown in **Figure 2.24b** and, using this information, the 1D spectrum of **Figure 2.24a** can be deconvoluted; the result is shown at the top of **Figure 2.24b**. In this spectrum, four main signals are observed, two of them with quadrupolar broadening. These two signals are characterized by quadrupolar coupling values of Cq_1 = 4.1 MHz and Cq_2 = 5.4 MHz and asymmetry factors of η_1 = 0.71 and η_2 = 0.54. These are similar to that observed for Na1 type in $Na_2Ti_3O_7$ (c.f. **Figure 2.4a**) [13] which corresponds to a low symmetry site. Additionally, the two other main signals which show no quadrupolar broadening appear close to 0 ppm. These signals also resemble that assigned to Na2 in $Na_2Ti_3O_7$, which is characterized by a negligible quadrupolar broadening, as these Na^+ are located at a site with higher symmetry and presumably higher mobility [13]. The split of each ^{23}Na signal of $Na_2Ti_3O_7$ into two slightly different chemical shifts in **NHTO-H_2O** could be attributed to the different environment generated by the partial Na^+ and H^+ occupancies. Additionally, a small non quadrupolar component appears which can be related to the presence of hydrated Na^+ at the surface of the particles. This is in agreement with the presence of a small amount of absorbed water at around 4.5 ppm of ^{1}H-ssNMR spectrum (**Figure 2.24c**). Unfortunately the accurate quantification of the distinct Na^+ populations in the material by MQMAS is difficult due to the different magnitudes of the quadrupolar interactions.

The ^{1}H-ssNMR spectrum of **NHTO-H_2O** is shown in **Figure 2.24c**. Besides the small signal arising from a minor content of water around 4.5 ppm as mentioned above, one main signal is observed at around 11.5 ppm which is assigned to structural hydrogen. The shift is in agreement with the H^+ resonances obtained previously in

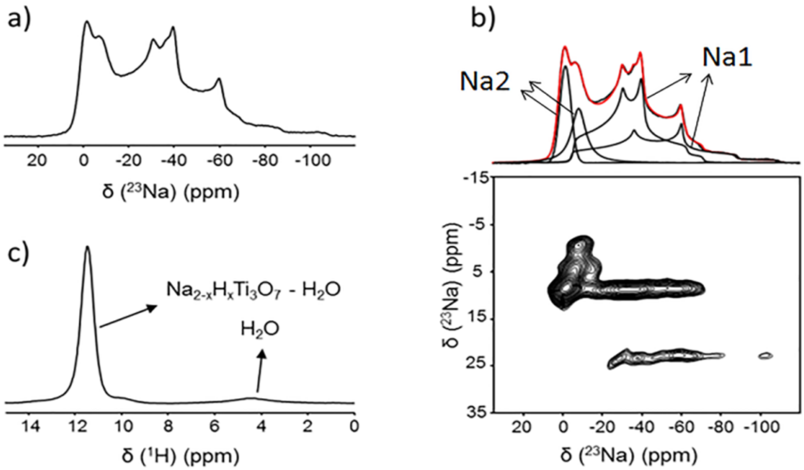

Figure 2.24: a) ^{23}Na-ssNMR, **b)** ^{23}Na-MQMAS and **c)** ^{1}H-ssNMR spectra of **NHTO-H_2O**. The resulting deconvolution of the 1D spectrum (**a**) considering the signals obtained in the MQMAS spectrum is shown at the top of **figure b.**

$H_2Ti_3O_7$ phase, where two types of H^+ give one signal and the third one has another chemical shift with the relative population of 3:1 and not 1:1 [10].

The ^{23}Na-ssNMR spectrum of **NHTO-HCl** is shown in **Figure 2.25a** and, as for **NHTO-H_2O**, the 1D signal can only be deconvoluted after careful inspection of the MQMAS spectrum (**Figure 2.25b**). In this case the two quadrupolar signals observed are the main component. These ^{23}Na NMR signals obtained from the deconvolution shown at the top of **Figure 2.25b** are characterized by quadrupolar coupling constants Cq_1 = 4.0 MHz and Cq_2 = 3.6 MHz and asymmetry factors η_1 = 0.66 and η_2 = 0.02. These quadrupolar coupling constants and asymmetry factors are in agreement with the values obtained for Na1 in **NHTO-H_2O**. This suggests that during the ion exchange process in acidic medium almost all Na^+ of the Na2 position of $Na_2Ti_3O_7$ are replaced first, presumably due to a higher mobility of Na^+ in this partially substituted site.

The ^{1}H-ssNMR spectrum of **NHTO-HCl** (**Figure 2.25c**) is very similar to the one observed for the $H_2Ti_3O_7$ phase [10], with a main signal at 12.5 ppm and a minor signal at 11.5 ppm, although with different relative intensities (1.8:1) which suggests the presence of at least two or maybe three types of H^+ as in the $H_2Ti_3O_7$.

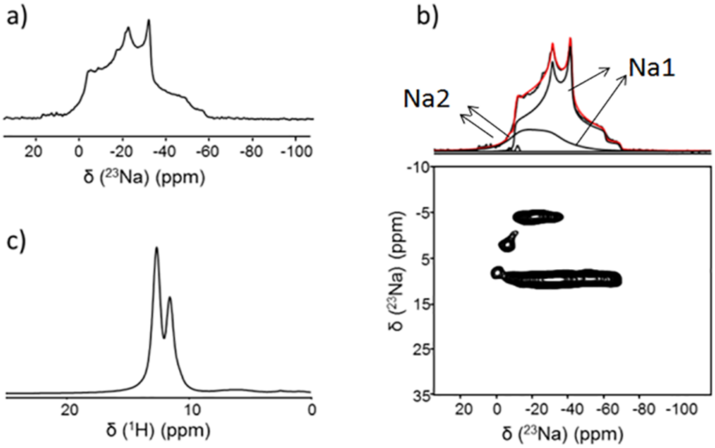

Figure 2.25: a) ^{23}Na-ssNMR, **b)** ^{23}Na-MQMAS and **c)** ^{1}H-ssNMR spectra of **NHTO-HCl**. The resulting deconvolution of the 1D spectrum (**a**) considering the signals obtained in the MQMAS spectrum is shown at the top of **figure b.**

2.4.2.6. Powder Neutron Diffraction (PND)

PND data of the mixed compositions were obtained at D1B instrument (ILL, Grenoble) at λ = 1.28 Å. The refinement of both neutron data has been processed in several steps since the Na^+ and H^+ coordinates were unknown prior to this work. From the results of ED, *C*2/*m* space group is chosen to index both patterns and refined zero, scale factor and the cell and profile parameters. Using the atomic structure of $H_2Ti_3O_7$ as starting point [8], the atomic coordinates of the Ti-O framework are refined, where in the case of **NHTO-H$_2$O** sample the Ti-O bond distances were constricted. Na^+ and H^+ are then located by difference Fourier maps using GFourier software [34]. These are shown in **Figure 2.26** for **NHTO-H$_2$O** sample, where it can be seen that, at y = 0.0 (**Figure 2.26a**), the Fourier map presents positive residual nuclear scattering density at 4*i* Wyckoff positions, which would correspond to Na^+ (Na1 and Na2) since Na^+ has a positive nuclear scattering factor. On the other hand, at y = 0.5 (**Figure 2.26b**), negative residual nuclear scattering density can be observed at 4*i* (H1) and 2*a* Wyckoff positions (H2) which would correspond to H^+ owing to its negative scattering factor [35]. In the case of **NHTO-HCl** sample (**Figure 2.27**), Na^+ and H^+ are found more or less at the same atomic positions as in **NHTO-H$_2$O** sample. However, one extra very intense peak appears at another 4*i* Wyckoff position (H3) (**Figure 2.27b**), which would be indicative of three different H^+ instead of two. In this sample the negative scattering intensity related to H^+ in 2*a* sites (H2) only became visible after the other two H^+ (H1 and H3) were included in the structural model.

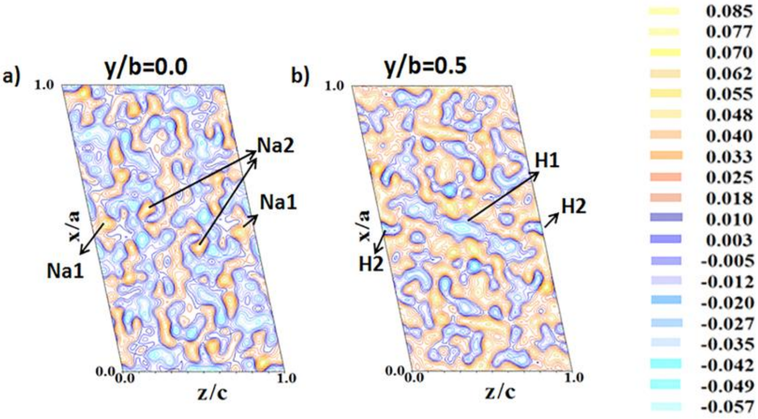

Figure 2.26: Difference Fourier maps at **a)** y = 0.0 and **b)** y = 0.5 of **NHTO-H_2O**. Orange line positive and blue lines negative nuclear scattering.

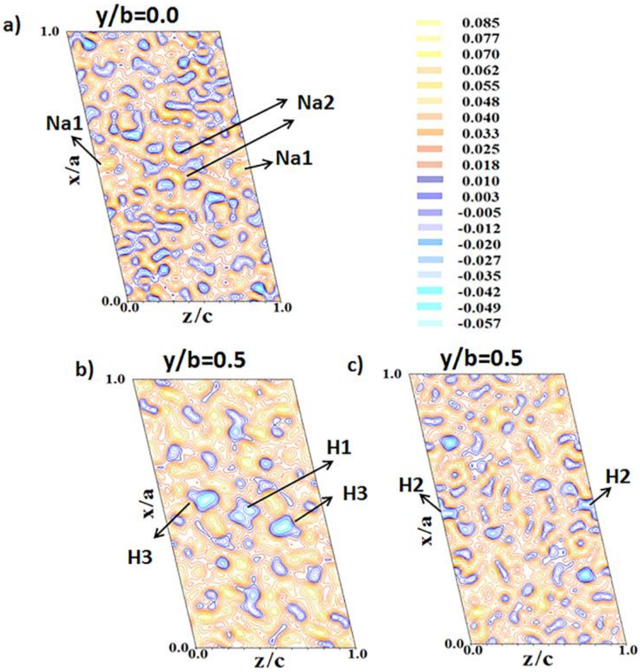

Figure 2.27: Difference Fourier maps at **a)** y = 0.0 and **b,c)** y = 0.5 of **NHTO-HCl**. Orange line positive and blue lines negative nuclear scattering.

The atomic positions determined from the Fourier difference maps were then introduced in the structural model to be further refined. After that, the B_{iso} factors and atomic occupancies were also refined by constraining the B_{iso} factor for the same type of atoms, with the simultaneous refinement of all parameters in the last stage of the refinement. **Figure 2.28** shows the Rietveld fit of both samples. As mentioned before (in the PXRD **2.4.2.1. section**) the **NHTO-H_2O** has as impurity $Na_2Ti_6O_{13}$ which is formed during the ion exchange process. The cell parameters, reliability factors, final atomic positions, B_{iso} factors, atomic occupancies and reliability factors obtained from the PND refinement are given in **Table 2.13** and **Table 2.14**.

The resulting structures obtained by the refinement of neutron diffraction data for **NHTO-H_2O** (**Figure 2.29a**) and **NHTO-HCl** samples (**Figure 2.29b**) are sketched below.

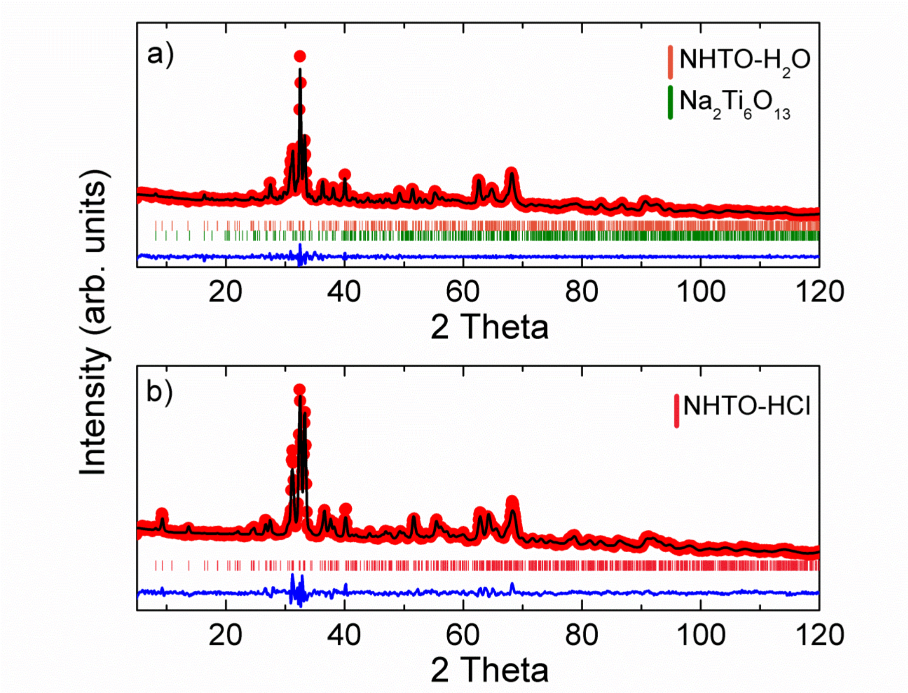

Figure 2.28: Rietveld refined PND pattern collected at λ = 1.28 Å in D1 instrument of ILL for **a)** **NHTO-H_2O** (orange vertical bars), $Na_2Ti_6O_{13}$ impurity (green vertical bars) and **b)** **NHTO-HCl** (pink vertical bars) samples. Observed (red points), calculated (black line) and difference (blue line).

The main structural differences between both samples would therefore be the negligible occupancy of Na2 and the presence of a third type of H^+ in **NHTO-HCl**. Interestingly also three types of H^+ have been found in $H_2Ti_3O_7$ at similar positions, which is in agreement with the similar ^{1}H-ssNMR spectrum [10]. The slight differences being most probably due to the fact that Na^+ are in the interlayer spaces and its presence influences on the H^+ environments. The fact that Na^+ and H^+ are located in different positions is a consequence of their different ionic radius. Indeed, Na^+ are located in prismatic holes as in $Na_2Ti_3O_7$, while the smaller H^+ are located in the same plane as oxygen (020), as it occurs in $H_2Ti_3O_7$.

Table 2.13: Refined cell parameter, atomic positions, B_{iso} and SOF and reliability factors obtained from PND refinement of **NHTO-H_2O**.

Cell parameter

a (Å)	*b* (Å)	*c* (Å)	*β* (º)
16.395(2)	3.7574(5)	9.273(1)	102.65(1)

Atomic position, Biso and SOF

Atom	Wyckoff	SOF	*x* (Å)	*y* (Å)	*z* (Å)	*Biso* (Å^2)
Ti1	4*i*	1.0	0.204(3)	0	0.228(4)	2.1(4)
Ti2	4*i*	1.0	0.173(2)	0	0.539(5)	2.1(4)
Ti3	4*i*	1.0	0.144(1)	0	0.820(1)	2.1(4)
O1	4*i*	1.0	0.149(2)	0	0.048(3)	1.3(1)
O2	4*i*	1.0	0.119(2)	0	0.324(3)	1.3(1)
O3	4*i*	1.0	0.069(2)	0	0.581(3)	1.3(1)
O4	4*i*	1.0	0.018(2)	0	0.850(4)	1.3(1)
O5	4*i*	1.0	0.328(2)	0	0.171(3)	1.3(1)
O6	4*i*	1.0	0.260(1)	0	0.452(3)	1.3(1)
O7	4*i*	1.0	0.244(1)	0	0.749(3)	1.3(1)
Na1	4*i*	0.650(4)	0.530(4)	0	0.855(8)	0.845(4)
Na2	4*i*	0.618(3)	0.422(4)	0	0.540(8)	0.845(4)
H1	4*i*	0.50	0.019(2)	0	0.5073(5)	0.132(8)
H2	2*a*	0.467(3)	0	0	0	0.121(8)

Reliability factors

χ^2	R_p	R_{wp}	R_e	R_F
2.33	12.6	12.6	8.24	0.72

Table 2.14: Refined cell parameter, atomic positions, isotropic B_{iso} and SOF and reliability factors obtained from PND refinement of **NHTO-HCl**.

Cell parameter

a (Å)	*b* (Å)	*c* (Å)	*β* (º)
16.351(2)	3.7494(4)	9.262(1)	103.134(7)

Atomic position, Biso and SOF

Atom	Wyckoff	SOF	*x* (Å)	*y* (Å)	*z* (Å)	*Biso* ($Å^2$)
Ti1	4*i*	1.0	0.230(2)	0	0.218(3)	0.5(2)
Ti2	4*i*	1.0	0.179(2)	0	0.514(4)	0.5(2)
Ti3	4*i*	1.0	0.125(2)	0	0.807(4)	0.5(2)
O1	4*i*	1.0	0.170(1)	0	0.035(2)	0.90(6)
O2	4*i*	1.0	0.149(1)	0	0.325(2)	0.90(6)
O3	4*i*	1.0	0.079(1)	0	0.595(3)	0.90(6)
O4	4*i*	1.0	0.016(1)	0	0.856(2)	0.90(6)
O5	4*i*	1.0	0.353(1)	0	0.186(2)	0.90(6)
O6	4*i*	1.0	0.288(1)	0	0.447(2)	0.90(6)
O7	4*i*	1.0	0.240(1)	0	0.750(2)	0.90(6)
Na1	4*i*	0.45(5)	0.519(4)	0	0.967(6)	1.2(2)
Na2	4*i*	0.18(6)	0.402(1)	0	0.645(6)	1.2(2)
H1	4*i*	0.50	0.016(3)	0	0.488(7)	0.228(6)
H2	2*a*	0.29(3)	0	0	0	0.228(6)
H3	4*i*	0.73(4)	0.038(2)	0	0.225(4)	0.228(6)

Reliability factors

χ^2	R_p	R_{wp}	R_e	R_F
6.36	16.3	16.2	6.44	3.07

The occupancy values of Na^+ and H^+ can be correlated with the ion exchange sequence and therefore with the mobility of each type of crystallographic position. Only H1 is fully occupied in both compounds (note that, since it is a split position, full occupancy is 0.50 as the two neighbouring positions cannot be occupied simultaneously) and for that reason it is the first H^+ to completely fill the position close to Na2. Na2 is therefore the first Na^+ to be replaced (since Na1 has higher occupancy in both samples) which is in agreement with the almost complete disappearance of the non-quadrupolar signal in the ^{23}Na-ssNMR of **NHTO-HCl** (**Figure 2.25b**). Moreover, H3 only appears in this sample and consequently this is the last H^+ position to be occupied. The occupancies obtained by PND data of the rest of Na^+ and H^+ are given in **Table 2.13** and **Table 2.14** for **NHTO-H$_2$O** and **NHTO-HCl**, respectively. Taking into account these values an average composition of $Na_{1.3}H_{0.7}Ti_3O_7$ for **NHTO-H$_2$O** and $Na_{0.6}H_{1.4}Ti_3O_7$ for **NHTO-HCl** has been calculated, which is in good agreement with the results of chemical analyses (**Table 2.12**) and ssNMR data (**Figure 2.24** and **Figure 2.25**). Note that the amount of Na^+ estimated

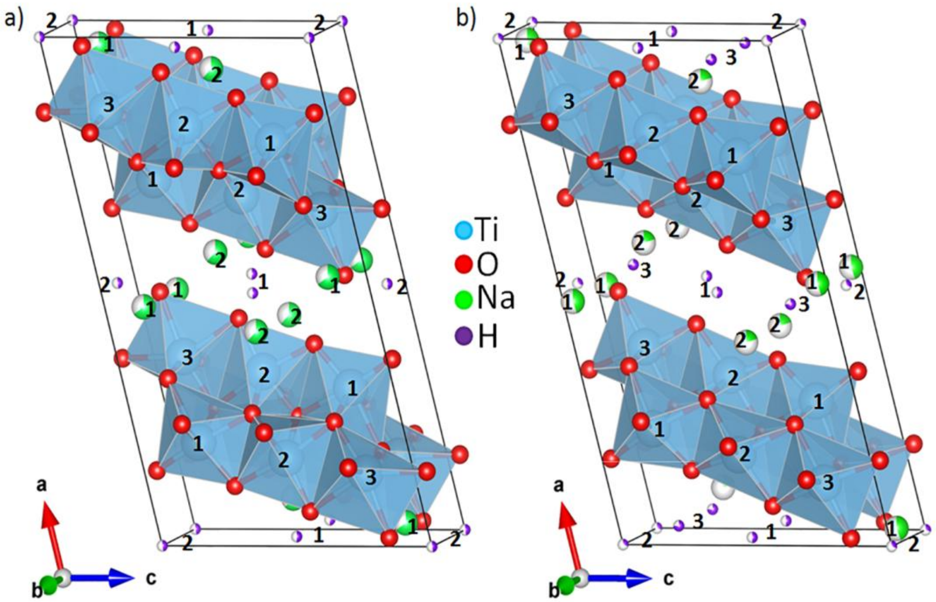

Figure 2.29: Resulting structure for **a)** **NHTO-H_2O** and **b)** **NHTO-HCl**, respectively with the corresponding Ti^{4+}, Na^+ and H^+ labelled with 1, 2 and 3. The fractional occupancies of Na^+ and H^+ are indicating by the colour ratio.

by Vegard's law taking into account a linear evolution of the *a* cell parameter only fits well for **NHTO-HCl** sample (**Table 2.11**), which could be due to the fact that **NHTO-H_2O** composition is close to where the symmetry change from $P2_1/m$ to $C2/m$ occurs and deviates from a unique Vegard law.

Compared with previously reported compositions, **NHTO-H_2O** ($Na_{1.3}H_{0.7}Ti_3O_7$) is closer to that reported by Izawa *et al.* ($Na_{1.43}H_{0.57}Ti_3O_7$, S.G: $P2_1/m$, **Figure 2.1a**) [7], while the composition of **NHTO-HCl** ($Na_{0.6}H_{1.4}Ti_3O_7$) is similar to that reported by Feist *et al.* ($Na_{0.8}H_{1.2}Ti_3O_7$ S.G: $C2/m$, **Figure 2.1b**) [8]. Despite Mori *et al.* predicted $P2_1/m$ for H^+ contents between 0 and 0.75 by first-principle calculations [9] we have found that this is not the case for **NHTO-H_2O**. Whether a symmetry change occurs around this composition cannot be confirmed with our present results. In any case, for the compositions richer in H^+ our indexation is in very good agreement with both DFT calculations and the results of Feist *et al*.

In **Figure 2.30** it can be observed that the octahedra are quite distorted with respect to $H_2Ti_3O_7$. **NHTO-H_2O** sample shows higher distortion more similar as $Na_2Ti_3O_7$, although the four samples (**NTO-CO-Air**, **NHTO-H_2O**, **NHTO-HCl** and **HTO**) exhibit distorted octahedra. In order to compare the distortion between them the bond-length distortion parameter (DI) has been calculated (**Eq. 2.1**) [36, 37]. The **NHTO-H_2O** shows more distorted octahedra with respect to **NHTO-HCl** and **HTO**, and almost the same DI to **NTO-CO-Air**. Meanwhile the DI value of **NHTO-HCl** is more similar to that of **HTO** which indicates that for higher Na^+ amounts, higher the distortion (**Table 2.15**). For a better analysis of the distortion the rest of Ti-O bond distances of **NHTO-H_2O** and **NHTO-HCl** are collected **Table 2.16**. Although there are some differences between the Ti-O bond distances (the main differences are in bold) both are within the same range as reported for $H_2Ti_3O_7$ by Feist *et al*. and Eguía-Barrio *et al*. (see **Table 2.17**), with the greatest differences is found in Ti3 octahedron.

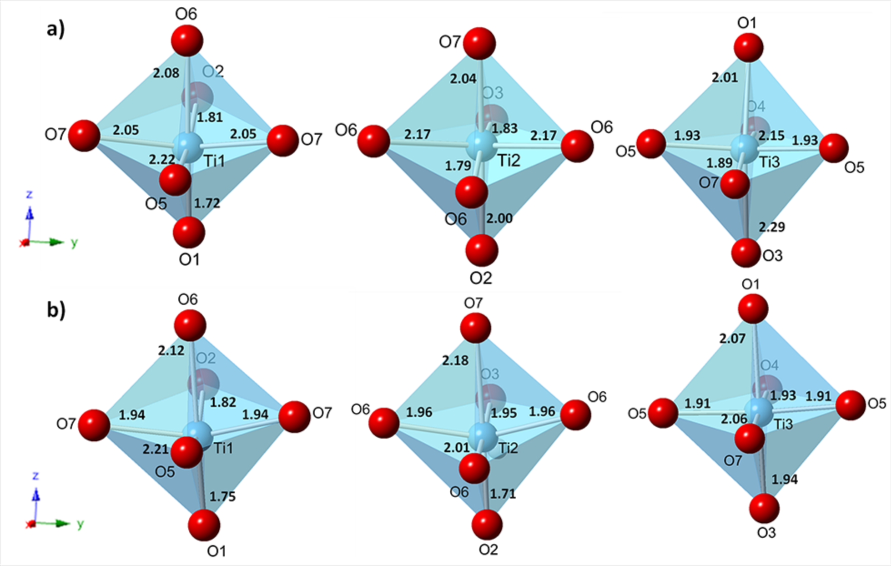

Figure 2.30: $[TiO_6]$ octahedra of **a) NHTO-H_2O** and **b) NHTO-HCl** samples.

Table 2.15: Bond-length distortion values (DI) of **NTO-CO-Air**, **NHTO-H_2O**, **NHTO-HCl** and **HTO**.

Sample	Bond-length distortion: DI(Ti-O)
NTO-CO-Air	0.066
NHTO7-H_2O	0.068
NHTO7-HCl	0.049
HTO	0.035

$$DI = \frac{1}{6}\sum_{i=1}^{6}\left[\frac{d_i - d_m}{d_m}\right]^2 ; where\ d_i = (Ti - O)\ and\ d_m =< Ti - O > \qquad \textbf{(Eq. 2.1)}$$

Table 2.16: Bond distances (Å) of **NHTO-H$_2$O** and **NHTO-HCl** samples.

NHTO-H$_2$O

	Ti1-O (Å)	Ti2-O (Å)	Ti3-O (Å)	Na1-O (Å)	Na2-O (Å)	H1-O (Å)	H2-O (Å)	H3-O (Å)
O1	1.72(5)		2.01(3)	2x 2.99(5)				
O2	1.81(6)	**2.00(5)**			2x 2.44(5)			
O3		1.83(6)	**2.29(3)**		2x 2.21(6)	0.94(4) 1.49(4)		
O4			**2.15(4)**	2x 1.89(1)				1.48(3)
O5	2.22(6)		2x 1.93(7)	2.38(7)				
O6	**2.08(5)**	**1.79(6)** 2x **2.17(2)**			2.60(6)			
O7	2x **2.05(2)**	**2.04(4)**	**1.89(2)**					

NHTO-HCl

	Ti1-O (Å)	Ti2-O (Å)	Ti3-O (Å)	Na1-O (Å)	Na2-O (Å)	H1-O (Å)	H2-O (Å)	H3-O (Å)
O1	1.75(3)		2.07(4)	2x 3.05(5)				
O2	1.82(4)	**1.71(4)**			2x 2.10(8)		1.84(3)	
O3		1.95(4)	**1.94(4)**		2x 2.98(7)	1.26(5) 1.57(5)		
O4			**1.93(4)**	2x 2.65(3)			1.02(3)	1.42(1)
O5	2.21(4)		2x 1.91(1)	2.76(7)				
O6	**2.12(3)**	**2.01(4)** 2x **1.96(1)**			2.29(1)			
O7	2x **1.94(1)**	**2.18(4)**	**2.06(4)**					

Table 2.17: Comparison of average Ti-O bond distances with literature values.

Group	Ti-O bond distances (Å)	Average Ti-O distance (Å)
NHTO-H$_2$O	1.72(5) - 2.29(3)	2.00(4)
NHTO-HCl	1.75(3) - 2.18(3)	1.96(3)
Feist *et al.* [8]	1.707(1) - 2.267(1)	1.97(3)
Eguía-Barrio *et al.* [10]	1.72(2) - 2.25(2)	1.96(3)

This distortion explains the larger *c* cell parameter in comparison with $H_2Ti_3O_7$ (**Table 2.11**). As mentioned previously, the *a* cell parameter is longer with respect to that of $H_2Ti_3O_7$ as a result of a larger interlayer space (2.78 Å and 2.62 Å for **NHTO-H_2O** and **NHTO-HCl** respectively, and 2.53 Å for $H_2Ti_3O_7$). Interestingly, H3 (only observed in **NHTO-HCl**), H2 and Na1 are bonded to the same oxygen (O4). This is the only oxygen in the structure which is bonded to one titanium atom (Ti3) and therefore has a more basic character, becoming more susceptible to form H bonds which in turn are proposed to be responsible of the symmetry change from $P2_1/m$ to $C2/m$.

2.4.2.7. Fourier Transform Infrared Spectroscopy (FTIR)

The formation of H bonds, and hence the reason of the symmetry change, has been corroborated by FTIR. A comparison of the spectra of samples **NTO-CO-Air**, **NHTO-H_2O**, **NHTO-HCl** and **HTO** is shown in **Figure 2.31**.

In the FTIR spectra of all samples the stretching and bending vibrations bands of Ti-O bonds are found at low wavelengths (940 - 460 cm^{-1}). As mentioned above, the **NTO-CO-Air** sample exhibits the -CO stretching vibrations band of Na_2CO_3, but not the -OH bands. On the contrary, **NHTO-H_2O**, **NHTO-HCl** and **HTO** samples exhibit the H-bonded since stretching band of free -OH at high wavelength (~ 3550 cm^{-1}), and O-H bond at average wavelength of 3000 cm^{-1} as well as bending band at 1630 cm^{-1} are observed. The free -OH signal corresponds to H2 of **NHTO-H_2O** and **NHTO-HCl** which is located at the origin (**Table 2.13** and **Table 2.14**), whilst the –OH stretching band/s corresponds to the other type of H^+ (H1 and H3). More precisely the lower –OH stretching band at 2900 cm^{-1} and 2874 cm^{-1} corresponds to H1 of **NHTO-H_2O** and **NHTO-HCl**, respectively while the higher band observed at 3091 cm^{-1} in **NHTO-HCl** samples corresponds to H3 which has shorter O–H distance [15, 38].

These -OH band/s and -OH free signal can be correlated with the ^{1}H-ssNMR signals. **NHTO-H_2O** shows free -OH (H2) and one –OH stretching (H1) band in FTIR which correspond to one signal in ^{1}H-ssNMR spectrum (these two H^+ types appear at similar chemical shift) while **NHTO-HCl** exhibits extra –OH stretching peak as well as two ^{1}H-NMR signals as in $H_2Ti_3O_7$ [10]. The similarities between the FTIR and ^{1}H-ssNMR spectra of **HTO** and **NHTO-HCl** suggest that the latter compound also presents three types of H^+ as was determined by PND.

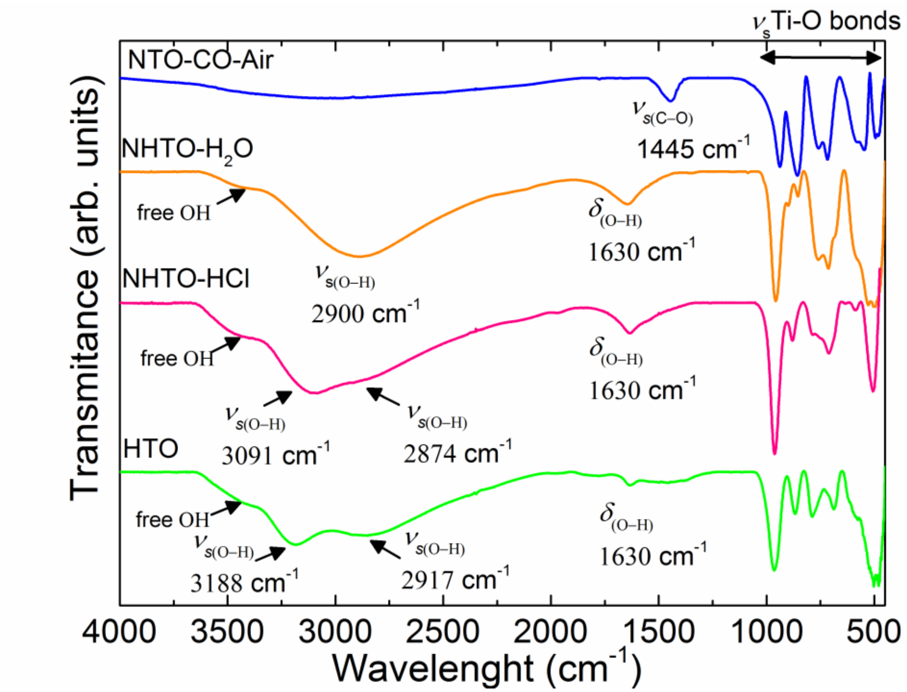

Figure 2.31: FTIR spectra from 4000 cm^{-1} to 500 cm^{-1} of **NTO-CO-Air** (blue), **NHTO-H_2O** (orange), **NHTO-HCl** (pink) and **HTO** (green) samples.

2.4.3. Electrochemical characterization of $Na_{2-x}H_xTi_3O_7$ ($0 \leq x \leq 2$)

Electrochemical performance of **NHTO-H_2O** and **NHTO-HCl** samples was analyzed and compared to the reference **NTO-CO-Air** and **HTO** samples. The electrodes formulation were 70:20:10 ($Na_{2-x}H_xTi_3O_7$:carbon Super C65:PVdF) and they were tested in half-cells using Na disks as counter electrode and 1 M $NaClO_4$ in EC:PC as electrolyte at 0.1C in the same voltage range as for **NTO-CO-Air** (0.05 - 1.6 V *vs.* Na^+/Na), except **HTO** which has been cycled between 0.9 - 2.2 *vs.* Na^+/Na since in a previous work the best results have been found at this voltage range [10].

2.4.3.1. Electrochemical performance using PVdF as binder

NTO-CO-Air sample shows two plateaux in the 1st cycle: one at 0.7 V corresponding to the mainly irreversible reaction with carbon Super C65 (used as conductive additive) and SEI layer formation, and the other at 0.3 V, which corresponds to the reversible insertion of two Na^+ into $Na_2Ti_3O_7$ [2, 24]. On the contrary, only one plateau appears in $H_2Ti_3O_7$ at 1.3 V corresponding to the

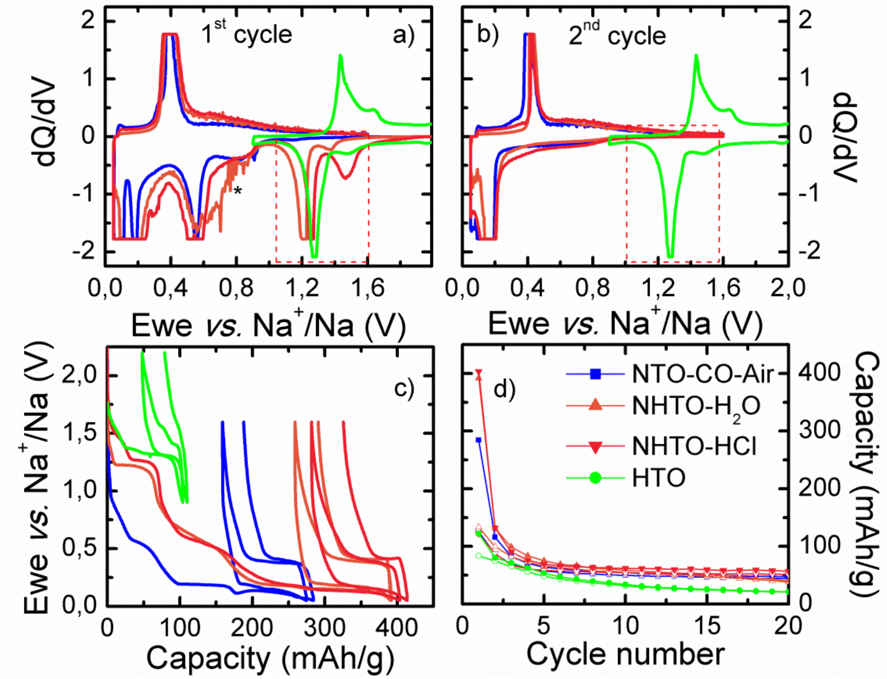

Figure 2.32: dQ/dV *vs.* voltage of the **a)** 1st and **b)** 2nd cycles. (red square irreversible plateau at 1.25 V) **c)** Voltage *vs.* capacity corresponding to the 1st and 2nd cycles. **d)** Capacity **vs.** cycle number. **NTO-CO-Air** (blue), **NHTO-H_2O** (orange), **NHTO-HCl** (pink) and **HTO** (green).

reversible insertion of one Na^+ as previously reported [10]. The electrochemical behaviour of **NHTO-H_2O** and **NHTO-HCl** samples has similarities with both end members since three different plateaux can be observed in the 1st cycle at 1.25 V, 0.7 V and 0.3 V. The plateau at 0.7 V is the reaction of Na^+ with carbon Super C65 and SEI layer formation, as occurs in **NTO-CO-Air**, which is mostly irreversible. The other two plateaux correspond to the Na^+ insertion into the structure, the plateau at 1.25 V not being reversible (see red square), as shown in the derivative curve of the first two cycles (**Figure 2.32a** and **Figure 2.32b**). The appearance of two plateaux in the 1st cycle is indicative of the fact that Na^+ are inserted into different environments that are generated by the presence of both Na^+ and H^+ in the structure. The plateau around 1.3 V was also observed when acetone was used to prepare slurries and attributed to Na^+ by H^+ exchange from water in acetone [6]. In the following cycles however, the behaviour is the same as for **NTO-CO-Air** (**Figure 2.32c**) and, althought the mixed compositions exhibit higher capacities in the first Na^+ insertion process, the irreversible capacity is also higher. Moreover, upon cycling their reversible capacities become close to that of **NTO-CO-Air**, presenting a considerable capacity fading as usually found for this compound (**Figure 2.32d**) [3, 4].

2.4.3.1.1. Structural evolution upon cycling of $Na_{2-x}H_xTi_3O_7$ (0<x<2)

In order to understand the electrochemical behaviour during the 1st Na^+ insertion in $Na_{2-x}H_xTi_3O_7$ (0<x<2), the mechanism of Na^+ insertion of sample **NHTO-HCl** was further studied by *in-situ* PXRD. For this, 70% of **NHTO-HCl** powder has been mixed with a 30% of carbon Super C65 and assembled on a homemade cell design based on a 1-inch Swagelok cell. The *in-situ* PXRD data were collected every 30 min between 2 Theta = 8 - 35 º during the 1st Na^+ insertion (**Figure 2.33**).

The mechanism of both end members of the solid solution is different. $Na_2Ti_3O_7$ compound follows a biphasic process during the plateau at 0.3 V *vs.* Na^+/Na, finally obtaining at the end on the insertion process a composition of $Na_4Ti_3O_7$; a process that is reversed upon Na^+ extraction [2]. On the other hand, $H_2Ti_3O_7$ has a more complex mechanism, until 0.6 mol of Na^+ are inserted (around 1.5 V *vs.* Na^+/Na) a solid solution mechanism can be identified and $H_2Na_xTi_3O_7$ compositions that keep the $H_2Ti_3O_7$ structure (*C*2/*m*) are formed. After 0.6 Na^+ per formula unit and until 1.0 mol of Na^+, during the plateau (1.3 V *vs.* Na^+/Na), a biphasic reaction mechanism is observed; and PXRD data can be indexed with $Na_2Ti_3O_7$ space group $P2_1/m$. And at end of the reduction state (at 0.9 V *vs.* Na^+/Na) the biphasic reaction coexists with the solid solution region, and it has been suggested that Na^+ and H^+ coexist in the interlayer spacing since it has been found that H^+ remain in the structure and are mainly extracted upon Na^+ extraction (upon oxidation) [10].

NHTO-HCl sample seems to follow a different mechanism than $Na_2Ti_3O_7$ and $H_2Ti_3O_7$. The evolution of the cell parameters has been performed by Le Bail refinements on each PXRD pattern and the composition has been roughly calculated by assuming that *a* cell parameter follows a linear evolution of Vegard's law (**Figure 2.34**). The OCV pattern is indexed with *C*2/*m* space group and the cell parameters are *a* = 16.355(4), *b* = 3.7489(6), *c* = 9.271(2) and *β* = 103.11(3) and the estimated composition is $Na_{0.39}H_{1.61}Ti_3O_7$ (in very good agreement with the composition obtained by PND).

Upon decreasing the voltage, until 1.4 V *vs.* Na^+/Na, **NHTO-HCl** follows a solid solution mechanism (black region in **Figure 2.33**), where the *a* cell parameter increases and *c* cell parameter decreases (**Figure 2.34**). Since *a* corresponds to the stacking direction, the interlayer distance increases to accommodate Na^+. After this region and until 1.20 V a biphasic mechanism coexists with a solid solution (red

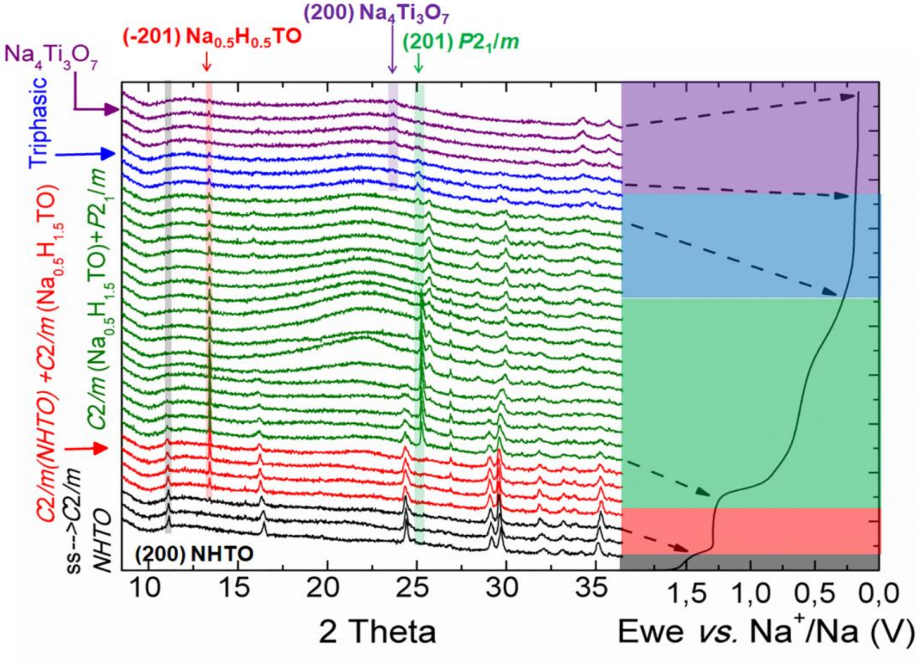

Figure 2.33: Evolution of *in-situ* PXRD patterns during the 1st Na$^+$ insertion of **NHTO-HCl** sample.

region in **Figure 2.33**). Similar behaviours have been observed in several Na-based materials where a solid solution region coexists with a biphasic mechanism; for example the already mentioned H$_2$Ti$_3$O$_7$ [10] and the cathode material NaFePO$_4$ [39, 40]. The patterns have been indexed with the same space group ($C2/m$) but the composition of Na$^+$/H$^+$ is complete different for the two phases. The initial phase achieves a composition of Na$_{0.48}$H$_{1.61}$Ti$_3$O$_7$ at 1.2 V *vs.* Na$^+$/Na; while the composition of the new phase would be close to Na$_{0.5}$H$_{1.5}$Ti$_3$O$_7$ which remains constant until almost the end of the reduction (0.16 V *vs*. Na$^+$/Na). It is interesting that this latter composition is the one found after 8th weeks of air exposure of Na$_2$Ti$_3$O$_7$ and is one of the most stable compositions reported by Mori *et al.*[9].

With further decreasing the voltage until 0.3 V *vs.* Na$^+$/Na, besides the reflexions of the stable Na$_{0.5}$H$_{1.5}$Ti$_3$O$_7$ phase, the initial phase (Na$_{0.39}$H$_{1.61}$Ti$_3$O$_7$) which has been indexed by $C2/m$ space group evolves into a slightly different structure since new reflexions appear, for example (201) and that have to be indexed with $P2_1/m$ space group as Na$_2$Ti$_3$O$_7$ (green region in **Figure 2.33**). The cell parameters of this new phase are evolving from a = 8.516(2), b = 3.799(1), c = 9.143(1) and β = 101.50(2) at 1.2 V, which corresponds to a composition of Na$_{1.19}$H$_{1.61}$Ti$_3$O$_7$; to a = 8.631(6), b = 3.822(3), c = 9.186(6) and β = 102.39(8), corresponding to a composition of

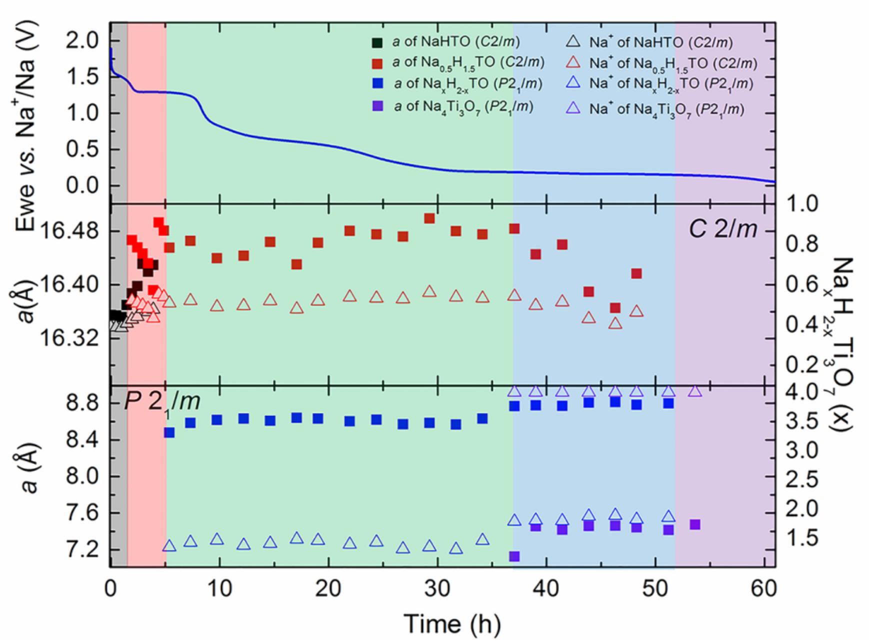

Figure 2.34: Evolution of the *a* cell parameter of **NHTO-HCl** during the 1st Na^+ insertion. Black region: solid solution ($Na_{0.39+x}H_{1.61}Ti_3O_7$, S.G: *C2/m*), red region: biphasic ($Na_{0.39+x}H_{1.61}Ti_3O_7$ + $Na_{0.5}H_{1.5}Ti_3O_7$), green region: another biphasic region ($Na_{0.5}H_{1.5}Ti_3O_7$ + $Na_{0.39+x}$ $H_{1.61-y}Ti_3O_7$, S.G.: *P*2_1/*m*), blue region: triphasic mechanism ($Na_{0.5}H_{1.5}Ti_3O_7$ + $Na_{0.39+x}$ $H_{1.61-y}Ti_3O_7$ + $Na_4Ti_3O_7$) and violet region: $Na_4Ti_3O_7$ formation.

$Na_{1.46}H_{1.61}Ti_3O_7$ at 0.3 V. Hence this second biphasic region coexist with a solid solution one. In this region a broad peak is appeared at 2 Theta = 20 ^{o} close to 0.6 V which is not related with the $Na_{2-x}H_xTi_3O_7$ phase. The background should almost not change during the performance and hence that broad peak might correspond to some product/s formed from electrolyte decomposition since at that operate voltage the electrolyte is outside of electrochemical stability window (ESW).

Later in the voltage region of 0.3 - 0.16 V, during the plateau, a triphasic region is observed (blue region in **Figure 2.33**). Although the refinement of the patterns is difficult because of the broadening of peaks these three phases are identified as $Na_{0.5}H_{1.5}Ti_3O_7$ (*C*2/*m*), $Na_{1.46+x}H_{1.61-y}Ti_3O_7$ (*P*2_1/*m*) and $Na_4Ti_3O_7$.

At the end of the 1st Na^+ insertion only the peaks of $Na_4Ti_3O_7$ (purple region in **Figure 2.33**) can be shown but unfortunately the refinement is not possible, due to the broadening of the peaks.

Comparing the mechanism of **NHTO-HCl** with that of the end members, the studied sample follows a combination of both: in the beginning of the Na^+ insertion process it has a similar behaviour as $H_2Ti_3O_7$ while at the end of the process it behaves more like $Na_2Ti_3O_7$.

The presence of $Na_4Ti_3O_7$ at the end of the process advocates that in the 1st cycle H^+ are extracted, explanning why in this case the plateau at 1.2 V, corresponding with the existence of H^+, is not reversible.

2.4.3.2. Electrochemical performance using Na-CMC as binder

From the results obtained in the **section 2.4.3.1.**, it can be concluded that the spontaneous exchange of Na^+ by H^+ in $Na_2Ti_3O_7$ only affects the electrochemical behaviour of the 1st cycle and the material behaves as $Na_2Ti_3O_7$ from there on. In other words, the transformation into $Na_{2-x}H_xTi_3O_7$ ($0<x<2$) that occurs upon air or water exposure reverts during the 1st cycle of the battery. Therefore, it can be anticipated that water can be used as solvent in electrode preparation as well as F-free binders like Na-CMC, which have resulted in better capacity retention in other Na-based anode material such as $Na_2Ti_6O_{13}$ [27], hard carbon (HC) [28], Co_3O_4 [29], sodium terephthalate organic electrode [30] and TiO_2 [31].

In order to identify the extent of Na^+ and H^+ exchange after electrode preparation the XRD of the electrode was collected and is compared in **Figure 2.35** with that of the starting material, **NTO-CO-Air** and **HTO**. Although the position and intensity of diffraction peaks can be indexed with the $P2_1/m$ space group, the lower *a* cell parameter, determined by Le Bail refinement, indicates that the amount of Na^+ should be lower than 2 Na^+ per formula unit, hence ion exchange occurs. The composition has been roughly estimated from the *a* cell parameter evolution assuming that it follows Vegard's law, resulting in $Na_{1.6}H_{0.4}Ti_3O_7$, which would confirm that the structural change occurs between a Na^+ content of ~ 1.3 - 1.6 per formula unit since **NHTO-H_2O** sample ($Na_{1.3}H_{0.7}Ti_3O_7$) crystallizes in $C2/m$ space group.

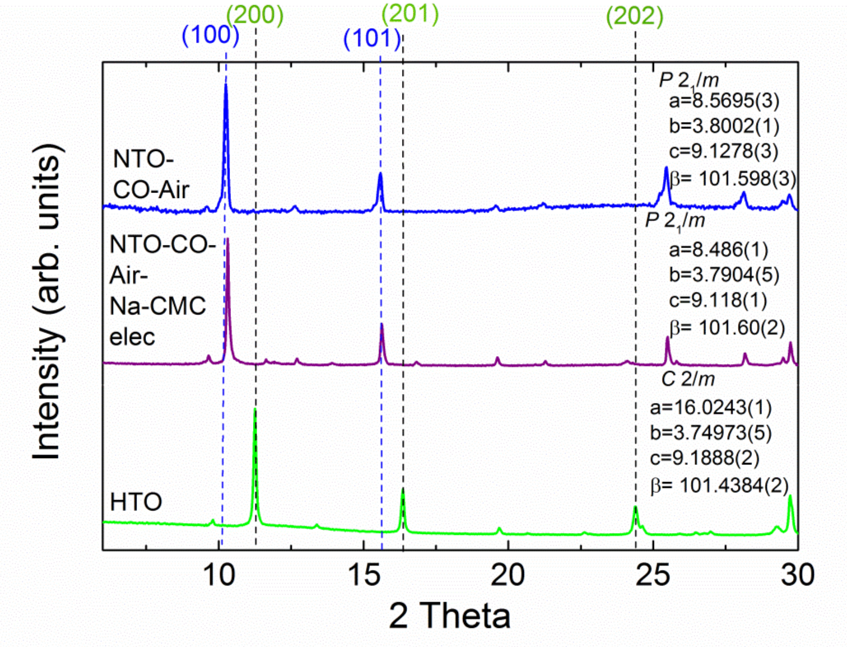

Figure 2.35: XRD data of pristine **NTO-CO-Air** (blue), $Na_{1.6}H_{0.4}Ti_3O_7$ Na-CMC electrode and **HTO** (green). The cell parameters of $Na_{1.6}H_{0.4}Ti_3O_7$ have been determined by Le Bail refinement.

In **Figure 2.36a** the galvanostatic curves of the two tested formulations (organic and aqueous medium) prepared using the same starting material, **NTO-CO-Air** sample, are compared. Contrary to the PVdF electrode, the Na-CMC electrode exhibits the plateau at 1.25 V in the 1st cycle like **NHTO-H_2O** and **NHTO-HCl** samples. This indicative of a certain extent of Na^+/H^+ ionic exchange during electrode preparation as expected from the evolution of *a* cell parameter. The plateau at 1.25 V disappears in subsequent cycles and the electrode even exhibits a better performance than that prepared using organic solvent and PVdF as binder. The irreversible capacity of the 1st cycle, which is related to the decomposition of the electrolyte and in consequence with the SEI layer formation, is considerably reduced (see **Table 2.18**). The Coulombic efficiency of the following cycles is largely improved (75% *vs.* 88% for the 2nd cycle). Moreover, the capacity retention (**Figure 2.36b**) is drastically enhanced. More insights regarding binder and SEI stability will be given in **chapter 3**, with the help of XPS and ^{19}F-ssNMR experiments.

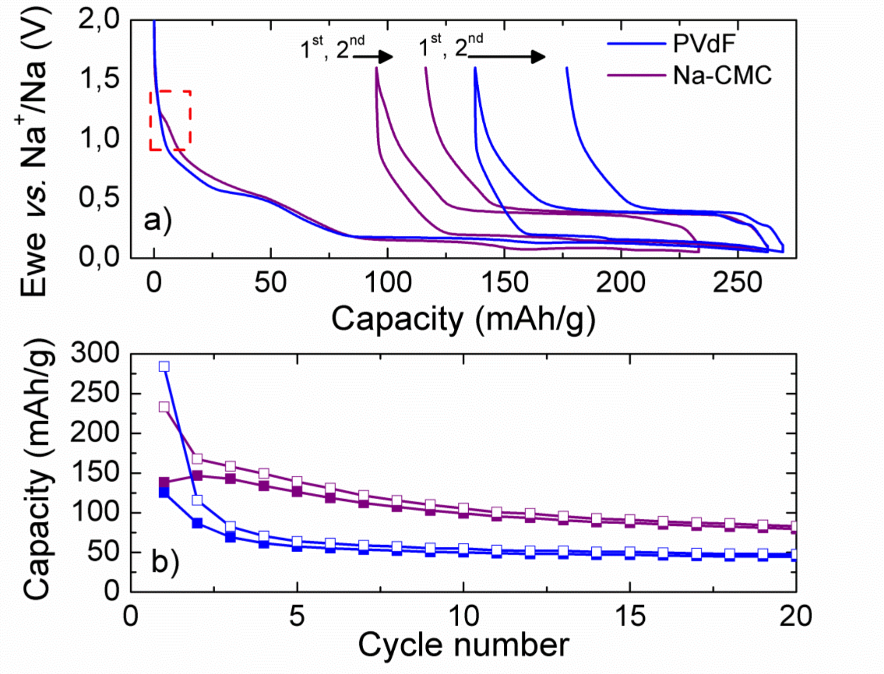

Figure 2.36: a) Voltage *vs.* capacity corresponding to the 1st and 2nd cycle and **b)** capacity evolution of the first 20 cycle of **NTO-CO-Air** using PVdF (blue) or Na-CMC (purple) as binder.

Table 2.18: Capacity values and capacity retention obtained of the 20th cycle using PVdF or Na-CMC as binder of uncoated **NTO-CO-Air** at 0.1C over voltage range 0.05 - 1.6 *vs.* $Na^{+/}Na$.

Parameters	PVdF	Na-CMC
1st Na^+ insert. capacity (mAh/g)	284	233
1st Irreversible. capacity (mAh/g)	159	95
Capacity retention at 20th cycle	35%	57%

Additionally this result demonstrates that, despite the structure and composition of $Na_2Ti_3O_7$ are modified when exposed to water, electrodes can be prepared in aqueous media and benefit from the positive attributes of water soluble binders like Na-CMC. Therefore, this improvement using aqueous binder has been applied to the sample that shows the best electrochemical performance **NTO-OH-Ar-C**. As has been done previously XRD data of Na-CMC electrode has been collected and interestingly, the XRD pattern of this sample has to be indexed with *C2/m* space group as the same as **NHTO-H_2O**, **NHTO-HCl** and **HTO** (**Figure 2.37**). Therefore, the C-coating does not protect from Na^+/H^+ ion exchange since the ions can across through the carbon layer. The composition has been roughly estimated to be

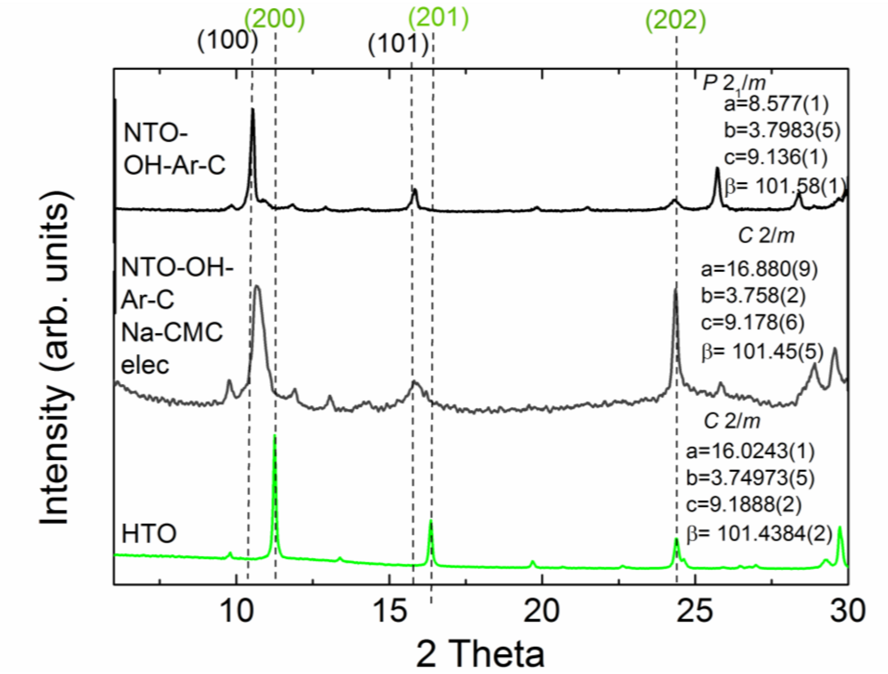

Figure 2.37: XRD data of pristine **NTO-OH-Ar-C** (black), $Na_{1.5}H_{0.5}Ti_3O_7$ Na-CMC electrode (gray) and **HTO** (green). The cell parameters of $Na_{1.5}H_{0.5}Ti_3O_7$ have been determined by Le Bail refinement.

$Na_{1.5}H_{0.5}Ti_3O_7$; and hence the structural change occurs around 1.5 - 1.6 Na^+ per formula unit.

In the galvanostatic curves (**Figure 2.38a**), as is expected, the Na-CMC electrode has an extra plateau at 1.25 V in the 1st cycle, in very good agreement with the Na^+/H^+ ionic exchange that occurs during electrode preparation and the plateau disappears as expected in the following cycles. The electrochemical performance of this electrode is quite similar to that prepared with PVdF as binder. The capacity values and the capacity retention are comparable (**Figure 2.38b** and **Figure 2.38c**); the main difference being the 1st cycle irreversible capacity, with better reversibility for Na-CMC electrode (**Table 2.19**). However, this electrode exhibits a higher irreversibility than the electrode prepared with the uncoated sample (see **Table 2.18**), which is related to the porous texture of the carbon which results in a larger surface area for SEI layer formation. In any case, C-$Na_2Ti_3O_7$ electrodes can also be prepared in aqueous media since shows a good electrochemical performance although a structure change occurs.

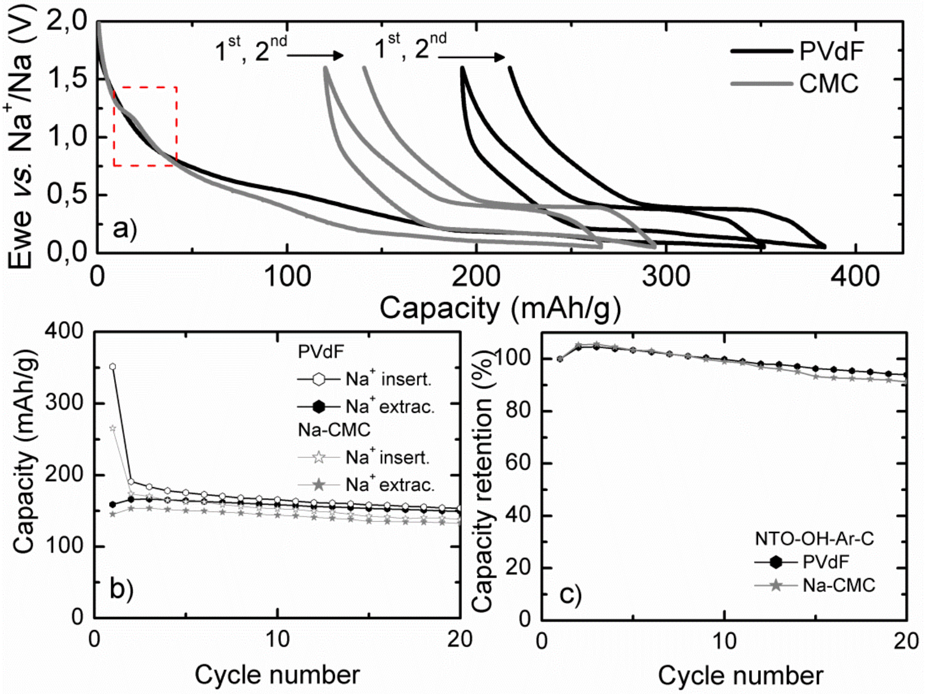

Figure 2.38: a) Voltage *vs.* capacity corresponding to the 1st and 2nd cycle, **b)** capacity evolution and c) capacity retention of the first 20 cycle of **NTO-OH-Ar-C** using PVdF (black) or Na-CMC (gray) as binder.

Table 2.19: Capacity values and capacity retention obtained of the 20th cycle using PVdF or Na-CMC as binder of coated **NTO-OH-Ar-C** at 0.1C over voltage range 0.05 - 1.6 *vs.* $Na^{+/}Na$.

Parameters	PVdF	Na-CMC
1st Na^+ insert. capacity (mAh/g)	352	266
1st Irreversible. capacity (mAh/g)	192	120
Capacity retention at 20th cycle	94%	91%

Henceforth, the possibility to use the aqueous binder gives the opportunity to build more environmentally friendly NIBs.

2.5. Conclusions

The impact of several synthesis parameters, on the electrochemical performance of $Na_2Ti_3O_7$ has been shown. By rationalizing the effect of such synthesis parameters the electrochemical performance of $Na_2Ti_3O_7$ has been considerably improved.

First, an important improvement is already achieved when the material is synthesised from NaOH instead of Na_2CO_3 as Na source, since no Na excess is required and therefore no residual unreacted precursor appears in the sample.

Further improvement of the electrochemical performance can be achieved by controlling the atmosphere during the cooling process. When Ar atmosphere is used it is possible to avoid surface corrosion resulting from the interaction between $Na_2Ti_3O_7$ particles and atmospheric water and CO_2; while when cooled in air, results in the formation of passivating Na_2CO_3. The effect of the cooling atmosphere has a stronger impact than the Na precursor in the electrochemical properties. Indeed, due to the low working voltage of $Na_2Ti_3O_7$, SEI layer formation is expected, and since Na_2CO_3 exhibits a high solubility in the commonly used organic electrolyte, the stability of this SEI layer will be affected in presence of Na_2CO_3.

The last synthesis parameter studied has been the addition of a C-coating synthetic step, in combination with the previously mentioned parameters (i.e. NaOH as Na precursor and Ar atmosphere upon cooling). An almost homogeneous 6.0 nm C-coating is obtained and is believed to behave as protecting layer, increasing the conductivity and improvement the electrochemical performance, leading to 78% of charge capacity retention in the 100th cycle.

The moisture and water stability of $Na_2Ti_3O_7$ are also analysed since will determine the storage and electrode preparation conditions, and will therefore impact in the final cost of the battery. In both environments a spontaneous exchange of Na^+ by H^+ is found.

Two mixed compositions have been prepared by ion exchange at different pH: $Na_{1.3}H_{0.7}Ti_3O_7$ and $Na_{0.6}H_{1.4}Ti_3O_7$. Their exact structure is solved and, for the first time, the unit cell has been univocally indexed and the Na^+ and H^+ positions have been determined. Both samples crystallize in a C-centred unit cell with AB $[TiO_6]$ layer stacking sequence (S.G: $C2/m$) as $H_2Ti_3O_7$. Two types of Na^+ and two types of H^+ are found for the Na^+-rich sample, while one extra H^+ (H3), as in $H_2Ti_3O_7$, is found for the H^+-rich sample.

The electrochemical experiments and *in-situ* PXRD show that after the 1st cycle the behaviour of the mixed compositions is very similar to that of their precursor $Na_2Ti_3O_7$, and therefore, although $Na_2Ti_3O_7$ is unstable when is stored in air or in contact with water and exchanges Na^+ by H^+, this does not have a relevant impact on the electrochemical properties, finally allowing storage in a non-dry atmosphere.

This behaviour also allows the use of aqueous binders such as Na-CMC, which is environmentally friendly compared to PVdF. The use of Na-CMC results in an increase of the 1st cycle reversible capacity and better capacity retention in the uncoated sample; while the coated sample shows similar capacity retention as when PVdF is used. Henceforth, $Na_2Ti_3O_7$ represents a low-cost, environmentally friendly option as NIBs anode material, since is made of earth abundant elements and can be processed following environmentally friendly and low-cost routes.

2.6. References

---

[1] M.M. Doeff, J. Cabana, M. Shirpour, Titanate anodes for sodium ion batteries, J. Inorg. Organomet. Polym. 24 (2014) 5-14.

[2] P. Senguttuvan, G. Rousse, V. Seznec, J.M. Tarascon, M.R. Palacín, $Na_2Ti_3O_7$: lowest voltage ever reported oxide insertion electrode for sodium ion batteries, Chem. Mater. 23 (2011) 4109-4111.

[3] H. Pan, X. Lu, X. Yu, Y.S. Hu, H. Li, X.Q. Yang, L. Chen, Sodium storage and transport properties in layered $Na_2Ti_3O_7$ for room-temperature sodium-ion batteries, Adv. Energy Mater. 3 (2013) 1186-1194.

[4] A. Rudola, K. Saravanan, C.W. Mason, P. Balaya, $Na_2Ti_3O_7$: and intercalation based anode for sodium-ion battery applications, J. Mater. Chem. A 1 (2013) 2653-2662.

[5] J. Xu, C. Ma, M. Balasubramanian, Y.S. Meng, Understanding $Na_2Ti_3O_7$ as an ultra-low voltage anode material for a Na-ion battery, Chem. Comm. 50 (2014) 12564-12567.

[6] J. Navas-Avendaño, A. Morales-García, A. Ponrouch, G. Rousse, C. Frontera, P. Senguttuvan, J.M. Tarascon, M.E. Arroyo-de Dompablo, M.R. Palacín, Taking steps forward in understanding the electrochemical behaviour of $Na_2Ti_3O_7$, J. Mater. Chem A 3 (2015) 22280-22286.

[7] H. Izawa, S. Kikkawa, M. Koizuml, Ion exchange and dehydration of layered titanates, $Na_2Ti_3O_7$ and $K_2Ti_4O_9$, J. Phys. Chem. 86 (1982) 5023-5026.

[8] T.P. Feist, P.K. Davies, The soft chemical synthesis of TiO_2(B) from layered titanates, J. Solid State Chem. 101 (1992) 275-295.

[9] M. Mori, Y. Kumagai, K. Matsunaga, I. Tanaka, First-principles investigation of atomic structures and stability of proton-exchanged layered sodium titanate, Phys. Rev. B 79 (2009) 144117-1-6.

[10] A. Eguía-Barrio, E. Castillo-Martínez, M. Zarrabeitia, M.A Muñoz-Márquez, M. Casas-Cabanas, T. Rojo, Structure of $H_2Ti_3O_7$ and its evolution during sodium insertion as anode for Na ion batteries, Phys. Chem. Chem. Phys 17 (2015) 6988-6994.

[11] S. Andersson, A.D. Wadsley, The crystal structure of $Na_2Ti_3O_7$, Acta. Cryst. 14 (1961) 1245-1249.

[12] K. Kataoka, N. Kijima and J. Akimoto, Ion-exchange synthesis, crystal structure, and physical properties of hydrogen titanium oxide $H_2Ti_3O_7$, Inorg. Chem. 52 (2013) 13861-13864.

[13] M. Zarrabeitia, E. Castillo-Martínez, J.M. López Del Amo, A. Eguía-Barrio, M.A. Muñoz-Márquez, T. Rojo, Identification of the critical synthesis parameters for enhanced cycling stability of Na-ion anode material $Na_2Ti_3O_7$, Acta Mater. 104 (2016) 125-130.

[14] D. Massiot, F. Fayon, M. Capron, I. King, S. Le Calvé, B. Alonso, J.O. Durand, B. Bujoli, Z. Gan, G. Hoatson, Modelling one-and two-dimensional solid-state NMR spectra, Magn. Reson. Chem. 40 (2002) 70-76.

---

[15] B. Stuart; Infrared Spectroscopy: Fundamentals and Applications, John Wyley &Sons, Ltd ISBNs: 0-470-85427-8, (2004).

[16] J. Kim, Y. Hong, K.S. Ryu, M.G. Kim, J. Cho, Washing effect of a $LiNi_{0.83}Co_{0.15}Al_{0.02}O_2$ cathode in water, Electrochem. Solid State Lett. 9 (2006) A19-A23.

[17] V. Duffort, E. Talaie, R. Black, L.F. Nazar, Uptake of CO_2 in Layered P2-$Na_{0.67}Fe_{0.5}Mn_{0.5}O_2$: insertion of carbonate anions, Chem. Mater. 27 (2015) 2515-2524.

[18] https://www.ncnr.nist.gov/resources/n-lengths/elements/c.html (accessed May 2015).

[19] G. V. Zhuang, G. Chen, J. Shim, X. Song, P.N. Ross, T.J. Richardson, Li_2CO_3 in $LiNi_{0.8}Co_{0.15}Al_{0.05}O_2$ cathodes and its effects on capacity and power, J. Power Sources 134 (2004) 293-297.

[20] J. Kim, Y. Hong, K.S. Ryu, M.G. Kim, J. Cho, Washing effect of a $LiNi_{0.83}Co_{0.15}Al_{0.02}O_2$ cathode in water, Electrochem. Solid State Lett. 9 (2006) A19-A23.

[21] M. Sathiya, K. Helmatha, K. Ramesha, J.M Tarascon, A.S. Prakash, Synthesis, structure and electrochemical properties of the layered sodium insertion cathode material: $NaNi_{1/3}Mn_{1/3}Co_{1/3}O_2$, Chem. Mater. 24 (2012) 1846-1853.

[22] F. Aguesse, J.M. López Del Amo, V. Roddatis, A. Aguadero, J.A. Kilner; Enhancement of the grain boundary conductivity in ceramic $Li_{0.34}La_{0.55}TiO_3$ electrolytes in a moisture-free processing environment; Adv. Mater. Inter. 1 (2014) 910-924.

[23] S.S. Zhang, Insight into gassing problem of Li-ion battery, Frontier in Energy Research 2 (2014) Article 59 1-4.

[24] M.A. Muñoz-Márquez, M. Zarrabeitia, E. Castillo-Martínez, A. Eguía-Barrio, T. Rojo, M. Casas-Cabanas, Composition and evolution of the solid-electrolyte interphase in $Na_2Ti_3O_7$ electrodes for Na-ion batteries: XPS and Auger parameter analysis, ACS Appl. Mater. Interfaces 7 (2015) 7801-7808.

[25] S.H Woo, Y. Park, W.Y. Choi, N.S. Choi, S. Nam, B. Park, K.T. Lee, Trigonal $Na_4Ti_5O_{12}$ phase as an intercalation host for rechargeable batteries, J. Electrochem. Soc. 159 (2012) A2016-A2023.

[26] J. Xu, C. Ma, M. Balasubramanian, Y.S. Meng, Understanding $Na_2Ti_3O_7$ as an ultra-low voltage anode material for a Na-ion battery, Chem. Comm. 50 (2014) 12564-12567.

[27] Y. Zhang, H. Hou, X. Yang, J. Chen, M. Jing, Z. Wu, X. Jia, X. Ji, Sodium titanate cuboid as advanced anode material for sodium ion batteries, J. Power Sources 305 (2016) 200-208.

[28] M. Dahbi, T. Nakano, N. Yabuuchi, T.Ishikawa, K. Kuota, M. Fukunishi, S. Shibahara, J.Y. Son, Y.T. Cui, H. Oji, S. Komaba, Sodium carboxymethyl cellulose as a potential binder for hard-carbon negative electrodes in sodium-ion batteries, Electrochem. Commun. 44 (2014) 66-69.

---

[29] J. Ming, H. Ming, W.J. Kwak, C. Shin, J. Zheng, Y.K. Sun, The binder effect on an oxide-based anode in lithium and sodium-ion battery applications: the fastest way to ultrahigh performance, Chem. Comm. 50 (2014) 13307-13310.
[30] Y. Park, D.S. Shin, S.H. Woo, N.S. Choi, K.H. Shin, S.M. Oh, K.T. Lee, S.Y. Hong, Sodium terephthalate as organic anode material for sodium ion batteries, Adv. Mater. 24 (2012) 3562-3567.
[31] L. Wu, D. Buchholz, D. Bresser, L. Gomes-Chagas and S. Passerini, Anatase TiO_2 nanoparticles for high power sodium-ion anodes, J. Power Sources 251 (2014), 379-385.
[32] C. Fernandez, M. Pruski, Probing quardupolar nuclei by solid-state NMR spectroscopy: recent advances, Top. Curr. Chem., 306 (2012) 119-188.
[33] L. Frydman, J.S. Harwood, Isotropic spectra of half-integer quardupolar spins from bidimensional magic-angle spinning NMR, J. Am. Chem. Soc. 117 (1995) 5367-5368.
[34] J. Rodriguez-Carvajal, Recent advances in magnetic structure determination by neutron powder diffraction, Physica B 192 (1993) 55-69.
[35] https://www.ncnr.nist.gov/resources/n-lengths/ (accessed December 2015)
[36] M. Wildner, On the geometry of $Co(II)O_6$ polyhedra in inorganic compounds, Z. Kristallogr. 202 (1992) 51-70.
[37] A, Ertl, J.M. Hughes, F. Pertlik, F.F. Foit, S.E. Wright, F. Brandstätter, B. Marler, Polyhedron distortions in tourmaline, The Can. Mineral. 40 (2002) 153-162.
[38] E. Pretsch, P. Bühlmann, C. Affolter, A. Herrera, R. Matínez, Determinación estructural de compuestos orgánicos, Elsevier España S.L. Barcelona, España (2002).
[39] M. Casas-Cabanas, V.V. Roddatis, D. Saurel, P. Kubiak, J. Carretero-Gonzálex, V. Palomares, P. Serras, T. Rojo, Crystal chemistry of Na insertion/deinsertion in $FePO_4$-$NaFePO_4$, J. Mater Chem. 22 (2012) 17421-17423.
[40] M. Galceran, D. Saurel, B. Acebedo, V.V. Roddatis, E. Martin, T. Rojo, M. Casas-Cabanas, The mechanism of $NaFePO_4$ (de)sodiation determined by in situ X-ray diffraction, Phys. Chem. Chem. Phys. 16 (2014) 8837-8842.

3 $Na_2Ti_3O_7$ as anode material for NIBs: transport properties and study of the SEI layer

This chapter is focused on the study of the electronic/ionic properties of $Na_2Ti_3O_7$ and composition, stability and evolution of the SEI (Solid Electrolyte Interphase) formed on $Na_2Ti_3O_7$ anode during electrochemical cycling. These properties have been investigated in two different samples, synthesised by two different routes: **NTO-CO-Air** and enhanced **NTO-OH-Ar-C**. The electronic/ionic properties and the stability of the SEI layer have been determined by Electrochemical Impedance Spectroscopy (EIS). The composition, evolution as well as the stability of the formed SEI layer has been investigated by X-ray photoelectron spectroscopy (XPS), combining conventional XPS experiments with the analysis of the Auger parameter and depth profiling studies which have been carried out by two different approaches: ion beam treatment for the **NTO-CO-Air** sample and high energy XPS (HAXPES) for the **NTO-OH-Ar-C** sample. Finally, the SEI layer of the best performing sample (**NTO-OH-Ar-C**) has been further studied in a full-cell configuration using $NaFePO_4$ as counter electrode.

3.1. Introduction

As it has been discussed in **chapter 2**, the $Na_2Ti_3O_7$ is a promising negative electrode for rechargeable NIBs [1]. However, it shows poor capacity retention (c.f. **Figure 2.9**) owing to the presence of Na_2CO_3 on the $Na_2Ti_3O_7$ particles which is formed after the interaction of the titanate particles with the atmospheric water and CO_2. Different improvement routes have been followed in the last years: optimizing the electrode preparation by ball milling [2] and using different electrolytes and binders [3]. However, further improvements are needed for the $Na_2Ti_3O_7$ electrochemical properties to become an electrode of choice in NIBs. In our case, the capacity retention has been enhanced until reaching 78% after 100 cycles by avoiding the presence of Na_2CO_3 and growing a C-coating on the $Na_2Ti_3O_7$ particles (**chapter 2**).

Another important issue should be taken into account when dealing with capacity fading: the formation of a stable SEI layer. In general, the formation of the SEI layer reduces the battery capacity affecting its life time; however, at the same time, this passivation layer and its properties are crucial for the electrode stability and for the correct battery operation [4]. Since the reversible Na^+ insertion/extraction reaction of $Na_2Ti_3O_7$ occurs at a very low voltage (0.3 V *vs*. Na^+/Na) [1] and it is not inside the electrochemical stability window (ESW) of the organic electrolyte (c.f. **Figure 1.10**) a reduction of the electrolyte is expected leading to the SEI layer formation. Despite the electrode/electrolyte interphase is a crucial factor for the battery operation, the morphology, composition and properties of the SEI layer on $Na_2Ti_3O_7$ were not investigated until 2013. Pan *et al.* reported a combined HRTEM and FTIR study where, at the end of the Na^+ insertion, a Na_2CO_3–based SEI layer with a thickness of 2 – 5 nm was found to grow in this anode material; followed by a partial decomposition of the SEI upon oxidation [3]. This suggests that the SEI layer on the $Na_2Ti_3O_7$ particles is unstable during cycling, contributing to the low capacity retention. However, this latter study was mainly supported by TEM observations which only provided local information of the SEI on some grains of $Na_2Ti_3O_7$. Additionally, FTIR experiments do not provide the composition of the surface but in a bulk region. Hence, more information of the SEI obtained from long-range surface specific techniques would be more than welcome.

Up to date, the transport properties of $Na_2Ti_3O_7$ have been investigated by density functional theory (DFT) [3] which demonstrate that upon Na^+ insertion the formation energy of $Na_{2+x}Ti_3O_7$ ($0<x\leq2$) is thermodynamically stable. Furthermore, the theoretical calculations concluded that the excess ionized electron from the

inserted Na^+ occupied the t_{2g} orbital of Ti 3*d* conduction band, inducing a transition from electronically insulator to conductor. However, this transition has never been experimentally evidenced. Finally, regarding the ionic conductivity, the DFT demonstrated that Na^+ diffuses mainly along the layers with a small energy barriers and high diffusion coefficient which will facilitate the electrochemical reactions [3]. Therefore the transport properties, which influence on the electrochemical performance among other factors, will not be the triggering factor of the poor capacity retention.

3.2 Transport and interphase properties study by EIS

The cyclic voltammentry (CV) and EIS experiments were carried out with laminate electrodes prepared with a 70:20:10 ($Na_2Ti_3O_7$: Super C65:PVdF) formulation and assembled in Swagelok type cells using metallic Na disks as counter and reference electrodes and 1 M $NaClO_4$ in EC:PC as electrolyte. All tests were carried out at room temperature in the 0.05 - 1.6 V *vs.* Na^+/Na voltage window using a VMP3 potentiostat (Bio-Logic). CV was performed in two electrode Swagelok type cells at 0.40 mV/s scan rate. Meanwhile, EIS experiments were conducted in three electrode Swagelok type cells collecting the data every 25 mV in the 5 mHz - 100 kHz frequency range.

The stability of the SEI layer and the electrode transport properties have been investigated by means of EIS which depending on the frequency range will be used to monitor different processes: below 1 Hz EIS will provide information on the ionic diffusion, between ~ 2 kHz - 10 Hz on the charge transfer (SEI and not SEI related) and, finally, above 1 kHz the SEI layer stability will be evaluated. The results will be presented for the two materials prepared namely, **NTO-CO-Air** and **NTO-OH-Ar-C**.

3.2.1. NTO-CO-Air sample

The CV curve corresponding to the 1st and 2nd cycles of the **NTO-CO-Air** sample is shown in **Figure 3.1**. In the 1st cycle, two main reduction peaks can be observed at 0.32 V and 0.05 V along with a shoulder between 0.5 - 0.9 V *vs*. Na^+/Na, as well as one reversible oxidation peak at 0.34 V. The peak at 0.05 V corresponds to the insertion of Na^+ into $Na_2Ti_3O_7$ (Ti^{4+}/Ti^{3+}) and the peak at 0.34 V to the reversible Na^+ extraction. Although, the electrolyte reduction reaction starts around 0.9 V, as can be inferred from the shoulder between 0.5 and 0.9 V *vs.* Na^+/Na, the main peak associated to this process appears at 0.32 V. The reduction feature is mostly irreversible, as confirmed by the CV curve in the voltage range 0.2 - 1.0 V where only a broad shoulder can be observed in the inset. In the following cycles a broad

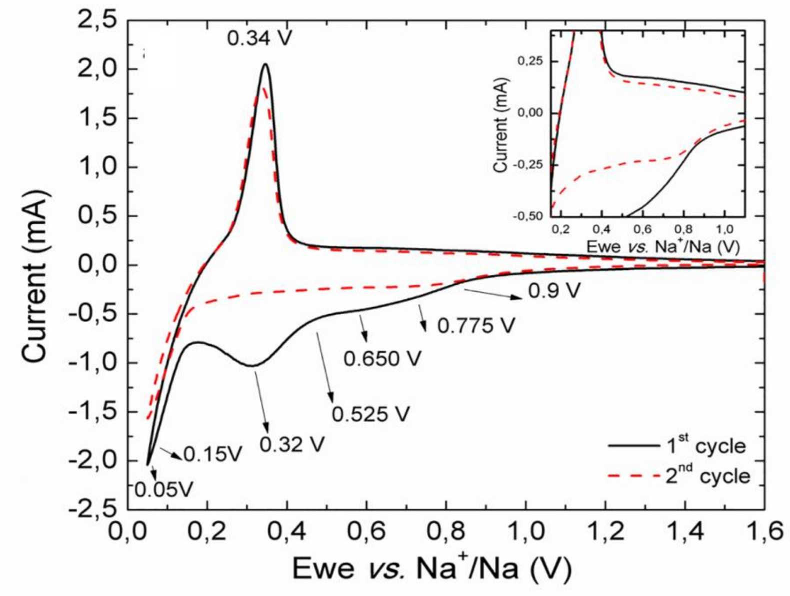

Figure 3.1: CV curve of the 1st (black) and 2nd (red) cycles of **NTO-CO-Air** at 0.40 mV/s scan rate. The highlighted voltages points indicate were some of the EIS measurements have been performed. Inset shows a zoom of the CV curves between 0.2 - 1.0 V *vs*. Na$^+$/Na.

hump appears at 0.9 - 0.4 V which suggests the instability of the surface layer as well as the partial reversibility of the related process. This is in agreement with the poor capacity retention shown in **Figure 2.9** and with the continuous reduction of the electrolyte upon cycling previously reported [3].

The Nyquist plots, corresponding to the relevant potential values at which EIS measurements are performed, are shown in **Figure 3.2** and **Figure 3.3**. The impedance dispersion recorded at 1.0 V *vs.* Na$^+$/Na (**Figure 3.2**) features a very large arc as main feature which corresponds to a semicircle in the lowest-frequency (LF) region. When the dispersion is enlarged (see **inset**), further elements are revealed, namely a semicircle in the medium-frequency (MF) region which overlaps with a smaller semicircle at the highest-frequency (HF) limit. The MF and HF semicircles are commonly assigned to charge-transfer/accumulation of charge at double layer interface and Na$^+$ migration through SEI layer, respectively. As regards the prominent arc in the LF region, it has already been reported for Li$^+$ intercalation electrodes that this semicircle can be associated to an insulating behaviour at certain intercalation degrees [5, 6], ultimately attributed to the bulk electron conductivity of the active material.

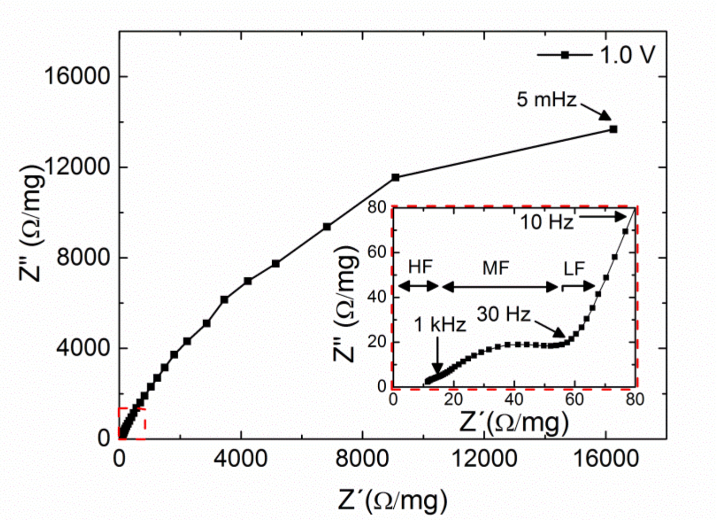

Figure 3.2: Nyquist plot of **NTO-CO-Air** upon Na$^+$ insertion at 1.0 V (x ≈ 0.0) *vs.* Na$^+$/Na. The inset shows the impedance spectrum from 100 kHz to 10 Hz.

When the potential is lowered to the 0.95 - 0.52 V range and the Na$^+$ content in the Na$_2$Ti$_3$O$_7$ electrode is increased (**Figure 3.3a**), the very large arc at LF starts progressively to contract (about one order of magnitude) and to bend onto the real axis. Meanwhile, as shown in **Figure 3.3b**, the MF to HF features remain practically unmodified. As the potential is further lowered down at 0.4 V and below, towards the Na$^+$ intercalation potential limit (**Figure 3.3c**), the LF semicircle abruptly decays and a sloping line, typical of a diffusive behaviour and a vertical line, which describes accumulation of charge (C_i = differential intercalation capacity) of a blocking electrode, is fully revealed below 1 Hz, while the two semicircles at MF and HF can be now more clearly appreciated (**Figure 3.3d**).

It is worth noting that the constant contraction of the LF semicircle as the Na$^+$ content increases in the Na$_2$Ti$_3$O$_7$ electrode is a peculiar trend of the subsequently acquired impedance dispersion. A similar behaviour has been experimentally observed by EIS in LiCo$_x$Ni$_{1-x}$O$_2$ cathodes (in this case during Li$^+$ extraction) and it has been attributed to the change in the bulk electronic conductivity which reveals a transition from insulator to conductor [5, 6, 7]. Therefore, it can be inferred that **NTO-CO-Air** sample also follows an bulk electronic conductivity change during Na$^+$ insertion: after complete oxidation (E = 1.0 V, Na$_{2+x}$Ti$_3$O$_7$, x ≈ 0.0) the active material behaves as an insulator showing a large LF semicircle (**Figure 3.2**) but, when the electrode is completely reduced (E = 0.05 V, Na$_{2+x}$Ti$_3$O$_7$, x ≈ 2.0) it becomes an electronic conductor and the radius of the LF semicircle stops decreasing (**Figure 3.3c** and **Figure 3.3d**) while the buried diffusion element is

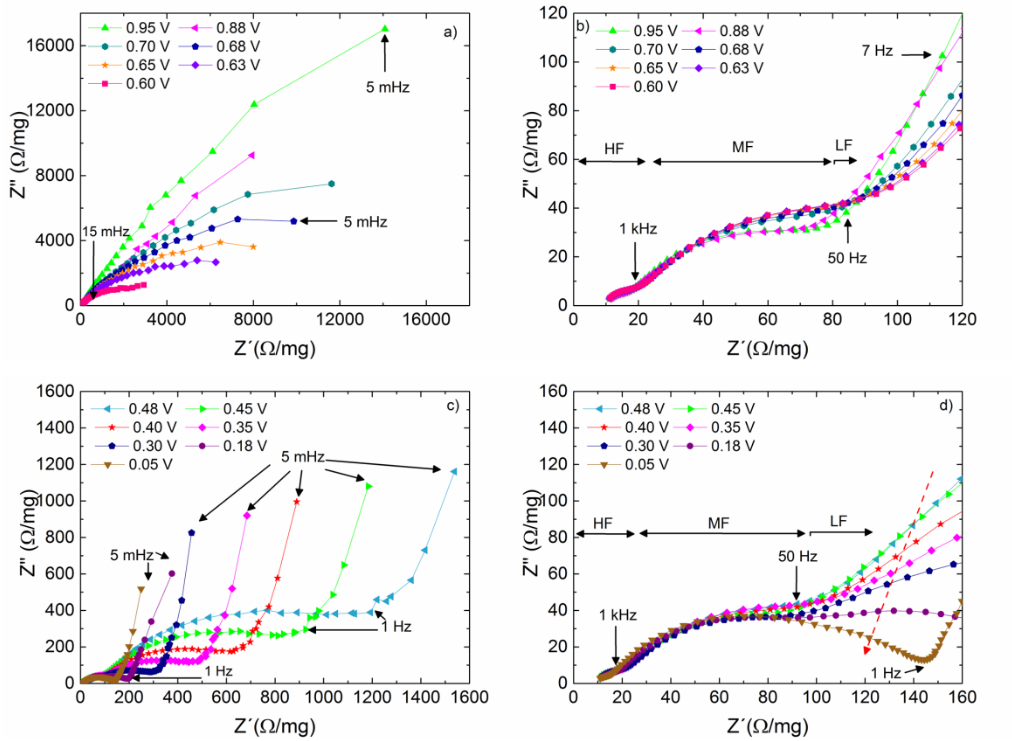

Figure 3.3: Nyquist plots of **NTO-CO-Air** upon Na^+ insertion at **a)** 0.95 V, 0.88 V, 0.70 V, 0.68 V, 0.65 V, 0.63 V, 0.60 V, **b)** zoom of **a** impedance data in the frequency range of 100 kHz-7 Hz. **c)** 0.48 V, 0.45 V, 0.40 V, 0.35 V, 0.30 V, 0.18 V and 0.05 V *vs.* Na^+/Na. **d)** Zoom of **c** impedance data from 100 kHz to 0.7 Hz.

revealed. Indeed, this is in agreement with the aforementioned first principles calculations of Pan *et al*. where the transition from insulator to electronic conductor was predicted [3].

Moreover, such behaviour seems to be reversible since the opposite behaviour during the Na^+ extraction can be observed (**Figure 3.4**). When the Na^+ content starts decreasing and the potential increases from 0.05 to 0.4 V (**Figure 3.4a**), the LF arc is close to the real axis and the diffusive line can clearly see but at higher voltage (**Figure 3.4b**) a very large arc progressively appears at LF and a sloping line typical of a diffusive behaviour is hidden by this semicircle. The insets of **Figure 3.4** show the medium- to high-frequencies features which remain practically unchanged as upon Na^+ intercalation.

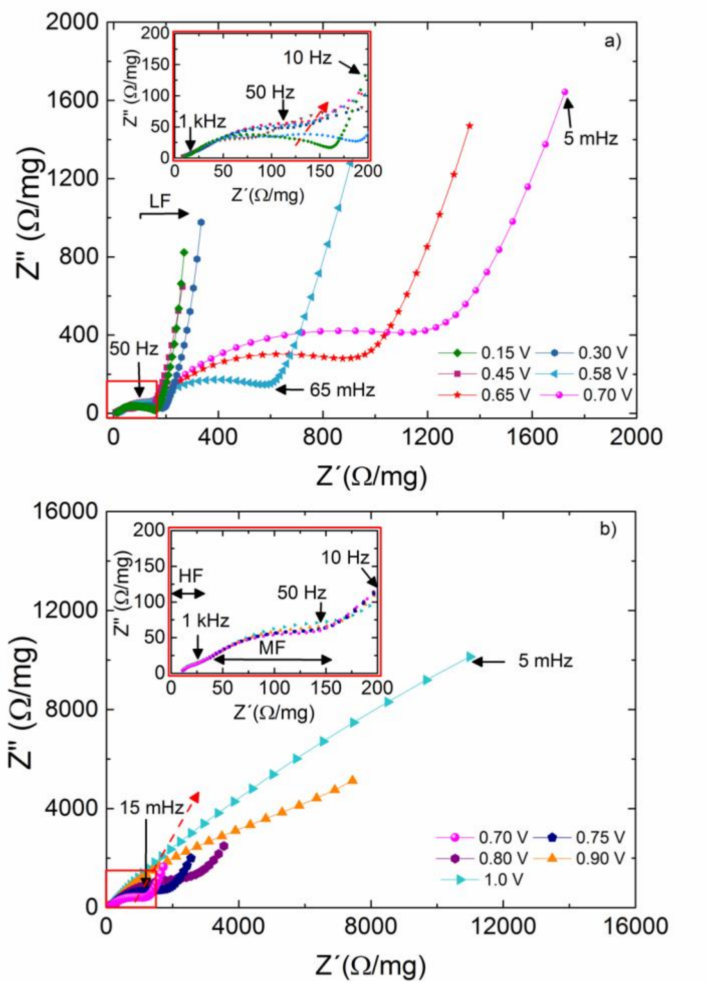

Figure 3.4: Nyquist plots of **NTO-CO-Air** upon 1st Na^+ extraction at **a)** 0.15 V, 0.30 V, 0.45 V, 0.58 V, 0.65 V, 0.70 V, **b)** 0.70 V, 0.75 V, 0.80 V, 0.90 V and 1.0 V *vs.* Na^+/Na. The insets the impedance data in the frequency range of 100 kHz to 10 Hz.

In order to confirm the insulator to conductor transition and the reversibility of the process, all the impedance dispersion spectra (200 spectra) have been fitted to an equivalent circuit previously used for intercalation cathodes in LIBs [5, 6, 7], where the different processes can be correlated with the polarization frequency [8]: the HF intercept onto the real axis is represented by electrolyte resistance (R_{sol}) and corresponds to the Na^+ resistance across the electrolyte; the HF semicircle is described by a resistance and a capacitance of the SEI layer (R_{SEI} and C_{SEI}); the MF semicircle is associated to the charge-transfer resistance (R_{CT}) and double layer capacitance (C_{DL}); the LF semicircle is modelled by two components, namely the bulk electronic resistance (R_{elec}) and the capacitance arising from the charge accumulation at the surface of the particles or at intraparticles crystallite domains (C_{elec}) [9]. All described components are connected in parallel. Finally, the sloping line in the lowest-frequency region can be described as a series of a Warburg diffusion element (Z_w), ascribed to the solid-state diffusion of the Na^+ inside the crystal, and an intercalation capacity (C_i). In order to validate the chosen equivalent circuit, two different equivalent circuits have been attempted: not taking (**Figure 3.5a**) and taking into account the R_{elec} and C_{elec} elements (**Figure 3.5b**); in other words, a two-arc *vs.* a three-arc model. As can be observed in **Figure 3.5a**, the two-arc model is not able to fit the impedance data in the whole range, displaying a large deviation at LF. Meanwhile the three-arc circuit (**Figure 3.5b)** delivers a good fit, confirming the need of an extra process associated with the R_{elec}, besides the common processes correlated with intercalation materials such as, R_{sol}, R_{SEI} II C_{SEI}, R_{CT} II C_{DL}, [8]. Hence, the three-arc circuit has been chosen to fit all impedance spectra. An example of the fitted impedance data presented in **Figure 3.3** is shown in **Figure 3.6** and, as can be seen in the graphs, there is still a slight deviation from the experimental data at very LF when the Na^+ insertion has not started yet (1.0 - 0.6 V voltage range). This deviation can be mainly attributed to two main reasons: an error when C_i is fitted owing to the overlapping of this contribution with the large LF arc; and/or very small C_i values so their determination becomes very hard when the Na^+ insertion is almost negligible. In **Table A.1** (appendix) the values of the resistance, capacitance and the Pearson distribution (X^2) of fitted impedance data are collected.

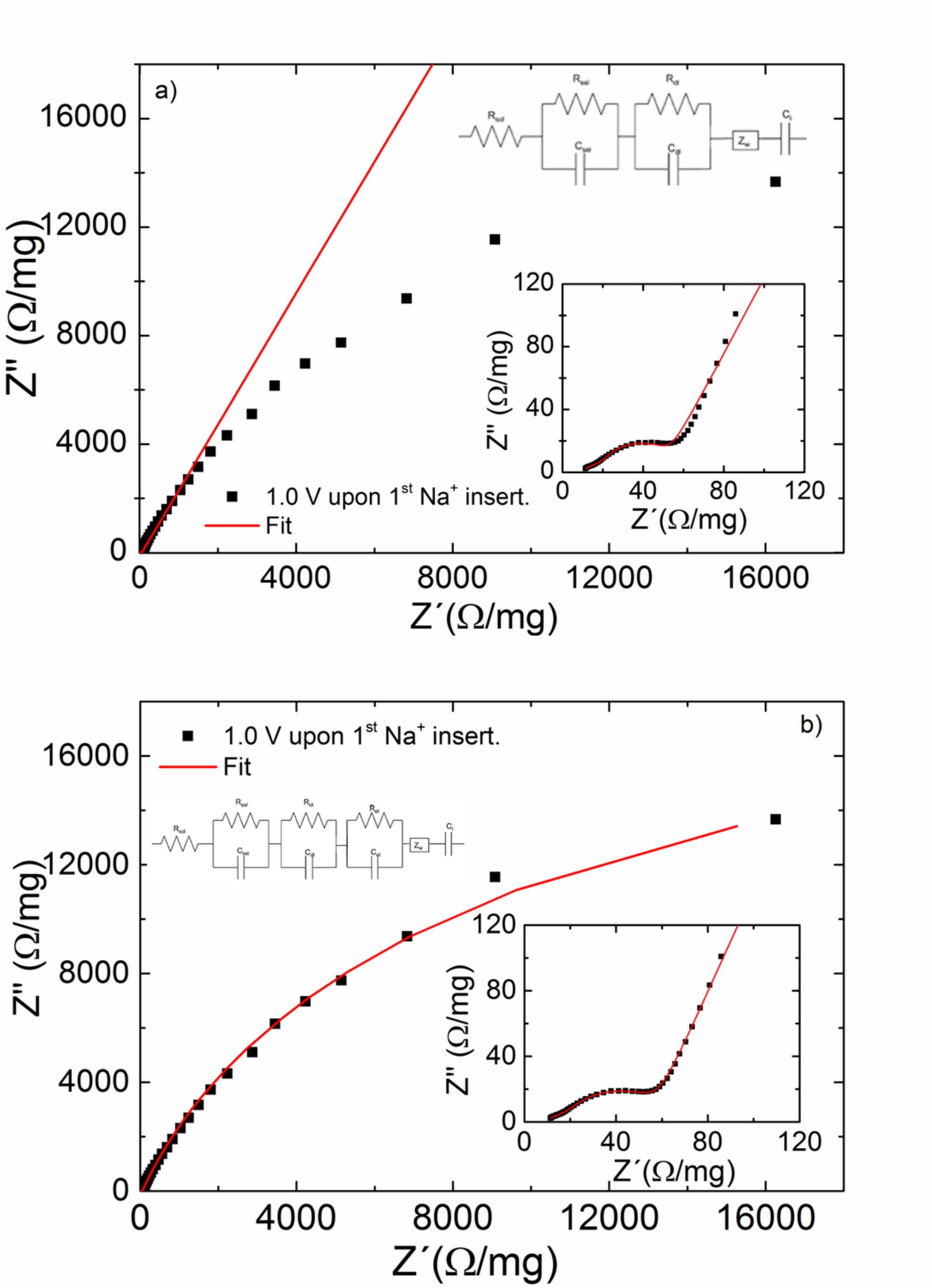

Figure 3.5: The equivalent circuit and the fitted data at 1.0 V upon 1st Na insertion taking into account **a)** two and **b)** three arcs to fit the impedance data of **NTO-CO-Air**. This circuit was included in the Boukamp software which was then used to obtain a fit to the experimental data. The insets show the impedance spectrum from 100 kHz to 7 Hz.

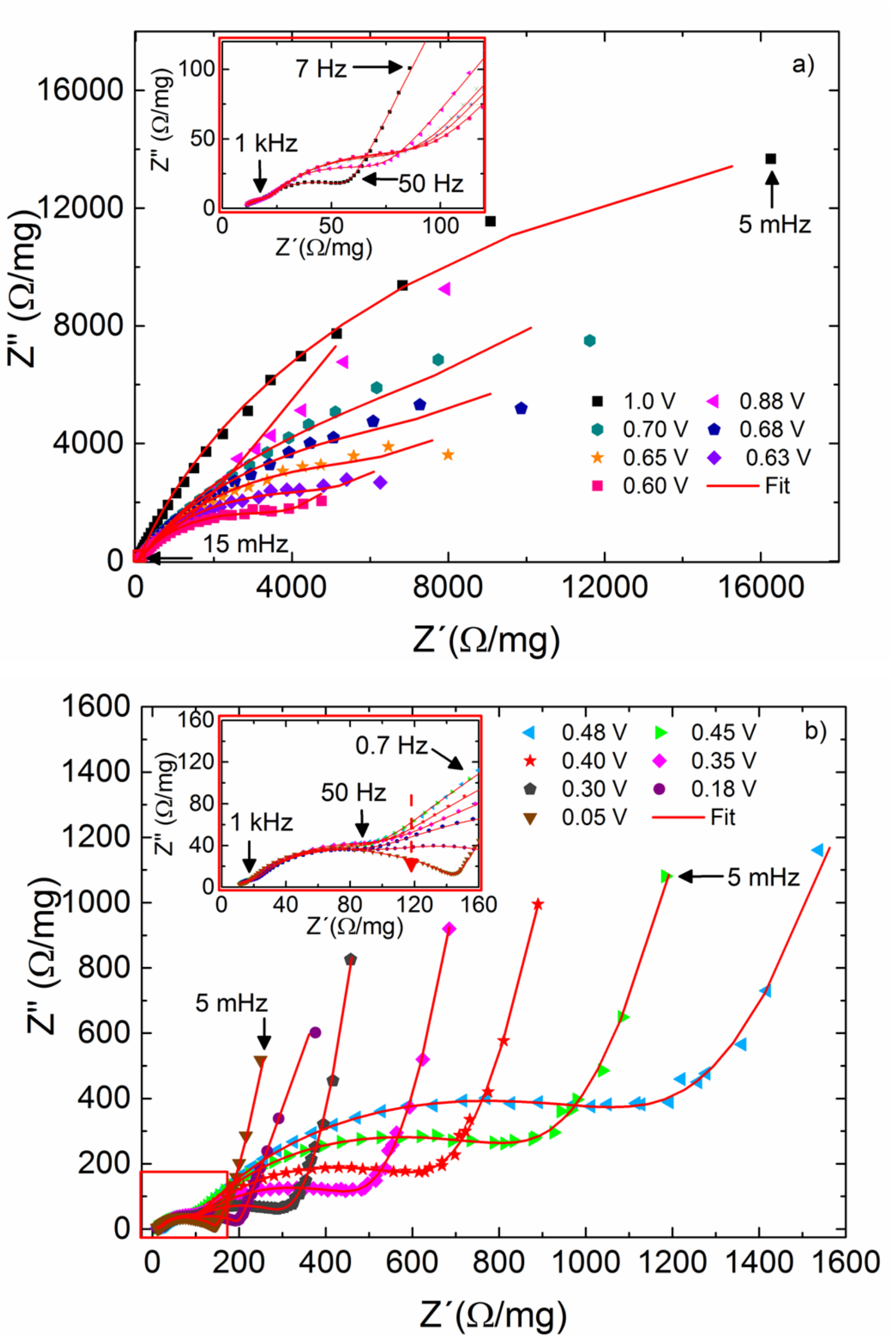

Figure 3.6: The fits of Nyquits plots of **NTO-CO-Air** at a) 1.0 V, 0.88 V, 0.70 V, 0.68 V, 0.65 V, 0.63 V, 0.60 V, **b)** 0.48 V, 0.45 V, 0.40 V, 0.35 V, 0.30 V, 0.18 V and 0.05 V *vs.* Na$^+$/Na. The insets show the impedance spectra from **a)** 100 kHz to 7 Hz b) 100 kHz to 0.7 Hz.

The overall trend of the resistance values, calculated from fitting the EIS spectra with Boukamp software [10] until X^2 values converge to around 10^{-5}, is reported in **Figure 3.7a** and directly compared with the voltage during the Na^+ insertion and extraction sweeps. During the fitting procedures, all C and Z_W elements have been substituted by constant phase elements (CPEs) in order to take into account any roughness or other deviation from ideal interfacial behaviour (more details in **section A.2.5.**) [11].

As already mentioned, the most relevant trend corresponds to the abrupt decay of the R_{elec} (blue points in **Figure 3.7a**) upon Na^+ insertion. The reversible behaviour can be observed during the Na^+ extraction since the high R_{elec} values are recovered. During the 1st insertion process a significant variation of R_{elec} around 0.6 V *vs.* Na^+/Na can be observed which is related to the irreversible reaction between $Na_2Ti_3O_7$ and C65 carbon [1]. As regards R_{CT} (green points in **Figure 3.7a**), the calculated values steadily increase during the first three cycles, which can be related with morphology changes of the $Na_2Ti_3O_7$ particles. The estimated values of α associated with R_{CT} confirm this hypothesis since it decreases upon cycling (**Figure 3.7b**), being α in the EIS fitting the exponential factor of CPEs that defines the surface homogeneity and roughness ($\alpha = 1$ for surfaces completely homogeneous and smooth) [11].

Moreover, by comparing the behaviours of R_{elec} and R_{CT} it is possible to describe the intercalation kinetics of **NTO-CO-Air**. When the potential is above 0.1 V *vs.* Na^+/Na the R_{elec} is higher than R_{CT}, but when the potential is under 0.1 V the $R_{elec}:R_{CT}$ ratio is reversed. This confirms that, prior to large Na^+ insertion, the **NTO-CO-Air** is an insulator and the intercalation kinetics are limited by the electronic conductivity but, when the amount of intercalated Na^+ increases, the $Na_{2+x}Ti_3O_7$ behaves as an electronic conductor and the kinetics are limited by the interfacial charge-transfer step.

Finally, the R_{sol} (black points in **Figure 3.7a**) is almost constant upon cycling. However, the R_{SEI} (red points in **Figure 3.7a**) has a similar reversible behaviour as that shown by the R_{elec}. The R_{SEI} is lower upon Na^+ insertion than after the extraction process. Upon Na^+ insertion, the SEI layer is forming and at further low voltage the SEI layer might be more homogeneous or smooth as suggested by the α value associated with SEI layer (**Figure 3.7c**) which gets closer to 1.0. Therefore, the R_{SEI} decreases whilst, upon Na^+ extraction, the SEI layer resistance increased due to a cracking of the SEI layer and/or partial dissolution of its components.

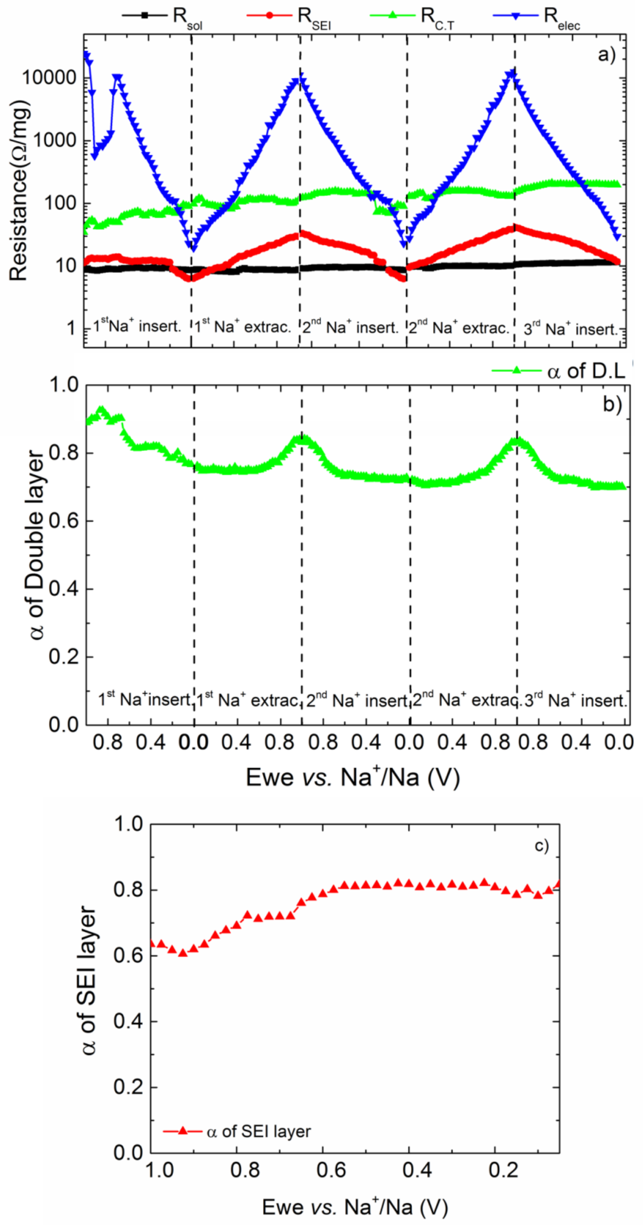

Figure 3.7: EIS performance of **NTO-CO-Air.** **a)** R_{sol} (black points), R_{SEI} (red points), R_{CT} (green points) and R_{elec} (blue points) behaviour and values during the first three electrochemical cycles *vs.* voltage (Ewe *vs.* Na^+/Na). Values for the exponential α factor of the CPE associated with **b)** C_{DL} and **c)** $C_{SEI.}$

This evidences the instability of the SEI layer upon Na^+ extraction at least during the first three cycles, which is in agreement with the capacity fading that shows this material (c.f. **Figure 2.9**).

3.2.2. NTO-OH-Ar-C sample

The Nyquist plots of the **NTO-OH-Ar-C** sample are shown in **Figure 3.8** and **Figure 3.9** which correspond to the same potential values already studied for the **NTO-CO-Air** sample. Analogously to what has been observed for the **NTO-CO-Air**, the EIS data from the **NTO-OH-Ar-C** recorded at 1.0 V *vs.* Na^+/Na also reveals a very large arc in the LF region. A small curvature can observed at LF which is attributed to the R_{elec} of the active material. However, for the **NTO-OH-Ar-C** the R_{elec} value is half of that measured for the **NTO-CO-Air**. The reason of a lower R_{elec} might be originated by the higher content of conductive carbon; please note that besides the Super C65 conductive additive, the active material is coated with 6.0 nm of carbon that can enhance the electric conductivity [12]. The inset shows a slightly distorted semicircle at MF and HF regions originated by the overlap of the Na^+ migration through double layer interface of the particles with SEI layer.

Upon Na^+ insertion and therefore at lower voltage, the LF arc starts a progressive contraction getting closer to the real axis (**Figure 3.9a**). Close to the Na^+ intercalation voltage limit the straight line corresponding to the contribution from the Na^+ diffusion can be observed (**Figure 3.9b**). Again, as it occurs with the **NTO-CO-Air** sample, the R_{elec} change measured for the **NTO-OH-Ar-C** sample is reversible, when the Na^+ starts the deinsertion process the LF arc is progressively reduced towards the real axis (**Figure 3.9c**), but at higher voltage the LF arc grows

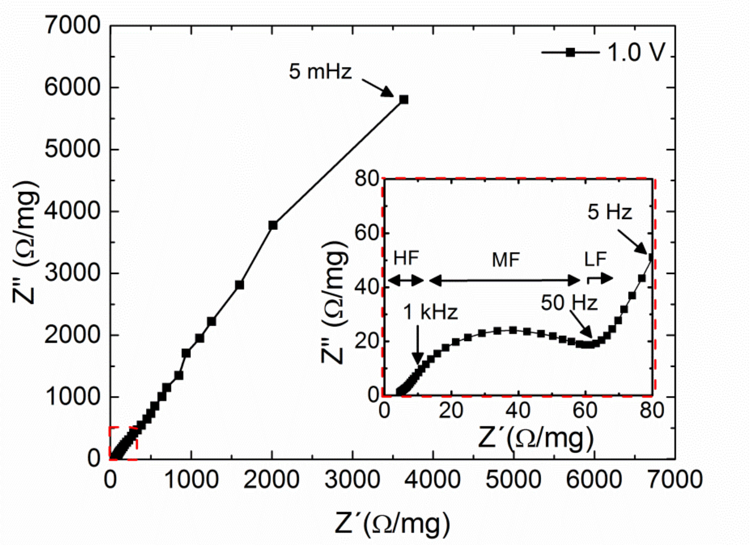

Figure 3.8: Nyquist plot of **NTO-OH-Ar-C** upon Na^+ insertion at 1.0 V (x ≈ 0.0) *vs.* Na^+/Na. The inset shows the impedance spectrum from 100 kHz to 5 Hz.

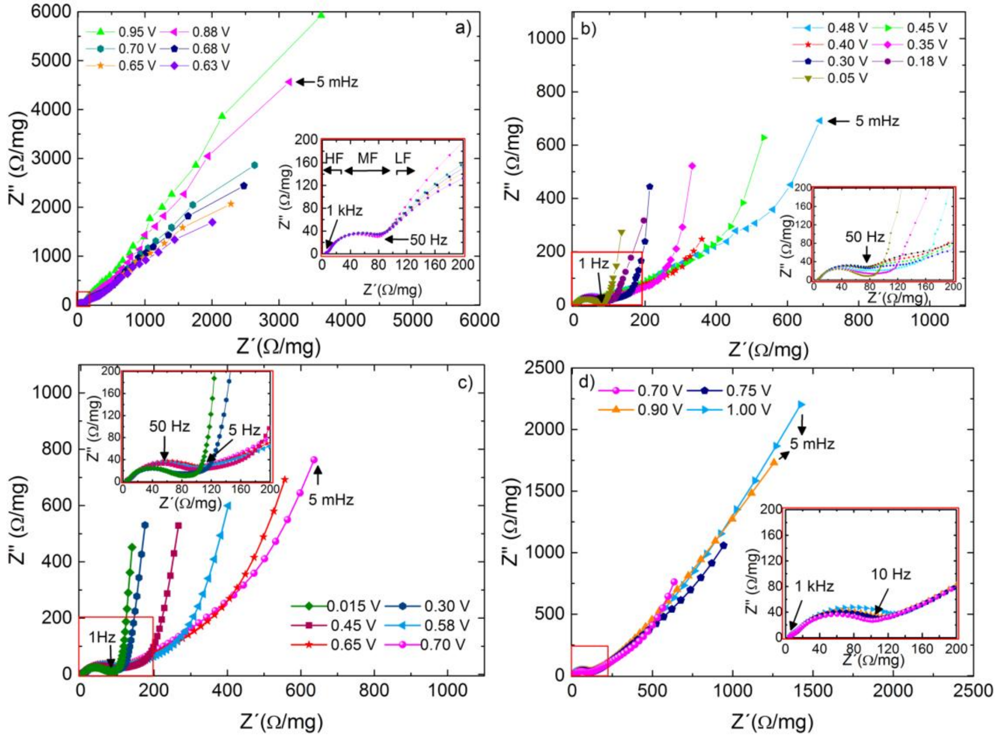

Figure 3.9: Nyquist plots of **NTO-OH-Ar-C** upon Na$^+$ insertion at **a)** 0.95 V, 0.88 V, 0.70 V, 0.68 V, 0.65 V, 0.63 V, **b)** 0.48 V, 0.45 V, 0.40 V, 0.35 V, 0.30 V, 0.18 V and upon 1st Na$^+$ extraction at **c)** 0.15 V, 0.30 V, 0.45 V, 0.58 V, 0.65 V, 0.70 V, **b)** 0.70 V, 0.75 V, 0.90 V and 1.0 V *vs.* Na$^+$/Na. The insets the impedance data in the frequency range of 100 kHz to **a,d)** 1 Hz, **b,c)** 15 mHz.

back while covering the straight line associated to Na$^+$ diffusion (**Figure 3.9d**). The insets show the medium- to high-frequency features which correspond to the R$_{CT}$ and R$_{SEI}$ that remain almost constant if compared with the R$_{elec}$ behaviour, similarly to the behaviour of the **NTO-CO-Air**.

In order to confirm that the **NTO-OH-Ar-C** sample undergoes the same transition from insulator to conductor and the resistances values are lower, all the impedance dispersion have been fitted by Boukamp software [10] until convergence of the X^2 value around 10^{-5}. The circuit that is employed for **NTO-OH-Ar-C** (**top** panel in **Figure 3.10**) is slightly modified if compared with the one used for **NTO-CO-Air**: an extra process associated to the C-coating is taken into account besides the R$_{sol}$ and R$_{SEI}$ II C$_{SEI}$ at HF, R$_{CT}$ II C$_{DL}$ at MF and R$_{elec}$ II C$_{elec}$, Z$_w$ and C$_i$ at LF. Although the C-coating is mainly homogenous, some carbon aggregation around the outermost surface is observed (c.f. **Figure 2.17**). Consequently, the diffusion of Na$^+$ will depend on the coating thickness. As can be observed in **Figure 3.10**, where the fitted impedance data is presented, the modified model fits well also at very LF when Na^+ are not inserted, in contrast with the **NTO-CO-Air** sample. This deviation, which for the **NTO-CO-Air** sample has been attributed to an error of the C_i fit, is almost negligible in the **NTO-OH-Ar-C** sample. In this case the R_{elec} is lower and hence only slightly overlaps with the C_i contribution, finally leading to a better fit. The obtained values of the resistance, capacitance and the Pearson distribution (X^2) of fitted impedance data of **Figure 3.10** are collected in **Table A.2** (appendix).

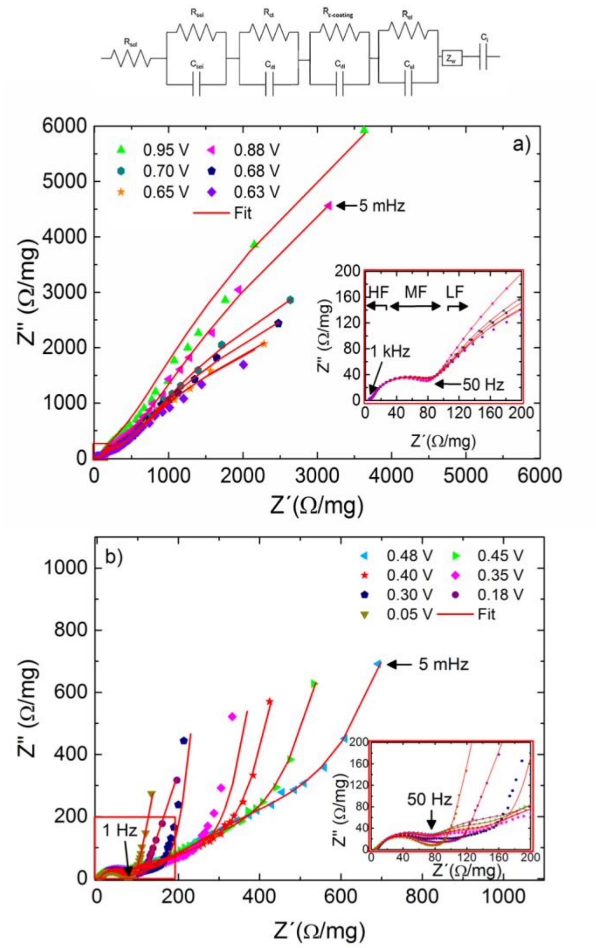

Figure 3.10: (**top**) The equivalent circuit used as input in the Boukamp software to fit the impedance data of the **NTO-OH-Ar-C**. Fits of Nyquits plots of **NTO-OH-Ar-C** at **a)** 0.95 V, 0.88 V, 0.70 V, 0.68 V, 0.65 V, 0.63 V **b)** 0.48 V, 0.45 V, 0.40 V, 0.35 V, 0.30 V, 0.18 V and 0.05 V *vs.* Na^+/Na. The insets show the impedance spectra from 100 kHz to ~ 30 mHz.

The overall trend of the resistance values *vs.* voltage during the three first cycles is reported in **Figure 3.11** and, as has been done with **NTO-CO-Air** sample, the Z_W and all capacitance elements have been substituted by CPEs in order to take into account the possible roughness, inhomogeneities and/or other deviation from ideal interfacial behaviour [11].

As mentioned before, the R_{elec} (blue points in **Figure 3.11**) observed at LF decay abruptly during Na^+ insertion and/or when the voltage is decreasing. The behaviour of R_{elec} is reversible and the starting values are recovered during Na^+ extraction. Regarding the process at MF there are two associated parameters: C-coating resistance ($R_{C\text{-}coating}$) and R_{CT}. Since both processes occur at the same time and the obtained capacitance and resistance values from the fits are very similar (expect during the 1st Na^+ insertion), it becomes very difficult to distinguish between them. However, the variations of the resistance during the cycling can clarify which values correspond to each process. Therefore, the $R_{C\text{-}coating}$ (cyan points in **Figure 3.11**) has been identified with the resistance that shows a higher value during the 1st Na^+ insertion and decreases at lower voltage while the R_{CT} (green points in **Figure 3.11**) is related with a more stable resistance. The behaviour of the $R_{C\text{-}coating}$ can be explained by the fact that, at the begging of the electrochemical cycling, the SEI layer will only form on the surface of the C-coated $Na_2Ti_3O_7$ particles and, hence, higher variations of the resistance will be observed in the coating surface than in the double layer of the particle. At further lower voltage values the resistance decreases since the surface become more homogeneous or smooth, as it is observed in the case of the SEI layer in the **NTO-CO-Air** sample. In contrast, the R_{CT} will not change significantly because the C-coating will protect the particles upon cycling. It is interesting to compare the trend of R_{CT} in the **NTO-OH-Ar-C** sample with the **NTO-CO-Air** sample, which in the latter sample increases gradually upon cycling while in the coated sample is almost constant showing a small variation between the oxidised ($Na_4Ti_3O_7$) and reduced ($Na_2Ti_3O_7$) states. This different behaviour might be because the C-coating involves an easier Na^+ insertion/extraction due to a larger specific surface that results in enhanced charge-transfer kinetics [8] which ultimately could be at the origin of a better electrochemical performance.

As it happens with the **NTO-CO-Air** sample, more information on the intercalation kinetics of the **NTO-OH-Ar** sample can be obtained comparing the behaviours of R_{elec} and R_{CT}. At potentials above 0.32 V *vs.* Na^+/Na the ratio $R_{elec}:R_{CT}$ is bigger than 1, whilst below 0.32 V the $R_{elec}:R_{CT}$ ratio is smaller than 1. This means that at the begging of the Na^+ insertion the intercalation kinetics are limited by the bulk electronic conductivity showing a insulator behaviour, but once the Na^+ content starts increasing significantly close to the insertion plateau, the **NTO-OH-Ar-C** material becomes electronic conductor and the kinetics are limited by the interfacial charge-transfer step. It is worth mentioning that the C-coated sample (**NTO-OH-Ar-C**) undergoes the transition to electronic conductor at higher voltage and lower Na^+ content than the **NTO-CO-Air**, which might be due to the C-coating that enhances the electric conductivity [12].

Finally, the processes at HF reveal that the R_{sol} (black points in **Figure 3.11**) is almost constant upon cycling and the R_{SEI} has a similar reversible behaviour as R_{elec}, already observed for **NTO-CO-Air** sample. The R_{SEI} (red points in **Figure 3.11**) is lower upon Na^+ insertion since a homogeneous SEI layer is forming and higher upon Na^+ extraction which can be related with the fact that during the Na^+ extraction the surface of the SEI layer is more inhomogeneous or rough. Moreover, it is interesting to notice that the variation between the lowest and highest value is one order the magnitude smaller in **NTO-OH-Ar-C** than in **NTO-CO-Air** sample, in other words, the kinetic properties of the SEI layer are more stable in the C-coated sample.

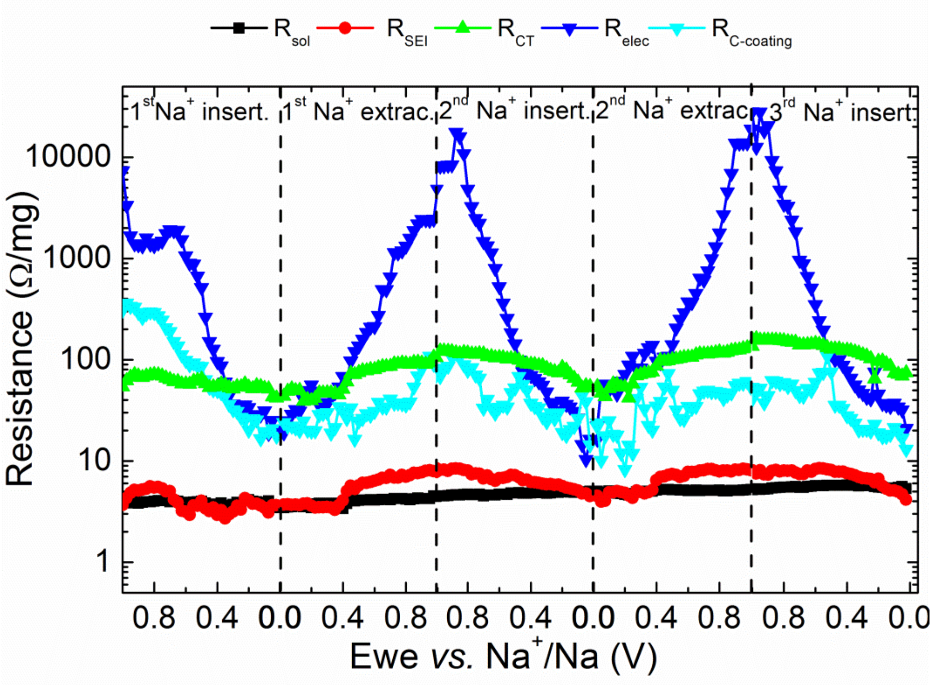

Figure 3.11: EIS performance of **NTO-OH-Ar-C**. R_{sol} (black points), R_{SEI} (red points), R_{CT} (green points) and R_{elec} (blue points) behaviour and values during the first three electrochemical cycles *vs.* voltage (Ewe *vs.* Na^+/Na).

3.3. SEI layer study by XPS

Besides the electrochemical characterisation, the SEI layer composition and stability for the electrodes under study was investigated by means of X-ray photoelectron spectroscopy (XPS) with a Mg K_α (1253.6 eV) non-monochromated X-ray source. The electrodes were cycled at 0.1C and were stopped at the required potential, rinsed with PC and dried in the glove box chamber before being inserted into the XPS vacuum chamber using an air-tight transfer system, never exposing the electrodes to air. The SEI layer formation and evolution of **NTO-CO-Air** and **NTO-OH-Ar-C** samples will be followed by XPS from C 1*s*, O 1*s*, F 1*s*, Cl 2*p* and Na 1*s* photoelectron peaks as well as the Na $KL_{23}L_{23}$ Auger peaks at different charge states during Na^+ insertion/extraction process. For both samples, conventional XPS data, compositional analysis following the study of the Auger parameter and *in-situ* depth profiling will be presented.

First of all it is important to take into account that the studied sample surface is not uniform, there are nonconducting microdomains from reduction products or/and residual salt of the electrolyte, therefore, a charging effect will take place. Thus, the absolute binding energies for cycled electrodes are slightly different to the ones reported in the literature. However, the majority of peaks can be assigned from relative peak positions obtained from binding energy differences and after calculation of the corresponding Auger parameter [13] which involves both photoelectron and Auger line energies and provides abundant information of the chemical state without the necessity to be concerned about charge corrections and work function measurements. Moreover, to corroborate the peak assignment reference compounds are measured such as C65 conductive additive, Na_2CO_3, PVdF and $NaClO_4$.

3.3.1. NTO-CO-Air sample in a half-cell

The XPS experiments have been conducted at the highlighted points of the galvanostatic curve, as shown in **Figure 3.12**, which are the most significant steps of the electrochemical process namely, before and after SEI formation, full Na^+ insertion and full Na^+ extraction.

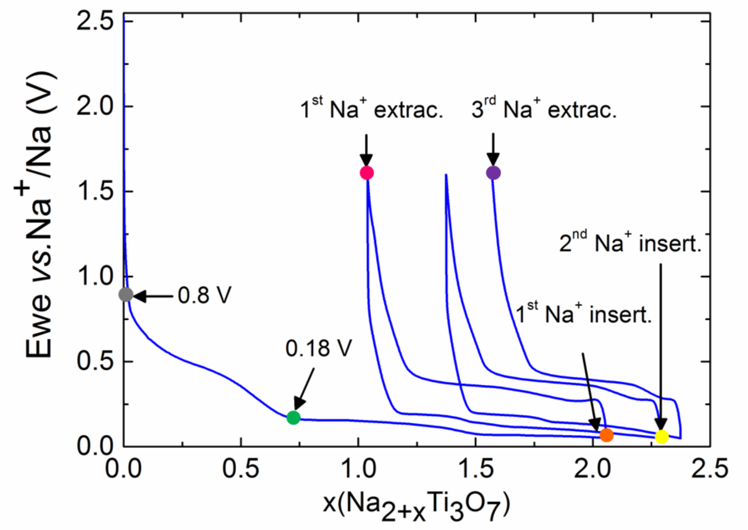

Figure 3.12: Galvanostatic cycling profile of **NTO-CO-Air** during the first cycles. The XPS measurements are performed in the highlighted points of the curve. Moreover, pristine and soaked electrodes are measured.

3.3.1.1. Conventional XPS study

The C 1*s* photoemission line (**Figure 3.13**.) will provide information about the electrolyte decomposition and also about the homogeneity/stability of the SEI layer; the latter can be inferred from the presence of a graphitic signal which should not be detected if a uniform and homogeneous SEI layer is formed. The unambiguous determination of the C-based compounds is not an straightforward task, therefore the assignments of the C 1*s* spectra components have been done on the basis of previous XPS studies of carbon-based materials [14].

The main component in the C 1*s* photoelectron peak of the pristine and soaked electrodes is the component at 284.4 eV assigned to graphitic-like compounds which in this case mainly corresponds to the conductive additive. This peak shows also an asymmetry towards high binding energies due to its conductor character [15]. This asymmetry is slightly extended by the presence of hydrocarbon with C-C and C-H bonds at around 285.0 eV [16]. In the 290.5 – 290.8 eV range, contributions from organic carbonate contamination and a shake-up feature corresponding to a Π−Π* transition typical of graphitic-like compounds are expected [17]. The presence of the PVdF ($-(CF_2-CH_2)_n-$) binder also can be seen in the pristine and soaked samples which is revealed by two equal peaks, one at 286.4 eV from the $-CH_2$ and another one at 290.9 eV from $-CF_2$, the latter will be overlapped with the Π−Π* transition [18].

As the Na^+ insertion process evolves, the graphitic-like signal (284.4 eV) progressively reduces its intensity as the surface layer grows on top of the electrode. It is worth mentioning here that although the main reaction peak of the SEI layer formation appears at 0.32 V, at 0.9 V already emerges a shoulder associated to the SEI formation process (**Figure 3.1**). Around 0.18 V the graphitic-like component disappears completely indicating that the SEI layer is fully formed and has reached a thickness of at least 5 nm, in agreement with the CV curve (**Figure 3.1**). The SEI layer thickness determination is based on the empirical relationship between the escape length of a photoelectron and its kinetic energy, these results are consistent with a minimum SEI layer thickness of 5 nm for photoelectrons with a kinetic energy around 1000 eV [19].

Upon Na^+ extraction, a small shoulder appears at 284.4 eV in the C 1*s* line from the underlying graphitic carbon indicating a thinning or cracking of the SEI layer. After a second Na^+ insertion, the shoulder disappears as the SEI layer grows back, fully covering the electrode surface again. This behaviour remains in the following cycles, as can be confirmed during the 3rd cycle after Na^+ extraction where a small shoulder appears again. The process of SEI layer formation upon Na^+ insertion and partial dissolution or/and crack upon extraction is repeated along several cycles, revealing an instability along electrochemical cycling which might be one of the factors that contributes to the huge capacity fading that shows **NTO-CO-Air** sample (c.f. **Figure 2.9**).

As the graphitic-like component disappears during Na^+ insertion other components become more prominent: carbon surrounded by one oxygen such as sodium alkoxide (NaOR) and poly(ethylene oxide) oligomer ($(\text{-}CH_2\text{-}CH_2\text{-}O\text{-})_n$; PEO) at 286.1 – 286.5 eV [20]; and carbons in a three-oxygen environment like Na_2CO_3 with contributions at 291 - 291.5 eV [20, 21] instead of 289.4 eV [22] and sodium alkyl carbonates ($NaCO_3R$, R = different long-chain alkyl groups) at 290 - 291 eV and 288 eV depending on the carbon in the alkyl group (R) [20, 21]. The observed energy shifts and discrepancies with tabulated values have its origin in differential charging effects. All these compounds with carbon-oxygen bonds are originated by the reduction of the electrolyte solvents which, during battery operation and due to the low working voltage of the anode material, are forced outside their EWS.

Finally, still focused on the C 1*s* peak, the evolution of F-based components, namely PVdF, during cycling (Na^+ insertion/extraction) will be followed. However, in this case, the $\text{-}CF_2$ and $\text{-}CH_2$ signals slightly shift to higher binding energies as the electrochemical process starts (**Figure 3.13**). This energy shift has been previously

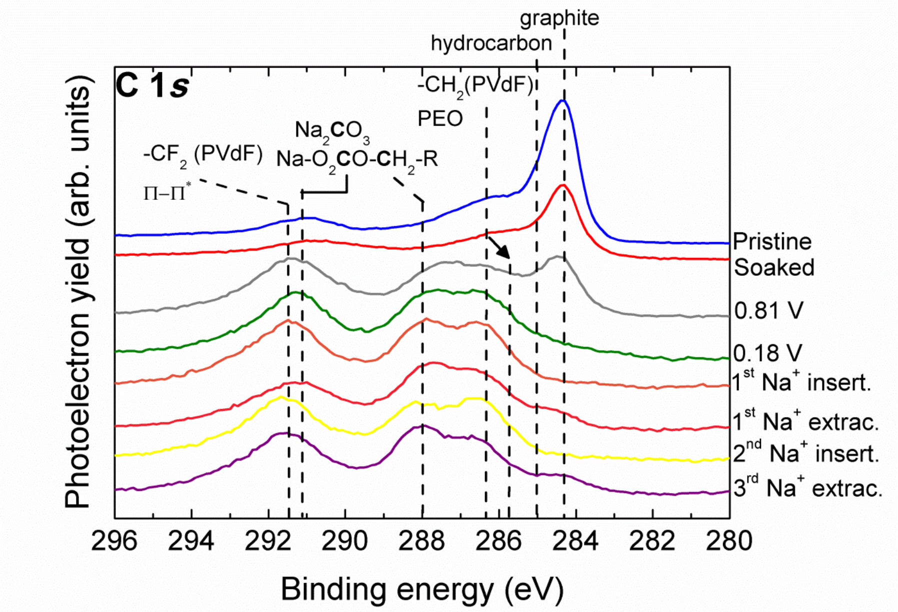

Figure 3.13: C 1*s* XPS photoelectron spectra of **NTO-CO-Air** electrodes before cycling (pristine and soaked in electrolyte) and at different points of Na^+ insertion/extraction curve as indicated in **Figure 3.12**.

reported [23]. Besides the effect of surface charging, it is related to the chemical interaction of Na^+ with PVdF, strongly influencing the PVdF fluorine electronic structure and perturbing the carbon backbone.

The XPS data from the F 1*s* photoemission line (**Figure 3.14**) are also of interest to study the evolution of F-based compounds such as PVdF and NaF. The main component of the F 1*s* peak corresponds to $-CF_2$ groups from PVdF at 688.15 eV in the pristine and soaked electrodes [18]. However, as it is observed in the C 1*s* spectrum, the $-CF_2$ component evolves towards higher binding energies (approximately to 689 eV) upon Na^+ insertion as a result of surface charging and Na^+ doping of PVdF [23]. Analogously to what happens with the graphitic-like signal in the C 1*s* peak, the $-CF_2$ component of the PVdF disappears after the SEI layer formation at 0.18 V and partially reappears after every Na^+ extraction step. This behaviour agrees with a partial dissolution (thinning/cracking) of the SEI layer that covers the whole electrode surface. Additionally, as soon as the electrode and electrolyte are in contact (soaked electrode prior to any electrochemical process) a faint peak corresponding to NaF (685 eV) appears [24, 25]. This is a consequence of a dehydrofluorination reaction of the PVdF binder that releases HF and then reacts with Na^+ of the $Na_2Ti_3O_7$ or $NaClO_4$ resulting in NaF formation, as it has been previously reported for LIBs [26].

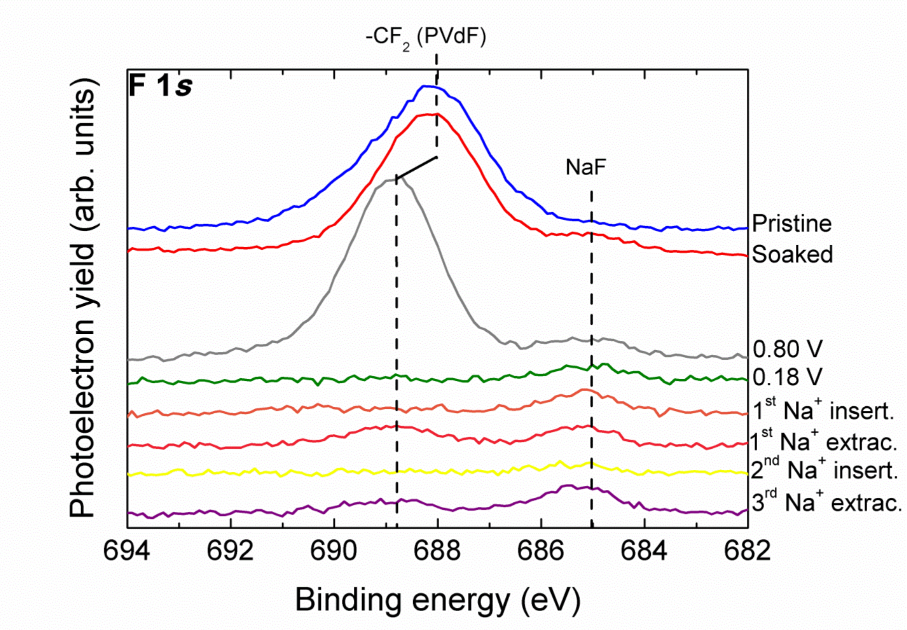

Figure 3.14: F 1*s* XPS photoelectron spectra of **NTO-CO-Air** electrodes before cycling (pristine and soaked in electrolyte) and at different points of the Na$^+$ insertion/extraction curve as indicated in **Figure 3.12**.

In order to confirm the NaF formation and PVdF evolution ^{19}F-ssNMR experiments were performed on several electrodes (**Figure 3.15**) at different charge states. The NaF signal at -221 ppm [27], even in the pristine electrode, reveals the formation of NaF and therefore the PVdF dehydrofluorination. Comparing the relative intensity of the PVdF and NaF peaks (taking the PVdF intensity as a reference) it can be concluded that the intensity of the NaF peak increases upon Na$^+$ insertion in good agreement with the XPS data. The only difference with the XPS data is found for the pristine sample, in this case XPS detects no NaF which, considering the ssNMR results, would indicate that NaF is only formed in the bulk region during electrode preparation and it starts forming in the surface once in contact with the electrolyte.

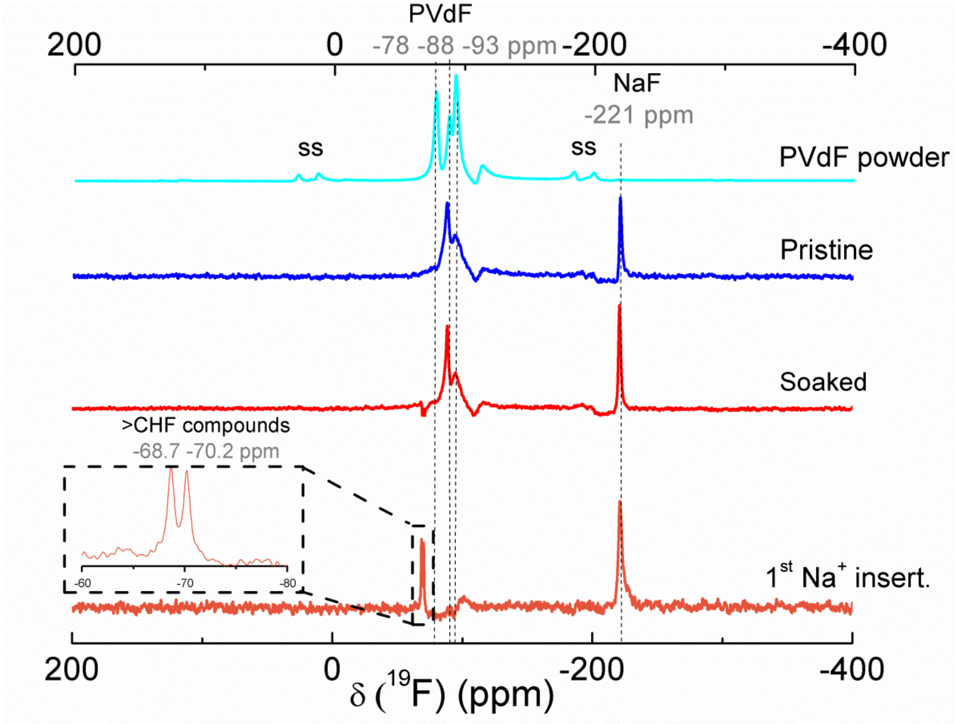

Figure 3.15: ^{19}F-ssNMR spectra of PVdF powder used as reference and **NTO-CO-Air** electrodes at different charge states namely pristine, soaked and 1st Na^{+} insertion until 0.05 V *vs.* Na^{+}/Na. The inset spectrum shows the evolution of the PVdF into new fluorinated compounds (-CHF and/or –CF$_2$). ss signs correspond to spinning side bands of the most intense isotropic signals.

Regarding the evolution of the PVdF, the ssNMR also confirmed this extent (**Figure 3.15**). The reference PVdF powder sample has typically three peaks at -78, -88 and -93 ppm in the ^{19}F-ssNMR spectrum [28]. Those signals disappear and a very narrow doublet appears at -68 and -70.2 ppm in the complete reduced electrode (1st Na^{+} insertion), which indicates the presence of residual -CHF and/or -CF$_2$ bonding, resulting from the degradation of PVdF. If we compare our electrodes performance with Na-CMC-based electrodes (c.f. **Figure 2.36**) [29], the PVdF decomposition (from electrode preparation until cycling performance) can be another factor originating the instability of the SEI layer that ultimately affects the larger capacity fading of PVdF-based Na$_2$Ti$_3$O$_7$ electrodes (c.f. **Figure 2.9**).

To understand better the composition of the surface layer, the O 1*s* photoemission line was also studied for the electrodes at different charge states. As it can be seen in **Figure 3.16**, the O 1*s* peaks of pristine and soaked electrodes have a main component at ~ 531 eV that corresponds to $Na_2Ti_3O_7$. The secondary peak at 532 - 533 eV can be attributed to some residual amount of carbonates, moisture and, for the soaked sample, also some residual $NaClO_4$. As the electrode starts inserting Na^+, a thick layer covering the electrode surface is quickly formed that is composed of Na_2CO_3 (~ 532.8 eV) and $NaCO_3R$ (~ 534 eV and ~ 532.9 eV), along with PEO (~ 533 eV), which consolidates at the end of the Na^+ insertion process [20, 30]. The PEO results from direct polymerization of EC where $Na_{2-x}CO_3R_x$ can act as catalysts [31, 32]. The PEO contribution in the O 1*s* spectrum is intensified upon Na^+ insertion process and attenuated upon Na^+ extraction, in agreement with the observed in the C 1*s* peak (286.5 eV), indicating a partial dissolution of this species during Na^+ extraction in **NTO-CO-Air** sample. The NaOR should also appear in the 531.5 – 532.5 eV range, but considering the overlapping with other components, it is very difficult to determine its existence [33]. Moreover, Na_2CO_3 and $NaCO_3R$ signals are also very close to PEO and it is not straightforward to establish that only PEO is dissolved upon Na^+ extraction. Finally, the contribution from traces of $NaClO_4$ (from electrolyte salt) appears at 533.8 eV. Although at ~ 535 eV, there is a component that corresponds to an overlayer of chemisorbed oxygen [14] as a result of the ClO_4^- anion dissociation where this process might be photoinduced by X-ray radiation [34, 35], further confirmation is needed from the Cl 2*p* peak.

In the Cl 2*p* photoelectron spectra of the electrodes at different charge states, the presence of $NaClO_3$ cannot be detected (**Figure 3.17**) which appears after the X-ray

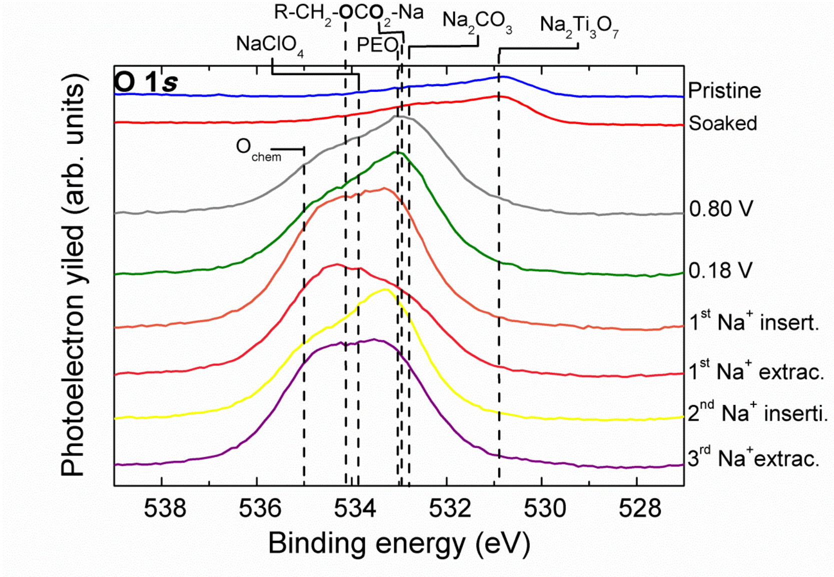

Figure 3.16: O 1*s* XPS photoelectron spectra of **NTO-CO-Air** electrodes before cycling (pristine and soaked in electrolyte) and at different points of the Na^+ insertion/extraction curve as indicated in **Figure 3.12**

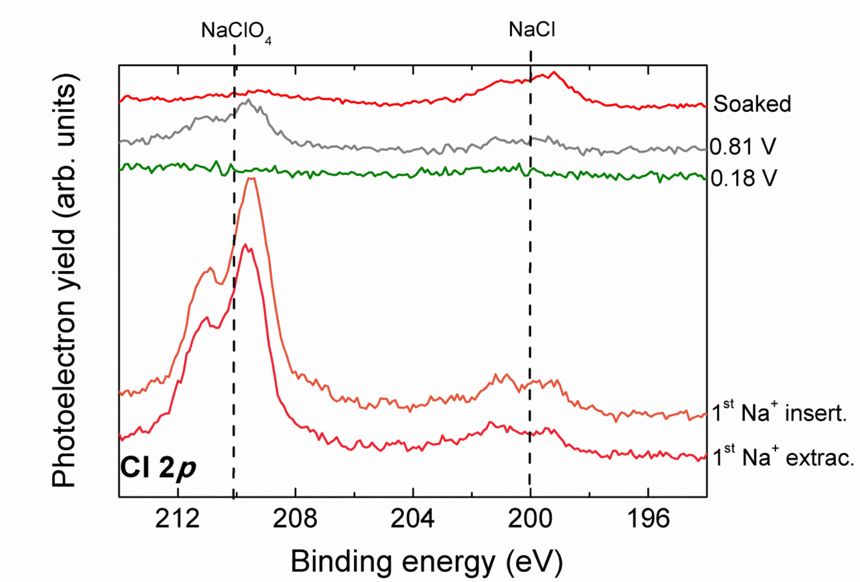

Figure 3.17: Cl 2*p* XPS photoelectron spectra of **NTO-CO-Air** electrodes soaked in electrolyte and at the 1st Na^+ insertion and extraction.

induced reduction of $NaClO_4$. This would agree with the NaCl being formed after electrolyte reduction and not induced by X-ray irradiation. The soaked electrode already shows NaCl, whereas the dominant component in the electrochemically cycled samples corresponds to $NaClO_4$ traces not removed during the electrode washing. One of the most striking features observed in Cl 2*p* spectra is the spontaneous formation of NaCl in the soaked electrode. This indicates a spontaneous formation of NaCl at the very beginning of the electrochemical test, prior to any cycling, which then will be buried by the other SEI components such as $NaCO_3R$ and Na_2CO_3. This extent will be further confirmed later taking into account the Auger parameter and the depth profiling analysis.

3.3.1.2. Auger parameter determination

As explained before, conventional XPS analysis is not sufficient to obtain a complete picture of the SEI layer evolution; the main reasons are the overlapping of several components in the photoelectron peaks and the partial surface charging which turns out to be a main drawback to determine an absolute binding energy calibration. Thus, the study of the Auger parameter ($\alpha + h\nu$) will be crucial to go one step further in the SEI layer study by facilitating the identification of surface components of the SEI layer and their evolution during electrochemical cycling. In this case, the Auger parameter is determined for Na photoemission line. The analysis of the Auger parameter (**Eq 3.1**) could be summarised as the study of the energy shift between the Na 1*s* photoelectron line and the Na $KL_{23}L_{23}$ Auger line.

$$\alpha + h\nu = E_K\ (KL_{23}L_{23}) +\ E_B(1s)\ (\mathbf{Eq.\,3.1})$$

where α+hν is the modified Auger parameter, E_K is the kinetic energy of the Na $KL_{23}L_{23}$ Auger electrons and E_B is the binding energy of the Na 1*s* photoelectrons. Therefore, to determine the Auger parameter, first one must determine the exact positions of the Na 1*s* and Na $KL_{23}L_{23}$ peaks. The experimental data were fitted using the CasaXPS software [36] and the results are presented in **Figure 3.19** where the fits of both peaks (Auger and photoemission) are shown for all electrodes. The obtained peak positions and the calculated Auger parameter, as well as the assigned compound, are collected in **Table A.5** (appendix) [37, 38].

The compounds determined from Auger parameter study mainly correspond to the outermost surface region. This because the photoelectron line (Na 1*s*) that is used to determine the Auger parameter has a high binding energy and, therefore, the photoelectrons that arrive to the detector will have a very low kinetic energy and a very short inelastic mean free path (IMFP, more details in **A.1.3.5.**) and will only scape from the first 1-4 nm.

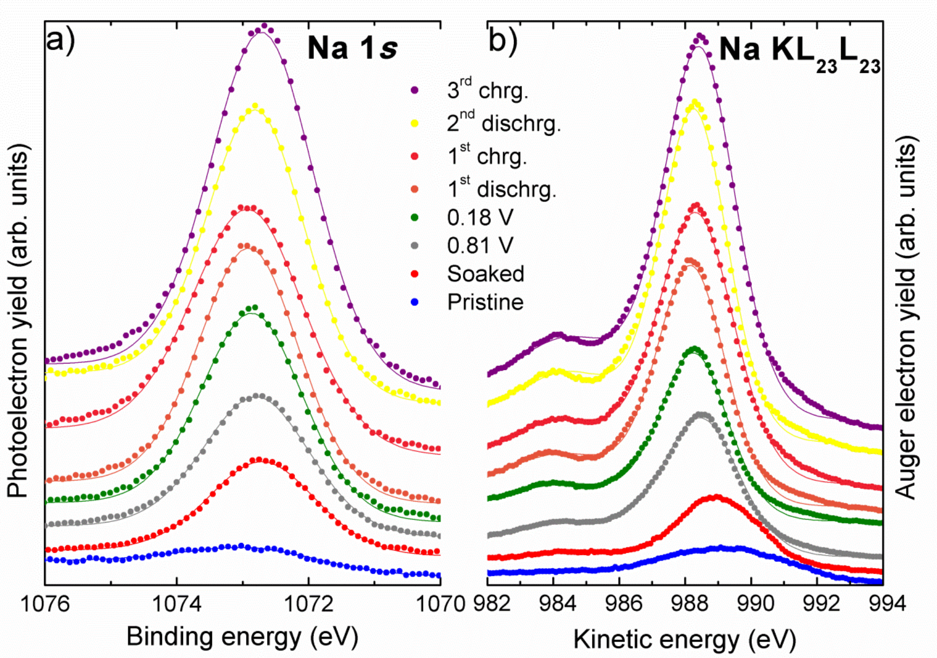

Figure 3.18: a) Na 1*s* photoelectron line and **b)** $NaKL_{23}L_{23}$ Auger transition of **NTO-CO-Air**. Points correspond to the experimental data and the solid lines to the fits.

The obtained Auger parameters at different states of charge are shown in **Figure 3.19**. The Auger parameter value for the pristine and soaked electrodes nicely fits with the sole presence of $Na_2Ti_3O_7$ (2062.0 eV) and NaCl (2061.8 eV), respectively [37, 38]. Besides the obvious presence of $Na_2Ti_3O_7$ on the pristine electrode, the NaCl formation has been already shown by conventional XPS analysis in the soaked electrode (**Figure 3.17**). As the 1st Na^+ insertion process starts, the formation of Na_2CO_3 is quickly evidenced by the reduction of the Auger parameter down to 2061.3 eV covering any trace of NaCl, in agreement with the Cl 2*p* spectrum (**Figure 3.17**). Following with Na^+ insertion, below 0.2 V *vs.* Na^+/Na, and also after the 2nd Na^+ insertion, a further reduction of the Auger parameter towards 2061.0 eV indicates that the Na_2CO_3 is partially covered by a $NaCO_3R$ (since the value of $NaCO_3R$ is not reported in the literature the Auger parameter of this compound is an estimation from $NaHCO_3$ and $NaCO_2$-based compounds which appear at energies below 2061.0 eV). Upon Na^+ extraction, the Auger parameter recovers the value corresponding to Na_2CO_3 which would agree with a partial dissolution of the $NaCO_3R$. This cyclic behaviour not only occurs in the 1st cycle but also in the following cycles, in agreement with the SEI evolution as inferred from the C 1*s* (**Figure 3.13**) and O 1*s* (**Figure 3.16**) photoelectron spectra.

Finally, NaF is not detected on the outermost surface region from the Auger parameter data (2060.1 eV would be the expected value for NaF) [38], due to the

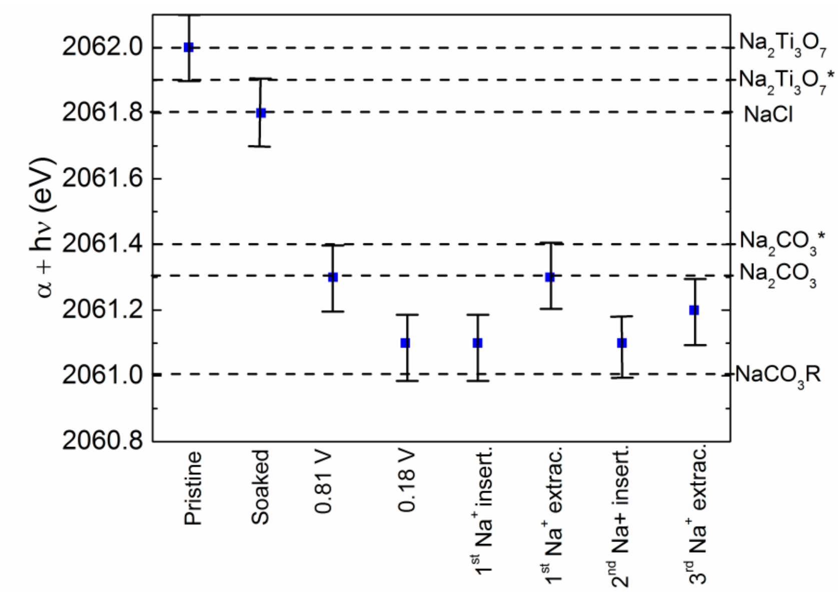

Figure 3.19: Auger parameter (α+hυ) for Na at different states of electrochemical cycling of **NTO-CO-Air** sample. Reference values obtained from [37, 38].

very short IMFP of Na 1*s* photoelectrons (**section A.1.3.5.**). Nevertheless, the NaF presence in the subsurface region has been previously confirmed by F 1*s* XPS and ^{19}F-ssNMR measurements. More information on this regard will be provided later with the depth profiling analysis.

3.3.1.3. Depth profiling by Ar^+ beam

As described in the Experimental section (appendix, **section A.1.3.5.**), the probing depth of laboratory-based XPS technique using Al K_α or Mg K_α X-ray sources is below 10 nm. Any further information from deeper regions can be obtained by performing a depth profiling analysis with an ion beam that gently removes the outermost surface layers. In our case we have used a 1 keV Ar^+ beam in order to get better understanding of the composition at different depths of the SEI layer. The studied charge states are at complete oxidation (1st Na^+ full insertion) and reduction (1st Na^+ full extraction).

Before discussing the results obtained from the depth profiling, it is worth mentioning that ion beam methods can damage or modify the sample surface and also induce the formation of new compounds. Therefore, long ion sputtering processes are not recommended and not more than 10 nm depth profiles are studied observing an overall of 20 nm of depth.

In **Figure 3.20**, the C 1*s*, F 1*s*, O 1*s* and Cl 2*p* photoelectron lines are collected at different depths at the end of the 1st Na^+ full insertion. The C 1*s* spectra show that after removing 1 nm (11 nm of probing depth) the graphite-like signal starts appearing while the $NaCO_3R$ and PEO disappear and after 5 nm (15 nm of probing depth) the graphite-like signal is almost fully developed. From the O 1*s* spectra, a similar behaviour can be observed since $NaCO_3R$, PEO and the chemisorbed oxygen layer disappears after etching 1 nm of the surface and the peak corresponding to $Na_2Ti_3O_7$ (~ 531 eV) emerges after 5 nm. Moreover, according to the O 1*s* and Cl 2*p* spectra, the residual $NaClO_4$ is also removed from the surface, while Na_2CO_3 and NaCl concentration increases on the subsurface as well as the NaF (see F 1*s* spectra).

Analyzing the C 1*s* and O 1*s* photoemission lines in **Figure 3.20**, it can be concluded that the initial estimation of SEI layer thickness (5 nm) is correct. In fact, after removing 5 nm of the electrode surface, the graphitic (284.4 eV) and $Na_2Ti_3O_7$ (531 eV) signals are recovered as the SEI layer is removed.

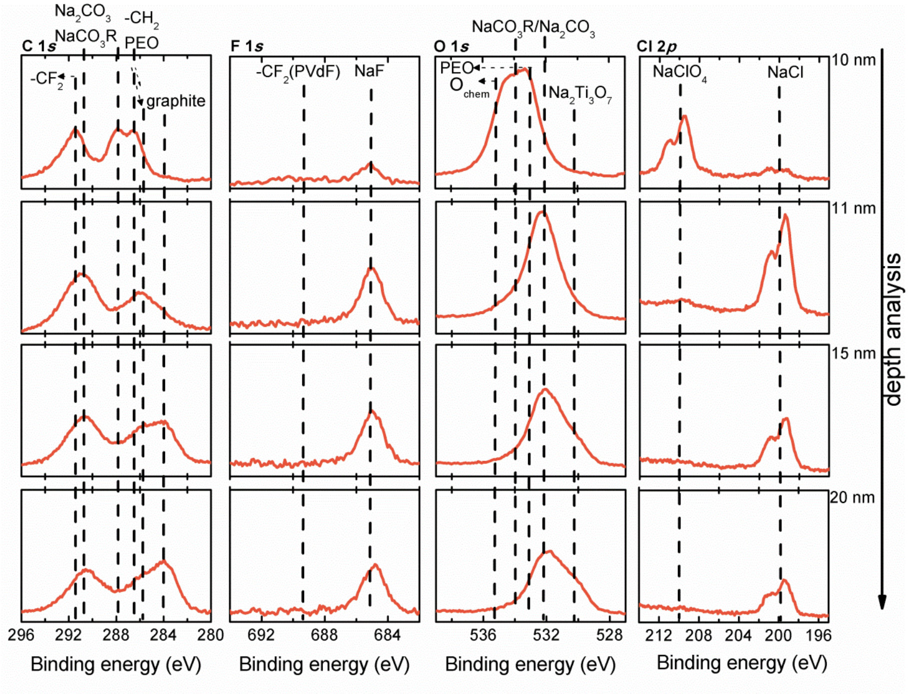

Figure 3.20: XPS spectra of C 1*s*, F 1*s*, O 1*s* and Cl 2*p* at different depth of **NTO-CO-Air** sample at 1st Na^+ insertion state. The 10 nm depth corresponds to the pristine surface prior to ion etching, while 11 nm, 15 nm and 20 nm spectra indicate the maximum probing depth after removing 1 nm, 5 nm and 10 nm of the surface by Ar^+ etching.

The analysis at different depths of C 1*s*, F 1*s*, O 1*s* and Cl 2*p* spectra after the 1st Na^+ full extraction are gathered in **Figure 3.21**. The composition of the SEI layer on the surface after one cycle is similar to the one obtained for the 1st Na^+ insertion state: $NaCO_3R$, Na_2CO_3, PEO, chemisorbed oxygen and residual $NaClO_4$. But in this case, the $–CF_2$ component in the F 1*s* peak of the PVdF binder appears again after 1 nm of etching due to the thinning of the SEI layer. After removing 1 nm of the SEI layer (totally observing down to 11 nm), $NaCO_3R$, PEO and chemisorbed oxygen disappears and NaF, NaCl and Na_2CO_3 become the main compounds. Moreover, in agreement with the early detection of the PVdF component in the F 1*s* peak, the graphitic signal that corresponds to the conductive additive appears after removing only 1 nm of sample surface, which would confirm the thinning of the SEI layer after one full cycle.

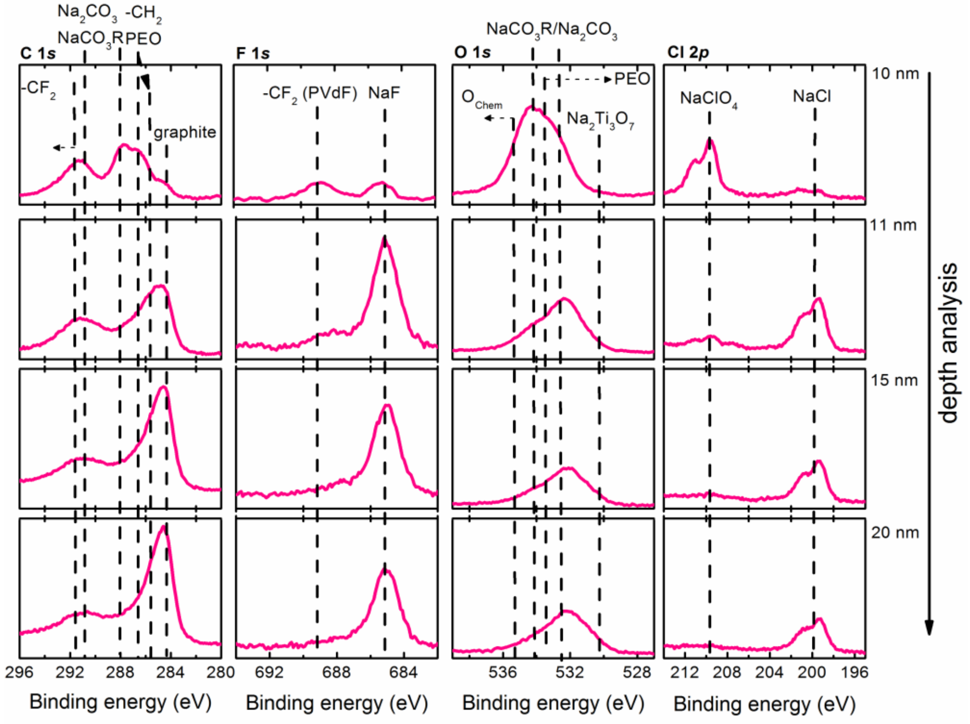

Figure 3.21: XPS spectra of C 1*s*, F 1*s*, O 1*s* and Cl 2*p* at different depth of **NTO-CO-Air** sample at 1st Na^+ extraction state. The 10 nm depth corresponds to the pristine surface prior to ion etching, while 11 nm, 15 nm and 20 nm spectra indicate the maximum probing depth after removing 1 nm, 5 nm and 10 nm of the surface by Ar^+ etching.

As a summary a schematic drawing of the SEI layer is shown in **Figure 3.22** which corresponds to the full 1st Na^+ insertion and extraction states taking into account the data obtained by conventional XPS, ^{19}F-ssNMR measurement, Auger parameter determination and depth profiling.

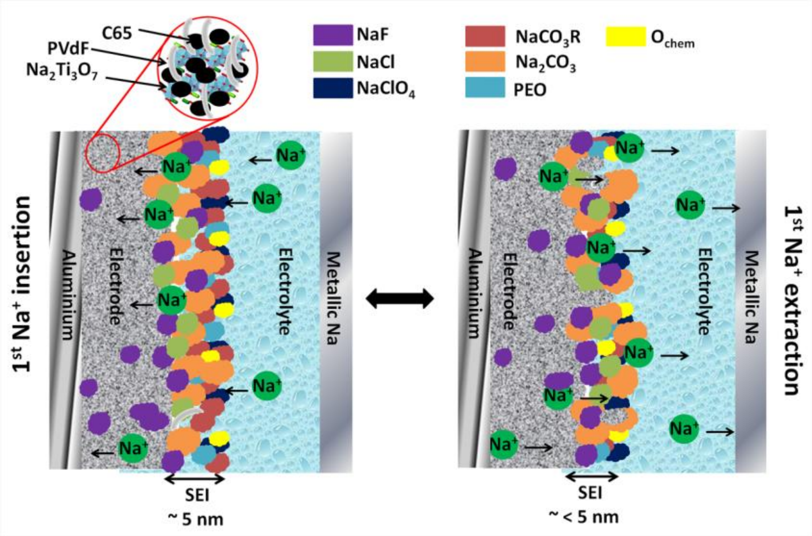

Figure 3.22: Schematic picture of the SEI layer at (left) 1st Na^+ insertion (right) 1st Na^+ extraction of **NTO-CO-Air** sample.

The SEI layer is formed a thickness around ~ 5 nm. On the bulk region of the $Na_2Ti_3O_7$ particles, NaF is spontaneously formed during the electrode preparation due to the PVdF dehydrofluorination reaction. Once the electrode is in contact with the electrolyte NaF layer grows up and the $NaClO_4$ salt decomposes spontaneously in NaCl without applying any current. Once the Na^+ insertion starts, the NaF and NaCl keep growing up and at further lower voltage the EC reduction in Na_2CO_3 covers the already formed inorganic layer of NaCl, NaF. At full Na^+ insertion state, a thin layer of 1 nm of chemisorbed oxygen, $NaCO_3R$ and PEO covers the inorganic underlying layer while at full Na^+ extraction state this outmost layer is partially dissolved in the electrolyte and/or cracked showing an unstable SEI layer. This instability might be one of the factors of the poor capacity retention that shows this **NTO-CO-Air** sample.

3.3.2. NTO-OH-Ar-C sample in a half-cell

Analogously to the XPS study carried out for **NTO-CO-Air**, the SEI layer of **NTO-OH-Ar-C** has been also investigated by XPS. In this case, considering the limitations of the depth profiling studies using ion beam techniques, the depth profiling was performed using high energy XPS (HAXPES). The difference with the **NTO-CO-Air** sample is that this time the SEI layer formation and evolution is investigated directly at OCV, 1st Na^+ insertion, 1st Na^+ extraction, 2nd Na^+ insertion and 3rd Na^+ extraction as highlighted in **Figure 3.23**.

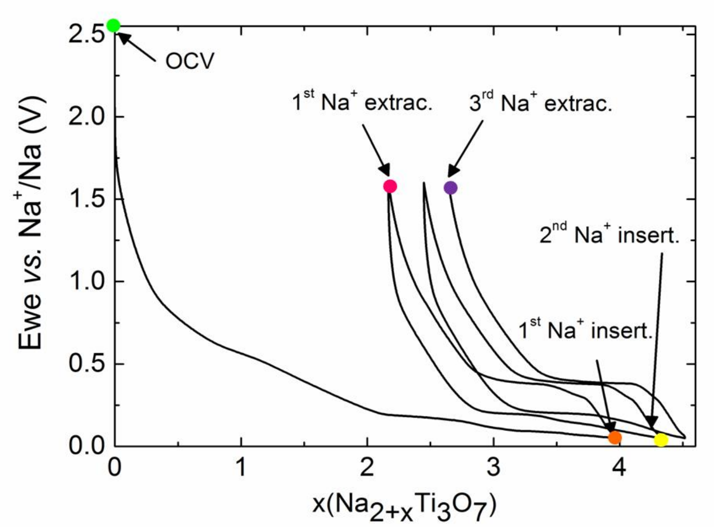

Figure 3.23: Galvanostatic cycling profile of **NTO-OH-Ar-C** during the first cycles. The XPS measurements are performed in the highlighted points of the curve. Moreover, pristine and soaked electrodes are measured.

The surface layer formed on this electrode has a similar nature to the one formed in the **NTO-CO-Air** electrode, therefore surface charging effects are expected during the photoemission experiments. For this reason, the combined approach of conventional XPS, Auger parameter and HAXPES experiments is needed.

3.3.2.1. Conventional XPS study

The C 1*s* photoemission line (**Figure 3.24**) will be used to follow the evolution of the electrolyte components (solvents: EC, PC and salt: $NaClO_4$) and binder (PVdF), these data will help us to understand how the SEI layer is formed and the stability of it.

As with the **NTO-CO-Air** sample (**section 3.3.1.1.**), the assignments of the C 1*s* components have been done on the basis of previous XPS studies [14]. The main component of the C 1*s* peak in the pristine and soaked electrodes is assigned to graphitic-like compounds at 284.4 eV which in this case corresponds to the conductive additive (C65) and the C-coating. The asymmetry of the peak is in agreement with the behaviour already observed in **NTO-CO-Air** samples [15]. The other binding energies observed at 286.4 eV and 290.9 eV correspond $-CH_2$ and $-CF_2$ group of the PVdF [18], respectively. The last PVdF component is overlapped with the Π−Π* transition from graphitic-like compounds [17].

Once the **NTO-OH-Ar-C** half-cell is assembled and the electrolyte is in contact with the electrode, the surface layer starts forming. In fact, the graphite-like signal decreases and the peak at 288 eV appears which corresponds to $NaCO_3R$ [20, 21]. Although $NaCO_3R$ should show another component at 291-291.5 eV, this is difficult to evaluate since it is overlapped with Na_2CO_3 and $-CF_2$ (PVdF) components [18, 20, 21]. The investigations with electrodes at OCV demonstrate that the existence of an electrochemical force drives the SEI layer formation because when the electrolyte is in contact with the working electrode without counter electrode (soaked sample), the surface layer formation does not start.

At the end of the 1st Na^+ insertion, the peak at 284.4 eV, which corresponds to graphitic-like signal, is completely extinguished. This means that the SEI layer totally covers the electrode surface with a thickness ~ 5 nm. Analogously to the behaviour of **NTO-CO-Air** sample, upon Na^+ extraction the graphitic-like signal appears again, indicating a thinning or cracking of the SEI layer. Moreover, the cyclic behaviour (2nd and 3rd cycle) observed for the **NTO-CO-Air** is also confirmed for the **NTO-OH-Ar-C** sample, as it can be inferred from the evolution of the shoulder assigned to graphitic-like carbon. Hence the SEI layer is not stable at least during the first three cycles, seriously affecting the capacity fading of this material [2, 3].

While the graphitic-like component disappears during Na^+ insertion, the contributions of inorganic compounds from the reduction of the electrolyte become more prominent: NaOR at 286.1 − 286.5 eV, Na_2CO_3 and $NaCO_3R$ at 290 - 291 and 288 eV and organic PEO polymer at 286.5 eV [20, 21].

Concerning the evolution of PVdF binder, in this case apparently the $–CF_2$ signal does not shift to higher binding energy as in **NTO-CO-Air** [23]. However, the OCV and Na^+ extraction electrodes show an asymmetry at towards high binding energies which corresponds to the shfit of this $–CF_2$ signal. For full Na^+ insertion electrode, the peak is more symmetric probably due to the contribution of the PVdF signal being covered by the formed SEI layer. This will be confirmed by the analysis of F 1*s* spectra.

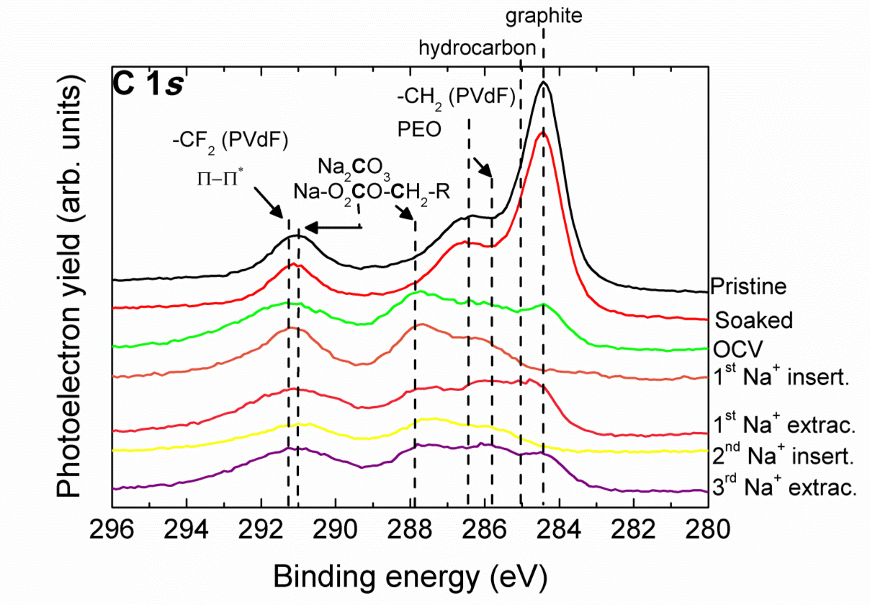

Figure 3.24: C 1*s* XPS photoelectron spectra of **NTO-OH-Ar-C** electrodes before cycling (pristine and soaked in electrolyte) and at different points of the Na^+ insertion/extraction curve as indicated in **Figure 3.23.**

In the F 1*s* photoemission line (**Figure 3.25**), the pristine and soaked electrodes show a main contribution at 688.2 eV corresponding to -CF_2 groups from PVdF [18]. This component disappears at complete reduction state and partially reappears after every oxidation step (Na^+ extraction process). This behaviour would agree with a partial dissolution of the SEI layer observed in the C 1*s* spectra. Moreover, it is in agreement with the lack of the asymmetry of –CF_2 signal in the C1 s peak of full Na^+ inserted electrodes. When the –CF_2 component is detected during cycling the high energy shift is observed, confirming the influence of surface charging and Na-doping of PVdF. Furthermore, a peak corresponding to NaF appears at 685 eV [24, 25] as a result of a dehydrofluorination reaction of the PVdF [26] already confirmed by ^{19}F-ssNMR (**Figure 3.15**). The soaked **NTO-OH-Ar-C** electrode does not show traces of NaF, which means that the C-coating is preventing the reaction of HF with the $Na_2Ti_3O_7$. Once the cells are assembled electrochemical cycling starts, the HF can interact with the Na^+ ions leading to the formation of NaF.

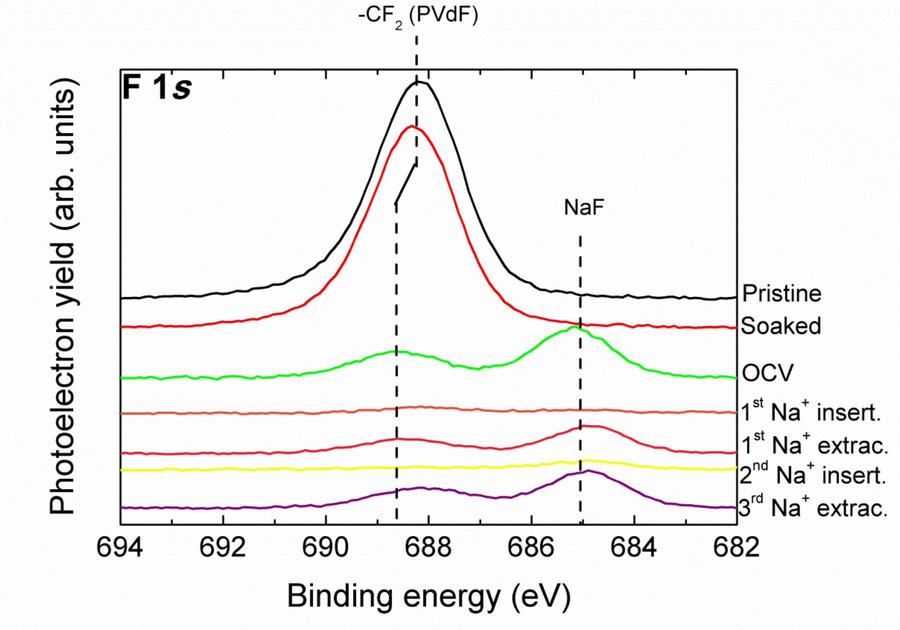

Figure 3.25: F 1*s* XPS photoelectron spectra of **NTO-OH-Ar-C** electrodes before cycling (pristine and soaked in electrolyte) and at different points of the Na^+ insertion/extraction curve as indicated in **Figure 3.23.**

Regarding the O 1*s* photoemission line, (**Figure 3.26**) the $Na_2Ti_3O_7$ at ~ 531 eV cannot be detected due to the C-coating which has a thickness around 6.0 nm. Instead, a residual amount of CO_3^{2-} appears at 532 - 533 eV on the pristine electrode as a result of interaction with moisture. For the soaked sample, in addition to the Na_2CO_3, $NaClO_4$ traces are detected. As the half-cell is assembled (OCV), a thick layer is formed covering the electrode surface, mainly composed of Na_2CO_3 (~ 532.3 eV), $NaCO_3R$ (~ 534 eV and ~ 532.5 eV) and PEO (~ 533 eV) [20]. The carbonates and semi-carbonates are a result of the electrolyte reduction while the PEO is formed by EC polymerization. The PEO contribution is intensified upon Na^+ insertion and attenuated upon extraction as observed in the C 1*s* spectra, however Na_2CO_3 and $NaCO_3R$ signals appear at very similar binding energy and it is complicated to establish which components are more stable. Some traces of $NaClO_4$ appear also at 533.8 eV, as well as chemisorbed oxygen [14] as a result of the ClO_4^- anion dissociation, but this will need further confirmation from Cl 2*p* photoelectron line data [34, 35]. Please note that the 1st Na^+ insertion state electrode shows a signal at ~ 529.4 eV assigned to MoO_3 from the sample holder which sometimes is detected due to a slight deviation of the analyser active [37].

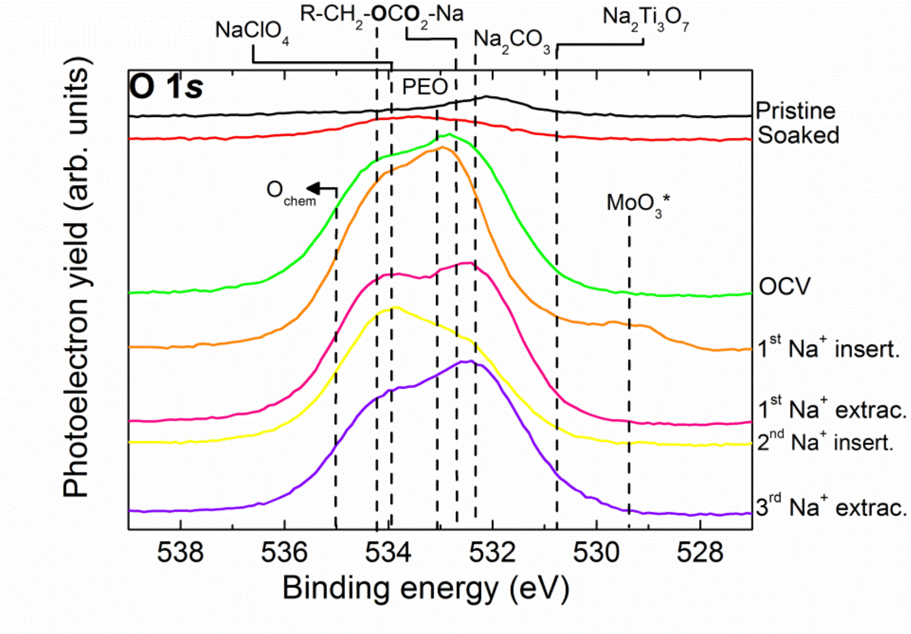

Figure 3.26: O 1*s* XPS photoelectron spectra of **NTO-OH-Ar-C** electrodes before cycling (pristine and soaked in electrolyte) and at different points of the Na^+ insertion/extraction curve as indicated in **Figure 3.23.**

As is explained in the **3.3.1.1. section**, the X-ray source can induce a photodecomposition of $NaClO_4$ in $NaClO_3$ and NaCl. However, although part of NaCl can be originated from this photodecomposition, the used X-ray beam conditions have avoided this process. Therefore, the majority of NaCl detected will be originated by $NaClO_4$ reduction due to electrochemical interactions. Hence, Cl 2*p* spectra (**Figure 3.27**) reveal that the NaCl is observed once the electrochemical cycling starts: the soaked electrode does not shown any signal at 200 eV (NaCl) in contrast to the OCV electrode. Moreover, in the Na^+ insertion and extraction electrodes show $NaClO_4$ traces from the electrode which are not removed during the electrode washing as in **NTO-CO-Air**. Hence the employed PC solvent to wash the electrode before the XPS measurement does not remove the $NaClO_4$ placed on the surface of the electrodes.

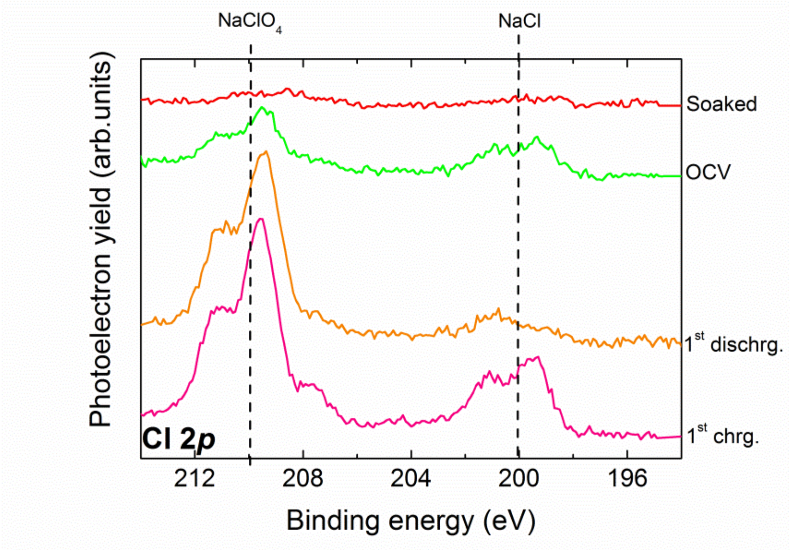

Figure 3.27: Cl 2*p* XPS photoelectron spectra of **NTO-OH-Ar-C** electrodes soaked in electrolyte, at OCV and at the 1st Na^+ insertion and extraction.

3.3.2.2. Auger parameter determination

The Na Auger parameter is determined also for **NTO-OH-Ar-C** electrodes following **Eq 3.1**. The fitting of the experimental data (Na 1s and $NaKL_{23}L_{23}$ peaks) performed with CasaXPS software [36] is collected in **Figure3.28** and the values in **Table A.6**. (appendix).

The Auger parameter (**Figure 3.29**) of the pristine electrode reveals the presence of Na_2CO_3 (2061.3 eV) [37, 38], in agreement with the XPS results obtained from the O 1*s* spectrum. Since the $Na_2Ti_3O_7$ is covered by a C-coating it is not possible to detect the $Na_2Ti_3O_7$. Once the electrode is in contact with electrolyte and upon electrochemical cycling the formation of $NaCO_3R$ covers the electrode surface [37, 38] which is practically constant during electrochemical cycling.

In this situation, given the low probing depth of the Na Auger parameter, NaF and NaCl are not found because the formation of a surface layer covers any trace of these two compounds. However, its presence has been previously confirmed by XPS data from F 1*s* (**Figure 3.25**) and Cl 2*p* (**Figure 3.27**) peaks. HAXPES data will provide more information on this regard.

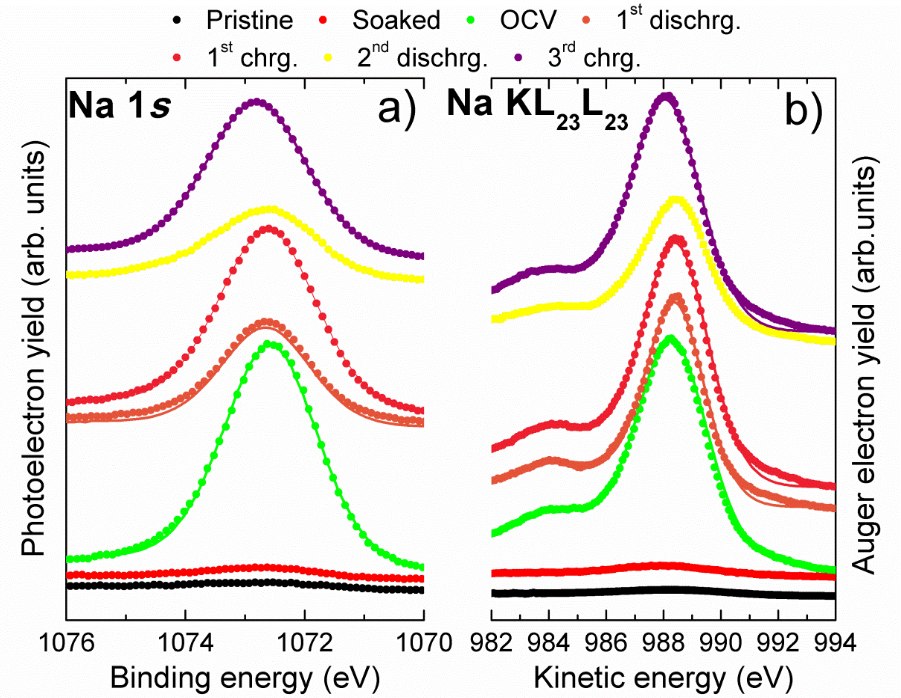

Figure 3.28: a) Na 1*s* photoelectron line and **b)** $NaKL_{23}L_{23}$ Auger transition of **NTO-OH-Ar-C**. Points correspond to the experimental data and the solid lines to the fits.

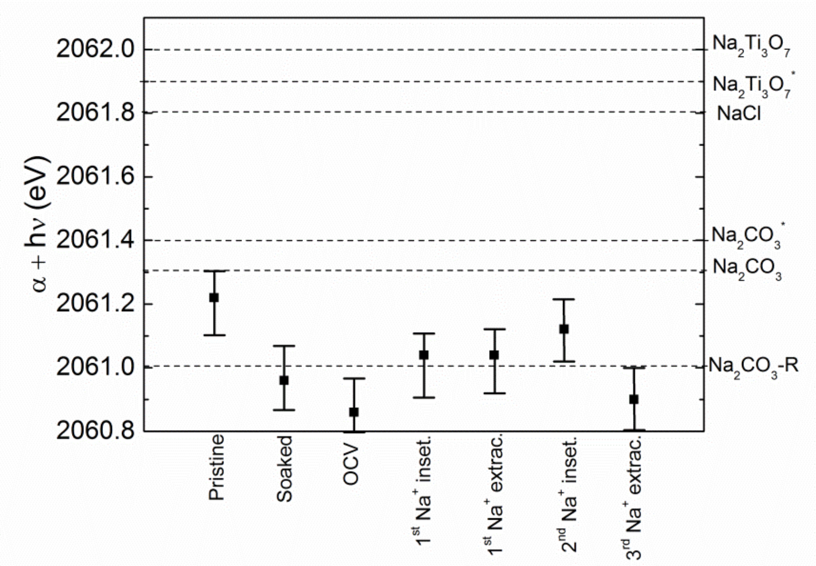

Figure 3.29: Auger parameter (α+hν) for Na at different states of electrochemical cycling of **NTO-OH-Ar-C** sample. Reference values obtained from [37, 38].

3.3.2.3 Depth profiling by HAXPES

The composition of the surface layer (around the first 10 nm) can be determined combining XPS and Auger parameter study. However, for a better understanding of the SEI layer higher photon energies are used which provide more depth penetration avoiding the problems of ion beam induced damage. The C 1*s*, F 1*s* and O 1*s* core level HAXPES spectra are analysed for the pristine, 1st Na^+ insertion and extraction electrodes, as has been carried out to **NTO-CO-Air** sample by Ar^+ etching, at different photon energies: 3000 eV (20 nm of depth), 5000 eV (30 nm) and 7000 eV (40 nm) (HAXPES). These data can be compared with conventional XPS data collected using a 1253.6 eV source. In general, the C 1*s*, F 1*s* and O 1*s* HAXPES spectra at different photon energies are similar, the main difference is found between the first 10 nm and the subsurface region, hence the SEI layer thickness is <10 nm.

Figure 3.30 shows the spectra of the C 1*s*, F 1*s* and O 1*s* for the pristine electrode. Conventional XPS data ($h\nu$ = 1253.6 eV) show that C-coating fully covers the $Na_2Ti_3O_7$ active material and only PVdF (688 eV in the F 1*s* peak), Na_2CO_3 (290 - 291 eV in the C 1*s* peak) and traces of C-O and C-H based compounds can be detected. Increasing the photon energy, the collected photoelectrons show the underlying $Na_2Ti_3O_7$ active material (component at 531 eV on the O 1*s* peak) at the same time the signal from Na_2CO_3 and other compounds is drastically reduced. Meanwhile, the PVdF concentration is kept constant. Interestingly NaF is not observed in the first 40 nm and this suggests that the C-coating protect the PVdF from dehydrofluorinated reaction in agreement with conventional XPS F 1*s* data (**Figure 3.25**).

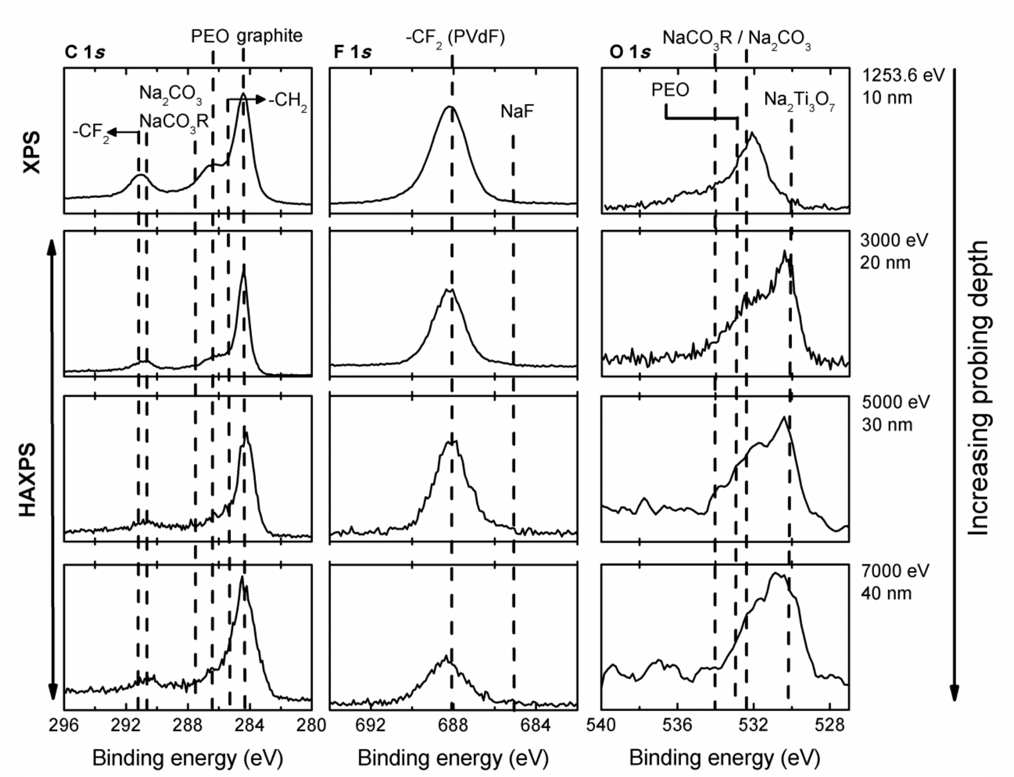

Figure 3.30: C 1*s*, F 1*s* and O 1*s* region of XPS (1253.6 eV) and HAXPES (at 3000 eV, 5000 eV and 7000 eV) of the pristine electrode of **NTO-OH-Ar-C** sample.

Figure 3.31 shows the spectra of the C 1*s*, F 1*s* and O 1*s* for the 1st Na^+ insertion electrode. The first 10 nm shows that the SEI layer fully covers the $Na_2Ti_3O_7$ active material where the main component of the surface with <10 nm are: Na_2CO_3, $NaCO_3R$, PEO and chemisorbed oxygen signal in C 1*s* and O 1*s* spectra. After increasing the photon energy, (20 nm of depth) the signals of those compounds remain, in contrast with the **NTO-CO-Air** electrode, might be due to a thicker SEI layer or more heterogeneously distributed. However, the graphitic and $Na_2Ti_3O_7$ signal on C 1*s* and O 1*s* spectra, cleary appear suggesting that the SEI layer is >10 nm but <20 nm. Additionally, a very large NaF peak appears at 685 eV while the small PVdF signal is observed at 688 eV in the F 1*s* spectrum.

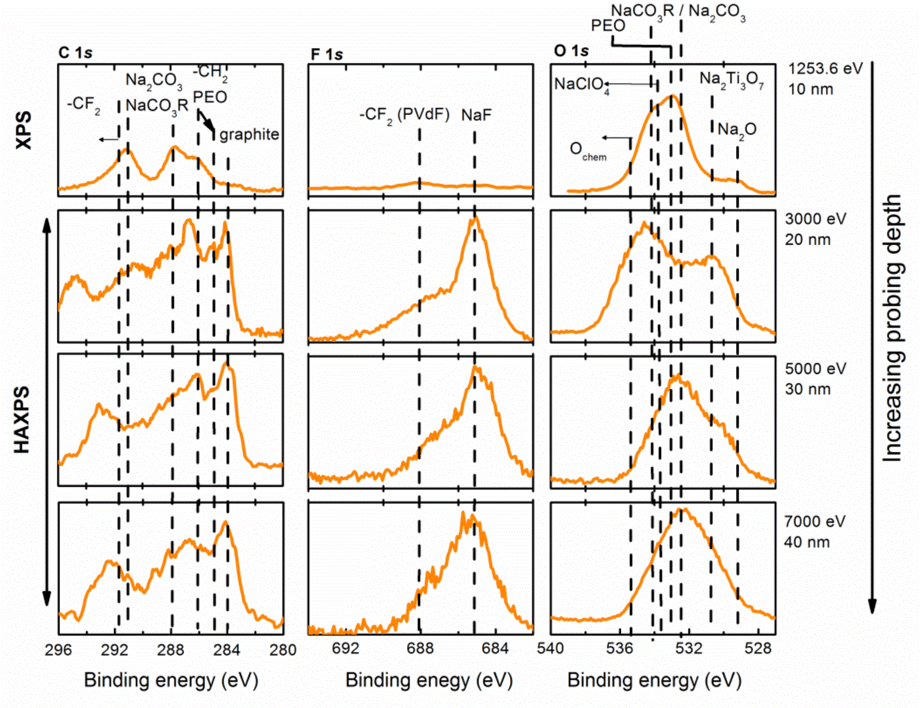

Figure 3.31: C 1*s*, F 1*s* and O 1*s* region of XPS (1253.6 eV) and HAXPES (at 3000 eV, 5000 eV and 7000 eV) of the 1st Na^+ insertion electrode of **NTO-OH-Ar-C** sample.

In **Figure 3.32** C 1*s*, F 1*s* and O 1*s* spectra are gathered at different depths of 1st Na^+ extraction state electrode. The 1st Na^+ extraction electrode shows a similar behaviour if compared with the Na^+ insertion electrode. The main difference is that at 20 nm of depth, the main component of the first 10 nm (Na_2CO_3, $NaCO_3R$, PEO and chemisorbed oxygen) almost disappear. Considering that at the same time the graphitic-like of C 1*s* and $Na_2Ti_3O_7$ of O 1*s* are detected, it can be concluded that the SEI layer at the extraction state is thinner than in the insertion. Finally, as regards the F 1*s*, while in the outmost surface the NaF is not observed, at higher depths a large amount of it can be found.

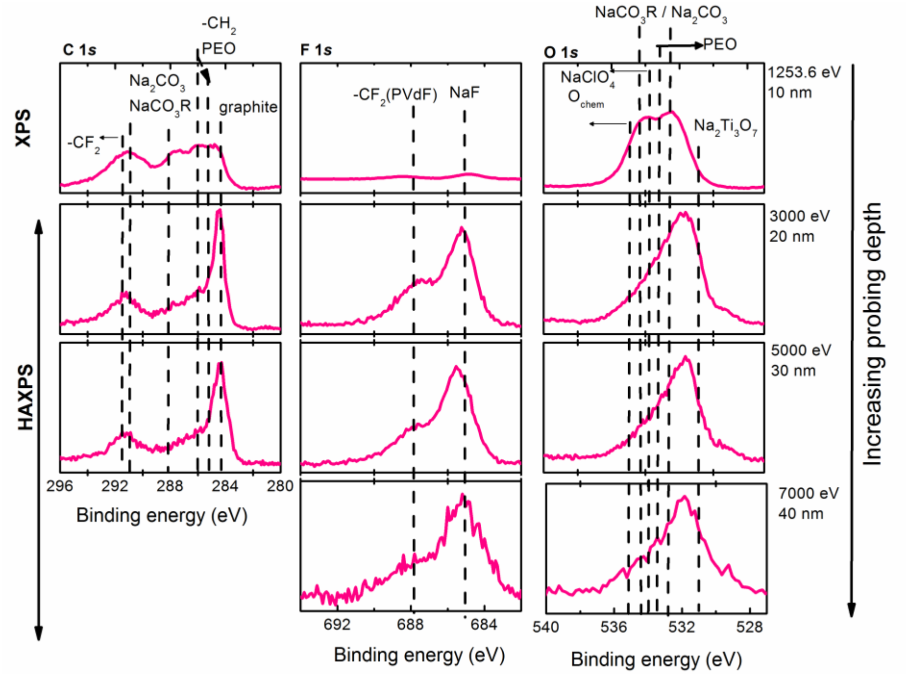

Figure 3.32: C 1*s*, F 1*s* and O 1*s* region of XPS (1253.6 eV) and HAXPES (at 3000 eV, 5000 eV and 7000 eV) of the 1st Na^+ extraction electrode of **NTO-OH-Ar-C** sample.

In conclusion taking into account the analysis of conventional XPS, Auger parameter and HAXPES spectra schematic picture of the SEI layer formed on **NTO-OH-Ar-C** is illustrated in **Figure 3.33**.

The composition of the SEI layer formed in NTO-OH-Ar-C is similar to the SEI layer of NTO-CO-Air, the main difference lies in the presence of Na_2CO_3 already in the pristine electrode due to the interaction with moisture and the lack of NaF in the

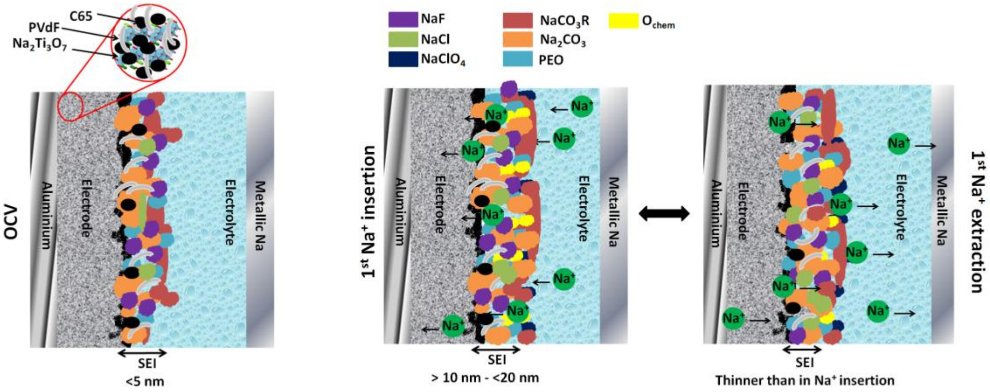

Figure 3.33: Schematic picture of the SEI layer at OCV (left), 1st Na^+ insertion (middle) 1st Na^+ extraction (right) of **NTO-OH-Ar-C** sample.

pristine and soaked sample since the protection provided by the C-coating against HF from the PVdF dehydrofluorination reaction. Moreover, the SEI layer of **NTO-OH-Ar-C** sample compared to the **NTO-CO-Air** sample shows higher stability as regards the outermost SEI region and greater thickness (10<x<20 nm) as it has been shown by Auger parameter analysis and HAXPES, respectively. The SEI layer is initially composed by Na_2CO_3 growing on the C-coating. When the cell is assembled the spontaneous decomposition reaction of $NaClO_4$ (electrolyte salt) and PVdF starts, covering partially the Na_2CO_3 layer which keeps growing since at low voltages the solvent of the electrolyte decomposes forming more Na_2CO_3. Finally the outermost layer of $NaCO_3R$, PEO and chemisorbed oxygen is formed. Although upon Na^+ extraction some compounds are partially dissolved the composition of the outward surface is almost the same as in the insertion state electrode, mainly composed by $NaCO_3R$. That better stability might be the reason of a better electrochemical performance.

3.3.3. NTO-OH-Ar-C sample in a full-cell

Recently, the instability in organic electrolyte of metallic Na has been reported [39]. Na/Na cell exhibited larger overpotential due to Na plating than Li/Li cell. Moreover, in the Na/Na CV curve more charge was recovered during the reduction than in oxidation, related with irreversible electrolyte decomposition and/or electrical contact loss between metallic Na and current collector. By EIS experiments were provided that the interfacial resistance ($R_{SEI}+R_{CT}$) increases upon time in Na/Na cell, in contrary to Li/Li which was almost stable. Hence, the SEI layer in Na/Na was continuously growing up and/or had an unstable behaviour. Additionally, when the same experiments were carried out in Hard Carbon (HC)/Na cell similar behaviour was followed as Na/Na. The interface resistance of HC and electrolyte became more resistive upon time.

Thus, the metallic Na can influence the stability and composition of the SEI layer formed on the intercalation material. Therefore, the SEI layer composition and stability of **NTO-OH-Ar-C** has been carried out using as counter another intercalation material, more precisely $NaFePO_4$; in order to observe the differences between the formed SEI layer on **NTO-OH-Ar-C**, when is testes in a half-cell and in a full-cell (**NTO-OH-Ar-C-FC**). As it has been performed for **NTO-OH-Ar-C** sample, the study of the SEI layer of **NTO-OH-Ar-C-FC** has been carried out by investigating the C 1*s*, O 1*s*, F 1s, Cl 2*p*, Na 1*s* photoelectron spectra and Na $KL_{23}L_{23}$ Auger peaks of the **NTO-OH-Ar-C-FC** and $NaFePO_4$ in OCV, 1st Na^+ insertion and 1st Na^+ extraction electrodes (**Figure 3.34**).

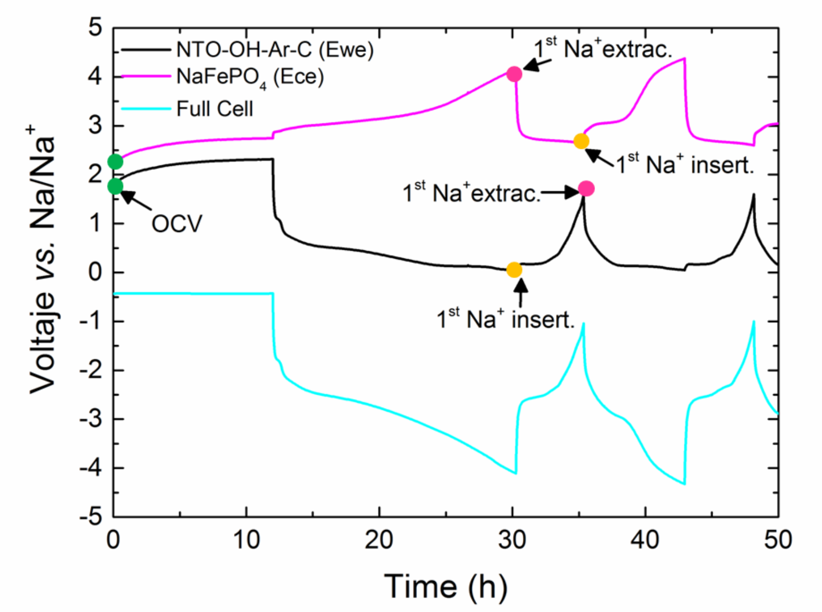

Figure 3.34: Galvanostatic cycling profile of **NTO-OH-Ar-C-FC** (black) as working electrode and $NaFePO_4$ (magenta) as counter electrode during the first cycles. The XPS measurements are performed in the highlighted points of the curve.

3.3.3.1. Conventional XPS

The main component of the C 1*s* peak in the OCV electrode of **NTO-OH-Ar-C-FC** (**Figure 3.35**) is shown at 284.4 eV and corresponds to graphitic-like compound [16], in contrary to observed in **NTO-OH-Ar-C** sample, since the graphitic peak is almost covered due to the SEI layer formation (**Figure 3.24**) from electrolyte salt decomposition. Therefore, when the cell is assembled in presence of metallic Na the electrolyte decomposition starts forming the SEI layer which almost covered complete the electrode. Meanwhile when metallic Na is not using it, the decomposition of the electrolyte at OCV is almost negligible.

At the 1st Na^+ insertion, however, the graphite peak at 284.4 eV is reduced, due to the SEI layer formation. Nevertheless, the peak is not complete covered as in **NTO-OH-Ar-C** sample. Hence the thickness of the SEI layer formed in **NTO-OH-Ar-C-FC** [18]. is thinner (<5 nm) than in **NTO-OH-Ar-C** and/or not covers complete the Super C65 and C-coating. As already it has been observed in **NTO-OH-Ar-C** sample, the SEI layer is partially dissolved and/or cracked since at 1st Na^+ extraction state the graphitic-like signal slightly increases. Therefore, although metallic Na is not employed the SEI layer either is stable.

During the insertion, when SEI layer is forming, the peaks at ~ 286 eV and 290 - 291 eV appear which corresponds to PEO and Na_2CO_3, respectively (notice that the latter peak is overlapped with -CF_2 (PVdF)) [18, 20, 21].

The C 1*s* photoelectron spectra of $NaFePO_4$ show that the thickness of the formed SPI layer is almost negligible. Since the graphite-like signal (284.4 eV) slightly decreases during the cycling. The formed very thin SPI layer is composed mainly by PEO (~ 286 eV) and Na_2CO_3 (290 - 291 eV), as the SEI layer of **NTO-OH-Ar-C-FC**, which during the Na^+ insertion into $NaFePO_4$ (or during Na^+ extraction in $Na_4Ti_3O_7$) are dissolved since the peaks are reduced [18, 20, 21].

The F 1*s* spectra (**Figure 3.36**) confirm the behaviour observed in C 1*s* photoelectron line. The main contribution in OCV electrode of **NTO-OH-Ar-C-FC** corresponds to –CF_2 at 688 eV from PVdF [18], hence the SEI layer is not formed at this state. However this signal decreases during the Na^+ insertion due to the formation of the SEI layer. But is not complete covered as in **NTO-OH-Ar-C** suggesting that the SEI layer is thinner. Meanwhile the –CF_2 peaks is reducing a peak at ~ 685 eV is developing, which is assigned to NaF [24, 25]. The latter signal lightly reappears during the Na^+ extraction in $Na_4Ti_3O_7$ which would be agree with already observe behaviour in C 1*s*, a partial dissolution of the SEI layer.

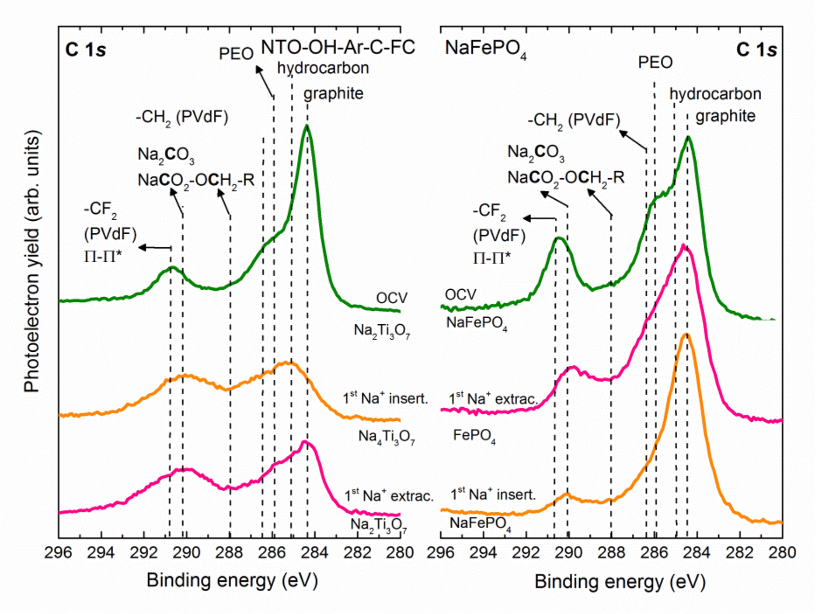

Figure 3.35: C 1*s* XPS photoelectron spectra of **NTO-OH-Ar-C-FC** electrodes at OCV, 1st Na^+ insertion and 1st Na^+ extraction.

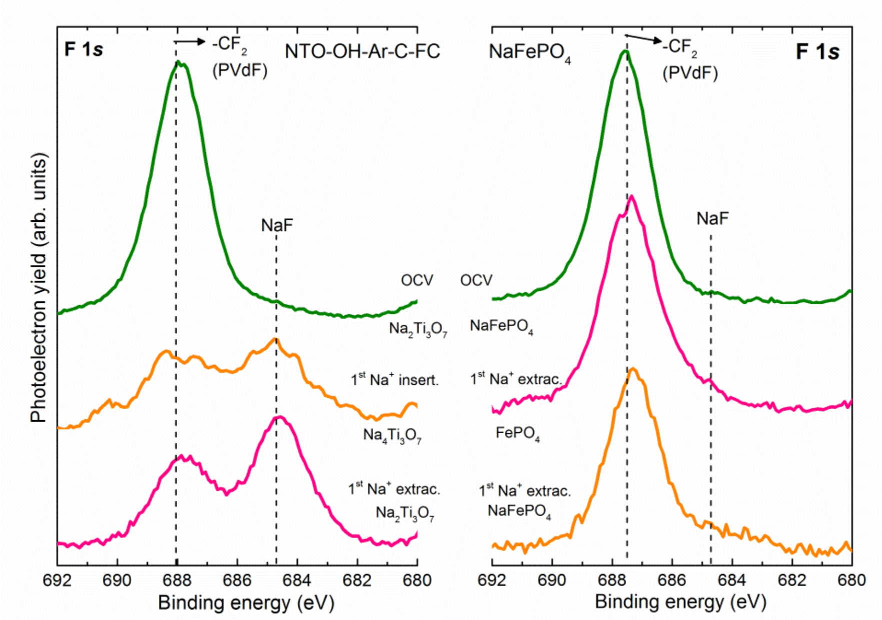

Figure 3.36: F 1*s* XPS photoelectron spectra of **NTO-OH-Ar-C-FC** electrodes at OCV, 1st Na^+ insertion and 1st Na^+ extraction.

As regards the F 1*s* spectra of $NaFePO_4$ the main component is the $-CF_2$ signal of the PVdF (688 eV), which is practically constant during the 1st cycling. Hence the SPI layer is almost stable and very thin, more that the SEI layer formed in **NTO-OH-Ar-C-FC**.

O 1*s* photoelectron spectrum (**Figure 3.37**) of **NTO-OH-Ar-C-FC** electrode at OCV shows a peak at ~ 532 eV from residual Na_2CO_3 due to the interaction with moisture. That signal is more developed during the cycling due to the formation of the SEI layer, mainly formed by Na_2CO_3 [20]. Additionally, the $Na_2Ti_3O_7$ at ~ 531 eV is possible to observe in all oxidation state due to the formation of a thin layer, which slightly increases during the extraction. Furthermore, some $NaCO_3R$ (~ 534 eV and ~ 532.5 eV) and PEO (~ 533 eV) species can be observed [20]. However, as already has been mentioned is difficult to establish which components correspond to that signals due to the similarity in the binding energy.

In the meanwhile the surface of $NaFePO_4$ electrode at OCV shows a peak of PO_4^{3-} group at ~ 531 eV from the active material and at lower contribution of Na_2CO_3 (532 eV) [20, 30]. During the cycling the peak corresponding to Na_2CO_3 (532 eV) increases while the peak of PO_4^{3-} (~ 531 eV) is lightly suppressed; suggesting the formation a SPI layer with a few nm of thickness.

Finally, Cl 2*p* spectra (**Figure 3.38**) show the $NaClO_4$ reduction from NaCl. In contrary to observe in **NTO-OH-Ar-C** sample, the OCV electrode of **NTO-OH-Ar-C-FC** does not exhibit NaCl. During the Na^+ insertion into $Na_2Ti_3O_7$ the NaCl is formed in the counter electrode (SPI layer, $NaFePO_4$) while during the Na^+ extraction is found in the SEI layer of **NTO-OH-Ar-C-FC**.

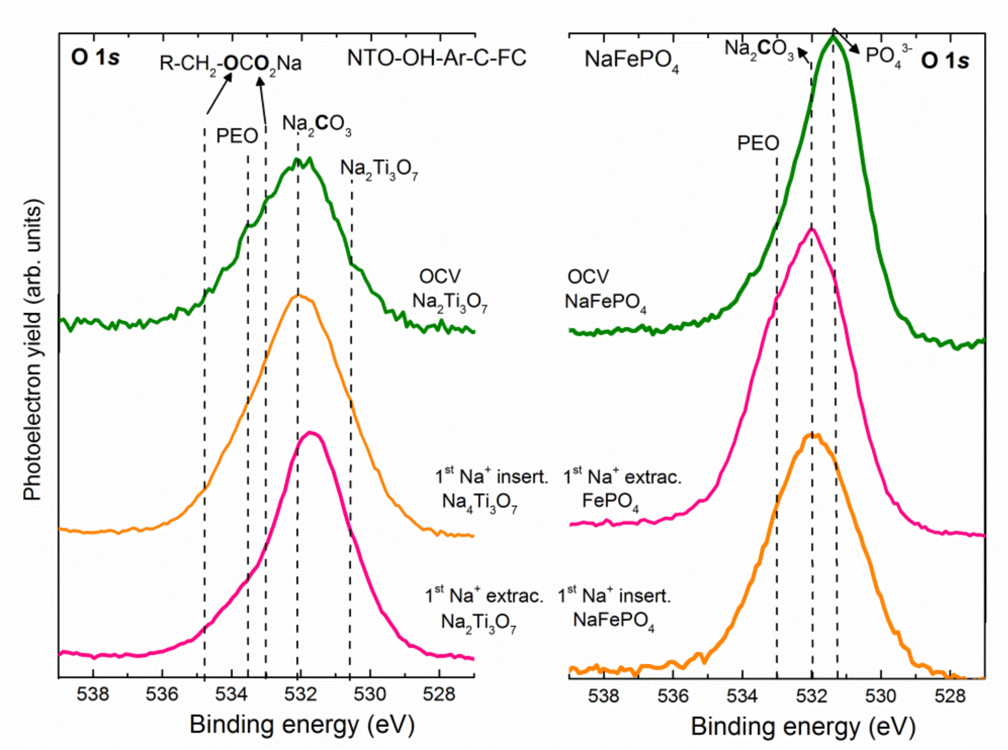

Figure 3.37: O 1*s* XPS photoelectron spectra of **NTO-OH-Ar-C-FC** electrodes at OCV, 1st Na^+ insertion and 1st Na^+ extraction.

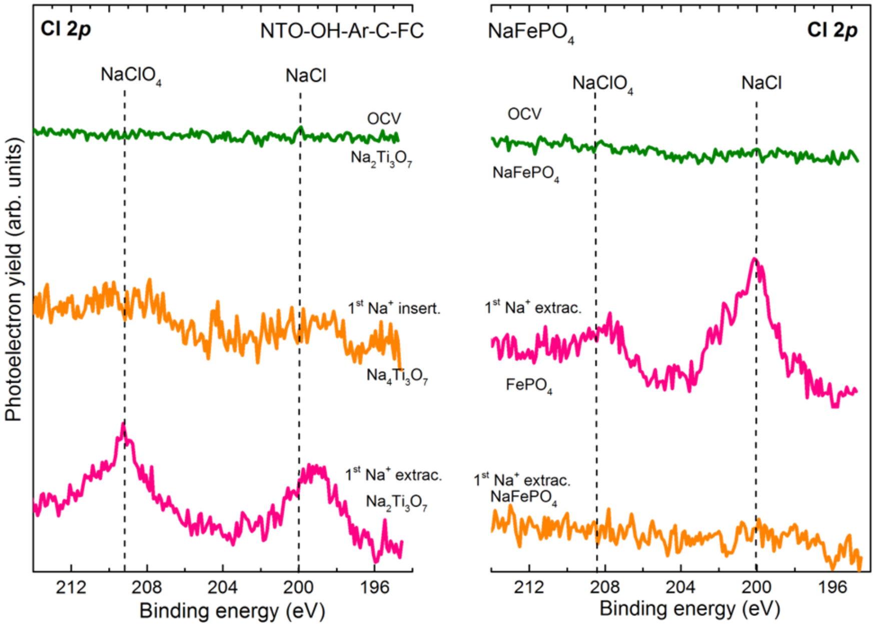

Figure 3.38: Cl 2*p* XPS photoelectron spectra of NTO-OH-Ar-C-FC electrodes at OCV, 1st Na^+ insertion and 1st Na^+ extraction.

3.3.3.2. Auger parameter determination

The Na Auger parameter is determined for NTO-OH-Ar-C-FC as it has been carried out for NTO-CO-Air and **NTO-OH-Ar-C** samples following the **Eq 3.1**. The data of Na 1s and $NaKL_{23}L_{23}$ peaks have been fitted with CasaXPS software [36] and are gathered in **Figure 3.38** and the values in **Table A.7**.

The Auger parameter of OCV, 1st Na^+ insertion and extraction electrodes (**Figure 3.39**) reveals that in these three charge states the main component of the outmost is Na_2CO_3 (2061 eV) [37, 38] in agreement with the O 1*s* photoelectron spectra (**Figure 3.37**). As occurs with **NTO-OH-Ar-C** sample, the outmost composition of the NTO-OH-Ar-C-FC sample is almost constant during the electrochemical cycling. However, in this case the main component is not $NaCO_3R$ but Na_2CO_3.

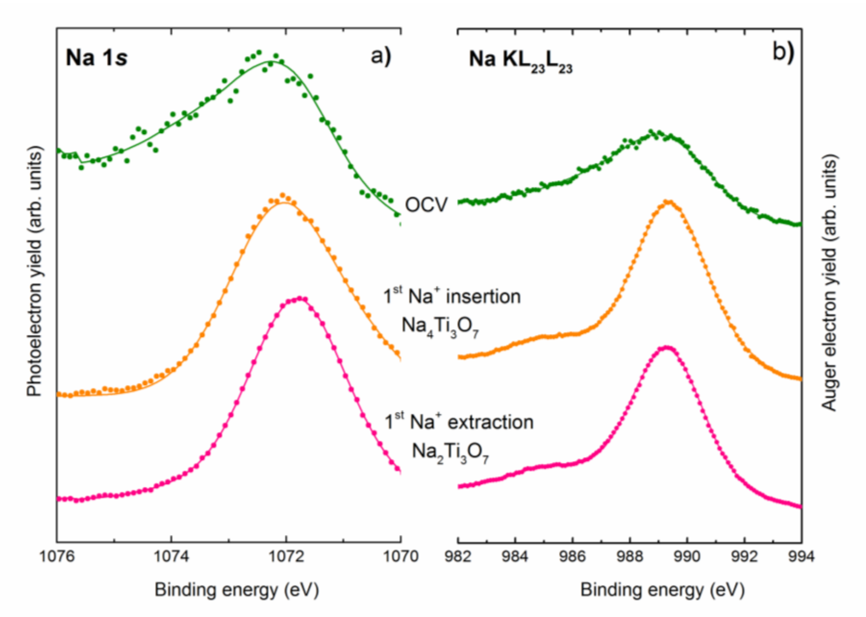

Figure 3.38: a) Na 1*s* photoelectron line and **b)** $NaKL_{23}L_{23}$ Auger transition of **NTO-OH-Ar-C-FC**. Points correspond to the experimental data and the solid lines to the fits.

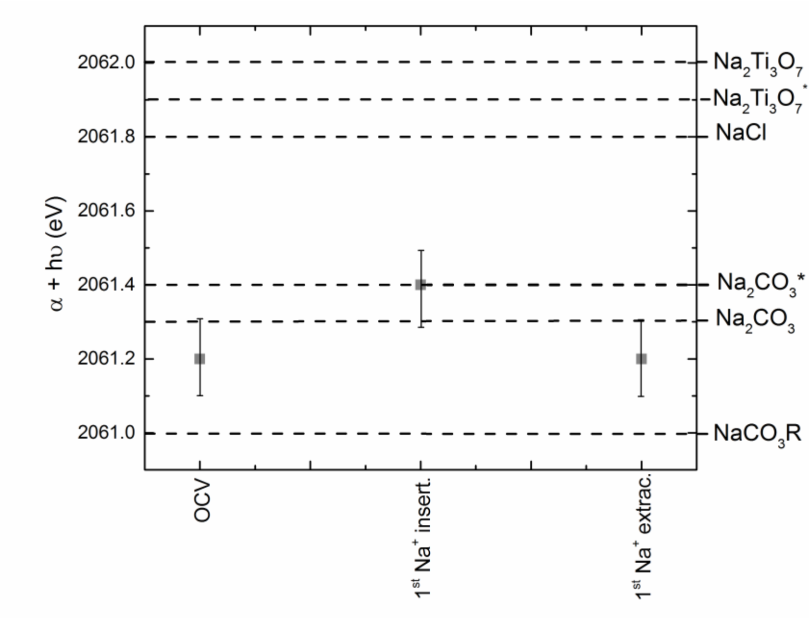

Figure 3.39: Auger parameter (α+hν) for Na at different states of electrochemical cycling of **NTO-OH-Ar-C-FC** sample. Reference values obtained from [37, 38].

As summary, the schematic picture of the SEI layer formed on **NTO-OH-Ar-C-FC** sample at OCV, 1st Na^+ insertion and extraction charge states is gathered in **Figure 3.40**, considering the analysis of conventional XPS and Auger parameter.

The main differences between the SEI layer formed in **NTO-OH-Ar-C** are that, the behaviour at OCV state, the outmost composition and the thickness. Firstly, the layer at OCV electrode does not show any NaF and NaCl from PVdF dehydrofluorination and $NaClO_4$ salt decomposition, respectively. Once the cell is assembled the spontaneous reactions do not occur in contrast to show the **NTO-OH-Ar-C** sample. The NaF formation takes place once the electrochemical cycling starts, while NaCl is only observed during the Na^+ extraction. Moreover, the outward is mainly composed by Na_2CO_3 in the three charge states showing a stable outward composition. In the 1st Na^+ insertion state a thin layer of NaF, $NaCO_3R$ and PEO is covered by Na_2CO_3. Meanwhile at 1st Na^+ extraction, the PEO and $NaCO_3R$ are partially dissolved and the Na_2CO_3 layer covers mainly the NaF and NaCl layer. Finally, the SEI layer is thinner (<5 nm) than in **NTO-OH-Ar-C** sample as suggest the graphite peak in C 1*s* and the $Na_2Ti_3O_7$ peak in O 1*s* photoelectron spectra.

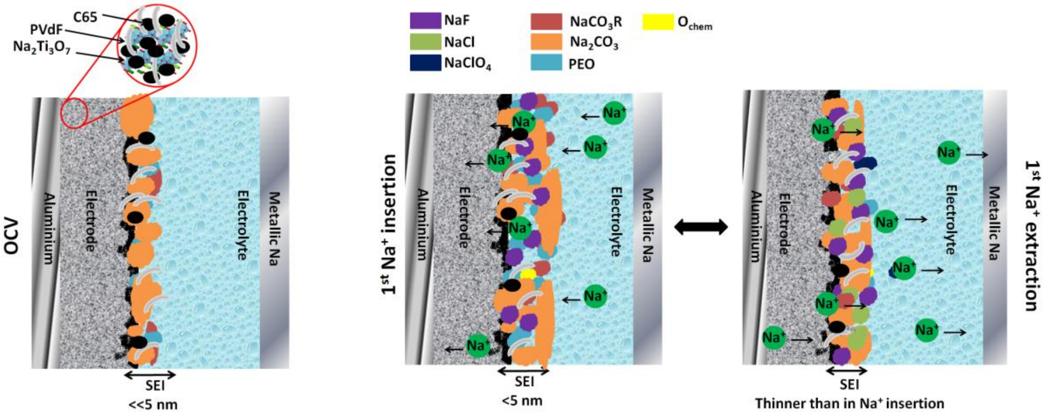

Figure 3.40: Schematic picture of the SEI layer at OCV (left), 1st Na^+ insertion (middle) 1st Na^+ extraction (right) of **NTO-OH-Ar-C-FC** sample.

3.4. Conclusions

In this chapter further insight into the behaviour, performance and stability of $Na_2Ti_3O_7$ electrodes has been provided.

The electrochemical impedance spectroscopy experiments have provided a first direct experimental evidence of the reversible transition from electronic insulator to conductor in all studied $Na_2Ti_3O_7$ electrodes upon Na^+ insertion. Hence, the electrons have better conduction behaviour along the material which facilitates the Na^+ insertion/extraction process.

Despite the transition has been observed for all studied samples, after comparing the resistance values of both samples, the C-coated sample delivers, in all different processes, lower and more stable resistance. The bulk electronic resistance is reduced due to the C-coating increases the electronic conductivity. Additionally, the charge-transfer process shows that in the C-coated sample the Na^+ insertion and extraction are similar, while in the non-coated sample, the Na^+ insertion is easier than the extraction one. Therefore, the C-coating has a clear positive effect on the material.

Moreover, the SEI layer behaviour has been also evaluated by EIS and XPS. The SEI resistance obtained from the EIS experiments show an instable SEI layer in the non-coated sample, contributing to the capacity fading, while the C-coated sample has a more stable SEI layer, the reason being the C-coating suppressing the interaction between the active material and electrolyte. In fact, it presents capacities closer to the expected theoretical values and better capacity retention, further confirming the benefits of the C-coating.

The combination of conventional XPS, Auger parameter determination and depth profiling analysis has provided more information about the stability of the SEI layer as well as on the layer composition and structure.

The SEI layer formed upon Na^+ insertion in $Na_2Ti_3O_7$ electrodes in a half-cell is composed of a thin overlayer of chemisorbed oxygen, $NaCO_3R$, PEO and some residual $NaClO_4$ that covers the solid layer of Na_2CO_3, NaF and NaCl. The PEO and alkyl/carbonate are formed by EC reduction while NaCl and NaF are spontaneously formed by the decomposition of the electrolyte salt once in contact with the electrode and electrolyte and PVdF dehydrofluorination reactions during electrode preparation, respectively. Upon Na^+ extraction the SEI is cracked and $NaCO_3R$ and PEO partially dissolved. Again, the partial dissolution/cracking is less pronounced for the C-coated sample, in agreement with a “higher” stability of the SEI layer resistance with respect to the non-coated sample.

The full-cell shows a similar behaviour as both studied samples in a half-cell, since a partial dissolution of PEO/$NaCO_3R$ happen during the Na^+ extraction. However, some difference can be found, since the outmost surface is mainly composed by Na_2CO_3 and more important the OCV shows a higher stability since the salt decomposition and PVdF dehydrofluorination do not occur at this state in contrast to the samples tested in a half-cell.

The SEI layer of $Na_2Ti_3O_7$ electrodes in a half-cell and full-cell are mainly formed by inorganic compounds, as it has been found for other anode materials such as HC; in contrast to the SEI layer of LIBs which mainly is formed by organic compounds. Moreover the SEI layer of the studied electrodes is thinner (~ 5nm) than the SEI layers reported for LIBs (>20 nm) [40]. Additionally, the SEI layer in LIBs shows higher stability than the SEI layer studied here: $Na_{2-X}CO_3R_x$ salts have higher solubility than $Li_{2-X}CO_3R_x$ salts in the common organic electrolytes [41] originating a continuous SEI reformation upon Na^+ extraction.

Furthermore, the XPS experiments along with ^{19}F-ssNMR studies have confirmed the degradation of the PVdF binder through dehydrofluorination reaction leading to the formation of HF and the evolution of the $-CF_2$ groups. This degradation has been already observed during the electrode preparation process for non-coated sample while the C-coating avoided the NaF formation during the electrode preparation. However, once the cell is assembled using as counter metallic Na the reaction takes place anyway; while when another intercalation material is used as counter electrode the reaction occurs later, when the Na^+ insertion process starts.

Consequently, the instability of the SEI layer which involves a continuous electrolyte reduction and the PVdF binder degradation will contribute to the capacity fade shown by the $Na_2Ti_3O_7$ anode material. Therefore the PVdF binder and common organic electrolytes are far from ideal. One of the alternatives already proposed for $Na_2Ti_3O_7$ and other electrode materials (HCs and Sb) is the use of aqueous binder such as sodium alginate (NaAlg) or Na-CMC, although their performance is not comparable to their Li counterparts. Moreover, for $Na_2Ti_3O_7$ was tested with NaAlg as binder with several electrolytes salts such as $NaClO_4$ and NaFSI and in all cases capacity fading was observed [3]. Only it is possible to improve the $Na_2Ti_3O_7$ electrochemical performance by coating with carbon as it is shown in the **chapter 2**, most probably due to the decrease of the catalytic activity of the titanate with the electrolyte rendering a more stable system.

3.5. References

---

[1] P. Senguttuvan, G. Rousse, V. Seznec, J.M. Tarascon, M.R. Palacín, $Na_2Ti_3O_7$: lowest voltage ever reported oxide insertion electrode for sodium ion batteries, Chem. Mater. 23 (2011) 4109-4111.

[2] A. Rudola, K. Saravanan, C.W. Mason, P. Balaya; $Na_2Ti_3O_7$: an intercalation based anode for sodium-ion battery applications; J. Mater. Chem. A 1 (2013) 1653-2662.

[3] H. Pan, X. Lu, X. Yu, Y.S. Hu, H. Li, X.Q. Yang, L. Chen; Sodium storage and transport properties in layered $Na_2Ti_3O_7$ for room-temperature sodium-ion batteries; Adv. Energy Mater. 3 (2013) 1186-1194.

[4] J. Vetter, P. Novák, M.R. Wagner, C. Veit, K.C. Möller, J.O. Besenhard, M. Winter, M. Wohlfahrt-Mehrens, C. Vogler, A. Hammouche, Ageing mechanisms in lithium-ion batteries, J. Power Sources 9 (2005) 269-281.

[5] F. Croce, F. Nobili, A. Deptula, W. Lada, R. Tossici, A. D´Epifanio, B. Scrosati, R. Marassi, An electrochemical impedance spectroscopy study of the transport properties of $LiNi_{0.75}Co_{0.25}O_2$, Electrochem. Commun. 1 (1999) 605-608.

[6] F. Nobili, F. Croce, R. Tossici, I Meschini, P. Reale, R. Marassi, Sol-gel synthesis and electrochemical characterization of Mg-/Zr-doped $LiCoO_2$ cathodes for Li-ion batteries, J. Power Sources 197 (2012) 276-284.

[7] F. Nobili, S. Dsoke, M. Minicucci, F. Croce, R. Marassi, Correlation of AC-impedance an in-situ X-ray spectra of $LiCoO_2$, J. Phys. Chem. B 110 (2006) 11310-11313.

[8] E. Barsoukov, J.R. Macdonald; Batteries, in: Impedance spectroscopy theory, experiment and application; 2nd ed., John Wiley & Sons Inc., Hoboken, New Jersey, 2005, pp 444-469.

[9] C.G. Granqvist, Electrochromic materials: Microstructure, electronic bands, and optical properties, Appl. Phys. A 57 (1993) 3-12.

[10] B.A. Boukamp, A Nonlinear Least Squares Fit procedure for analysis of immittance data of electrochemical systems, Solid State Ionics 20 (1986) 31-44.

[11] E. Barsoukov, J.R. Macdonalds; Theory: The Electrical Analogs of Physucal and Chemical Processes, in Impedance spectroscopy. theory, experiment and applications, 2nd ed., John Wiley & Sons Inc., Hoboken, New York, 2005, pp. 27-75.

[12] H.S. Kim, M. Kong, K. Kim, I.J. Kim, H.B. Gu, Effect of carbon coating on $LiNi_{1/3}Mn_{1/3}Co_{1/3}O_2$ cathode material for lithium secondy batteries, J. Power Sources 171 (2007) 917-921.

[13] C.D. Wagner, A.Joshi, The Auger parameter, its utility and advantages: A review, J. Electron. Spectrosc. 47 (1988) 283-313.

[14] Y. Xie, P.M.A. Sherwood, X-Ray Photoelectron-Spectroscopic studies of carbon fiber surfaces. Part XII: The effect of microware plasma treatment on pitch-based carbon fiber surfaces; Appl. Spectrosc. 44 (1990) 797-803.

[15] http://www.xpsfitting.com/search/label/Graphite (acceded in August 2016)

[16] R.I.R. Blyth, H. Buqa, F.P. Netzer, M.G. Ramsey, J.O. Besenhard, P. Golob, M. Winter, XPS studies of graphite electrode materials for lithium ion batteries, App. Surface Sci. 167 (2000) 99-106.

[17] A.M. Bradshaw, S.L. Cederbaum, W. Domcked, U. Kraus; Plasmon coupling to core hole excitations in carbon; J. Phys. C: Solid State Phys. 7 (1974) 4503-4512.

[18] G. Beamson, D. Briggs; High Resolution XPS of Organic Polymers: The Scienta ESCA300 Database; John Wiley & Sons, Ltd: Chichester, UK, 1992.

[19] D.P. Woodruff, T.A. Delchar; Modern Techniques of Surface Science of surface science; Cambridge University Press: Cambridge, 1994.

[20] A.M. Andersson, A. Henningson, H. Siegbahn, U. Jansson, K. Edström, Electrochemically lithiated graphite characterized by photoelectron spectroscopy, J. Power Sources 119 (2003) 522-527.

[21] S. Komaba, W. Murata, T. Ishikawa, N. Yabuuchi, T. Ozeki, T. Nakayama, A. Ogata, K. Gotoh, K. Fujiwara, Electrochemical Na insertion and Solid Electrolyte Interphase for Hard-Carbon electrodes and application to Na-ion batteries, Adv. Funct. Mater. 21 (2011) 3859-3867.

[22] L. Baggetto, E. Allcorn, A. Manthiram, G.M. Veith, Cu_2Sb thin films as anode for Na-ion batteries, Electrochem. Commun. 27 (2013) 168-171.

[23] B. Xu, J. Choi, C.N. Borca, P.A. Dowben, Comparison of aluminum and sodium doped poly(vinylidene fluoride-trifluoroethylene) copolymers by x-ray photoemission spectroscopy, Appl. Phys. Lett. 78 (2001) 448-450.

[24] L. Bodenes, A. Darwiche, L. Monconduit, H. Martinez, The solid electrolyte interphase a key parameter of the high performance of Sb in sodium-ion batteries: comparative X-ray photoelectron spectroscopy study of Sb/Na-ion and Sb/Li-ion batteries, J. Power Sources 273 (2015) 14-24.

[25] L. Ji, M. Gu, Y. Shao, X. Li, M.H. Engelhard, B. W. Arey; W. Wang, Z. Nie, J. Xiao, C. Wang, J.G. Zhang, J. Liu, Controlling SEI formation on SnSb-porous carbon nanofibers for improves Na ion storage; Adv. Mater. 26 (2014) 2901-2908.

[26] R. Crowe, J. Pal, S. Badyal, Surface modification of Poly(vinylidene difluoride) (PVdF) by LiOH, J. Chem. Soc., Chem. Commun. (1991) 958-959.

[27] U. Groβ, S. Rüdiger, A.R Grimmer, E. Kemnitz, ^{19}F-NMR solid state investigations of monovalent alkali metal fluorides and tetra-alkylammonium fluorides, J. Fluorine Chem. 115 (2002) 193-199.

[28] S. Ando, K. Robin, U. Scheler, Fluorine-^{19}F NMR of solids containing both fluorine and hydrogen, Encyclopedia of Nuclear Magntic Resonance*;* Vol 9, John Wiley & Sons Ltd., Chichester, UK 2002.

[29] M. Zarrabeitia, E. Castillo-Martínez, J.M López Del Amo, A. Eguía-Barrio, M.A. Muñoz-Márquez, T. Rojo, M. Casas-Cabanas, Towards environmentally friendly Na-ion batteries: moisture and water stability of $Na_2Ti_3O_7$, J. Power Sources 324 (2016) 378-387.

[30] S. Malmgren, K. Ciosek, M. Hahlin, T. Gustafsson, M. Gorgoi, H. Rensmo, K. Edtröm, Comparing anode and cathode electrode/electrolyte interface composition and morphology using soft and hard X-ray photoelectron spectroscopy, Electrochim. Acta 97 (2013) 23-22.

---

[31] L. Vogdanis, W. Heitz, The polymerization of ethylene carbonate, Makromol. Chem., Rapid Commun. 7 (1986) 543-547.

[32] F.A. Soto, Y. Ma, J.M. Martinez de la Hoz, J. M. Seminariom P.B. Balbuena, Formation and growth mechanisms of Solid-Electrolyte Interphase layers in rechargeable batteries, Chem. Mater. 27 (2015) 7990-8000.

[33] L.J. Rendek, G.S. Chottiner, D.A. Scherson, X-ray Photoelectron Spectroscopy studies in ultrahigh vacuum, J. Electrochem. Soc. 149 (2002) E408-E412.

[34] R.G. Copperthwaite, J. Lloyd, Photoinduced descomposition of sodium perclorate and sodium chlorate when studied by X-ray Photoelectron Spectroscopy, J. Chem. Soc., Dalton Trans. (1977), 1117-1121.

[35] R.G. Copperthwaite; J. Lloyd, X-ray Photoelectron Spectroscopic (X-p.e.s) studies on in situ photoinduced decoposition of inorganic molecular ions, J. Chem. Soc. Dalton Trans. 74 (1978) 2252-2264.

[36] J. Walton, P. Wincott, N. Fairley, A. Carrick, Peak Fitting with CasaXPS a Casa pocket book, Accolyte Sicence, Knutsford, UK 2010.

[37] C.D. Wagner, W.M. Riggs, L.E. Davis, J.F. Moulder, G.E. Muilenberg, Handbook of X-Ray Photoelectron Spectroscopy; Perkin-Elmer Corporation, Physical Electronics Division, Eden Prairie, Minnesota, 1979, pp 170.

[38] **http://srdata.nist.gov/xps** (accessed December 2014).

[39] D.I. Iermakova, R. Dugas, M.R. Palacín, A. Ponrouch, On the comparative stability of Li and Na metal anode interfaces in conventional alkyl carbonate electrolytes, J. Electrochem. Soc. 162 (2015) A7060-A766.

[40] M. Nie, J. Demeaux, B.T. Young, D.R. Heskett, Y. Chen, A. Bose, J.C. Woicik, B.L. Lucht, Effec of vinylene carbonate and fluoroethylene carbonate on SEI formation on graphitic anodes in Li-ion batteries, J. Electrochem. Soc. 162 (2015) A7008-A7014.

[41] A. Ponrouch, D. Monti, A. Boschin, B. Steen, P. Johansson, M.R. Palacín, Non-aqueous electrolytes for sodium-ion batteries, J. Mater. Chem. A 3 (2015) 22-42.

4 P2-$Na_{2/3}[Fe_{1/2}Mn_{1/2}]O_2$ as cathode material for NIBs: electrochemical and transport properties and study of the SPI layer

This chapter is focused on the study of the one of the most promising cathode material, P2-$Na_{2/3}[Fe_{1/2}Mn_{1/2}]O_2$. Firstly the structural, morphological and electrochemical characterization will be shown, studying the impact of the electrolyte and working voltage range on the electrochemical properties by galvanostatic and EIS experiments. The latter tests have been allowed a deeper understanding of its capacity degradation and transport properties which have been correlated with the structural evolution during the Na^+ deintercalation/ intercalation process. Secondly, the thorough study of formed SPI layer by EIS and conventional XPS will be detailed.

4.1. Introduction

Layered oxides generally exhibit high specific capacities although, due to their structural changes, where the [T_MO_2] layer (T_M= one or more transition metal) are glided, during Na^+ deintercalation/intercalation process, the capacity retention remains to be improve [1]. Among them, one of the most promising layered oxides in terms of cost and energy density is P2-$Na_{2/3}[Fe_{1/2}Mn_{1/2}]O_2$. [2]. However, as most of layered oxides the capacity retention should be enhanced. In the recent years several approaches have been carried out in order to obtained acceptable capacity retention [3, 4, 5, 6, 7] being the most beneficial initiative the control of the working voltage "window" where the most plausible reason of that improvement can be linked with the structural evolution. However, it has not experimentally corroborated yet [5, 6, 7, 8].

Its reaction mechanism is illustrated in **Figure 4.1** and during the 1st Na^+ deintercalation P2-$Na_{0.67}[Fe(III)_{0.5}Mn(IV)_{0.5}]O_2$ (*P*6_3/*mmc*) shows a solid solution region in the voltage range of 2.0 - 4.0 V (blue region in **Figure 4.1**) where Fe^{2+} oxidized to Fe^{3+} around 3.5 V while Mn keeps the initial oxidation state (Mn^{4+}) obtaining a final composition of P2-$Na_{0.34}[Fe(IV)_{0.5}Mn(IV)_{0.5}]O_2$ at 4.0 V. The solid solution mechanism is identifying since the *a* parameters decreases while *c* parameter increases due to the Na^+ are extracting from the interlayer space leading to repulsion between [T_MO_2] slabs (**Figure 4.1**). Above 4.0 V and until 4.1 V a biphasic region (purple region in **Figure 4.1**) is shown, which is assigned to P2 (*P*6_3/*mmc*) and OP4-type structure. The Na^+ amount is decreased from 0.34 to 0.26 per formula unit. At the end of the deintercalation process (4.1 - 4.25 V *vs.* Na^+/Na) a single OP4-type structure is identified (violet region in **Figure 4.1**) where around 0.21 Na^+ remain in the structure [9]. The structure type of the high voltage phase is still controversial, due to the structural disorder increases and is dificult to determine the exact structure. On the one hand, in several works it has been identified as OP4-type, which consists of a mixture of O and P stacking type due to the gliding of [T_MO_2] and indexed by *P*6_3 [10] or *P*-6*m*2 [2, 9] space group. On the other hand, by means of Pair Distribution Function (PDF), which is a sensitive technique for disordered materials, it has been proposed to crystallize in a bi-layer O2 stacking type where the interplanar cations form a stable tetrahedral environment [5]. Even so, the formation of the high voltage structure, either OP4 or O2-type is reversible when Na^+ are intercalating into structure and first a single phase (OP4) and later a biphasic region (PO4+P2ss) is observed until 3.10 V or 0.45 Na^+ are inserted (violet region in **Figure 4.1**). In the following solid solution region (*a* and *c* cell parameters values show the opposite behaviour corroborating the reversibility of this region also. During the transition from OP4 to P2-type the oxidation state of iron is reduced from Fe^{4+} to Fe^{3+} ($Na_{0.45}[Fe(III)_{0.5}Mn(IV)_{0.5}]O_2$) while in the solid solution region the manganese is reduced (from Mn^{4+} to Mn^{3+}) obtaining a composition of $Na_{0.75}[Fe(III)_{1/2}Mn(III)_{1/2}]O_2$ at 2.0 V. Finally, below 2.0 V (yellow region in **Figure 4.1**) P2 phase, coexists with a new distorted P2 orthorhombic phase (S.G: *Cmcm*), where the final composition is close to $Na_{0.95}[Fe(III)_{1/2}Mn(III)_{1/2}]O_2$ [9]. E*x-situ* and *in-situ* XRD exhibit that the structural evolution is complete reversible although a slightly broadening of the peaks in the 2nd cycle suggests that the crystallinity of the material is reducing upon cycling [8]. That might be linked to the fact that $[T_MO_2]$ layers are glided to change from P2 to OP4-type structure and from ordered P2 to disordered P2 structure and hence some defects and/or staking faults might be create during cycling giving rise to the impoverishment of the electrochemical properties.

Hence, the structural changes might be one of the reasons of the capacity degradation, although the interaction between the electrode and the electrolyte, in other words the SPI layer formation, would be other important factor to take it into account since its properties can influence on the electrochemical performance. Whilst it is true that $P2\text{-}Na_{0.67}[Fe_{0.5}Mn_{0.5}]O_2$ operates inside the electrolyte electrochemical stability window (ESW) of $NaPF_6$ in EC:DMC (c.f. **Figure 1.10**) and hence a not huge influence of that can be expected. The SPI layer formation of $P2\text{-}Na_x[Co_{2/3}Mn_{2/9}Ni_{1/9}]_2$ was recently reported and electrolyte decomposition products were already observed at the begging of electrochemical cycling such as, Na_2CO_3, NaF and phosphate [11]. The reason of that high reactivity might be the air sensitive behaviour of the Na-based cathode and/or the high reactivity observed in Na-based organic electrolyte when a cell is assembled.

4.2. Synthesis of $P2\text{-}Na_{2/3}[Fe_{1/2}Mn_{1/2}]O_2$

$P2\text{-}Na_{2/3}[Fe_{1/2}Mn_{1/2}]O_2$ was synthesized by solid state method mixing in stoichiometric amounts $Na_2CO_3.H_2O$, Fe_2O_3 and Mn_2O_3 in a mortar for 2 h. The mixed powder was compressed in pellets and heated up to 900 ^oC for 12 h under air atmosphere followed by liquid nitrogen quenching [2]. The obtained sample **P2-NFMO** was transferred and stored in an Ar-filled glove box in order to avoid any contact with the atmosphere since Na-layered oxides can easily react with moisture and water resulting in Na^+/H^+ ion exchange and can also trap water molecules in the interlayer space [12, 13].

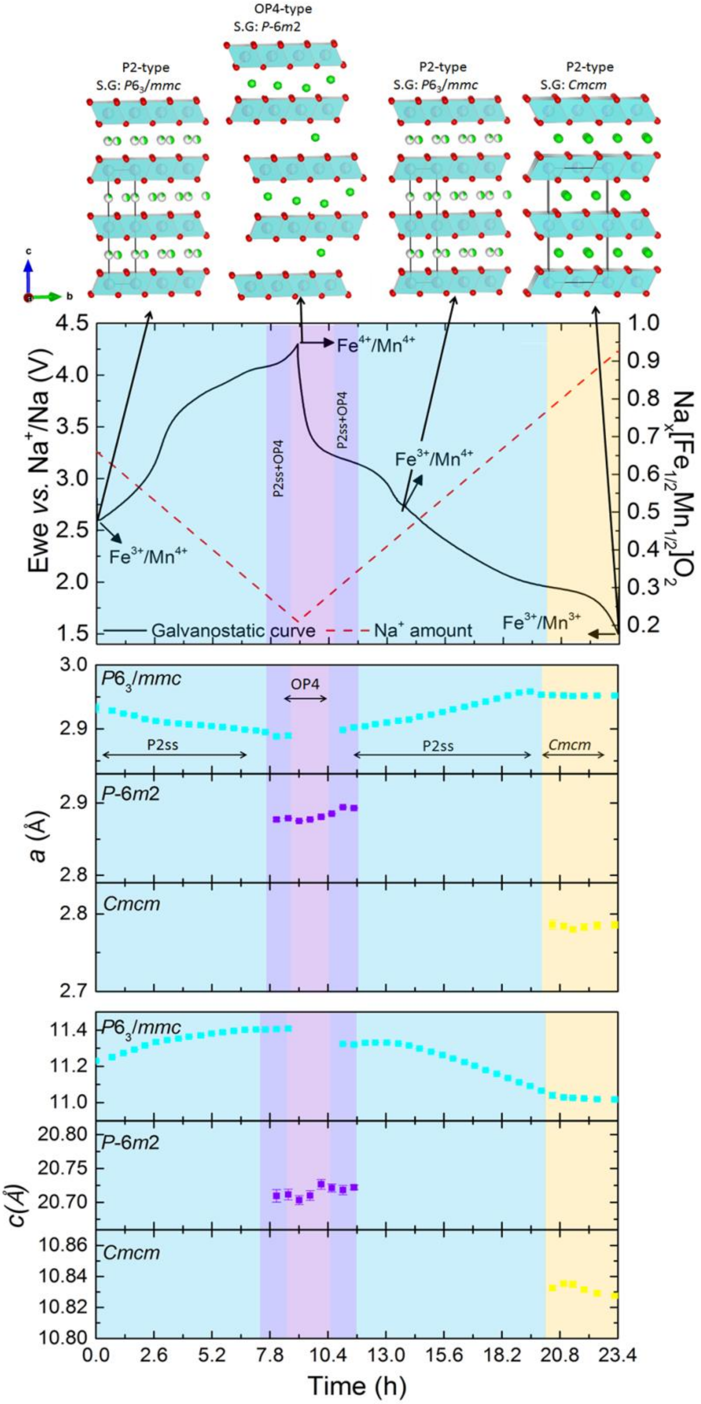

Figure 4.1: Structural evolution (top), galvanostatic curve (middle) and evolution of the *a* and *c* cell parameter upon the 1st cycle. Modified from [9]

4.3. Structural and morphological characterization

4.3.1. Powder X-ray Diffraction (PXRD)

The PXRD pattern of **P2-NFMO** are refined by Le Bail method taking as starting parameters those of reported by Yabuuchi *et al* and the zero factor, cell and profile parameters have been refined [2]. **Figure 4.2** shows a pure P2 type structure with ABBA staking sequence and the refined cell parameters are in good agreement with previously reported data (see **Table 4.1**).

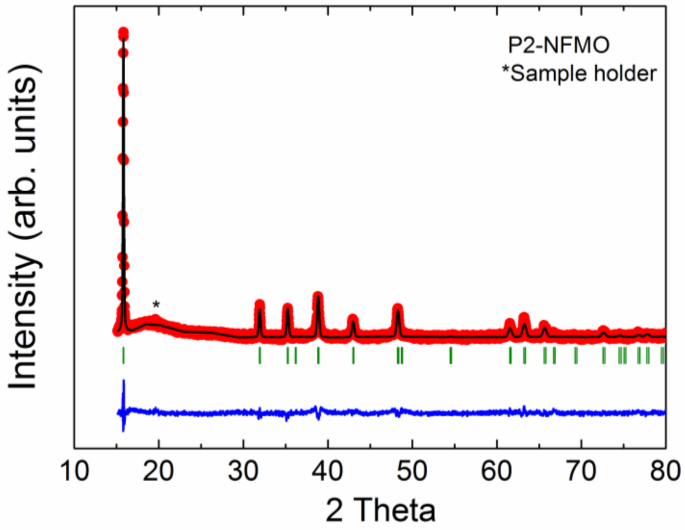

Figure 4.2: PXRD of **P2-NFMO** sample refined by Le Bail method. Observed (red point), calculated (black line), difference (blue line) and Bragg position (green vertical bar).

Table 4.1: The refined cell parameters of **P2-NFMO** ($P6_3/mmc$) determined by Le Bail method from PXRD data at room temperature.

a (Å)	*c* (Å)
2.9396(3)	11.209(3)

4.3.2. Scanning Electron Microscopy (SEM)

SEM image of **Figure 4.3a** shows that particle size is heterogeneous since several submicron size particles are observed. Higher magnification image reveals that the **P2-NFMO** crystallizes as hexagonal platelets of 3.0 - 3.5 µm (**Figure 4.3b**). Additionally, laser diffraction particle size distribution analysis shows that 90% of the particles measure around 30 µm or even smaller while the 10% of them are around 6 µm or lower than that (**Figure 4.3c**), suggesting the heterogeneous particle size distribution already observed by SEM.

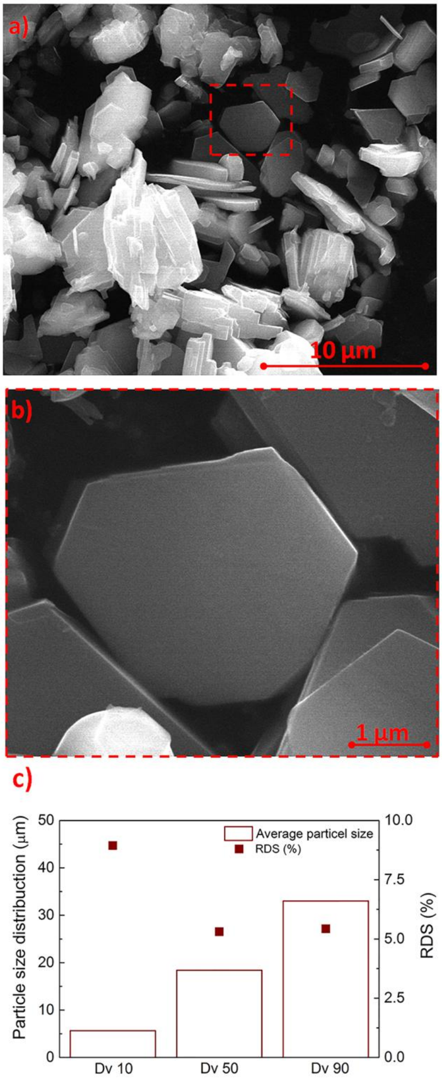

Figure 4.3: SEM images of **P2-NMFO** with a **a)** 6000 and **b)** 30.000 of magnification. **c)** Particle size distribution obtained by laser diffraction (points RDS%).

4.4 Electrochemical characterization

4.4.1. Galvanostatic experiments

Galvanostatic experiments were carried out with laminate electrodes prepared with a 80:10:10 (P2-$Na_{2/3}[Fe_{1/2}Mn_{1/2}]O_2$:carbon Super C65:PVdF) in half-cells using Na disk as counter electrode. Two different combinations were tested: 1 M $NaClO_4$ in EC:PC and 1 M $NaPF_6$ in EC:DEC. These two mixtures of electrolyte were employed since there is not a “standard” electrolyte to test the electrochemical properties of this material [2, 6, 8, 14] and these two combinations were chosen because one is the most commonly organic electrolyte (1 M $NaClO_4$ in EC:PC) and the other one (1 M $NaPF_6$ in EC:DEC) shows good electrochemical performance for other cathode materials. All tests have been done at 0.05C rate in two different working voltage windows: 1.50 - 4.25 V (**P2-NFMO-LV**) and 2.0 - 4.0 V (**P2-NFMO-SV**) *vs.* Na^+/Na. All processes, from laminates preparation to cells assembled were carried out inside the glove box to avoid the interaction with the atmosphere due to the high reactivity of this cathode material.

4.4.1.1. Impact of the electrolyte

On one hand, the effect of the electrolyte in the common used voltage range of 1.5 - 4.25 V has been studied [2, 6, 7, 8]. The voltage profiles of the first five cycles of **P2-NFMO-LV** using both electrolytes: 1 M $NaClO_4$ EC:PC (**Figure 4.4a**) and 1 M $NaPF_6$ EC:DEC (**Figure 4.4b**) are shown. Both cells exhibit a similar voltage profile, as expected; during the 1st Na^+ extraction the Fe^{3+}/Fe^{4+} redox reaction is observed at 3.5 V while upon Na^+ insertion two plateaux occur, first the reversible Fe^{4+}/Fe^{3+} reaction around 3.5 V and later, at 2.4 V *vs.* Na^+/Na approximately the Mn^{4+}/Mn^{3+} redox reaction. This second process does not take place during the 1st Na^+ extraction since the initial oxidation state of Mn is already 4+. Regarding the 1st irreversible capacity, both electrolytes exhibit similar values where ~ 0.25 Na^+ more are inserted into the structure. Hence using different electrolytes cannot enhance this reversibility, suggesting that this behaviour is intrinsic of the material. However, the main difference is observed during the Na^+ insertion. Since when 1 M $NaClO_4$ EC:PC is employed a higher irreversible capacity is shown during the cycling while with 1 M $NaPF_6$ EC:DEC the capacity keeps almost constant. **Figure 4.4c** and **Figure 4.4d** show the Na^+ insertion capacities, Coulombic efficiency and capacity retention, respectively upon Na^+ extraction/insertion. As it is observed in the 1st cycles, **P2-NFMO-LV** shows higher capacities with 1 M $NaClO_4$ than with 1 M $NaPF_6$ salt however the capacity retention is slightly worse (see **Table 4.2**). The Coulombic efficiency is almost similar in both cases, lower at the begging and after 10 cycles is close to 100%. This lower value can be related with the electrolyte decomposition reactions. The slightly better behaviour by NaPF$_6$ salt has been already observed in other layered oxides, such as Na$_x$CoO$_2$ [15] and NaNi$_{0.5}$Mn$_{0.5}$O$_2$ [16]. However, the Na$_x$CoO$_2$ layered oxide provides worse Coulombic efficiency with NaPF$_6$ while, **P2-NFMO-LV** shows similar values close to 99.8% for both salts.

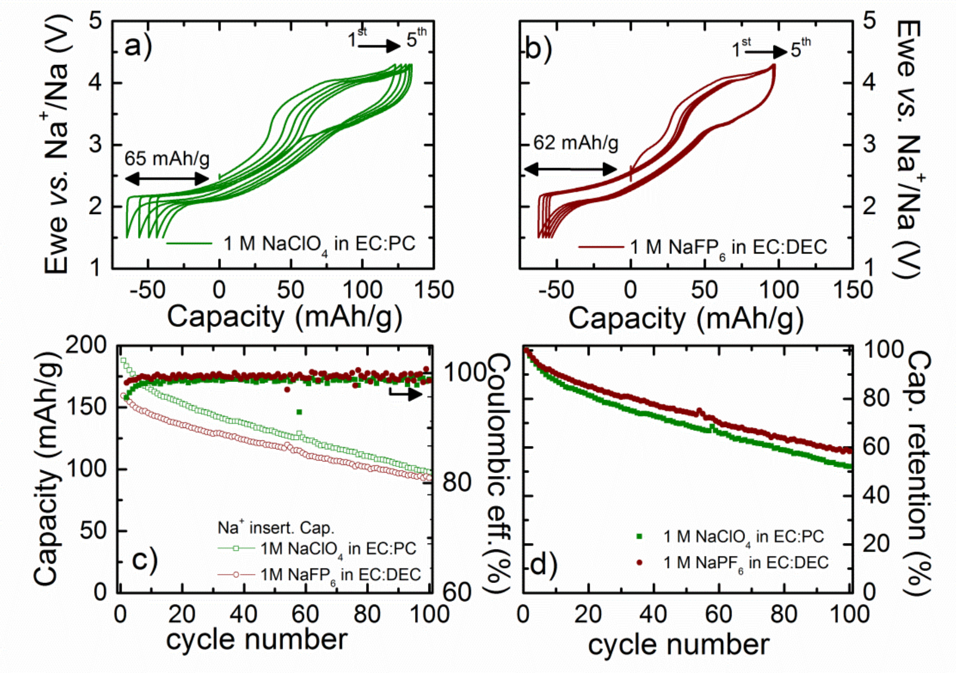

Figure 4.4: Voltage *vs.* capacity curves of the 1st-5th cycles of **P2-NFMO-LV** using as electrolyte **a)** 1 M NaClO$_4$ in EC:PC (olive) and **b)** 1 M NaPF$_6$ in EC:DEC (wine). **c)** Na$^+$ insertion capacity and Coulombic efficiency **d)** capacity retention (taking into account the 1st insertion capacity as reference) *vs.* cycle number over voltage range of 1.5 - 4.25 V *vs.* Na$^+$/Na.

Table 4.2: Capacity values and capacity retention obtained of the 20th and 100th cycle using two different electrolytes: 1 M NaClO$_4$ EC:PC and 1 M NaPF$_6$ EC:DEC at 0.05C over voltage window 1.5 – 4.25 V *vs.* Na$^+$/Na.

P2-NFMO-LV	1 M NaClO$_4$ in EC:PC	1 M NaPF$_6$ in EC:DEC
1st Na$^+$ extrac. capacity (mAh/g)	123	100
1st Irreversible. capacity (mAh/g)	65	62
Capacity retention at 20th cycle	81%	85%
Capacity retention at 100th cycle	50%	60%

Although, the electrochemical performance of **P2-NFMO-LV** has not shown a large improvement using 1 M $NaFP_6$ in EC:DEC as electrolyte, it has been chosen to study the SPI layer stability and composition in order to better comparison with the SPI layer formed in the other studied high voltage polyanionic cathode material (**chapter 5**).

4.4.1.2. Impact of the working voltage range

On the other hand, the impact of the working voltage "window" is studied in order to observe if at narrower voltage range the cycling performance is enhanced as already was observed by several groups [5, 6, 7, 8] since the structural transition at high voltage is avoided. However, in this study both structural changes are prevented: from P2 to OP4-type and from ordered P2 to disordered P2 since the tests has been carried out in the voltage range of 2.0 - 4.0 V *vs.* Na^+/Na (**P2-NFMO-SV**). However, the transition from order to disorder P2 already started close to 2.0 V.

Despite the Na^+ insertion capacities of **P2-NFMO-SV** are lower than that of **P2-NFMO-LV** (**Figure 4.5a**) the capacity retention is more stable (**Figure 4.5b**). The **P2-NFMO-SV** shows lower capacities since when lower upper cut-off voltage is used the complete extraction of Na^+ do not occur and hence some of the specific capacity of the material is disregarded. Moreover, the capacity of **P2-NFMO-LV** decays abruptly and at 30th cycle the insertion capacity is the same as **P2-NFMO-SV**. Hence, although would might think that using at higher cut-off voltage the capacity is improved as well as the performance of the battery, in the long term cycling is a drawback as can be observed in **Figure 4.5b**. The capacity retention of **P2-NFMO-LV** after 30 cycles is 30% worse than **P2-NFMO-SV**. The reason of that enhancing might be related with the absence of structural changes during cycling, however, this is not clear yet.

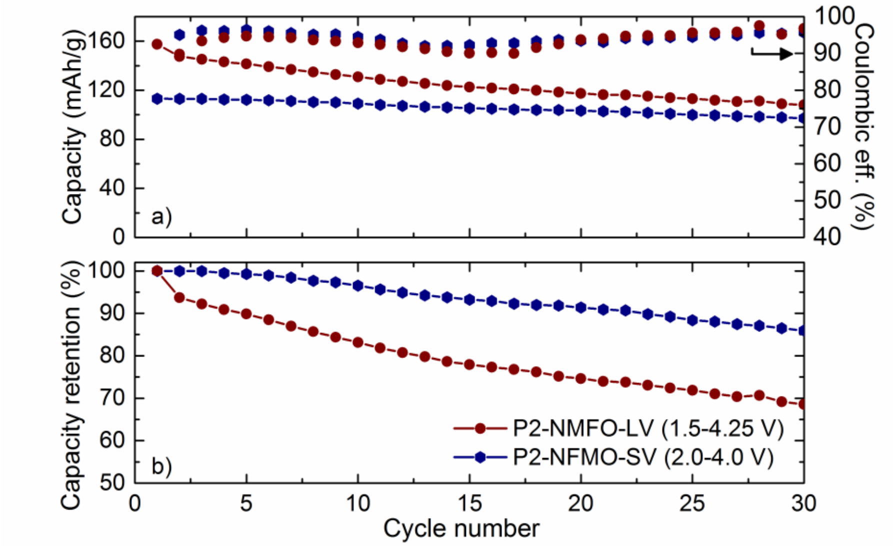

Figure 4.5: a) Na$^+$ insertion capacity and Coulombic efficiency *vs*. cycle number and **b)** capacity retention (taking into account the 1st insertion capacity as references) over voltage window 1.5-4.25 V (**P2-NFMO-LV**, wine) and 2.0-4.0 V (**P2-NFMO-SV**, navy) *vs.* Na$^+$/Na.

4.4.2. Transport and interphase study by EIS

The EIS experiments were carried out to correlate the transport properties with the capacity degradation which mainly depends on the voltage range as it has been observed in **section 4.4.1.2.** and will be discussed below in more detail. Moreover, this set of experiments will provide additional information about the stability of the SPI layer which appears above 1 kHz.

The experiments were performed in three electrode Swagelok cell in two voltage windows: 1.5 - 4.25 V (**P2-NFMO-LV**) and 2.0 - 4.0 V (**P2-NFMO-SV**) *vs.* Na$^+$/Na using 1 M NaPF$_6$ in EC:DEC as electrolyte and Na disk as counter and reference. All tests were carried out at room temperature using a VMP3 potentiostat (Bio-Logic) collecting the data every 45 mV in 5 mHz - 100 kHz frequency range.

4.4.2.1. P2-NFMO-LV sample

The Nyquist plot of the impedance dispersion recorded at OCV (2.43 V *vs.* Na$^+$/Na) is shown in **Figure 4.6**, where three semicircles are observed at different frequencies: at low-frequency (LF) below 1 Hz, at medium-frequency (MF) between 5 kHz-10 Hz and at high-frequency (HF) above 5 kHz which is better observed once the dispersion is enlarged (**see inset**). Additionally, in the lowest frequency region (40 mHz - 5 mHz) a sloping line at 45° with respect to the *x* axis (real part, Z´) can be observed which corresponds to the Na^+ solid-state diffusion through the electrode crystal.

The HF semicircle can be assigned to the Na^+ migration through SPI layer. Although at OCV the oxidation of the electrolyte and subsequent formation of SPI is not expected, the active material reactivity towards air exposure and the possible dehydrofluorination reaction of PVdF, already observed in other Na-based material (c.f **chapter 3**) [11, 17], might contribute to form a surface layer (Na_2CO_3 and NaF). That is responsible of the observed process at HF. The MF arc corresponds to charge-transfer resistance (R_{CT}) and accumulation of charge in the interfacial double layer, while the process at LF region can be correlated to the changes in the crystalline structure that can influence the bulk electronic conductivity as has been described by Barsoukov *et al.*[18] Indeed, similar behaviour at LFs has been observed in the $Li_xCo_{1-x}Ni_xO_2$ lithium layered oxide and additionally in the $Na_2Ti_3O_7$ (c.f. **chapter 3**). This process has been correlated with the bulk electronic resistance (R_{elec}) in both cases [19, 20, 21]. Concerning the $Li_xCo_{1-x}Ni_xO_2$, the semicircle at LF evolves during Li^+ extraction and the radius of the arc decreases

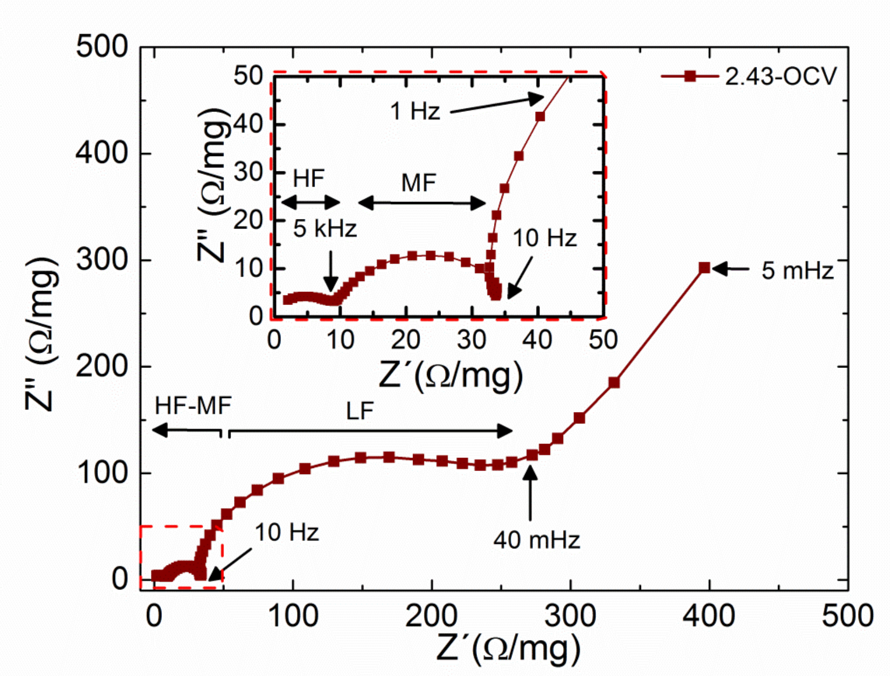

Figure 4.6: Nyquist of **P2-NFMO-LV** at OCV (2.43 V *vs.* Na^+/Na). The inset shows the impedance data from 100 kHz to 1 Hz.

(less resistance) which can be ascribed to a transition from insulator to conductor. This transition is originated by the reduction of *a* cell parameter, hence decreasing the T_M-T_M distance and triggering an increase of the bulk electronic conductivity [22]. The $Na_2Ti_3O_7$ also experiences transition conductivity but in this case is associated to Na^+ intercalation; the excess of ionized electrons from inserted Na^+ occupy the t_{2g} orbits of the conduction band of Ti 3*d* and will induce the conductivity transition [21].

Besides the OCV charge state, the **P2-NFMO-LV** sample was studied by EIS during the first Na^+ extraction. The Nyquist plots shown in **Figure 4.7** correspond to some of the most relevant potential values of the 1st Na^+ extraction. The main changes are observed in the radius of the large arc at LF which changes with the voltage, indicating a variation of the bulk electronic resistance (R_{elec}) upon Na^+ extraction.

Below 3.00 V (**Figure 4.7a**), the R_{elec} or the radius of the LF arc is almost constant. In the 3.00 - 3.33 V voltage range, the R_{elec} starts increasing, getting a maximum and doubling the value at 3.23 V *vs.* Na^+/Na (**Figure 4.7b**) with respect to the values measured at 3.00 V. However, before reaching 4.00 V when the Na^+ content decreases more abruptly (around and after the Fe^{3+}/Fe^{4+} redox plateau), the LF arc starts progressively to contract (reducing the R_{elec}) one order of magnitude and the slopping line typically of the diffusion clearly arises in the graph (**Figure 4.7c**). Nevertheless, at high voltage (above 4.00 V *vs.* Na^+/Na) the radius of LF semicircle starts increasing again (as the R_{elec} is increased) becoming the main feature of the Nyquist plot at the end of the Na^+ extraction (**Figure 4.7d**).

Regarding the semicircles at MF and HF, i.e. the arcs associated to the R_{CT} and SPI layer resistance (R_{SPI}), the radius of the first process mentioned (charge-transfer) is constantly increasing during the Na^+ extraction, while the latter one (SPI layer) increases until 3.00 V (**Figure 4.7a**) to remain almost constant afterwards. Such behaviour might be correlated with a homogeneous and quite stable SPI layer during the electrochemical cycling. However, this will be further confirmed in the next section by XPS experiments.

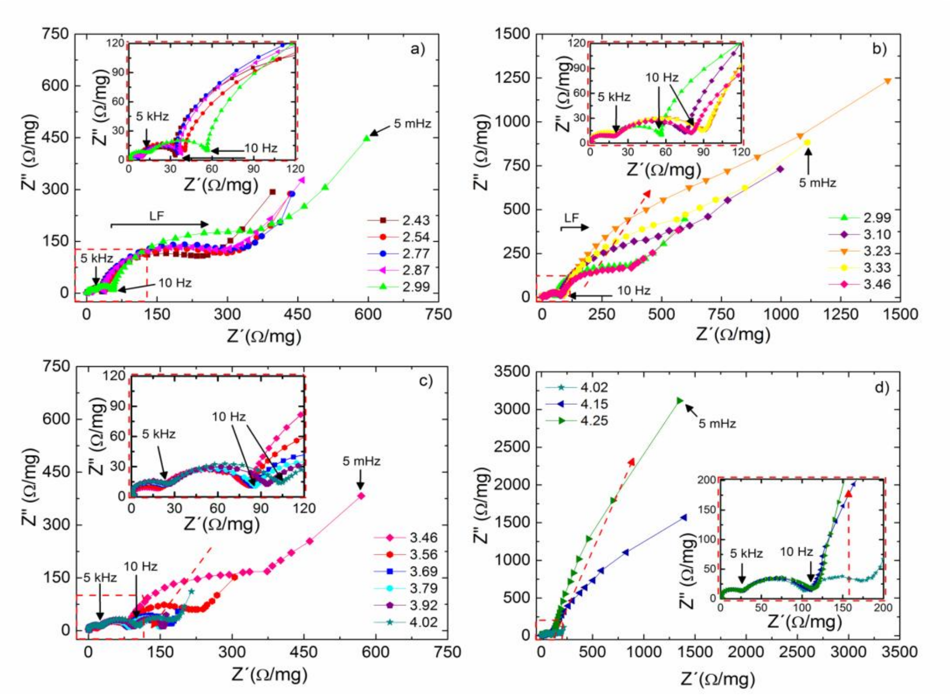

Figure 4.7: Nyquist of **P2-NFMO-LV** during the 1st Na^+ extraction at **a)** 2.43 V (x≈ 0.0), 2.54 V (x≈ 0.0), 2.77 V (x≈ 0.05), 2.87 V(x≈ 0.08), 2.99 V (x≈ 0.10) **b)** 2.99 V (x≈ 0.10), 3.10 V (x≈ 0.11), 3.23 V (x≈ 0.12), 3.33 V (x≈ 0.12), 3.46 V (x≈ 0.12), **c)** 3.46 V (x≈ 0.12), 3.56 V (x≈ 0.13), 3.69 V (x≈ 0.16), 3.79 V (x≈ 0.18), 3.92 V (x≈ 0.22), 4.02 V (x≈ 0.25), **d)** 4.02 V (x≈ 0.25), 4.15 V (x≈ 0.38) and 4.25 V (x≈ 0.45) *vs.* Na^+/Na. The inset shows the impedance data from 100 kHz to 1 Hz.

Furthermore, the **P2-NFMO-LV** exhibits the opposite behaviour upon Na^+ insertion (**Figure 4.8**). At high voltage a huge arc appears at LF (**Figure 4.8a**) but as the voltage decreases and after the Fe^{3+}/Fe^{4+} plateau (3.5 V), when the Na^+ amount is significantly increased, the arc radius is continuously reducing until the half-cell voltage is around 2.5 V (**Figure 4.8b**). From 2.5 V until 2.0 V, the LF arc radius decreases (**Figure 4.8c**). Finally, the arc radius is substantially enlarged below 2.0 V (**Figure 4.8d**). Hence the LF process shows a reversible behaviour during the cycling performance. Meanwhile, the R_{CT} and R_{SPI} (MF and HF arcs) remain almost constant, although the R_{CT} shrinks slightly in the 3.45 - 2.64 V voltage range (**Figure 4.8b**).

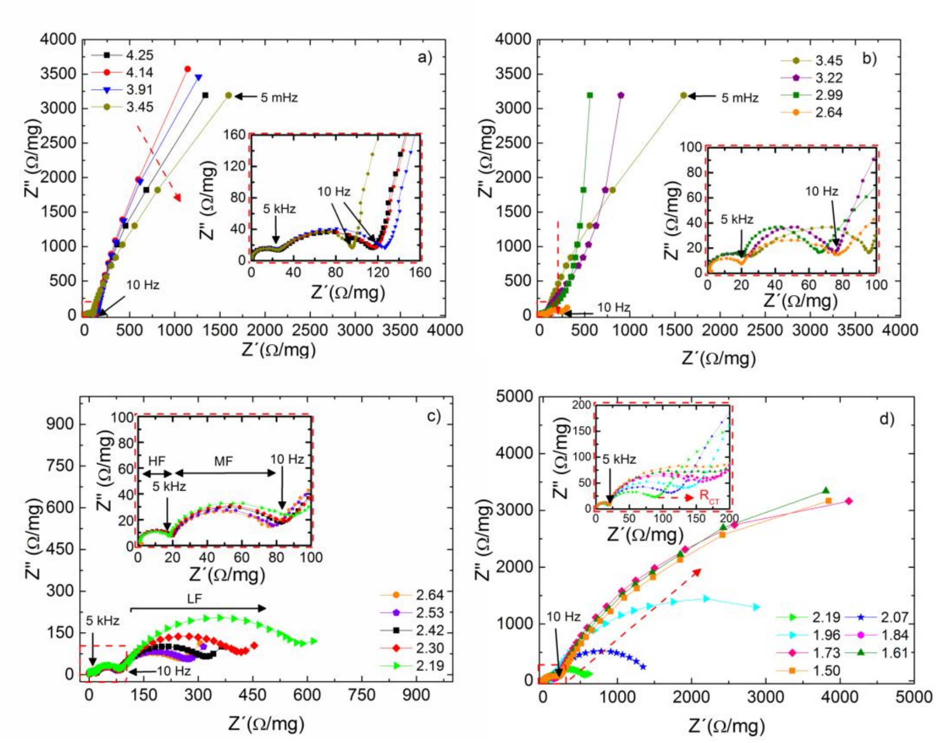

Figure 4.8: Nyquist plot of **P2-NFMO-LV** during the 1st Na^+ insertion at **a)** 4.25 V (x≈ 0.20), 4.14 V (x≈ 0.20), 3.91 V (x≈ 0.22), 3.45 V(x≈ 0.28), **b)** 3.45 V (x≈ 0.28), 3.22 V (x≈ 0.34), 2.99 V (x≈ 0.44), 2.64 V (x≈ 0.51), **c)** 2.64 V (x≈ 0.68), 2.42 V (x≈ 0.58), 2.30 V (x≈ 0.60), 2.19 V (x≈ 0.64), **d)** 2.19 V (x≈ 0.64), 2.07 V (x≈ 0.38), 1.96 V (x≈ 0.76), 1.84 V (x≈ 0.80), 1.73 V (x≈ 0.81), 1.61 V (x≈ 0.82) and 1.50 V (x≈ 0.83) *vs.* Na^+/Na. The inset shows the impedance data from 100 KHz to 1 Hz.

In order to carry out a thorough analysis of the stability and reversibility of the three processes during cycling, the collected impedance data (133 impedance spectra in total) have been fitted with the Boukamp´s software [23] and using the same equivalent circuit successfully used for the $Na_2Ti_3O_7$ (**Figure 3.5b**) [21] and other intercalation materials [19, 20, 22]. This model is based on the following parameters: Na^+ resistance across the electrolyte (R_{sol}), resistance and capacitance of the SPI layer (R_{SPI} and C_{SPI}), charge-transfer resistance (R_{CT}), double layer capacitance (C_{DL}), bulk electronic resistance (R_{elec}), capacitance arising from charge accumulation at the surface of the particles or at intraparticles crystallite domains (C_{elec}), Warburg diffusion (Z_w) related to the solid-state diffusion of the Na^+ inside the crystal and intercalation capacity (C_i) due to the charge accumulation (more details in **section A.2.5**) [20, 24]. The resistance and capacitance of each process are connected in parallel. Moreover, to take into account any deviation from an ideal material such as surface inhomogeneity, roughness or degree of polycrystallinity, the Z_w and C elements have been replaced by CPE (Constant Phase Element) in the fits (more details in **section A.2.5**). Although all collected EIS spectra have been fitted (133 spectra in total), as example some impedance fits are shown in **Figure 4.9** and the values obtained from the fit are collected in **Table A.3**. The goodness of the fits proves that the used equivalent circuit fits well the collected experimental impedance data and would agree with the proposed model.

Indeed, the overall trend of the resistance values obtained by the fit of all impedance spectra measured during the first two cycles is shown in **Figure 4.10** with respect to the voltage and Na^+ inserted into **P2-NFMO-LV**.

As it has been previously observed in the Nyquist plot (**Figure 4.7** and **Figure 4.8**) the R_{SPI} is almost constant (red points in **Figure 4.10**). At the beginning of the cycling (OCV), a low R_{SPI} is detected which can be ascribed to a thin Na_2CO_3 and NaF layer that covers the pristine electrode; will be later discussed at the light of XPS experiments. Above 3.00 V, and after a minor increase, the R_{SPI} is stabilized

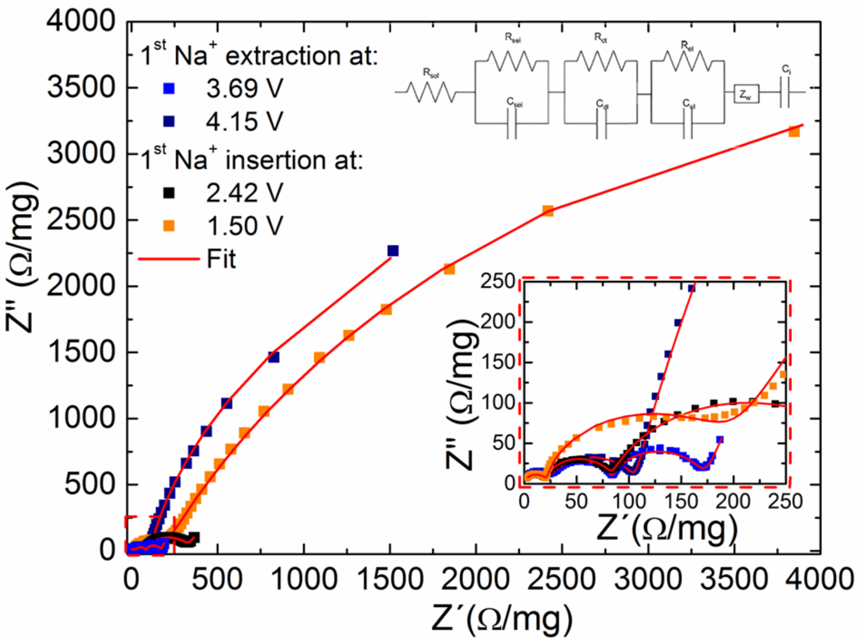

Figure 4.9: The fits of the impedance data of **P2-NFMO-LV** cycled in the voltage window of 1.5-4.25 V at 3.69 V and 4.15 V upon Na^+ deintercalation and at 2.42 V and 1.50 V upon Na^+ intercalation, respectively. The inset shows the fits from 100 kHz to 1 Hz and the employed circuit for the fits.

suggesting the formation of a stable SPI layer.

The R_{CT} (green points in **Figure 4.10**), in contrast, increases during the electrochemical cycling, which can be correlated with the complex structural evolution of the active material during cycling. The **P2-NFMO-LV** sample suffers two phase transitions in each Na^+ deintercalation/intercalation process. Therefore, the formation of grain boundaries might be expected for this material. The transport properties will be perturbed by these grain boundaries, reducing the conductivity and hence increasing the resistance [18].

As occurs with R_{CT}, the R_{elec} at LF (blue points in **Figure 4.10**) continuously increases upon cycling although several oscillations take place depending on the voltage which are related to the structural evolution of **P2-NFMO-LV**. In general (except for 1st Na^+ extraction), during the solid solution region of P2 (blue region in **Figure 4.10**), the R_{elec} decreases upon Na^+ extraction and increases upon Na^+ insertion. This means, that **P2-NMFO-LV** becomes a better electronic conductor during the Na^+ extraction. During this process the *a* cell parameter (c.f. **Figure 4.1**) [9], which corresponds to T_M-T_M planes, is reduced leading to an increase of the bulk electronic conductivity (reduces the R_{elec}). Meanwhile, during the Na^+ insertion the opposite process occurs, confirming the reversible behaviour of the electronic conductivity. Moreover, the increment that occurs at 3.0 - 3.3 V in the 1st Na^+ extraction is because the electron transfer is easier in the Fe^{3+}/Fe^{4+} couple (3.5 V) than when Mn^{4+} and Fe^{3+} are in the material [8].

However, when structural transitions take place the trend is interrupted. At high voltage, 4.1 V, during the Na^+ extraction the transition from P2 to OP4 (violet region in **Figure 4.10**) the R_{elec} suffers a large increment. Meanwhile, in the OP4 solid solution (pink region in **Figure 4.10**) is stabilized. Below 2.0 V (yellow region in **Figure 4.10**) and during the Na^+ insertion another phase transition takes place, from ordered to disorder P2, again drastically increasing the R_{elec} value. These increments of R_{elec} at 4.1 V and 2.0 V reduced drastically the bulk electronic conductivity of **P2-NMFO-LV**.

These phase transitions, despite being reversible, lead to an overall increase of the R_{CT} and R_{elec} values with respect to the 1st cycle. Hence, the active material becomes a poorer conductor upon cycling. This might be originated by the creation of defects and/or staking faults during the phase transitions. Since the $[Fe_{1/2}Mn_{1/2}O_2]$ layers are glided above 4.00 V to form the OP4-type and therefore some staking faults can appears losing crystallinity and creating defects. These can ultimately increase the R_{elec}. The estimated values of α confirm this hypothesis since it decreases during the electrochemical cycling (**Figure 4.10b**). The α is the exponential factor of electronic CPE and depends strongly on the surface homogeneity, roughness and degree of polycrystallinity ($\alpha = 1$ a ideal surface) [18].

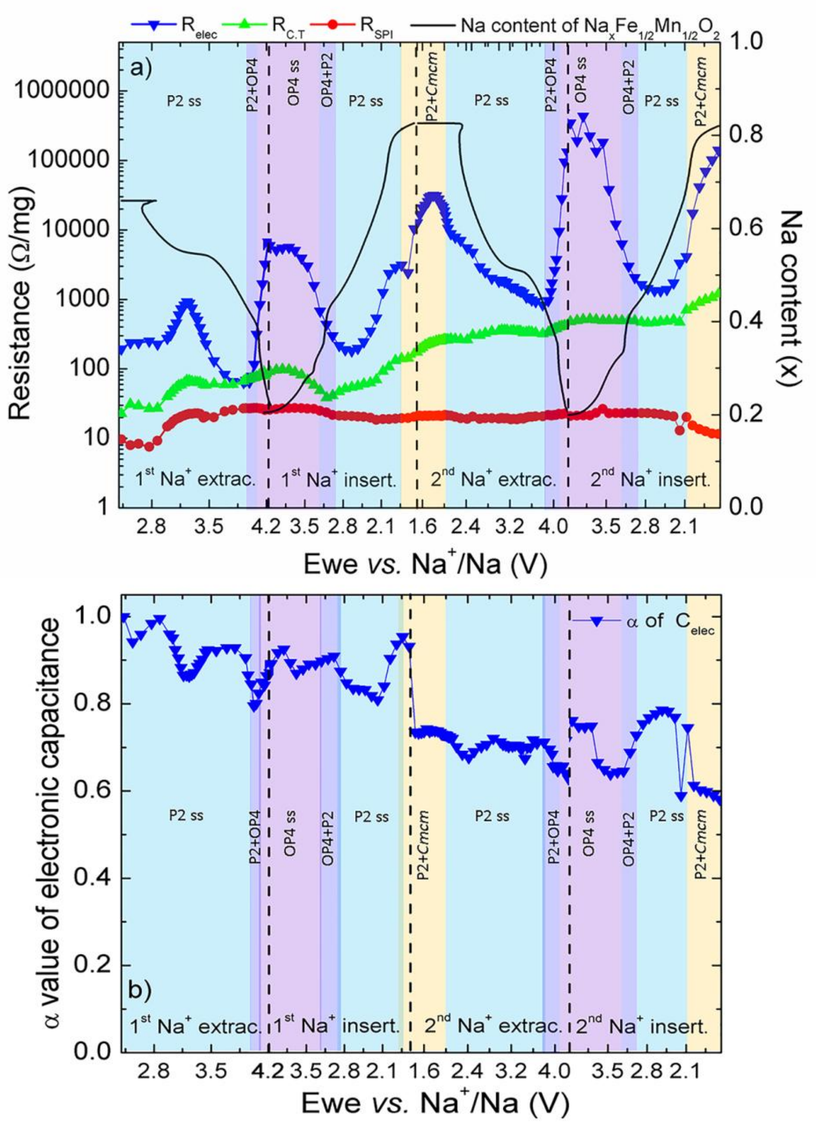

Figure 4.10: The fitted values upon the first two cycles by Boukamp´s software of the cycled electrode between 1.5 - 4.25 V *vs.* Na^+/Na. (**P2-NFMO-LV**) **a)** R_{SPI} (red points), $R_{C.T}$ (green points), R_{elec} (blue points) and **b)** α factor of the CPE associated with C_{elec}. The structural evolution during the Na^+ extraction/insertion of **P2-NMFO** has been

Moreover, beyond the 2nd cycle, the radius of the LF arc greatly increases and already in the 4th cycle, the main feature of the impedance data corresponds to the LF arc. This means that the R_{elec} constantly increased during cycling, significantly reducing the bulk electronic conductivity of the **P2-NFMO-LV** sample (**Figure 4.11**).

Therefore, although the structural evolution during electrochemical performance is complete reversible, the broadening of the XRD peaks after several cycles corroborate that the crystallinity is losing (see inset of **Figure 4.11d**), in very good agreement with α factor of the electronic CPE. The reason of this loss can be related with the defects/staling faults that increase in each phase transition and/or the crystal size is reducing. This large increase in the R_{elec} observed upon cycling might be the responsible for the poor electrochemical performance of this material.

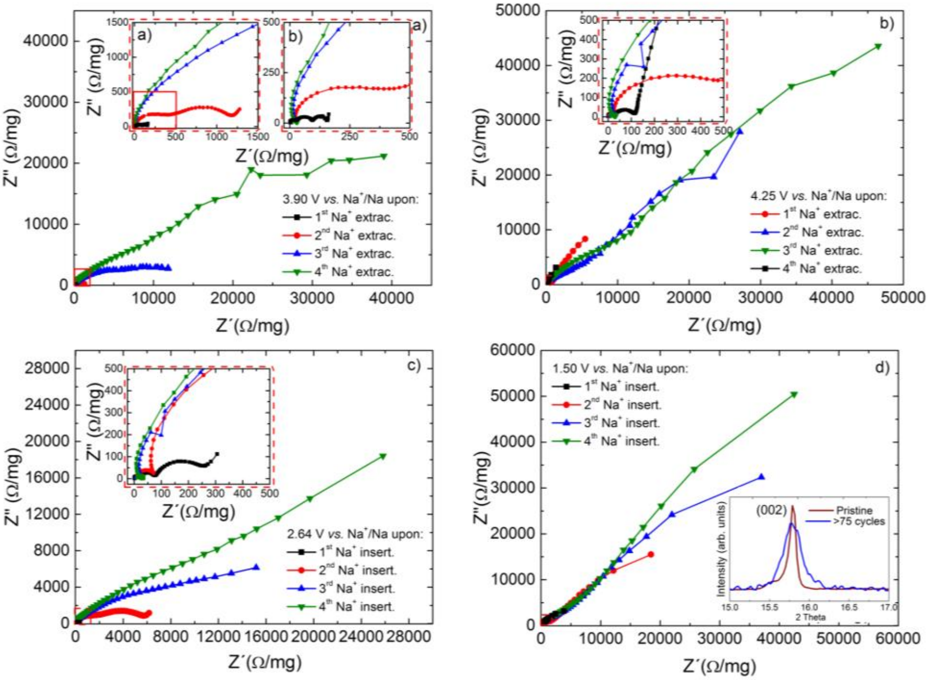

Figure 4.11: The Nyquist plot of **P2-NFMO-LV** during the first four cycle upon Na^+ extraction at **a)** 3.90 V and **b)** 4.25 V and Na^+ insertion at **c)** 2.64 V and **d)** 1.50 V. 1st cycle black, 2nd cycle red, 3rd cycle blue and 4th cycle green. The inset shows the impedance data from 100 kHz to 1 Hz and the inset of d) the XRD patterns of (002) reflexion: pristine (wine) and after >75 cycles (blue).

4.4.2.2. P2-NFMO-SV sample

One of the best approaches to enhance the capacity retention of this layered oxide is by controlling the working voltage window, obtaining the best results in the 2.0 - 4.0 V voltage range [10]. Therefore, in order to study mainly the behaviour of the R_{elec} without the influence of the more “problematic” phase transition (P2 → OP4), the same EIS experiment presented in **section 4.4.2.1** was carried out in the 4.0 - 2.0 V *vs.* Na^+/Na voltage range (**P2-NFMO-SV**) where only the solid solution P2 occurs. Hence the formation of other phases namely OP4 and distorted P2 are avoided. However, the latter phase appears around 2.0 V and some influence can be observed.

The Nyquist plot of the impedance at OCV (2.68 V *vs.* Na^+/Na) of **P2-NFMO-SV** (**Figure 4.12**) shows a lineshape very similar to the one from **P2-NFMO-LV** sample (**Figure 4.6**). However, when the impedance data is zoomed in the HF range and compared with the spectrum at OCV of **P2-NFMO-LV** the resistance corresponding to the SPI layer is lower (the radius of the arc is smaller). That could be associated to the formation of Na_2CO_3 on the particle surface, owing to a high reactivity against air exposure. In **P2-NFMO-SV** might be slightly thinner if compared to the one used previously with a wider voltage widow (**P2-NFMO-LV**). Even so, it exhibits three semicircles at same frequencies: LF region below 1 Hz, MF region between 5 kHz-10 Hz and HF region above 5 kHz with a sloping line at lowest-frequency which

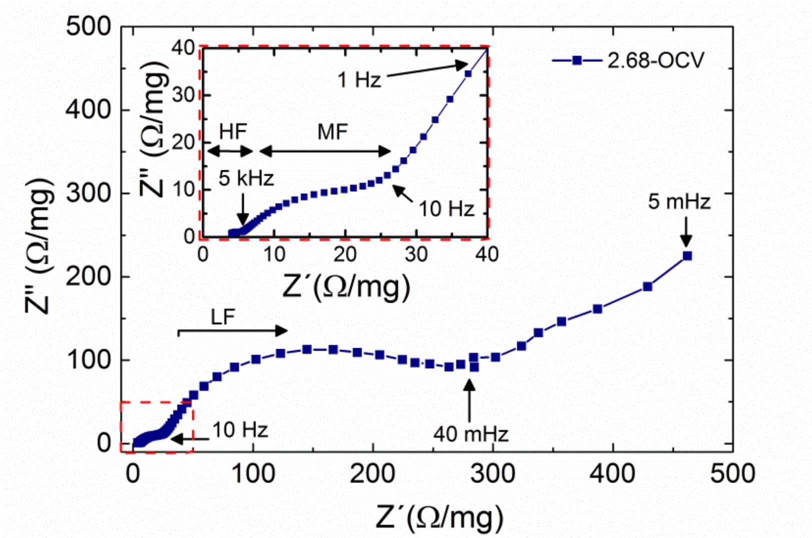

Figure 4.12: Nyquist of **P2-NFMO-SV** at OCV (2.68 V *vs.* Na^+/Na). The inset shows the impedance data from 100 kHz to 1 Hz.

corresponding to the Na$^+$ solid-state diffusion through the crystal, analogously to the **P2-NMFO-LV** sample.

In the Nyquist plots of **Figure 4.13**, several impedance spectra measured during the 1st cycle are shown. Since the employed voltage range avoids the structural evolution from P2 to OP4 during the Na$^+$ extraction, the radius of the LF arc is more stable than in the **P2-NFMO-LV** sample. In the 3.0 - 3.3 V voltage range only shows an oscillation (**Figure 4.13a**) and a larger increment at 2.0 V (**Figure 4.13d**). The change at 3.0 - 3.3 V is associated to the electron transfer since when Fe is in the oxidation state 3+ prevents the electronic transfer [8]. While the increment at low voltage (2.0 V) is due to the phase transition from order to disorder P2 (this transition starts at this voltage).

During the Na$^+$ extraction at upper voltage than 3.28 V the radius of the LF arc (**Figure 4.13b**) starts progressively to reduce. Hence the R_{elec} is also decreasing and in turn the bulk electronic conductivity increases. That happen because the

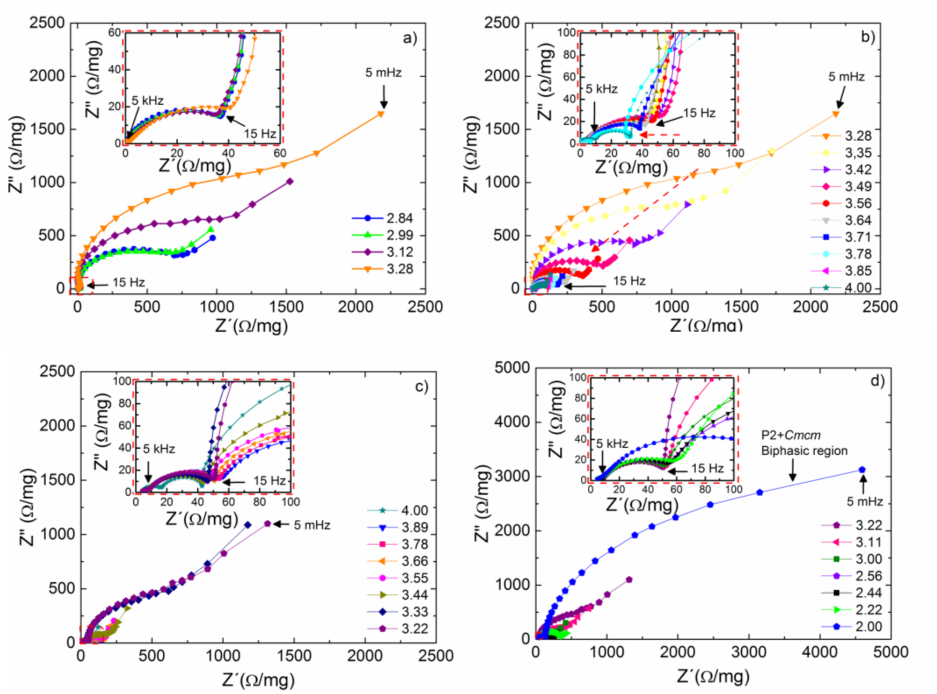

Figure 4.13: Nyquist of **P2-NFMO-SV** during the 1st Na$^+$ extraction at **a)** 2.84 V, 2.99 V, 3.12 V, 3.28 V **b)** 3.28 V, 3.35 V, 3.42 V, 3.49 V, 3.56 V, 3.64 V, 3.71 V, 3.78 V, 3.85 V and 4.00 V and during the Na$^+$ insertion process at **c)** 4.00 V, 3.89 V, 3.78 V, 3.66 V, 3.55 V, 3.44 V, 3.33 V, 3.22 V, **d)** 3.22 V, 3.11 V, 3.00 V, 2.56 V, 2.44 V, 2.22 V and 2.00 V *vs.* Na$^+$/Na. The inset shows the impedance data from 100 kHz to 1 Hz.

distance between T_M-T_M are shortened and hence the electrons can be conducted more easily along the T_M-T_M axis. While during the 1st Na^+ insertion process the **P2-NFMO-SV** shows the opposite behaviour (**Figure 4.13c** and **Figure 4.13d**).

Moreover, the radius of the semicircle correlated with the R_{CT} at MF, remains almost constant. While the radius of the SPI layer semicircle at HF increases during the Na^+ extraction and close to 3.5 V is stabilized. It keeps constant during the Na^+ insertion as **P2-NFMO-LV** which suggests that a stable SPI layer is formed also in **P2-NFMO-SV** electrode.

As it has been done with the other electrode, the impedance data collected (76 spectra in total) in the voltage range of 2.0 - 4.0 V have been fitted with Boukamp´s software [23] using the same equivalent circuit presented in **chapter 3** and **section 4.4.2.1**. The capacitances and Z_W also have been replaced by CPE to take into account any surface inhomogeneity, roughness or degree of polycrystallinity of the electrode/particles (more details in **section A.2.5**). Some of these fits fitted are presented in **Figure 4.14** and the fitted values are collected in **Table A.4** confirming that also in this case the used circuit is suitable for the EIS experimental data.

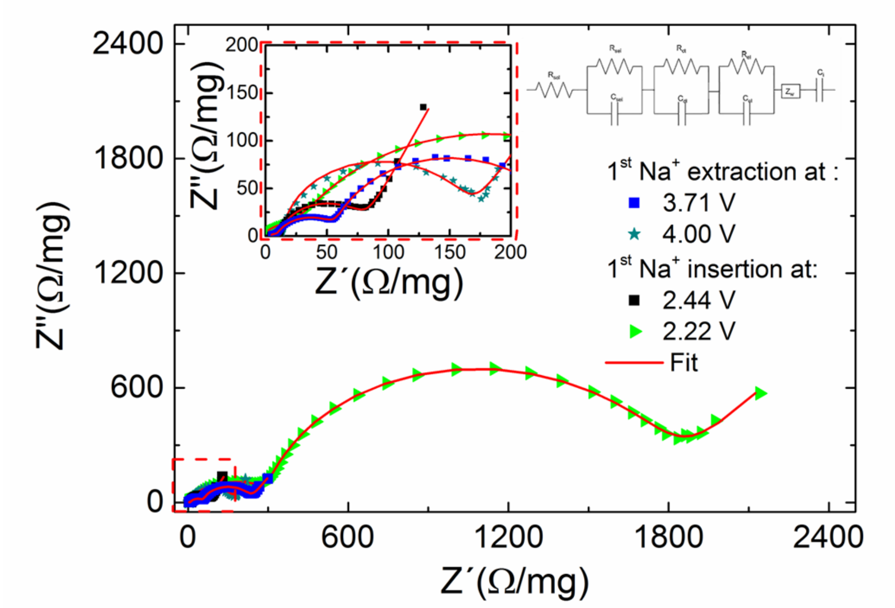

Figure 4.14: The fits of the impedance data of **P2-NFMO-SV** cycled in the voltage range of 2.0-4.0 V at 3.71 V and 4.00 V upon Na^+ deintercalation and at 2.44 V and 2.22 V upon Na^+ intercalation, respectively. The inset shows the fits from 100 kHz to 5 Hz and the utilized circuit for the fits.

The overall resistance behaviour obtained from the fits of all impedance data of **P2-NFMO-SV** during the first two cycles is shown in **Figure 4.15**. The R_{SPI} (red points in **Figure 4.15**) experiences very small variations. Its initial value is lower than in **P2-NFMO-LV** and close to 3.5 V, the R_{SPI} is stabilized around a fixed value. The drop at 2.1 V during the 2nd Na^+ extraction might be correlated with changes in the surface of the SPI layer but after further cycling the R_{SPI} is kept constant. The R_{CT} (green points in **Figure 4.15**) increases gradually during the electrochemical cycling, analogously to the **P2-NFMO-LV** case (**Figure 4.10**). Although the increment of the R_{CT} value is smaller than that observed in **P2-NFMO-LV** sample due to the P2-OP4 transition is avoided and therefore the formation of grains boundaries are reduced.

The most interesting behaviour corresponds to the R_{elec} (blue points in **Figure 4.15**), which is correlated with the structural evolution during electrochemical cycling leading to a loss of the electronic conductivity. During the Na^+ deintercalation process, the R_{elec} value decreases and the material becomes a better electronic conductor owing to the reduction of the T_M-T_M distance. Upon Na^+ intercalation, the active material exhibits the opposite tendency becoming an electronic insulator. However, since the transition from P2 to OP4 phase at high

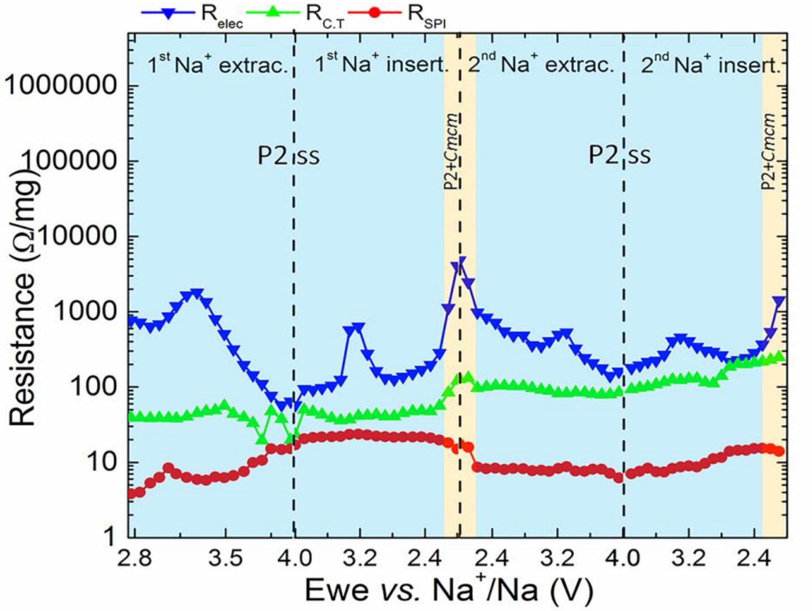

Figure 4.15: The fitted values upon the first two cycles of **P2-NFMO-SV** by Boukamp´s software of R_{SPI} (red points), R_{CT} (green points), R_{elec} (blue points). This electrode has been cycled in the voltage range 2.0-4.0 V *vs.* Na^+/Na.

voltage is avoided (c.f. **Figure 4.1**), the R_{elec} values are more stable if compared with the **P2-NFMO-LV** sample. Hence, not drastic changes can be observed, only close to 2.0 V, where a P2 to disorder P2 phase transition takes place (yellow region in **Figure 4.15**). This transition increases significantly the R_{ele}. Besides this resistance change associated to a phase transition, around 3.2 V in all measured cycles, an increase of the R_{elec} is observed because the electron transfer is blocked when the Mn and Fe are in 4+ and 3+ oxidation state, respectively.

The total resistance increased progressively upon cycling (1st, 2nd, 3rd, 4th, 10th, 20th) (**Figure 4.16**) with a much lower rate than for **P2-NFMO-LV** sample (**Figure 4.11**). The latter sample shows a huge increase of the R_{elec} only in the first four cycles due to the phase transition at high voltage. For the **P2-NMFO-SV** sample, the total resistance is one order of magnitude smaller in the 4th cycle. Furthermore, in the 20th cycle, the total resistance is still lower than the one for the **P2-NFMO-LV** electrode in the 4th cycle (**Figure 4.11**).Finally, the total resistance at 2.0 V for the **P2-NFMO-SV** sample, which is close to the transition phase and hence the increment of the resistance is expected, is still one order of magnitude lower.

Hence the **P2-NFMO-LV** (1.5 - 4.25 V *vs.* Na^+/Na) shows an initial R_{elec} that continuously increases during cycling, with a drastic increase in the first four cycles. Meanwhile the **P2-NFMO-SV** (2.0 - 4.0 V *vs.* Na^+/Na) exhibits more stable behaviour during the electrochemical cycling without jumps/drops, finally leading to a better capacity retention. Therefore, it is confirmed that the bulk electronic resistance increase associated to the high voltage phase transition from P2 to OP4 which is one of the origin of the reported capacity loss. Therefore, avoiding this transition phase by using a smaller voltage window (cut-off at 4.0 V) a better electrochemical performance is obtained; delivering better capacity retention as it has been shown in **Figure 4.5**.

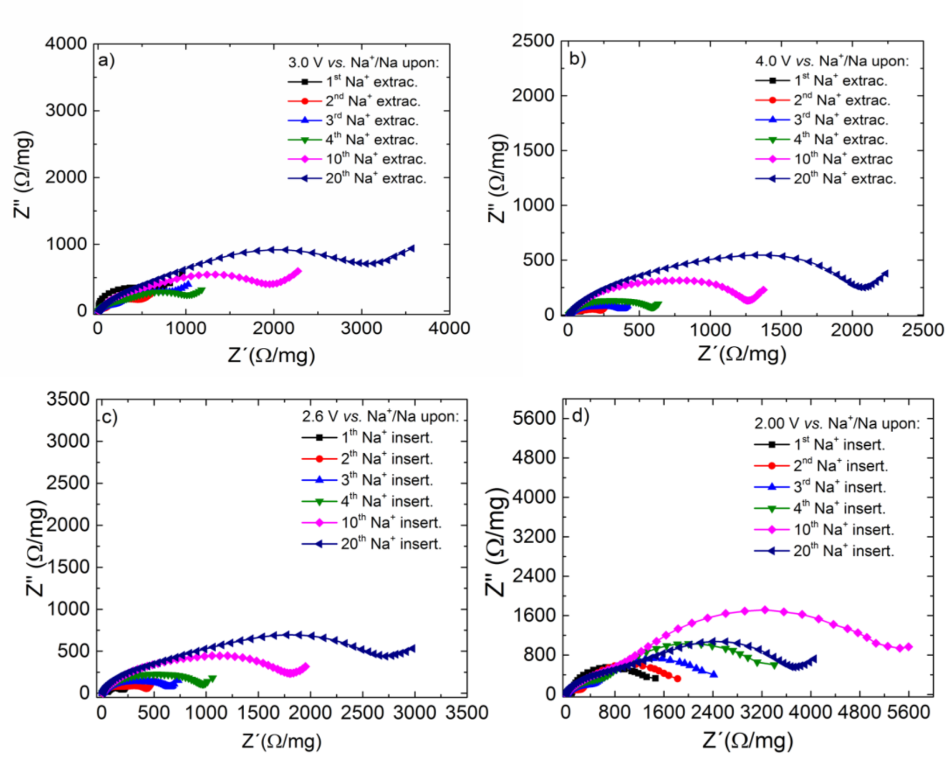

Figure 4.16: The Nyquist plot of **P2-NFMO-SV** during Na$^+$ extraction at **a)** 3.0 V and **b)** 4.0 V and Na$^+$ insertion at **c)** 2.6 V and **d)** 2.0 V. 1st cycle black, 2nd cycle red, 3rd cycle blue, 4th cycle green, 10th cycle pink and 20th cycle navy.

4.5. SPI layer study by XPS

The evolution, composition and stability of the SPI layer on **P2-NFMO-LV** was investigated by means of XPS. The galvanostatic measurement were performed at 0.05C rate, stopping at selected points to carry out XPS measurement, rinsed with DEC and dried in the glove box chamber before inserted into the XPS vacuum chamber by a filled transfer system, never exposing the electrodes to air.

The SPI layer formation and stability is followed by analysing the C 1*s*, O 1*s*, Na 1*s*, F 1*s* and P 2*p* photoelectron lines. Besides the complex composition of the electrode which is constituted by active material, conductive carbon (C65) and binder (PVdF), the SPI layer is formed by oxidation products of the solvent and/or electrolyte salt. Therefore the surface of the electrodes is a non-uniform layer of conducting and nonconducting microdomains that will be at the origin of surface charging effects. Thus, the absolute binding energies of some compounds slightly differed from the ones reported in the literature. However this difference can be partially avoided using a flood gun [25] which provides a steady flow of low-energy electrons that will compensate the charging effects. The photon energy used for most of the experiments was Al K_α ($h\nu = 1486.6$ eV). However, when overlapping of the photoelectron lines with the Auger lines occurs another photon energy was employed: Mg K_α ($h\nu = 1253.6$ eV). In addition, the Auger parameter estimation was not determined for this sample (**P2-NFMO-LV**) due to the formed SPI layer is very thin and not homogeneously distributed and the overlapping of signals does not allow this calculation. However, the Na 1*s* photoelectron spectra can give similar information, since the Na 1*s* photoelectrons have a rather high binding energy; therefore the detected photoelectrons will have a low kinetic energy and hence a very short inelastic mean free path (IMFP). As a result, the Na 1*s* line will only provide information about the outermost surface region of the electrode.

The study is performed at different voltage values during Na^+ extraction/insertion process as highlighted in the galvanostatic profile of **Figure 4.17**. Additionally the pristine electrode is measured as reference.

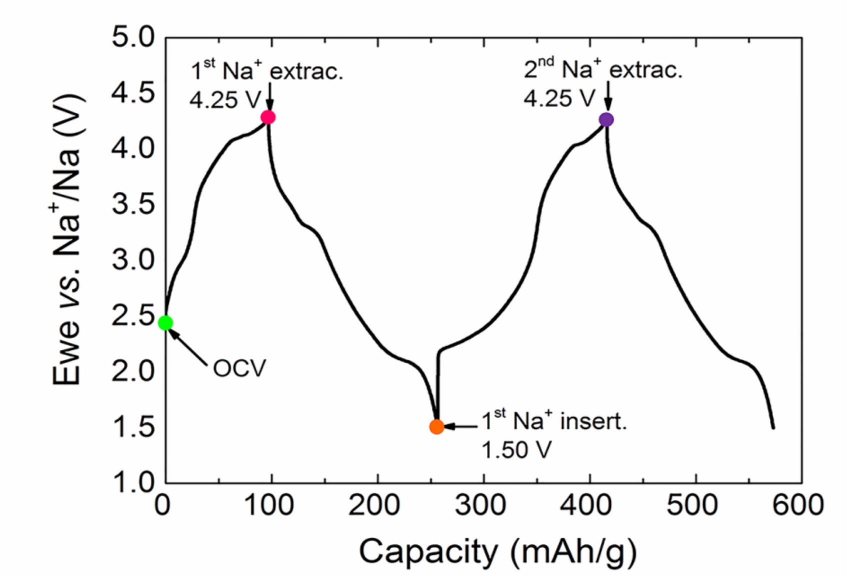

Figure 4.17: Galvanostatic cycling profile of **P2-NFMO-LV** during the first cycles in the voltage range of 1.5 – 4.25 V *vs.* Na^+/Na. The XPS measurements are performed in the highlighted points of the curve. Moreover, pristine electrode is measured.

4.5.1. Conventional XPS study

Figure 4.18 shows the C 1*s* photoemission line of the **P2-NFMO-LV** electrode at different charge states which provides crucial information about the electrolyte decomposition and the stability of the SPI layer. The main peak of the pristine sample, located at 284.4 eV, is assigned to graphitic-like compound which corresponds to the conductive additive C65 [26]. As already detailed in **chapter 3**, **section 3.3.1.1.** beside the inherent asymmetry of the graphite peak [27] and the presence of hydrocarbons (C-H or C-C bonds) at 285.0 eV [26] several overlaps are expected in the C 1*s* signal namely Π–Π* transition with -CF_2 group of PVdF at 290-291 eV [28]. Additionally PVdF exhibits another peak corresponding of -CH_2 group at 286.2 eV [29]. It is expected that some Na_2CO_3 covers the outward surface of the pristine electrode, already observed in other Na-based layered oxides. That might explain the reason of show a semicircle at HF which is correlated with the SPI resistance [11]. However the signal should be appear around 290.5 - 291.0 eV overlapping with the –CF_2 peak. Hence, it is necessary to analyze the O 1*s* photoelectron spectrum.

The C 1*s* spectrum of the electrode at OCV is similar to the one from the pristine electrode. Although for the OCV sample a peak around 286.3 eV from C-O-C compounds such as polyethylene oxide (PEO) [30] is detected which results from direct polymerization of EC [31].

At 4.25 V, after full Na^+ are extracted, the shape of the C 1*s* photoelectron line is almost similar to OCV electrode which advance that the SPI layer is quite thin and almost stable. However, the graphitic peak at 284.4 eV undergoes an intensity reduction owing to the formation of a discontinuous and/or very thin (<5 nm) SPI layer on the electrode surface. The SPI layer at 4.25 V *vs.* Na^+/Na is mainly constituted by C-O-C-based compounds such as PEO ($(\text{-}CH_2\text{-}CH_2\text{-}O\text{-})_n$), already present at OCV [30], and Na_2CO_3 resulting from the electrolyte oxidation [16, 26]. Therefore, although the working voltage range of **P2-NFMO-LV** is inside the ESW of the commonly organic electrolyte [32] and hence the electrolyte oxidation is not expected, the decomposition process already starts at OCV.

The intensity of the graphite-like signal is further reduced at full Na^+ insertion state and at the same time, the peak at 287 - 288 eV evolves indicating that $NaCO_3R$ are formed at the electrode surface [30]. Interestingly the $NaCO_3R$ formation is reversible and the peak disappears after the 2nd Na^+ extraction, showing almost the same C 1*s* spectrum as the one from the electrode stopped after the 1st Na^+

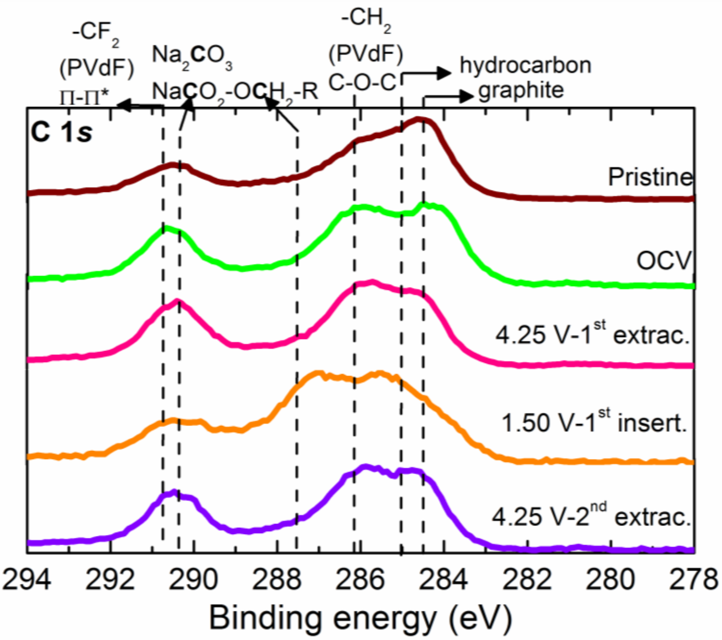

Figure 4.18: C 1*s* photoelectron spectra of **P2-NFMO-LV** electrode before cycling (pristine) and at different charge states during Na^+ extraction/insertion curve as indicated in **Figure 4.17**.

extraction cycle. Other Na-based layered oxides have shown a similar trend [11]. However, although the SPI layer undergoes a partial reversible dissolution of $NaCO_3R$ it should be take into account that the SPI layer is very thin and/or discontinuous and the amount that is dissolved during the extraction is very low.

The O 1*s* spectra is featured in **Figure 4.19a** and the main component in all studied charge states corresponds to Na_2CO_3 at ~ 532 eV [16, 33]. Therefore, as expected, the O 1*s* spectra confirm that the active material particle surface is covered by Na_2CO_3 even before the electrode is in contact with the electrolyte. In fact, the majority of layered oxides, including the P2-$Na_{2/3}[Fe_{1/2}Mn_{1/2}]O_2$, are very sensitive to air exposure and formation of Na_2CO_3 will occur during the synthesis process [11, 13]. The secondary peak at ~ 530.5 eV in the pristine electrode is assigned to the active material P2-$Na_{2/3}[Fe_{1/2}Mn_{1/2}]O_2$ which disappears once the electrode is in contact with the electrolyte. At the same time the formation of C-O-C compounds and Na_2CO_3 cover the outermost surface. Since not active material is observed at different charge state on O 1*s* spectra but graphite signal from C65 is shown in C 1*s* spectra of all electrodes (**Figure 4.18**). Considering that, the Na_2CO_3 is formed on the surface of the active material while at full Na^+ insertion state the $NaCO_3R$ covers slightly the C65 surface. This is in agreements with O 1*s* spectra

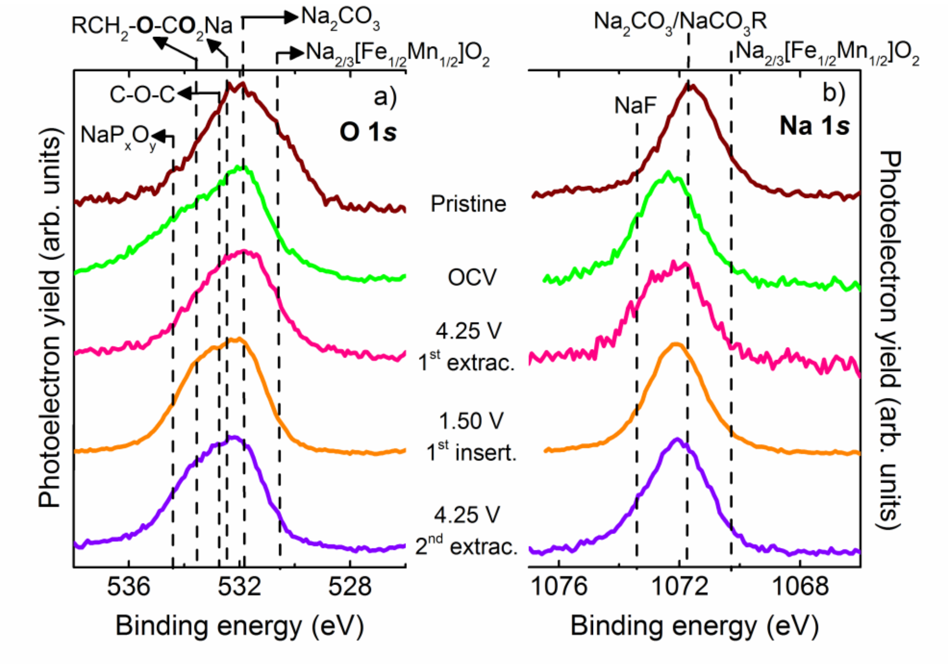

Figure 4.19: a) O 1*s* and **b)** Na 1*s* photoelectron spectra of **P2-NFMO-LV** electrode before cycling (pristine) and at different charge state during Na^+ extraction/insertion curve as indicated in **Figure 4.17**. The O 1*s* spectra have been measured by K*α* Mg sources.

since the shape is almost stable during cycling, but just at full Na^+ insertion state the corresponding peaks of $NaCO_3R$ develop (532.5 and 534 eV) [30]. Hence the SPI layer is thinner than 5 nm and not homogeneously distributed. Moreover, at higher binding energy, above 534 eV, the presence of the electrolyte salt decomposition products such as fluorophosphates, can be detected [34].

The Na 1*s* photoelectron line is more sensitive for the outmost area of SPI layer. **Figure 4.19b** shows that the main compound at the outward of the SPI layer corresponds to Na_2CO_3 (~ 1072 eV) in all charge states in agreement with C 1*s* and O 1*s* spectra. Additionally, at lower binding energy close to 1070 eV, the contribution of the active material can be marginally observed along with traces of NaF at 1073.5 eV [11]. The NaF might be originated from the electrolyte salt ($NaFP_6$) decomposition, although having some NaF originated by the dehydrofluorination reaction of the PVdF cannot be ruled out; as it has been already observed in the studied $Na_2Ti_3O_7$ anode (see **chapter 3**, **Figure 3.15**).

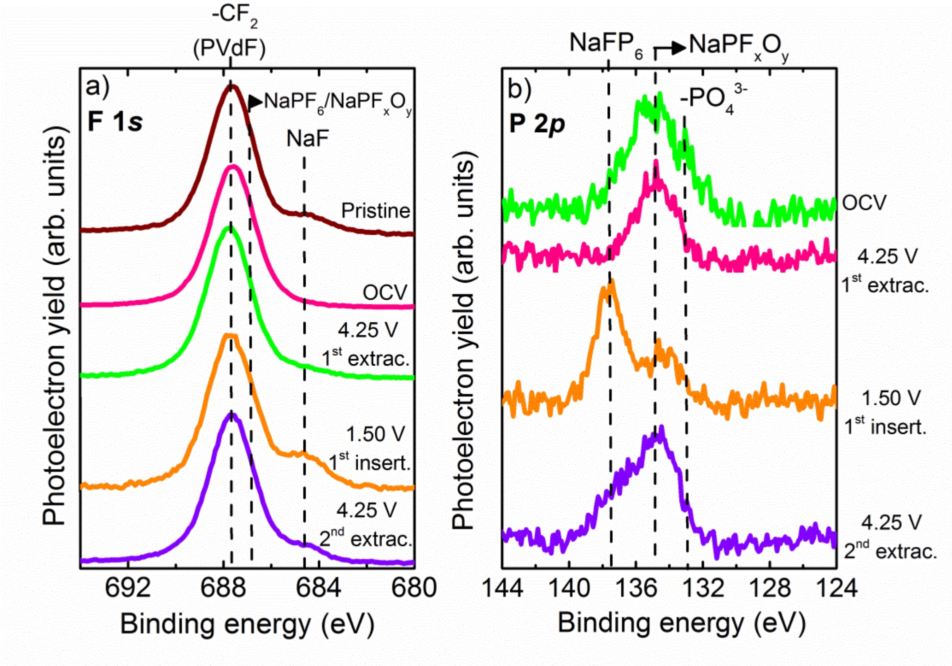

Figure 4.20: a) F 1*s* and **b)** P 2*p* photoelectron spectra of **P2-NFMO-LV** electrode before cycling (pristine) and at different charge state during Na^+ extraction/insertion curve as indicated in **Figure 4.17**.

The main component of the F 1*s* XPS peak (**Figure 4.20a**) corresponds to the $-CF_2$ group of PVdF (~ 688 eV) is always visible during the electrochemical cycling, verifying that the SPI layer is thin and not homogenously distributed [29]. In agreement with the Na 1*s* spectrum, the F 1*s* peak from the pristine sample also exhibited traces of NaF (~ 685 eV) from the decomposition of PVdF [17]. Moreover, the NaF signal exhibits a cyclic behaviour during the Na^+ extraction/insertion, disappearing and appearing, respectively. The source of NaF in the pristine electrode comes from PVdF dehydrofluorination reaction while for the other electrodes the origin of NaF not only comes from PVdF, in addition from the decomposition products of the salt since another decomposition product appears: $NaPF_xO_y$ around 687 eV.

The P 2*p* photoelectron peaks (**Figure 4.20b**), besides traces of $NaPF_6$ (~ 138 eV) not removed during electrode washing, reveal the decomposition products of the electrolyte salt such us fluorophosphates ($NaPF_xO_y$, at 135 eV) and phosphates (PO_4^{3-}, 133 eV) [35, 36]. Interestingly, at OCV the salt is already decomposed showing $NaPF_xO_y$ which is the main compound in P 2*p* spectra of all samples except on the 1st Na^+ insertion where the large amount of unwashed $NaPF_6$ is covering part of the $NaPF_xO_y$ signal. At the light of these data, it can be concluded that

$NaFP_6$ spontaneously decomposes forming $NaPF_xO_y$ even before the electrochemical cycling starts; analogously to the $NaClO_4$ in the $Na_2Ti_3O_7$ negative electrode (see **chapter 3, Figure 3.17**) [17].

4.6. Conclusions

The P2-$Na_{2/3}[Fe_{1/2}Mn_{1/2}]O_2$ layered oxide is a promising cathode for Na-ion batteries that shows capacity degradation during cycling [5, 8, 10], independently of the electrolyte choice. However, a capacity retention improvement has been shown by controlling the working voltage range. The sample tested with a larger voltage window of 1.5 - 4.25 V shows much lower capacity retention than the sample which has been tested at a smaller voltage window of 2.0 - 4.0 V *vs.* Na^+/Na. The EIS experiments have been carried out in both voltage windows (1.5 - 4.25 V and 2.0 - 4.0 V *vs.* Na^+/Na) and both experiments show that in the P2 solid solution region (2.0-4.0 V *vs.* Na^+/Na) the bulk electronic resistance during the Na^+ extraction is reduced while during insertion the bulk electronic resistance increases. During the Na^+ deintercalation the *a* cell parameter is reduced and hence the T_M-T_M distance is shorter, increasing the conductivity along *a*. However, during the Na^+ intercalation the opposite behaviour is observed.

Moreover, comparing the behaviour of the bulk electronic resistance, the sample tested in a larger voltage window shows the transition phase from ordered P2 to disorder OP4 (close to 4.0 V) and hence the R_{elec} increases drastically. The reason is based on the formation of staking faults and defects. Moreover, although the behaviour is almost reversible the values of R_{elec} increases even more in the following cycles, showing higher resistance or lower conductivity during the electrochemical cycling. Nevertheless, if a cut-off voltage is set before the P2-OP4 transition phase, the R_{elec} does not increase, with more stable values during cycling and providing better capacity retention.

Additionally, since the electrode/electrolyte interphase can also be another factor at the origin of the capacity degradation, a thorough study of the SPI layer has been carried out by means of XPS. As a result it has been found that (**Figure 4.21**) the pristine electrode, before any contact with the electrolyte, is already partially covered by Na_2CO_3 and NaF originated by the active material reactivity against air and the dehydrofluorination reaction of the PVdF, respectively.Once the electrode is assembled (OCV electrode) in a half-cell, in contact with the electrolyte and metallic Na, spontaneous decomposition of the $NaPF_6$ electrolyte salt and solvents lead to the formation of $NaPF_xO_y$ and species with C-O group such as PEO. At full Na^+ extraction state the SPI layer is mainly formed by inorganic compounds (Na_2CO_3, fluorophosphates and phosphate). Meanwhile at full Na^+ insertion state the presence of NaF and $NaCO_3R$ compounds is observed. Although, a partial dissolution of $NaCO_3R$ is observed the main component of the layer is Na_2CO_3

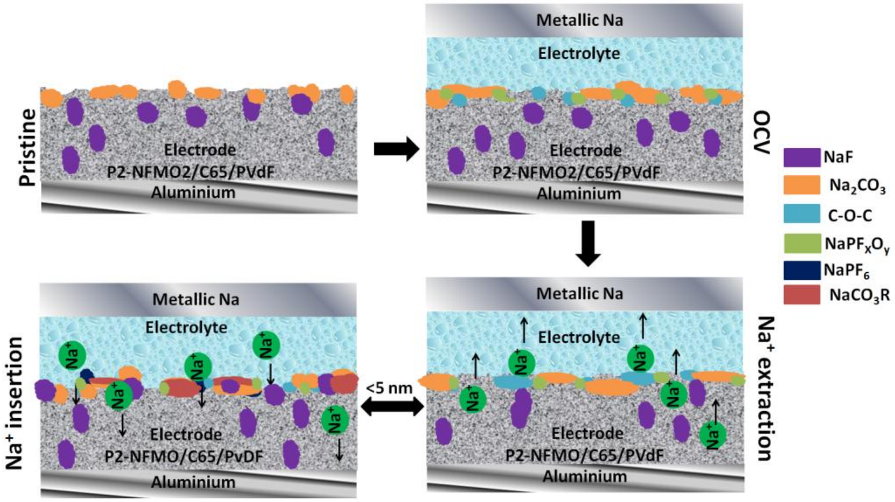

Figure 4.21: Schematic picture of the SPI layer at different oxidation states of **P2-NFMO-LV** sample.

which is observed in all oxidation state of the cycling. Moreover, always it is possible to observe the conductive additive Super C65 and the $-CF_2$ signal of the PVDF. Hence the SPI layer is almost stable mainly formed by inorganic compounds analogously to the SEI layer of negative electrodes, thin (<5 nm) and discontinuously distributed.

As conclusion, since almost stable SPI layer is formed with a few changes upon cycling but the bulk electronic resistance increases drastically when phase transition occurs at high voltage (from P2 to OP4), which gradually increases in the following cycles, the capacity degradation is linked with the structural transition upon cycling and not to electrode/electrolyte interphase.

.

4.7. References

---

[1] M.H. Han, E. Gonzalo, G. Singh, T. Rojo, A comprehensive review of sodium layered oxides: powerful cathodes for Na-ion batteries, Energy Environ. Sci. 8 (2015) 81-102.

[2] N. Yabuuchi, M. Kajiyama, J. Iwatate, H. Nishikawa, S. Hitomi, R. Okuyama, R. Usui, Y. Yamada, S. Komaba, P2-type $Na_x[Fe_{1/2}Mn_{1/2}]O_2$ made from earth-abundant elements for rechargeable Na batteries, Nat. Mater. 11 (2012) 512-517.

[3] M.H. Han, E. Gonzalo, N. Sharma, J.M. López del Amo, M. Armand, M. Avdeev, J.J. Saiz Gariotaonandia, T. Rojo, High-performance P2-phase $Na_{2/3}Mn_{0.8}Fe_{0.1}Ti_{0.1}O_2$ cathode material for ambient-temperature sodium-ion batteries, Chem. Mater. 28 (2016) 106-116.

[4] H. Yoshida, N. Yabuuchi, K. Kubota, I. Ikeuchi, A. Garsuch, M. Schulz-Dobrick, S. Komaba, P2-type $Na_{2/3}Ni_{1/3}Mn_{2/3-x}Ti_xO_2$ as new positive electrode for higher energy Na-ion batteries, Chem. Comm. 50 (2014) 3677-3680.

[5] E. Talaie, V. Duffort, H.L. Smith, B. Fultz, L.F. Nazar, Structure of the high voltage phase of layered $P2-Na_{2/3-z}[Mn_{1/2}Fe_{1/2}]O_2$ and the positive effect of Ni substitution on its stability, Energy Environ. Sci. 8 (2015) 2512-2523.

[6] J. Xu, S.L. Chou, J.L. Wang, H.K. Liu, S.X. Dou, Layered $P2-Na_{0.66}Fe_{0.5}Mn_{0.5}O_2$ cathode material for rechargeable sodium-ion batteries, Chem. Electro. Chem. 1 (2014) 371-374.

[7] Y. Bai, L. Zhao, C. Wu, H. Li, Y. Li, F. Wu, Enhanced sodium ion storage behavior of P2-type $Na_{2/3}Fe_{1/2}Mn_{1/2}O_2$ synthesized via a chelating agent assisted route, ACS Appl. Mater. Interfaces 8 (2016) 2857-2865.

[8] B. Mortemard de Boisse, D. Carlier, M. Guignard, L. Bourgeois, C. Delmas, P2-$Na_xMn_{1/2}Fe_{1/2}O_2$ phase used as positive electrode in Na batteries: structural changes induced by the electrochemical (de)intercalation process, Inorg. Chem. 53 (2014) 111977-11205.

[9] G. Singh, J.M. López del Amo, M. Galceran, S. Pérez-Villar, T. Rojo, Structural evolution during sodium deintercalation/intercalation in $Na_{2/3}[Fe_{1/2}Mn_{1/2}]O_2$, J. Mater. Chem. A 3 (2015) 6954-6961.

[10] W.K. Pang, S. Kalluri, V.K. Peterson, N. Sharma, J. Kimpton, B. Johannessen, H.K. Liu, S.X. Dou, Z. Guo, Interplay between electrochemistry and phase evolution of the P2-type $Na_x(Fe_{1/2}Mn_{1/2})O_2$ cathode for use in sodium-ion batteries, Chem. Mater. 27 (2015) 3150-3158.

[11] S. Doubaji, B. Philippe, I. Saadoune, M. Gorgoi, T. Gustafsson, A. Solhy, M. Valvo, H. Rensmo, K. Edström, Passivation layer and cathodic redox reactions in sodium-ion batteries probed by HAXPES, Chem. Sus. Chem. 9 (2016) 97-108.

[12] K. Kubota, S. Komaba, Review-practical issues and future perspective for Na-ion batteries, J. Electrochem. Soc. 162 (2015) A2538-A2550.

[13] M. Sathiya, K. Hemalatha, K. Ramesha, J.M. Tarascon, A.S. Prakash, Synthesis, structure, and electrochemical properties of the layered sodium insertion cathode material: $NaNi_{1/3}Mn_{1/3}Co_{1/3}O_2$, Chem. Mater. 24 (2014) 1846-1853.

---

[14] G. Singh, B. Acebedo, M. Casas-Cabanas, D. Shanmukaraj, M. Armand, T. Rojo, An approach to overcome first cycle irreversible capacity, Electrochem. Commun. 37 (2013) 61-63.
[15] J.J. Ding, Y.N. Zhou, X.Q. Yu, X.Q. Yang, .W. Fu, Electrochemical properties of P2-phase $Na_{0.74}CoO_2$ compounds as cathode material for rechargeable sodium-ion batteries, Electrochim. Acta 87 (2013) 388-393.
[16] S. Komaba, W. Murata, T. Ishikawa, N. Yabuuchi, T. Ozeki, T. Nakayama, A. Ogata, K. Gotoh, K. Fujiwara, Electrochemical Na insertion and solid electrolyte interphase for hard-carbon electrodes and application to Na-ion batteries, Adv. Funct. Mater. 21 (2011) 3859-3867.
[17] M.A. Muñoz-Márquez, M. Zarrabeitia, E. Castillo-Martínez, A. Eguía-Barrio, T. Rojo, M. Casas-Cabanas, Composition and evolution of the solid-electrolyte interphase in Na_2Ti_3O7 electrodes for Na-ion batteries: XPS and Auger parameter analysis, ACS Appl. Mater. Interfaces 7 (2015) 7801-7808.
[18] E. Barsoukov, J.Ross Macdonald, Impedance spectroscopy theory, experiment and application, 2nd ed., John Wiley & Sons Inc., Hoboken, New Jersey 2005.
[19] F. Croce, F. Nobili, A. Deptula, W. Lada, R. Tossici, A. D´Epifanio, B. Scrosati, R. Marassi, An electrochemical impedance spectroscopy study of the transport properties of $LiNi_{0.75}Co_{0.25}O_2$, Electrochem. Commun. 1 (1999) 605-608.
[20] F. Nobili, T. Tossici, R. Marassi, F. Croce, B. Scrosati, An AC impedance spectroscopy study of Li_xCoO_2 at different temperatures, J. Phys. Chem. B 106 (2002) 3909-3915.
[21] M. Zarrabeitia, F. Nobili, M.A. Muñoz-Márquez, T Rojo, M. Casas-Cabanas, Direct observation of electronic conductivity transitions and solid electrolyte interphase stability of $Na_2Ti_3O_7$ electrodes for Na-ion batteries, J. Power Sources 330 (2016) 78-83.
[22] F. Nobili, S. Dsoke, M. Minicucci, F. Croce, R. Marassi, Correlation AC-impedance and in situ X-ray spectra of $LiCoO_2$, J. Phys. Chem. B 110 (2006) 11310-11313.
[23] B. A. Boukamp, Parametic analysis using impedance spectroscopy: relationship between material properties and battery performance, Solid State Ionics 20 (1986) 31-44.
[24] F. Nobili, F. Croce, R. Tossici, I. Meschini, P. Reale, R. Marassi, Sol-gel synthesis and electrochemical characterization of Mg-/Zr-doped $LiCoO_2$ cathodes for Li-ion batteries, J. Power Sources 197 (2012) 276-284.
[25] C.D. Wagner, W.M. Riggs, L.E. Davis, J.F. Moulder, G.E. Mullenberg, Handbook of X-ray photoelectron spectroscopy, Perkin-Elmer Corporation, Physical Electronics Division, Eden Prairie, Minnesota 1979.
[26] R.I.R. Blyth, H. Buqa, F.P. Netzer, M.G. Ramsey, J.O. Besenhard, P. Golob, M. Winter, XPS studies of graphite electrode materials for lithium ion batteries, Appl. Surf. Sci. 167 (2000) 99-106.
[27] http://www.xpsfitting.com/search/label/Graphite (acceded in August 2016).
[28] A.M. Bradshaw, S.L. Cederbaum, W. Domcked, U. Kraus, Plasmon coupling to core hole excitations in carbon, J. Phys. C: Solid State Phys. 7 (1974) 4503-4512.

[29] G. Beamson, D. Briggs, High Resolution XPS of Organic Polymers: The Scienta ESCA300 Database, John Wiley & Sons, Chichester UK 1992.
[30] A.M. Andersson, A. Henningson, H. Siegbahn, U. Jansson, K. Edström, Electrochemically lithiated graphite characterized by photoelectron spectroscopy, J. Power Sources 119-120 (2003) 522-527.
[31] L. Vogdanis, W. Heitz, The polymerization of ethylene carbonate; Makromol. Chem., Rapid Commun. 7 (1986) 543-547.
[32] J.B. Goodenough, Y Kim, Challenges for rechargeable Li batteries, Chem. Mater. 22 (2010) 587-603.
[33] S. Malmgren, K. Ciosek, M. Hahlin, T. Gustafsson, M. Gorgoi, H. Rensmo, K. Edtröm, Comparing anode and cathode electrode/electrolyte interface composition and morphology using soft and hard X-ray photoelectron spectroscopy, Electrochim. Acta 97 (2013) 23-22.
[34] M. Khasanov, E. Pazhetnov, W.C. Shin, Dicarboxylate-substituted ethylene carbonate as an SEI-forming additive for lithium-ion batteries, J. Electrochem. Soc. 162 (2015) A1892-A1898.
[35] L. Bodenes, A. Darwiche, L. Monconduit, H. Martinez; The solid electrolyte interphase a key parameter of the high performance of Sb in sodium-ion batteries: comparative X-ray photoelectron spectroscopy study of Sb/Na-ion and Sb/Li-ion batteries; J. Power Sources 273 (2015) 14-24.
[36] N. Membreno, K. Park, J.B. Goodenough, K.J. Stevenson; Electrode/electrolyte interface of composite, Electrode/electrolyte interface of composite #-LiV(PO) cathodes in a non-aqueous electrolyte for lithium ion batteries and the role of the carbon additive, Chem. Mater. 27 (2015) 3332-3340.

5 $Na_4Co_3(PO_4)_2P_2O_7$ as cathode material of NIBs: electrochemical and transport properties and study of the SPI layer

This chapter is focused on the study of the highest voltage cathode material, $Na_4Co_3(PO_4)_2P_2O_7$, which displays an average operation voltage of 4.5 V *vs.* Na^+/Na (V). Firstly, the structural, morphological and electrochemical characterization have been carried out, as well as the study of the structural evolution during the electrochemical cycling by synchrotron XRD (HRXRD). Secondly, the transport properties have been studied by Electrochemical Impedance Spectroscopy (EIS). Finally, the evolution, composition and transport properties of the SPI layer have been investigated by EIS and X-ray Photoelectron Spectroscopy (XPS), the latter combining conventional XPS measurements (Mg K_α) and depth profiling by high energy XPS with a laboratory-based Ag L_α X-ray source.

5.1. Introduction

Mixed polyanions containing phosphate (PO_4^{3-}) and pyrophosphate ($P_2O_7^{4-}$) groups with general formula $Na_4T_{M3}(PO_4)_2P_2O_7$.(T_M = Co [1], Fe [2], Mn [3], Ni [4]) [5] have been recently reported as Na-ion cathode materials. The combination of these two polyanionic groups delivers higher theoretical capacity than the pyrophosphate compounds and allows reaching higher redox potential values, because of the inductive effect of polyanion groups, when compared to pure phosphates or pyrophosphates [6, 7]. By increasing the operating voltage, the lower capacity of polyanionic compounds is compensated and energy density values comparable to layered oxides are obtained. For example, the P2-$Na_x[Ni_{(1-x-y-z)}Mn_XMg_yTi_z]O_2$ layered oxide which is a cathode material used by Faradion company with a specific capacity of 146 mAh/g has a practical energy density of 467 Wh/Kg *vs.* HC [8], while $Na_4Co_3(PO_4)_2P_2O_7$ which has a specific capacity of 127 mAh/g can deliver 428 Wh/Kg *vs.* Na with an excellent retention.

The highest Na^+ insertion/extraction voltage (4.5 V *vs.* Na^+/Na) and a good theoretical capacity (127 mAh/g) are the reasons to choose $Na_4Co_3(PO_4)_2P_2O_7$ as cathode material for this study. During the Na deintercalation the Co^{2+} is completely oxidised to Co^{3+} with slightly distorted oxygen octahedral. In both cases the Co ions are stabilized in a high spin state. During this process 3 Na^+ are extracted one after the other, Na2, Na3 and finally Na4, only remaining the Na1 type and reaching a composition of $NaCo_3(PO_4)_2P_2O_7$ (**Figure 5.1**). The first-principles calculations suggest the possibility of increasing the operating voltage and removing all Na^+ obtaining Co^{4+} oxidation state at complete charge state ($Co_3(PO_4)_2P_2O_7$). However, from a practical point of view, it is very difficult to remove all Na^+ since large volume contraction is observed at voltage above 4.7 V. The experimental specific capacity of this material is not high if compared with other Na-based cathode materials: 95 mAh/g at 0.2C which is the 75% of the theoretical capacity. However, this drawback is compensated by three interesting properties, namely, high reaction voltage, negligible capacity fading after 100 cycles and very low 1st cycle irreversible capacity (c.f **Table 1.10**) [1, 9]. Additionally, there are reports of this compound being cycled at high current densities, 4250 mA/g (25C), with a reversible capacity of 80 mAh/g, becoming a very good candidate for high power applications [1]. Still, the $NaCo_3(PO_4)_2P_2O_7$ reaction mechanism has not been studied in detail, however, due to the several redox processes that appear in its CV curve [1], a multi-phase reaction mechanism can be expected, as is the case for $Na_4Mn_3(PO_4)_2P_2O_7$ [3]. On the contrary, isostructural $Na_4Fe_3(PO_4)_2P_2O_7$ follows a single phase reaction [10].

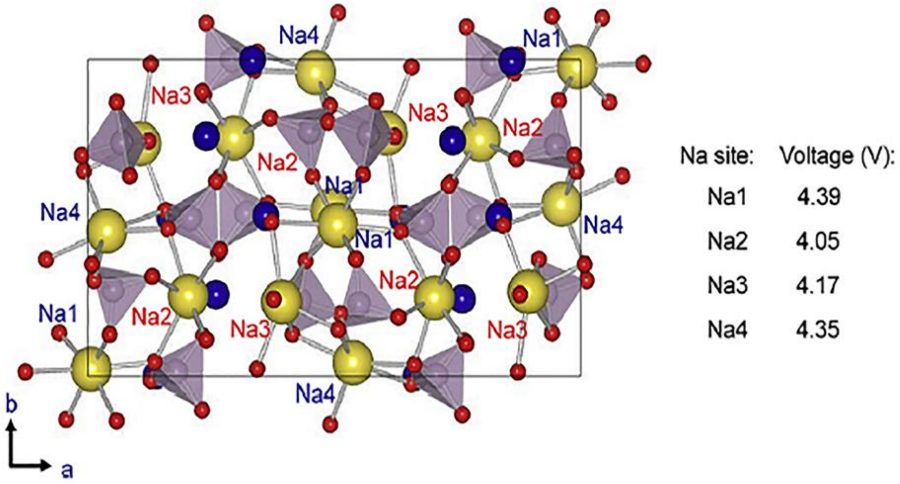

Na site:	Voltage (V):
Na1	4.39
Na2	4.05
Na3	4.17
Na4	4.35

Figure 5.1: Na coordination environments and calculated battery voltage after deintercalation of $Na_4Co_3(PO_4)_2P_2O_7$ to $Co_3(PO_4)_2P_2O_7$. 7-coordinated Na sited (yellow) and six coordinated Na sites (blue). Reprinted from [9]

Note that in NIBs voltage values are reported *vs.* Na^+/Na, therefore the high voltage stability limit of the electrolyte will be shifted towards higher values, providing the possibility to use high voltage insertion cathode materials. For example, the theoretical electrochemical stability window (ESW) of $LiFP_6$ in EC:DEC is around 1.0 - 4.7 V *vs.* Li^+/Li [11] although some side reactions occur above 3.0-3.5 V [12]. Meanwhile the theoretical EWS of $NaPF_6$ in EC:DMC exhibits good stability until 5.0 V *vs.* Na^+/Na, using as current collector Al and carbon gas diffusion layer as working electrode [13]. However, the formation of a SPI layer in $Na_4Co_3(PO_4)_2P_2O_7$ electrodes is already expected when the electrolyte is in contact with the electrode material prior to any electrochemical cycling [13], as it has been already observed in the studied layered oxide (**chapter 4**).

5.2. Synthesis of $Na_4Co_3(PO_4)_2P_2O_7$

$Na_4Co_3(PO_4)_2P_2O_7$ was synthesized by sol-gel method [1]. The precursors $Na_4P_2O_7$, $(CH_3COO)_2Co$ and $NH_4H_2PO_4$ were added stoichiometrically in a diluted HNO_3 solution with a proportion of 3 mol of HNO_3 per mole of total metal ions. Once the precursors were dissolved in the acidic media, ethylene glycol (EG) was added in a proportion of 3/4 mol of EG per mole of HNO_3. The liquid solution was stirred and heated up to 80 ^{o}C for 12 h until a gel was obtained. Then the gel was heated up to

300 °C for 3 h to remove the organic material and the obtained powder was compressed in pellets and annealed at 700 °C for 50 h in open air. The obtained **NCP** powder was mixed with two different carbon precursors so as to grow a C-coating on the active material. One of them was phthalocyanine (Ph), the same carbon precursor used to prepare the **NTO-OH-Ar-C** sample (see **2.2.4 section**). Several **NCP**:Ph weight ratios were tested (1:1, 2:1, 3:1, 4:1 and 5:1). Carbon Black Performance (CBP) (Cabot) was also used as carbon precursor in a weight ratio of 5:1. This second carbon precursor was tested because it shows similar properties as VGCF (Vapor-Grown Carbon Fiber) which has been successfully used for on this cathode material in the same ratio that it was studied in this work [1]. All samples were pyrolyzed at 700 °C during 5 h under Ar atmosphere obtaining in total five samples with different ratio of **NCP**:Ph (NCP-CP (x:1), x=1, 2, 3, 4, 5) and one extra sample with CBP (**NCP-C**).

5.3. Structural and morphological characterization

5.3.1. Powder X-ray Diffraction (PXRD)

The PXRD pattern of **NCP** has been refined by the Rietveld method taking as starting parameters those of PDF file 01-089-0579 (**Figure 5.2a**) and refining the zero and scale factor, cell and profile parameters, atomic positions and the overall isotropic displacement parameter (B_{ove}). The cell parameters, B_{ove} and reliability factors are collected in **Table 5.1**. The cell parameters are in agreement with previously reported data [14] and the pattern does not show any impurities. The PXRD patterns of C-coated samples **NCP-CP (5:1)** (this ratio was taken as example) and **NCP-C** are very similar to that of uncoated sample (see **Figure 5.2b** and **Figure 5.2c** for **NCP-CP (5:1)** and **NCP-C**, respectively) which indicates that the extra heat treatment to C-coat the material does not influence the structure of the material. Moreover, the refined atomic positions of the three samples (**NCP**, **NCP-CP (5:1)** and **NCP-C**) are collected in **Table 5.2** and they are also similar. The only difference is a broad peak around 2 Theta = 20 °, which is more pronounced in the **NCP-CP (5:1)** sample, and can be assigned to the carbon used to cover the active particles.

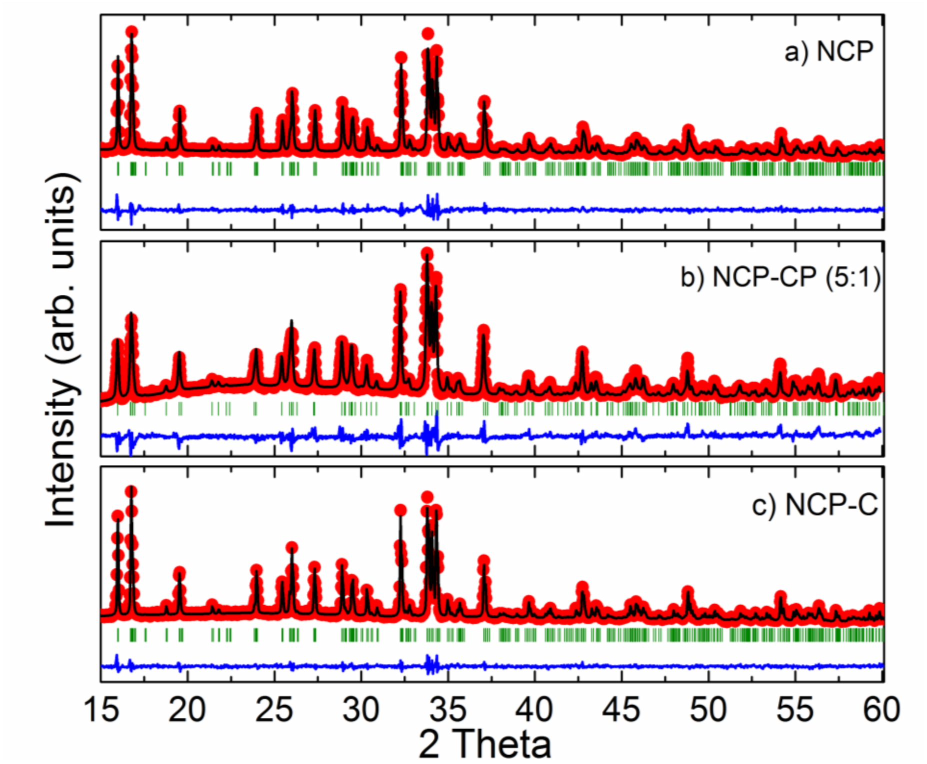

Figure 5.2: Rietveld refined PXRD data of **a)** uncoated **NCP** and C-coated **b)** **NCP-Ph (5:1)** and **c)** **NCP-C**. Observed (red points), calculated (black line), difference (blue line) and Bragg reflection (green vertical bars).

Table 5.1: Atomic positions, overall isotropic displacement parameters (B_{ove}) and reliability factors of uncoated **NCP** and C-coated **NCP-Ph (5:1)** and **NCP-C** samples ($Pn2_1a$) determined by Rietveld method from PXRD data at room temperature.

Cell parameters				
	a (Å)	*b* (Å)	*c* (Å)	B_{ove}(Å^2)
NCP	18.0392(5)	6.5203(2)	10.5127(2)	0.4(2)
NCP-CP (5:1)	18.056(2)	6.5278(6)	10.521(1)	0.9(3)
NCP-C	18.0441(2)	6.52621(8)	10.5178(1)	0.8(2)

Reliability factors					
	χ^2	R_p	R_{wp}	R_e	R_F
NCP	3.38	20.3	15.4	8.50	5.39
NCP-CP (5:1)	7.61	24.2	23.1	8.38	9.86
NCP-C	2.31	18.5	12.8	8.41	2.31

Table 5.2: Atomic positions and occupancies (SOF) of uncoated **NCP** and C-coated **NCP-CP (5:1)** and **NCP-C** samples (*Pn*2_1*a*) determined by Rietveld method from PXRD data at room temperature.

Atomic position and SOF

				NCP			**NCP-CP (5:1)**			**NCP-C**	
Atom	Wyckoff	SOF	*x* (Å)	*y* (Å)	*z* (Å)	*x* (Å)	*y* (Å)	*z* (Å)	*x* (Å)	*y* (Å)	*z* (Å)
Co1	4*a*	1.0	0.3375(9)	0.09(1)	0.506(2)	0.337(3)	0.16(3)	0.511(6)	0.3370(6)	0.113(8)	0.504(2)
Co2	4*a*	1.0	0.138(1)	0.58(1)	0.502(3)	0.141(3)	0.64(1)	0.500(8)	0.138(7)	0.598(8)	0.500(2)
Co3	4*a*	1.0	0.244(1)	0.31(1)	0.740(3)	0.249(4)	0.33(2)	0.743(9)	0.245(1)	0.328(8)	0.747(3)
P1	4*a*	1.0	0.290(2)	0.56(2)	0.511(5)	0.300(9)	0.588(2)	0.52(1)	0.291(1)	0.58(1)	0.514(4)
P2	4*a*	1.0	0.174(2)	0.08(1)	0.485(5)	0.174(8)	0.110(2)	0.495(9)	0.174(1)	0.110(9)	0.495(4)
P3	4*a*	1.0	0.565(2)	0.44(1)	0.733(5)	0.572(6)	0.50(2)	0.75(2)	0.566(1)	0.454(8)	0.733(4)
P4	4*a*	1.0	0.452(2)	0.13(1)	0.750(4)	0.448(7)	0.13(3)	0.72(1)	0.451(1)	0.139(8)	0.747(3)
O1	4*a*	1.0	0.214(4)	0.52(2)	0.624 (7)	0.22(1)	0.62(4)	0.65(2)	0.222(3)	0.55(1)	0.625(5)
O2	4*a*	1.0	0.344(5)	0.42(2)	0.486(9)	0.35(1)	0.45(2)	0.42(2)	0.345(4)	0.43(1)	0.467(6)
O3	4*a*	1.0	0.335(4)	0.73(2)	0.122(6)	0.33(1)	0.79(6)	0.55(2)	0.342(3)	0.76(1)	0.547(5)
O4	4*a*	1.0	0.240(4)	0.59(2)	0.392(8)	0.25(1)	0.60(5)	0.43(3)	0.238(3)	0.61(1)	0.393(7)
O5	4*a*	1.0	0.227(3)	0.10(2)	0.598(7)	0.23(1)	0.10(2)	0.62(2)	0.234(3)	0.14(1)	0.611(7)
O6	4*a*	1.0	0.112(4)	-0.11(1)	0.510(8)	0.11(1)	-0.07(4)	0.47(2)	0.115(3)	-0.117(9)	0.501(6)
O7	4*a*	1.0	0.234(3)	0.05(2)	0.374(7)	0.23(1)	0.12(5)	0.40(3)	0.223(3)	0.08(1)	0.394(6)
O8	4*a*	1.0	0.135(4)	0.28(1)	0.457(8)	0.14(1)	0.28(3)	0.46(2)	0.135(3)	0.28(1)	0.457(6)
O9	4*a*	1.0	0.487(5)	0.34(2)	0.691(5)	0.47(1)	0.395(6)	0.70(2)	0.484(3)	0.36(1)	0.694(4)
O10	4*a*	1.0	0.548(4)	0.55(2)	0.872(9)	0.54(1)	0.62(6)	0.86(2)	0.547(3)	0.55(1)	0.872(7)
O11	4*a*	1.0	0.617(3)	0.27(2)	0.75(1)	0.62(1)	0.29(4)	0.75(2)	0.619(2)	0.290(9)	0.753(7)
O12	4*a*	1.0	0.585(4)	0.59(2)	0.648(7)	0.59(1)	0.66(5)	0.65(2)	0.582(3)	0.62(1)	0.650(5)
O13	4*a*	1.0	0.457(4)	0.07(2)	0.874(9)	0.46(2)	0.09(6)	0.87(2)	0.459(3)	0.09(1)	0.872(7)
O14	4*a*	1.0	0.386(3)	0.18(1)	0.702(7)	0.37(1)	0.22(4)	0.70(2)	0.381(2)	0.18(1)	0.692(5)
O15	4*a*	1.0	0.490(5)	0.001(9)	0.648(7)	0.52(2)	-0.07(5)	0.63(2)	0.492(3)	0.01(1)	0.651(5)
Na1	4*a*	1.0	0.495(3)	0.80(2)	0.985(5)	0.48(1)	0.89(2)	0.99(2)	0.494(2)	0.50(1)	0.986(4)
Na2	4*a*	1.0	0.296(2)	0.83(1)	0.761(6)	0.304(8)	0.85(3)	0.76(1)	0.296(2)	0.843(9)	0.759(4)
Na3	4*a*	1.0	0.397(3)	0.40(1)	0.256(6)	0.396(8)	0.473()	0.25(2)	0.398(2)	0.423(9)	0.256(5)
Na4	4*a*	1.0	0.459(3)	0.66(1)	0.558(4)	0.447(8)	0.69(3)	0.55(1)	0.462(2)	0.675(9)	0.552(3)

5.3.2. Scanning Electron Microscopy (SEM)

SEM images have been taken before and after the annealing treatment when CBP is used as carbon precursor. Uncoated NCP (**Figure 5.3a**) is composed by big agglomerates of micrometric particles, with a heterogeneous size distribution ranging from 2 to 10 µm. Interestingly, the **NCP-C** sample (**Figure 5.3b**) exhibits particles surrounded by carbon nanotubes (C-NTs) instead of a C-coating, which would be the expected result since the employed carbon precursor does not exhibit nanotube morphology (see **section 5.3.3**). The particle size distribution obtained from laser diffraction particle size analysis indicates that the agglomerates of **NCP-C** are larger than those of NCP, with sizes in the 5 to 30 µm range (**Figure 5.3c**). The slightly higher sizes of C-coated sample might be originated by the fact that the carbon is surrounding the particles increasing the total size, and/or by lower dispersion behaviour of the C-coated sample which would need for a correct particle size characterisation.

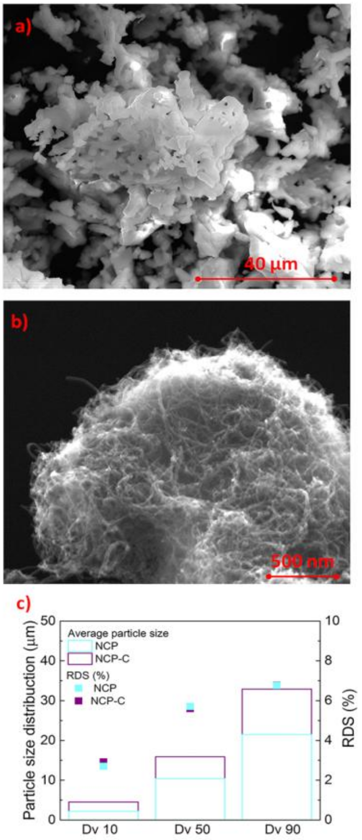

Figure 5.3: SEM images of **a)** uncoated NCP and **b)** **NCP-C**. **c)** Particle size distribution of NCP and **NCP-C** obtained by laser diffraction (points RDS%).

5.3.3. Transmission Electron Microscopy (TEM)

TEM image of the **NCP-CP (2:1)** **(Figure 5.4a**) does not show a carbon layer along with some unreacted carbon and **NCP-CP (4:1)** (**Figure 5.4b**) sample shows a non-uniform carbon layer with a thickness between 3.5 - 0.5 nm.

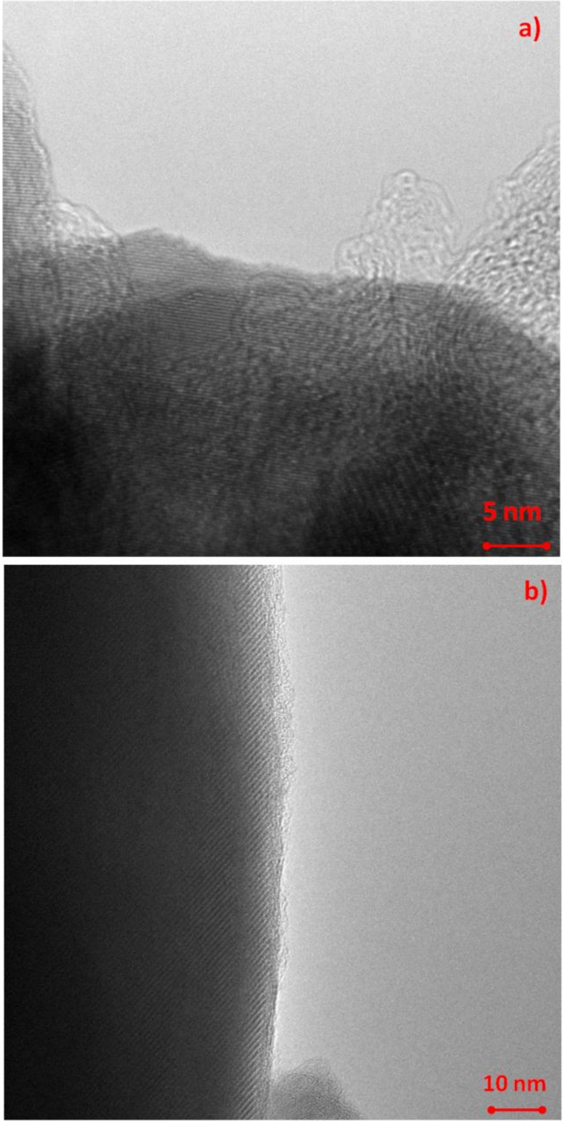

Figure 5.4: TEM images of NCP-CP sample in the weight ratio of **a) NCP-CP (2:1)** and **b) NCP-CP (4:1)**.

TEM images of the pristine CBP and the **NCP-C** particles are shown in **Figure 5.5**, from those the spherical particle morphology of the pristine CBP precursor (**Figure 5.5a**) an amorphous carbon layer would be expected to grow on the active material particles. Instead, TEM image of **NCP-C** shows that there are C-NTs as well as carbon spheres surrounding the active particles (**Figure 5.5b**). Hence the C-NTs are forming during the annealing treatment. Both spherical carbon and C-NTs create a conductivity percolation network that is expected to enhance the bulk electronic conductivity and hence the electrochemical properties, as will be shown later.

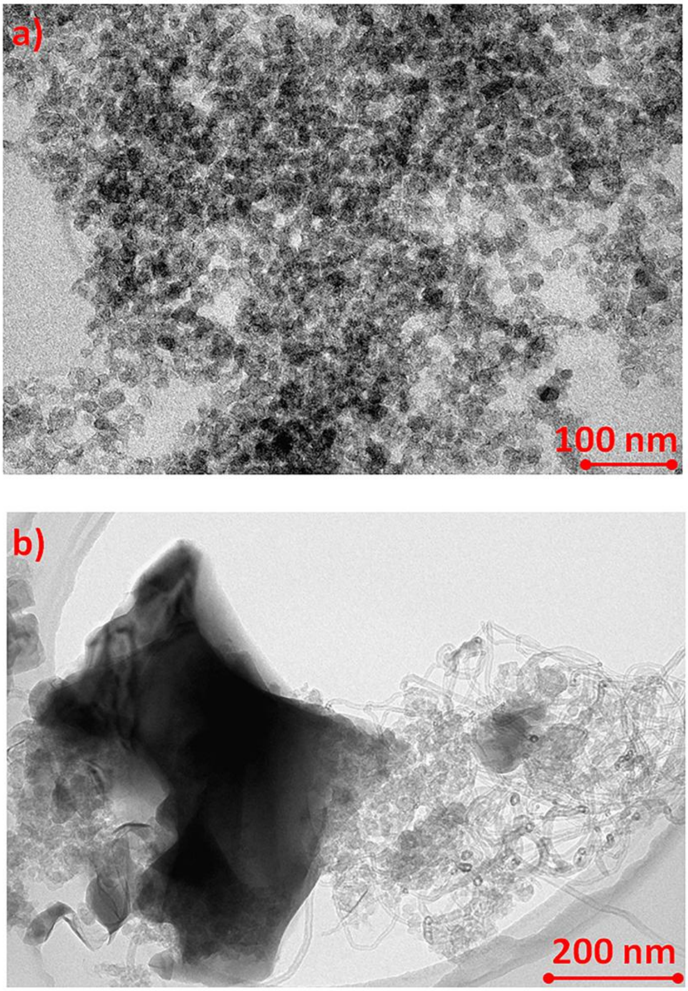

Figure 5.5: TEM images of **a)** carbon precursor CBP (Cabot) and **b NCP-C** sample.

5.3.4 Thermogravimetic analysis (TGA)

The carbon amount has been determined by TGA for all synthesized NCP-CP ((x:1), x= 1, 2, 3, 4, 5) samples. The results are collected in **Table 5.3** and two TGA curves from **NCP-CP (2:1)** and **NCP-CP (4:1)** samples are shown as example in **Figure 5.6**. For the **NCP-CP (1:1)** sample, the carbon weight is too high and a thick carbon layer is expected, while **NCP-CP (2:1)** and **NCP-CP (3:1)** samples show more typical values, around 10-5%. However, the TEM images (**Figure 5.4a**) provide that an unreacted carbon remains in **NCP-CP (2:1)** sample. Finally, for **NCP-CP (4:1)** and **NCP-CP (5:1)** samples, the carbon amount is very low, which can lead to a thin carbon layer as it has been observed by TEM image (**Figure 5.4b**). Hence, the best electrochemical performance is expected for **NCP-CP (2:1)** or **NCP-CP (3:1)** samples.

The carbon amount of the **NCP-C** sample was also determined by TGA analysis, resulting in 14 wt.% (**Figure 5.7**), which is slightly higher than in the previously studied **NTO7-OH-Ar-C** sample although lower amount of precursor was used.

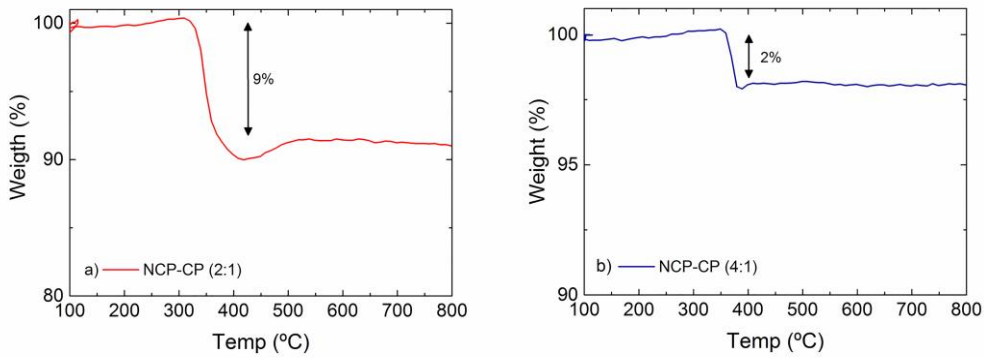

Figure 5.6: TGA analysis of **a) NCP-CP (2:1)** and **b) NCP-CP (4:1)** samples under air atmosphere heated up to 800 °C and cooled down to 30 °C.

Table 5.3: Carbon weight determined by TGA of C-coated **NCP-CP (1:1)**, **NCP-CP (2:1)**, **NCP-CP (3:1)**, **NCP-CP (4:1)** and **NCP-CP (5:1)** samples.

Sample	Carbon weight
NCP-CP (1:1)	25%
NCP-CP (2:1)	9%
NCP-CP (3:1)	5.8%
NCP-CP (4:1)	2%
NCP-CP (5:1)	<1%

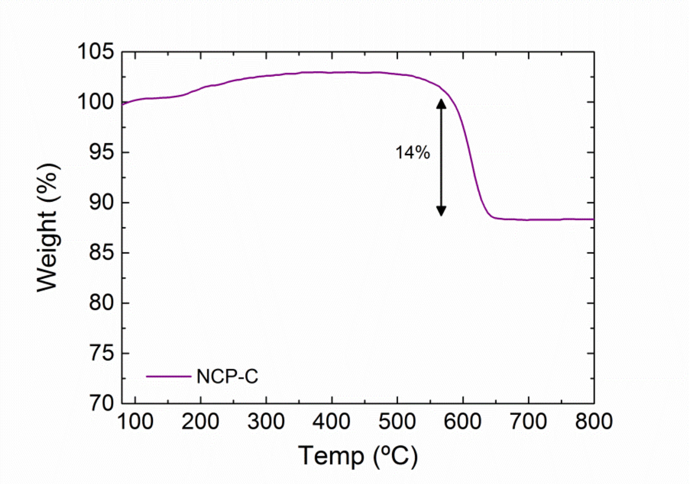

Figure 5.7: TGA analysis of **NCP-C** sample under air atmosphere heated up to 800 ^oC and cooled down to 30 ^oC

5.4. Electrochemical characterization

5.4.1. Galvanostatic experiments

Galvanostatic experiments have been carried out with laminate electrodes prepared with a 90:5:5 ($Na_4Co_3(PO_4)_2P_2O_7$:carbon Super C65:PVdF) in half-cells using Na disk as counter electrode and 1 M $NaPF_6$ in EC:DEC as electrolyte. All tests have been done at 0.2C rate in the 3.0 - 4.7 V *vs.* Na^+/Na voltage window.

The voltage profiles corresponding to the first two cycles of the studied samples are shown in **Figure 5.8**. The uncoated **NCP** sample (**Figure 5.8a**) shows low capacities and high 1st cycle irreversible capacity (more than half of the 1st Na^+ extraction capacity; see **Table 5.4**) and large polarization (~ 0.55 V).

On one hand, among the NCP-CP ((x:1, x = 1,2,3,4,5) samples, the delivered capacity strongly depends on the used mass ratio. In high amount of Ph-based samples, **NCP-CP (1:1)**, **NCP-CP (2:1)** and **NCP-CP (3:1)**, the 1st Na^+ extraction capacity is very low (9 - 54 mAh/g) and almost all of this capacity is irreversible after the 1st cycle. Besides this, although the polarization slightly decreases around 0.2 - 0.3 V (**Figure 5.8b**), comparable to the uncoated **NCP**, it is still very large. The capacity and reversibility improve by decreasing the carbon precursor content, due to the formation of a thinner and more homogeneous C-coating, obtaining the best capacity values for the **NCP-CP (4:1)** sample. Nevertheless, the obtained capacities are still lower than the values reported in the literature (55 - 73 mAh/g *vs.* 95

mAh/g) [1], because the formed C-coating is not uniform and does not have an optimum thickness (c.f. **Figure 5.4b**).

On the other hand, although a real C-coating layer (**Figure 5.5b**) and is not formed, **NCP-C** sample exhibits a similar galvanostatic profile and good electrochemical performance as reported in the literature (**Figure 5.8c**) [1]; albeit it exhibits slightly larger irreversible capacity in the 1st cycle than NCP-CP (x:1, x=1,2,3,4,5) samples (**Table 5.4**). This difference is most probably due to the high surface area that results from the formation of C-NTs which typically involve overall better electrochemical properties. As expected, Na^+ extraction occurs throughout reversible multi-step redox plateaux starting at 4.28 V and followed by six more plateaux with the last one at 4.65 V *vs.* Na^+/Na, providing an average voltage of 4.5 V *vs.* Na^+/Na (V). Moreover, in the following cycles, the capacity remains constant showing the best electrochemical performance. This improvement can be correlated with the fact that the C-NTs covering the $Na_4Co_3(PO_4)_2P_2O_7$ particles as well as the spherical CBP particles, are interconnecting the active particles and increasing the bulk electronic conductivity, hence, improving the electrochemical performance. As it has been previously mentioned, the polyanionic framework is in general more stable during electrochemical cycling than layered oxides, therefore while **P2-NFMO-LV** has 85% of capacity retention after 20 cycles, the **NCP-C** keeps between 99% and 94% after 20 and 100 cycles (**Figure 5.9**). Although the Columbic efficiency is around 85 - 90% at the beginning of the electrochemical cycling, after 10 cycles is close to 100%. This tendency has been already observed in **P2-NFMO-LV** and might be originated by electrolyte decomposition to form the SPI layer during the initial cycles. Since the **NCP-C** operates at higher voltage than the layered and also includes the high surface area of C-NTs, these decomposition reactions might be enhanced.

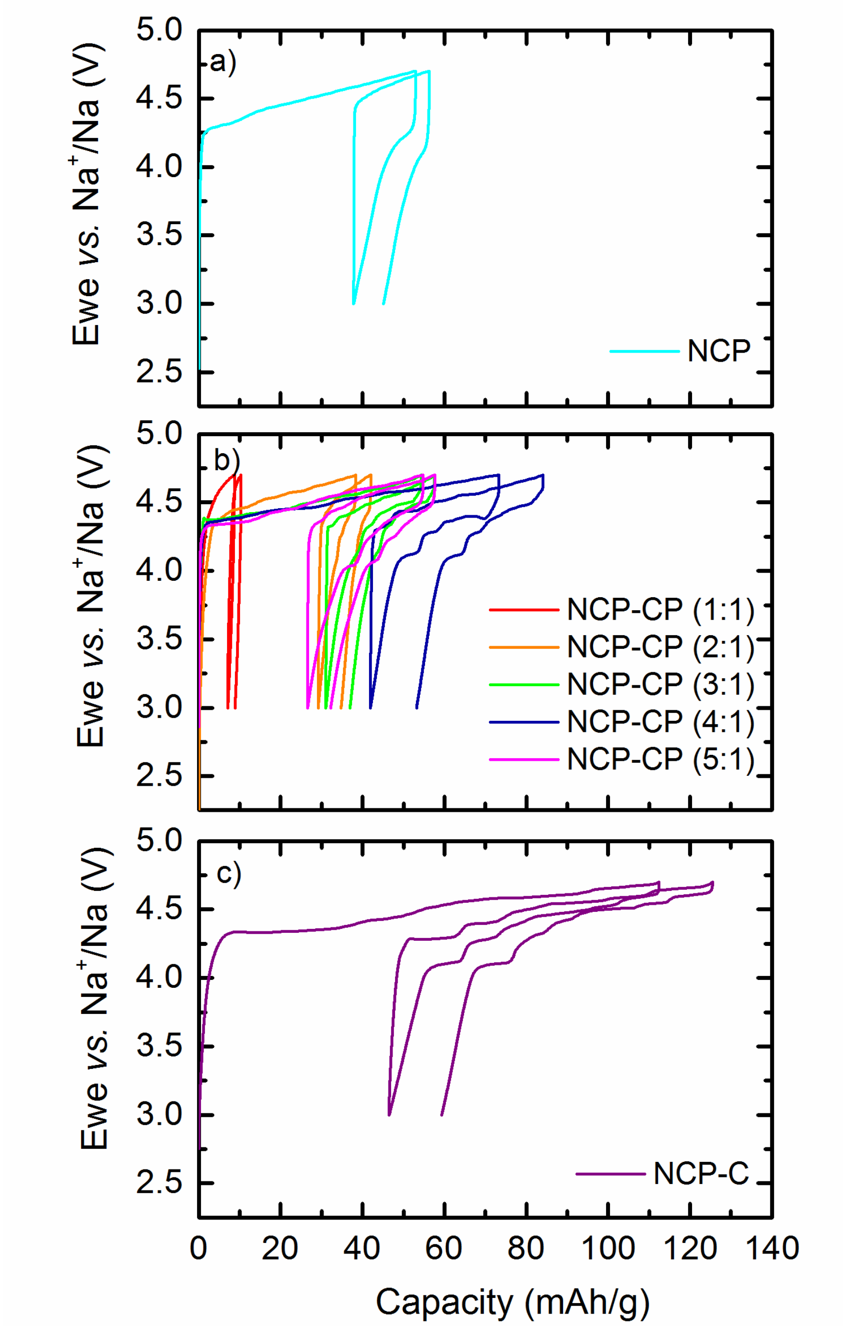

Figure 5.8: Voltage *vs*. capacity curves of the 1st and 2nd cycle of **a)** uncoated **NCP** (cyan), coated by Ph precursor **b) NCP-CP (1:1)** (orange), **NCP-CP (2:1)** (red), **NCP-CP (3:1)** (green), **NCP-CP (4:1)** (royal) and **NCP-CP (5:1)** (magenta) and **c)** coated by CBP precursor, **NCP-C** (purple).

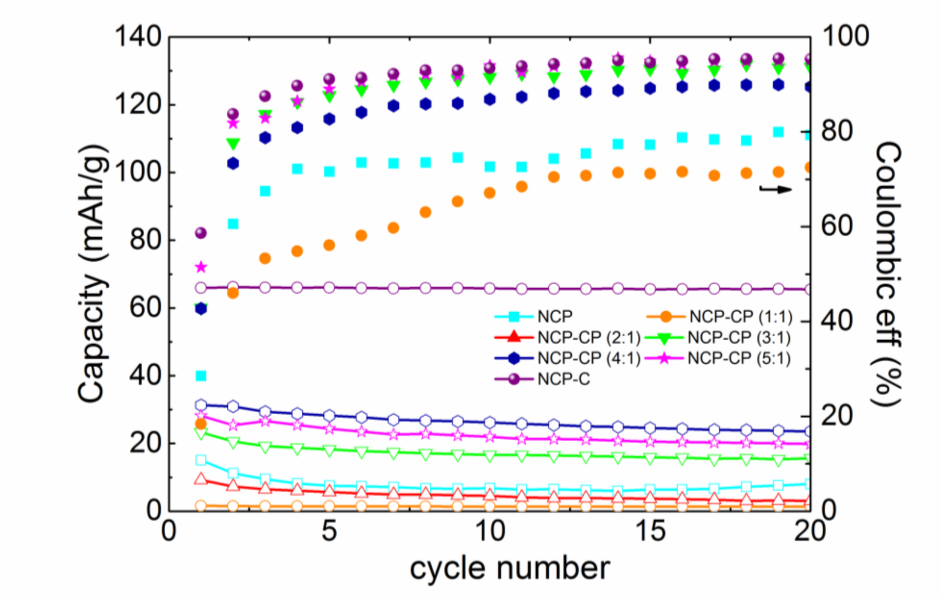

Figure 5.9: Capacity and Coulombic efficiency during the first 20 cycles of uncoated **NCP** (cyan) and coated: NCP-CP(x:1, x=1,2,3,4,5): **(1:1)** (orange), **(2:1)** (red), **(3:1)** (green), **(4:1)** (royal), **(5:1)** (magenta), and **NCP-C** (purple).

Table 5.4: Capacity values and capacity retention obtained of the 20th and 100th cycles of uncoated **NCP** and C-coated NCP-CP (x:1, x=1,2,3,4,5) and **NCP-C** at 0.2C over 3.0 - 4.7 V *vs.* Na^+/Na.

	NCP			**NCP-CP**			**NCP-C**
		(1:1)	**(2:1)**	**(3:1)**	**(4:1)**	**(5:1)**	
1st Na^+ extrac. capacity (mAh/g)	53	9	38	54	73	55	112
1st cycle Irreversible capacity (mAh/g)	38	7	29	31	42	27	46
Cap. reten. at 20th cycle	53%	-	-	67%	75%	70%	99%
Cap. reten. at 100th cycle	-	-	-	58%	-	50%	94%

In summary, the best results are obtained with the **NCP-C** sample, which has been chosen to further study the reaction mechanisms, the transport properties and the SPI layer stability and evolution.

5.4.1.1. Structural evolution upon cycling

In order to understand the reaction mechanism of NCP-based materials, **NCP-C** was further studied by *operando* synchrotron XRD (HRXRD). The data has been collected in the Powder Diffraction beamline at the Australian Synchrotron with a wavelength λ = 0.0688077 nm, which has been determined using the NIST 660b LaB_6 standard reference material. The electrochemical test has been done in a coin cell with a kapton window and the HRXRD data have been measured in transmission geometry, with a pattern collected every 20.5 min with an acquisition time of 2.4 min. The electrode was prepared with 3.3 mg of **NCP-C** and has been charged to 4.7 V at 40 mA/g and discharged to 3.0 V at 8 mA/g during the 1st cycle, while in following cycles a current density of 30 mA/g have been used. In this section a preliminary analysis of the data is given and the detailed structural refinement of HRXRD data is ongoing.

$Na_4Co_3(PO_4)_2P_2O_7$ is isostructural to $Na_4Fe_3(PO_4)_2P_2O_7$ and $Na_4Mn_3(PO_4)_2P_2O_7$ compounds, however they exhibit different reaction mechanism during the electrochemical cycling. The Fe compound follows a single phase reaction throughout the charge/discharge reactions [10], while the Mn compound shows a more complex mechanism. In this Mn-containing material, the initial α phase first follows a solid solution reaction until 3.9 V, approximately when 1.64 Na^+ have been extracted. Above 3.9 V a new β phase appears in the α phase matrix and hence a biphasic region is observed. When 2.24 Na^+ have been extracted the α phase completely transforms to β phase. Finally above 4.0 V a Na-poor new phase is detected (γ phase) [3].

Figure 5.10 shows the *in-situ* HRXRD data of the 1st and 2nd cycles at 2 Theta range of 4.2 - 7.6 ^{o}, where the more significant changes during cycling can be observed. While **Figure 5.11** shows the evolution of *a*, *b* and *c* parameters of the **NCP-C** phases during cycling. The (200), (011), (210) and (002) peaks of α phase (green) observed in **Figure 5.10** slightly shift towards higher 2 Theta values during the 1st Na^+ extraction, as can be also seen in **Figure 5.11**, in agreement with a solid solution mechanism until 4.57 V, approximately when 1.66 Na^+ ($Na_{2.34}Co_3(PO_4)_2P_2O_7$) have been extracted. After further increasing the voltage, a new phase (blue) appears (named β phase in analogy to the reported mechanism for $Na_4Mn_3(PO_4)_2P_2O_7$) with new peaks in the HRXRD patterns at 2 Theta = 4.55 ^{o}, 7.12 ^{o}, 7.47 ^{o} and 7.51 ^{o}. In this biphasic region, from 4.57 to 4.67 V in which both α and β phases coexist, the peaks of them still slightly shift towards higher 2 Theta values, as was observed in the Mn-based compound. However, in **NCP-C** the α phase never transforms completely to β phase during the Na^+ extraction, in contrast to what occurs with the Mn-based phosphate-pyrophosphate, always coexisting these two phases and the peaks that correspond to each phase slightly shifting during the following Na^+ insertion/extraction processes. Close to the upper cut-off voltage, at 4.67 V *vs.* Na^+/Na, when 2.6 Na^+ are extracted, a third Na-poor intermediate γ phase (magenta) emerges, which remains during the insertion until 3.50 V (insertion of ~ 2 Na^+). Additionally, at 4.55 V, when 0.22 Na^+ are inserted, a new σ phase (gray) appears. As occurs with the α (green), β (blue) and γ phases (magenta), the σ phase (gray) follows a solid solution behaviour and coexists with α and β phases during the following electrochemical cycling, as well as with γ phase in the 4.67 - 3.79 V voltage range. A similar behaviour is observed in the Mn-based phosphate-pyrophosphate, where a σ phase is only observed during the insertion and is attributed to a specific Na-vacancy ordering [3]. The evolution of the patterns during the Na^+ insertion do not show a complete reversible reaction mechanism since the α phase never reaches the initial 2 Theta and cell parameters values (**Figure 5.11**). However, after the 2nd cycle, the same peak evolution is observed suggesting that the phase evolution is completely reversible. Hence, the main difference with Mn compound is that the α phase never fully transforms to β phase and σ phase is observed during the extraction and insertion (except during the 1st Na extraction).

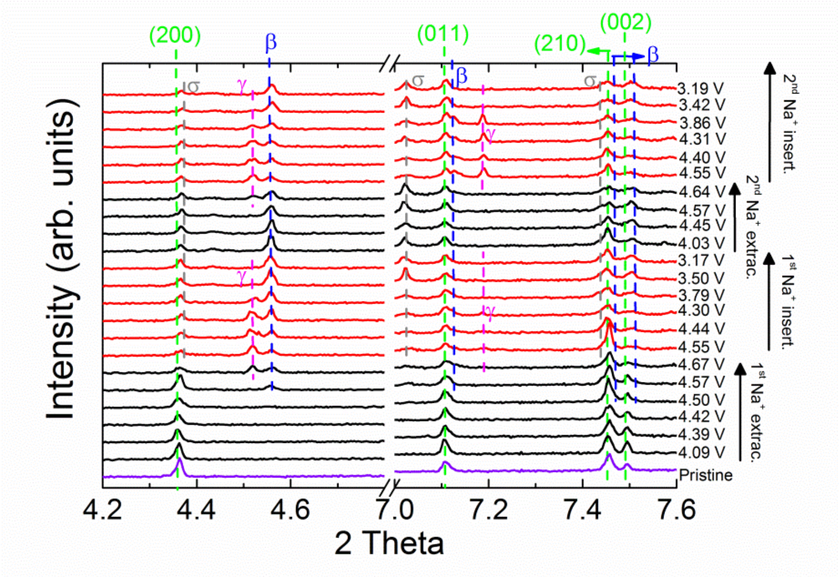

Figure 5.10: *In-situ* HRXRD pattners of **NCP-C** during the 1st and 2nd Na^+ deintercalation/intercalation cycles. Pristine (purple), during Na^+ extraction (black) and insertion (red) pattners. α phase (green), β pahse (blue), γ phase (magenta) and σ phase (gray).

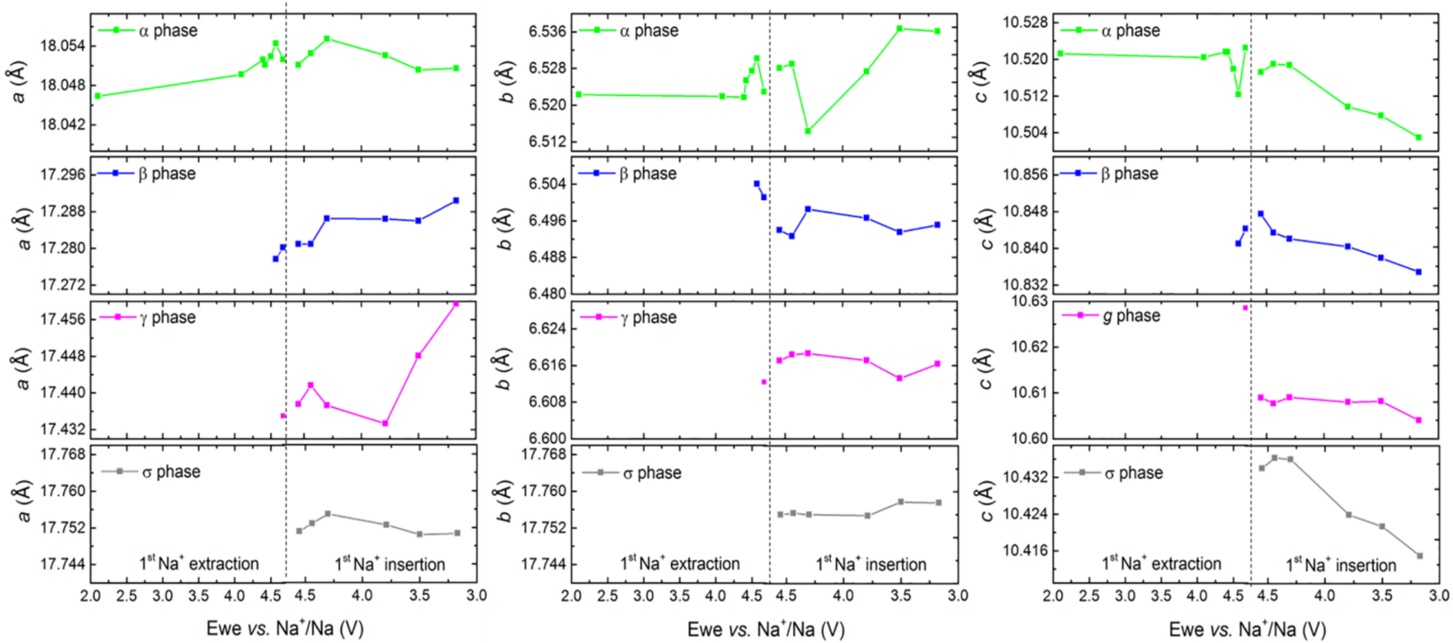

Figure 5.11: Evolution of the *a*, *b* and *c* parameters of **NCP-C** during the 1st cycle. α phase (green), β phase (blue), γ phase (magenta) and σ phase (gray), where all phases have been indexed by orthorhombic *Pn*2_1a.

In order to clarify the phase evolution of the **NCP-C** during electrochemical cycling, the voltage as a function of the Na^+ content has been plotted for the 1st cycle, showing the transition from one phase to another (**Figure 5.12**).

Therefore, although the presented and discussed results are preliminar and to fully determine the structural evolution of **NCP-C** during cycling it is necessary to refine all patterns and analyse more in detail the evolution of the cell parameters, it can be concluded that the **NCP-C** sample shows different structural evolution to that of the isostructural Fe- or Mn-based compounds, although the evolution is more similar to the Mn compound.

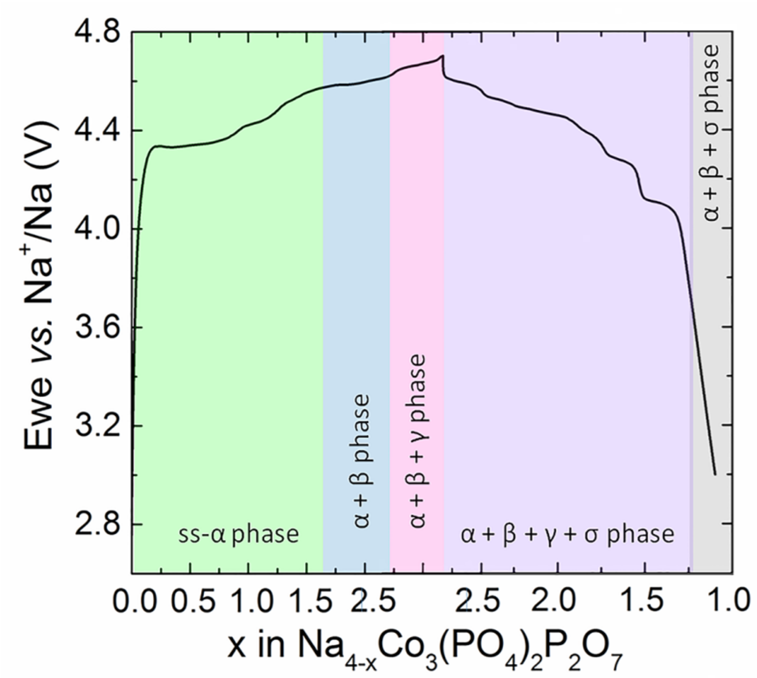

Figure 5.12: Voltage *vs*. Na^+ amount ($Na_{4-x}Co_3(PO_4)_2P_2O_7$ during the 1st cycle of **NCP-C**, correlated with phase evolution: α phase (green region), α + β phase (blue region), α + β + γ phase (magenta region), α + β + γ + σ (violet region) and α + β + σ phase (gray region).

5.4.2. Transport and interphase study by EIS

The EIS experiments were carried out in order to correlate the transport properties with the electrochemical properties and to obtain extra information about the stability of the SPI layer during the cycling of **NCP-C** sample.

Electrochemical tests were performed in three electrode Swagelok type cells using metallic Na disk as counter and reference electrodes, glass fibre as separator and 1 M $NaPF_6$ in EC:DEC (1:1) as electrolyte. The experiments were carried out at room temperature in the 4.0 - 4.7 V *vs.* Na^+/Na voltage range using a VMP3 potentiostat (Bio-Logic). The EIS spectra were collected every 45 mV in the frequency range 5 mHz - 100 kHz.

As can be observed in the dQ/dV curve (**Figure 5.13**), the multiredox reactions of the **NCP-C** sample occur in the 4.0 - 4.7 V *vs*. Na^+/Na voltage range. Therefore, although the galvanostatic measurements have been performed in the 3.0 - 4.7 V *vs*. Na^+/Na voltage window, the EIS experiments have been carried out in the redox reactions range, since not significant change is expected below 4.0 V. Additionally, the 1st cycle shows a different behaviour if compared with the following cycles, therefore, the EIS experiments have been performed in the 1st and 2nd cycles.

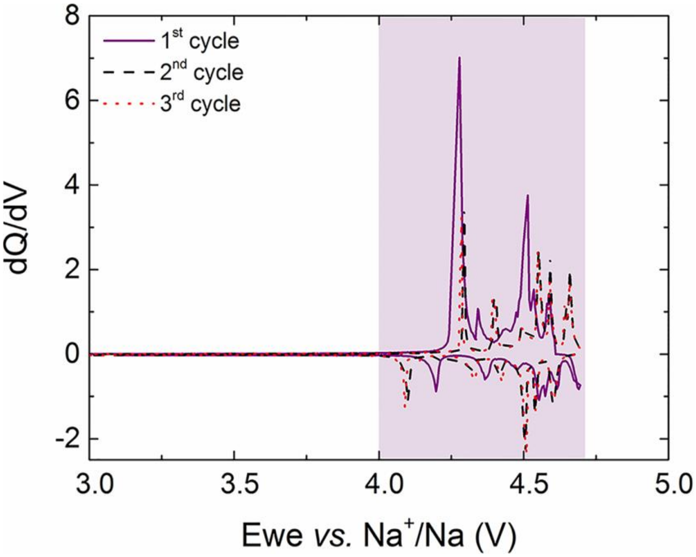

Figure 5.13: dQ/dV curve of the 1st (purple), 2nd (black) and 3rd (red) cycles of **NCP-C** sample tested in the voltage range of 3.0 - 4.7 V *vs.* Na^+/Na at 0.2C. The highlighted region of the curve corresponds to the voltage window where EIS measurements are performed.

Following with the same trend used with the other studied samples (**NTO-CO-Air**, **NTO-OH-Ar-C**, **P2-NFMO-LV** and **P2-NFMO-SV**), EIS experiments have been repeated several times for each cell in order to check the reproducibility of the obtained impedance data. However, although the cells show a reproducible behaviour, the obtained impedance data exhibit some inductance problems due to cell configuration, cables, and/or other external factor and has not been possible to collect a good data set. Despite only some data are suitable to perform a proper fit, the qualitative analysis also provides a lot of information. **Figure 5.14** shows the Nyquist plot of the impedance dispersion recorded at OCV (2.93 V *vs.* Na^+/Na), where one main semicircle is observed in the medium-frequency (MF) region (between 1.3 kHz - 10 Hz) and a smaller one at high-frequency (HF) (above 1.3 kHz, **see inset**). Finally, in the low-frequency (LF) region, a line of the Na^+ solid-solution diffusion can be shown. The main difference with any previously studied sample is that the **NCP-C** sample does not show any semicircle at LF as **NTO-CO-Air** (**section 3.2.1.**), **NTO-OH-Ar-C** (**section 3.2.2.**), **P2-NFMO-LV** (**section 4.4.2.1.**) and **P2-NFMO-SV** (**section 4.4.2.2.**) which has been ascribed to the bulk electronic resistance. This might be because the **NCP-C** sample has a very low bulk electronic resistance due to the active particles being interconnected by spherical CBP and C-NTs which substantially increase the bulk electronic conductivity. The main arc is assigned to charge-transfer resistance (R_{CT}) while the small semicircle above 1.3 kHz corresponds to the Na^+ migration through SPI layer. As in other studied samples, at OCV state is already possible to observe some resistance regarding the passivation layer since once the cell is assembled spontaneous reactions take place, such as salt decomposition forming an initial inorganic passivation layer. Additionally, the PVdF dehydrofluorination reaction is also expected (c.f. **Figure 3.15**) [15].

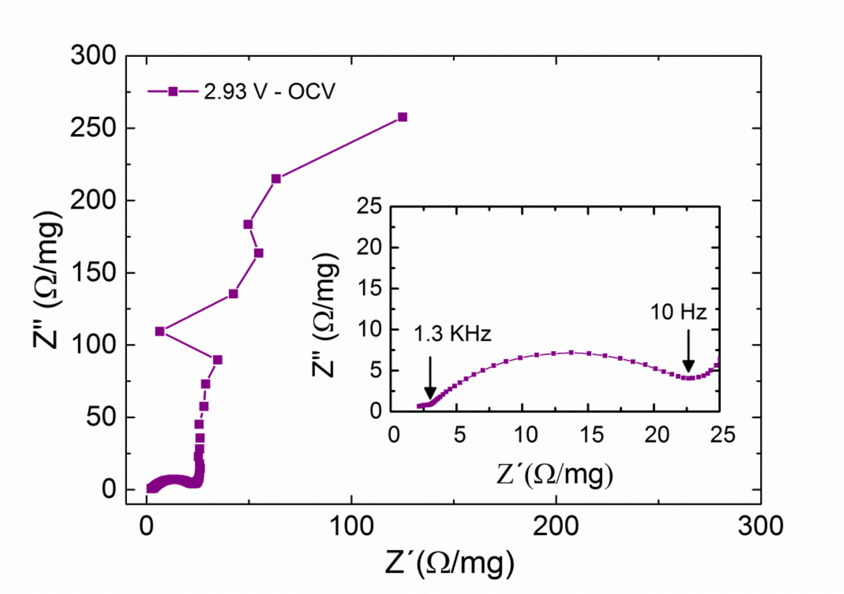

Figure 5.14: Nyquist of **NCP-C** at OCV (2.493 V *vs.* Na^+/Na). The inset shows the impedance data from 100 kHz to 10 Hz.

The Nyquist plots during the 1st and 2nd cycles are collected in **Figure 5.15**. As expected from the observed differences on the dQ/dV curve (**Figure 5.13**), the 1st and 2nd cycle Nyquist plots are completely different. The 1st cycle Nyquist plot shows lower total resistance than one from the 2nd cycle. Comparing the impedance data of the 1st cycle, the overall resistance of the 1st Na^+ extraction (**Figure 5.15a**) is lower than the 1st Na^+ insertion (**Figure 5.15b**) which in the 2nd cycle continuous increasing (**Figure 5.15c** and **Figure 5.15d**).

The small arc of the HF region is more visible in the 2nd cycle and its shape and value are almost constant during these first two cycles Taking into account the frequency region where the semicircle appears, it can be correlated with the resistance of the SPI layer [16] which, in light of the arc constant behaviour, is presumed to be a very stable SPI layer, as will be further discussed later. Additionally, the Na^+ resistance through the electrolyte (R_{sol}) is slightly smaller when $NaPF_6$ salt is used if compared with $NaClO_4$ (c.f **Table A.1**). This might be due to the larger polarization character of PF_6^- anions which would improve salt dissociation and enhance the ionic conductivity [17].

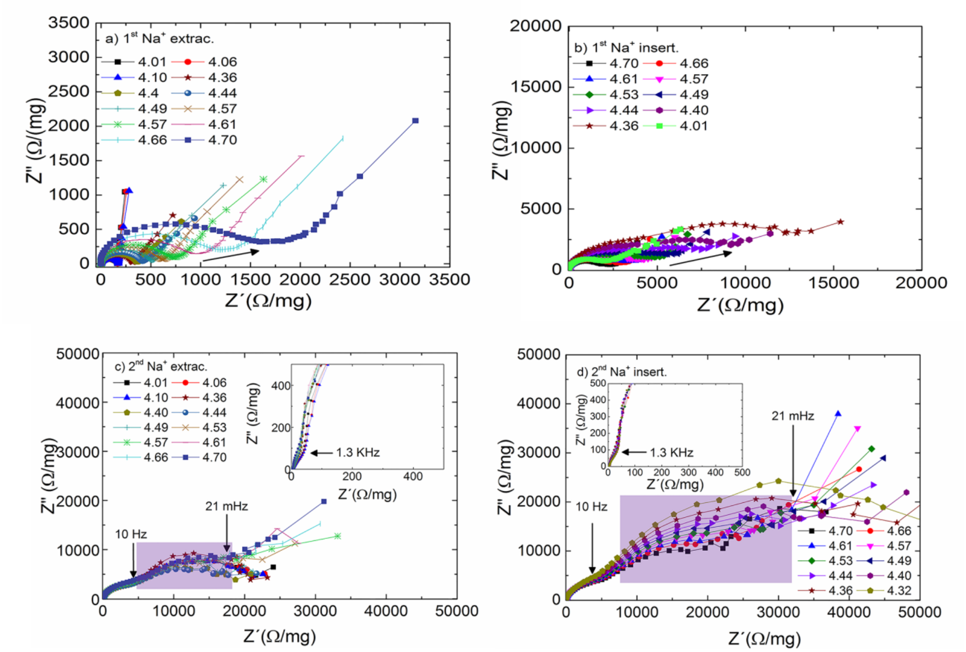

Figure 5.15: Nyquist plot of **NCP-C** during **a)** 1st Na^+ extraction **b)** 1st Na^+ insertion **c)** 2nd Na^+ extraction and **d)** 2nd Na^+ insertion at several voltages. The inset shows the impedance data from 100 kHz to 250 Hz.

As regards the main arc at MF above 10 Hz that corresponds to the $R_{CT,}$ it is observed a resistance increases during the 1st cycle; where the 1st Na^+ insertion is kinetically more sluggish than the 1st Na^+ extraction. However, in the 2nd cycle the semicircle above 10 Hz is almost constant and a new arc at LF is developed (highlighted region). The radius of that LF semicircle increases during the 2nd insertion (**Figure 5.15d**). The process which is happening is unknown, however, taking into account the frequency range, the arc position and the electrode configuration some hypothesis can be established. On one hand, the active material is interconnected by spherical CBP particles and C-NTs and might be that during the 1st cycle the electrode surface suffers some cracks and/or morphology changes. In this case Na^+ would show an extra resistance across the double layer of the particle surface, as has been reported for the **NTO-OH-Ar-C** sample (**section 3.2.2.**). On the other hand, other possible explanation would be related with the bulk electronic resistance. Although initially this electrode does not show a significant bulk electronic resistance, during the electrochemical cycling the bulk electronic conductivity could decrease due to a detachment of the carbon from the active material.

Despite the observed inductance in some data, some impedance data of the 1st Na^+ extraction process have been fitted by Boukamp´s software [18]. The equivalent circuit employed is shown in the **top** panel in **Figure 5.16** and is based on: Na^+ resistance across the electrolyte (R_{sol}), a resistance and a capacitance of the SPI layer (R_{SPI} and C_{SPI}), the charge-transfer resistance (R_{CT}), double layer capacitance (C_{DL}), a Warburg diffusion (Z_w) and an intercalation capacity (C_i) (more details in **A.1.4.5.**) [16]. Moreover, as it has been done previously with the other studied electrodes, the capacitances and Z_w elements have been replaced by CPE (Constant Phase Element) so as to take into account any deviation from ideal surface/interface. The values of R_{sol}, R_{SPI} and R_{CT} resulting from the fits are collected in **Table 5.5**. Moreover, the experimental Nyquist plots along with the fitted curves are shown in **Figure 5.16**.

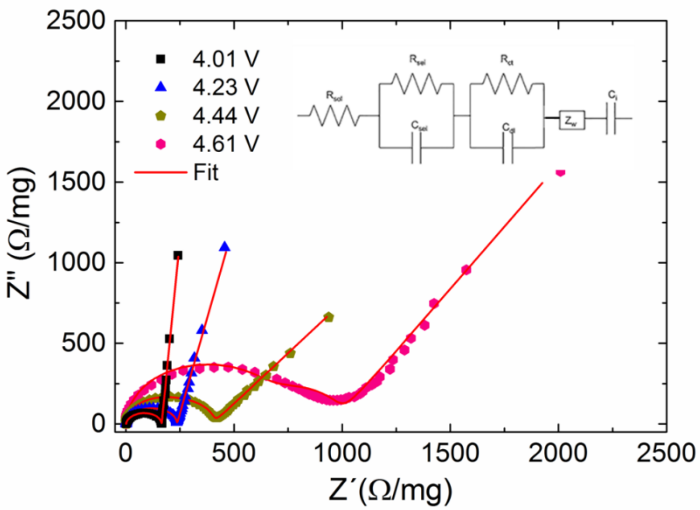

Figure 5.16: The fits of the impedance data of **NCP-C** sample during the 1st Na^+ deintercalation at 4.01 V (black), 4.23 V (blue), 4.4 V (dark yellow) and 4.61 V (pink). The inset shows the equivalent circuit used for the fits.

Table 5.5: The values of R_{sol}, R_{SPI} and R_{CT} resulting from the fits by Boukamp´s software of the impedance data at 4.01 V, 4.23 V, 4.44 V and 4.61 V during the 1st Na^+ extraction.

Voltage during the 1st Na extraction	R_{sol} (Ω/mg)	R_{SPI} (Ω/mg)	$R_{C.T}$ (Ω/mg)	X^2
4.01 V	1.43	61.02	103.24	$3.60 \cdot 10^{-4}$
4.23 V	1.61	99.46	135.31	$3.57 \cdot 10^{-4}$
4.44 V	1.51	151.04	247.11	$1.59 \cdot 10^{-3}$
4.61 V	1.51	280.33	677.00	$9.51 \cdot 10^{-3}$

Conversely, taking into account the obtained values and the trend of the impedance data observed in **Figure 5.15**, the $NaPF_6$ EC:DEC electrolyte shows very low resistance due to a higher ionic conductivity than $NaClO_4$ EC:PC [17]. The R_{SPI} increase might be due to the formation or instability of the layer. The R_{CT} shows a slow increase during the 1st Na^+ extraction which turns into a faster increase during the following 1st Na^+ insertion (**Figure 5.15**). In the following cycles, the R_{CT} is kept constant. Finally, although the **NCP-C** sample shows an outstanding bulk electronic conductivity, in the 2nd cycle an extra process associated to an increase in the bulk electronic resistance can be observed from the development of a new semicircle.

5.5. SPI layer study by XPS

The formed SPI layer onto **NCP-C** electrodes has been studied by conventional XPS using a Mg K_α X-ray source ($h\nu$ = 1253.6 eV). The SPI layer composition has been measured at different oxidation states during the electrochemical cycling as highlighted in the galvanostatic profile of **Figure 5.17**. The measurements on the pristine electrode have been used as a reference. Once the electrodes reached the desired charge state, the cells were disassembled and the electrodes were washed with DEC solvent and transferred to XPS chamber using an Ar filled transfer system, never exposing the electrodes to air.

The stability and evolution of the SPI layer have been monitored by measuring the Co 2*p*, C 1*s*, O 1*s*, Na 1*s*, F 1*s* and P 2*p* photoelectron lines. Indeed, the absolute binding energies of some of the components in these lines might be slightly shifted with respect to the reference values reported in the literature. However, the measured binding energies are in good agreement with the previously obtained values of this thesis (**NTO-CO-Air** (**section 3.3.1.**), **NTO-OH-Ar-C** (**section 3.3.2.**) and **P2-NFMO-LV** (**section 4.5.**)). Moreover, in contrast with the other studied samples, the **NCP-C** electrodes do not show charge effects since the active particles are interconnected by spherical CBP particles and C-NTs which increase the electronic conductivity avoiding any surface charging effect. Finally, as occurs with **P2-NFMO-LV** sample the Auger parameter estimation was not possible due to the thickness of the SPI layer and the overlapping of signals.

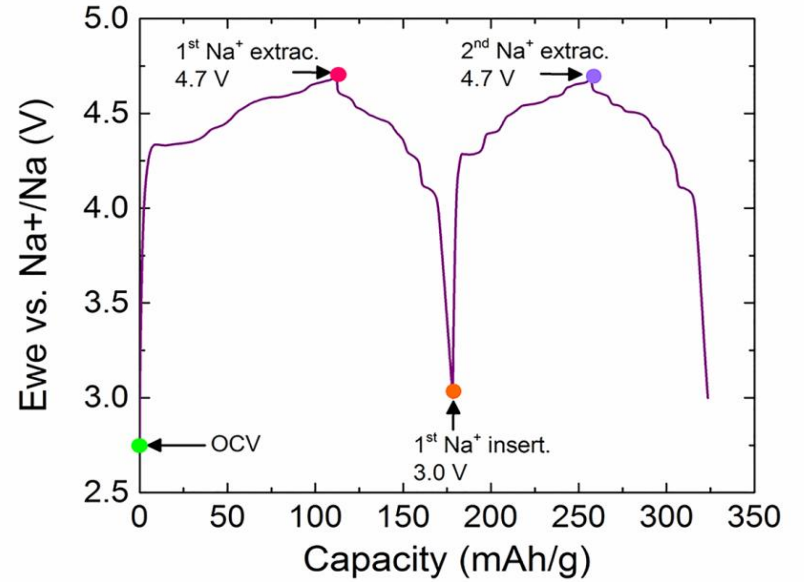

Figure 5.17: Voltage *vs.* capacity of the first two cycles of the **NCP-C** electrode tested in the voltage range of 3.0 – 4.7 V *vs.* Na^+/Na at 0.2C. The studied electrodes by XPS are highlighted in the profile; additionally, the pristine electrode has also been measured.

5.5.1. Conventional XPS study

The photoelectron spectra of the Co 2*p* is shown in **Figure 5.18**, where the data have been fitted by CasaXPS software [19]. In the **NCP-C** electrodes it has been possible to detect the transition metal by XPS, in contrast with other studied electrodes, possibly for the higher cross section of the Co element than Ti, Fe and Mn. Owing to the spin-orbit splitting, the Co 2*p* peak appears as two peaks Co $2p_{3/2}$ and Co $2p_{1/2}$, where the intensity ratio is 2:1 and the energy difference between them is close to 15 eV. Each part consists in a main peak and a satellite (s) towards higher binding energy. The satellite peak is a result of final state effects in the photoemission process. Furthermore, the pristine, OCV and 1st Na insertion electrode show an extra satellite (s*), which is characteristic of the presence of high spin Co^{2+} [20, 21]; which is in very good agreement with the first-principles calculations that provide that the Co^{2+} in $Na_4Co_3(PO_4)_2P_2O_7$ compounds are in high spin state [9].

Taking into account the binding energy of the Co $2p_{3/2}$ main peak together with the satellite peak, it will be possible to estimate the oxidation state of Co during the electrochemical cycling. As can be observed during the Na^+ extraction/insertion the overall shape of Co 2*p* spectra is almost constant, however three aspects can be highlighted: firstly, a slightly displacement of the Co 2$p_{3/2}$ main peak towards higher binding energies during the Na$^+$ extraction, secondly, the presence of an extra satellite at certain voltage and thirdly, the change on the relative area of the satellite with respect of the Co 2$p_{3/2}$ main peak. The values of the Co 2$p_{3/2}$ peak position and relative area are collected in **Table 5.6**.

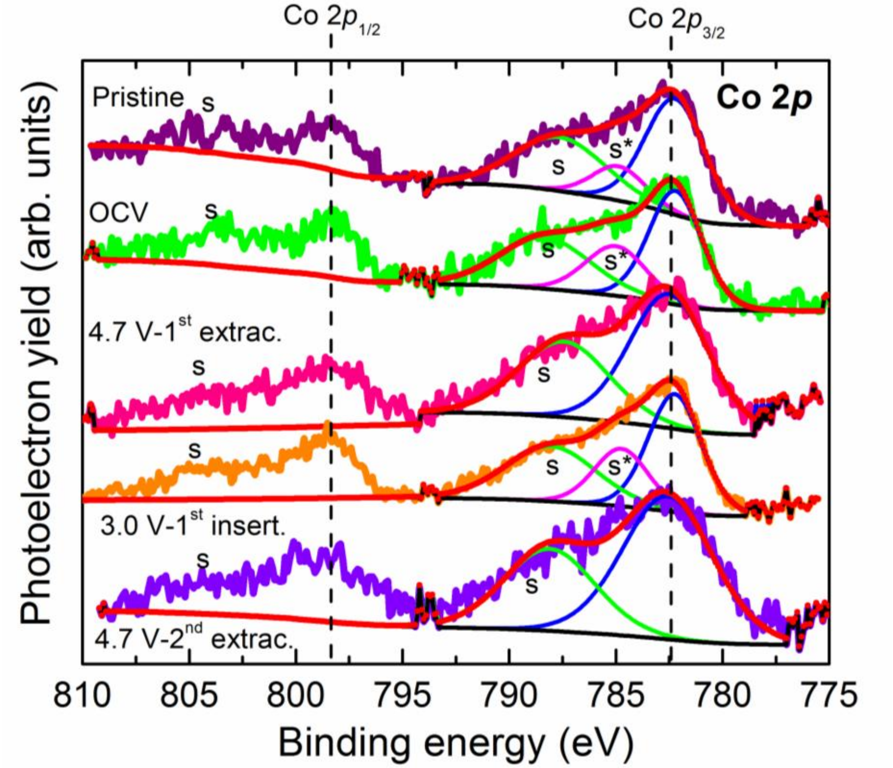

Figure 5.18: Co 2*p* photoelectron spectra of **NCP-C** electrode before cycling (pristine) and at different oxidation states during Na$^+$ extraction/insertion curve as indicated in **Figure 5.17**. The fits have been carried out by CasaXPS software [19].

Table 5.6: The binding energy of Co 2$p_{3/2}$ main peak and the satellite relative area (%) with respect the Co 2$p_{3/2}$ component.

Oxidation state	Co 2$p_{3/2}$ position (eV)	%sat. area
Pristine	782.2	7
OCV	782.2	7.7
1st Na$^+$ extrac. at 4.7 V	782.5	6.4
1st Na$^+$ insert. at 3.0 V	782.2	7.9
2nd Na$^+$ extrac. at 4.7 V	782.6	5.7

The Co 2$p_{3/2}$ binding energy and the relative area of the satellite peak are suitable tools to estimate the oxidation state. During the Na^+ extraction, the main peak shifted to higher binding energy while the relative area of the satellite decreases. Meanwhile during the Na^+ insertion similar values to that of pristine and OCV electrodes is observed. When the binding energy is shifted to toward higher binding energies suggests that the oxidation state is increased. Similar correlation can be carried out for the relative are of the satellite; since the decreasing of the satellite area means that is increasing the oxidation state. Therefore, taking into account the trend observed in **Table 5.6**, during the electrochemical cycling the oxidation state of the Co is changing. Although the values are different from those reported [22, 23, 24]; considering the stoichiometry of the compound and the observation of the extra satellite the possible change of the oxidation state is from Co^{2+} to Co^{3+}. The binding energy differences between the reference values reported in the literature and the obtained experimental values might be the variances of the Co environment: the reported reference values correspond to $LiCoO_2$ compounds where the Co^{3+} is octahedrally coordinated by oxygen while in **NCP-C** the Co^{2+} is surrounded by phosphate and pyrophosphate groups which can influence in the binding energy of the main peak and the satellite.

Regarding the evolution of the oxidation/reduction products of the electrolyte the C 1*s* photoelectron line is shown in **Figure 5.19**, from this peak it is also possible to obtain crucial information about the stability of the SPI layer. As occurs with the cathode layered oxide (**P2-NFMO-LV**), the main carbon component of the pristine electrode is located at 284.4 eV and is not only assigned to graphitic-like compounds from the conductive additive C65 but also to the CBP used for the C-coating. As expected, the graphitic-like component shows an asymmetry [25]. At higher binding energy the signals of hydrocarbons (C-H or C-C bonds; 285.0 eV) [26], $-CH_2$ and $–CF_2$ groups from PVdF (286.2 eV and 290.9 eV) [27] and the plasmon (Π−Π* transition) (290 - 291 eV) [28] (more details in **3.3.1.1.**) are displayed. Although these are the main peaks of the pristine electrode, the presence of some Na_2CO_3 from atmospheric contamination can be also detected (~ 290 – 291 eV) [29, 30], however, due to the signal overlapping is not possible to fully confirm only considering the C 1*s* spectrum.

As regards the evolution of the C 1*s* during the electrochemical cycling from OCV to the 2nd Na^+ extraction charge state, the spectra are very similar to the one from the pristine electrode; which suggests that the formed SPI layer is thin and/or discontinuous and thinner than the SEI layer. Indeed, in all studied oxidation states the main peaks are the graphite-like and the PVdF contributions. The most

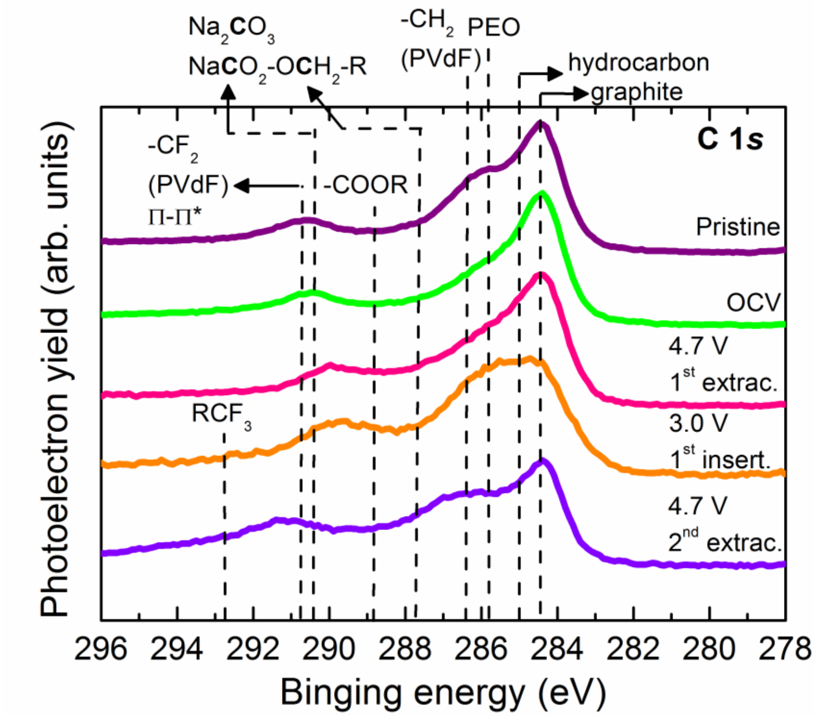

Figure 5.19: C 1*s* photoelectron spectra of **NCP-C** electrode before cycling (pristine) and at different oxidation states during Na^+ extraction/insertion curve as indicated in **Figure 5.17**.

significant features can be observed after the 1st Na^+ insertion at 3.0 V, where some new signals appear at 286.3 eV and 288.6 - 289.1 eV which correspond to C-O-C based compounds such as PEO [29], from direct polymerization of EC [31], and carboxyl (-COOH) or ester (-COOR) compounds from electrolyte reduction reaction [26]. Probably, more compounds resulting from electrolyte reduction appear such as Na_2CO_3 (290.5 - 291.0 eV) and $NaCO_3R$ (R= alkyl group with different long chain, at 288 eV and 290 - 291 eV) [15, 26]. However, due to the signal overlapping it is very difficult to corroborate. This will be further discussed during the analysis of the O 1*s* and Na 1*s* spectra. Nevertheless, it seems that the Na_2CO_3 and/or $NaCO_3R$ follow a reversible behaviour since both compounds disappear during the 2nd Na^+ extraction leading to a C 1*s* spectrum as that of the 1st Na^+ extraction electrode. Similar behaviour has been already observed in other Na-based cathode materials, such as **P2-NFMO** (in **chapter 4**) and P2-$Na_xCo_{2/3}Mn_{2/9}Ni_{1/9}O_2$ (x ~2/3) [21].

After a careful analysis of the O 1*s* and Na 1*s* spectra (**Figure 5.20**), it is possible to determine the evolution of the carbonaceous and oxygenated species such as, Na_2CO_3 and $NaCO_3R$. It is worth mentioning that owing to the low kinetic energy of

Na 1*s* photoelectrons, this spectrum provides information of the outmost region of the SPI layer. The Na_2CO_3 which appears at ~ 532 eV and ~ 1072 eV in the O 1*s* [15, 30, 32,] and Na 1*s* [21] spectra, can be found as the main component of the outermost surface region in almost all charge states. The Na_2CO_3 concentration changes during the 1st cycle, as can be observed from the O 1*s* peak which indicates a slight decrease of the Na_2CO_3 concentration during the Na^+ extraction and an increase during the Na^+ insertion (in contrast with the observations on **P2-NFMO-LV** sample, see **section 4.5.1**); while the $NaCO_3R$ (532.5 and 534 eV) has opposite behaviour. Still, a full verification is very difficult, since at similar binding energy (~ 534 eV) the fluorophosphates ($NaPF_xO_y$) species appear [21]. Additionally, at lower binding energy, around 531 eV, phosphate-based compounds [32] from active material ($Na_4Co_3(PO_4)_2P_2O_7$) and electrolyte salt decomposition products are shown, continuously changing during the electrochemical cycling: peak intensity decreases during the Na^+ insertion and increases upon extraction. The analysis of F 1*s* and P 2*p* photoelectron spectra is needed for better understanding.

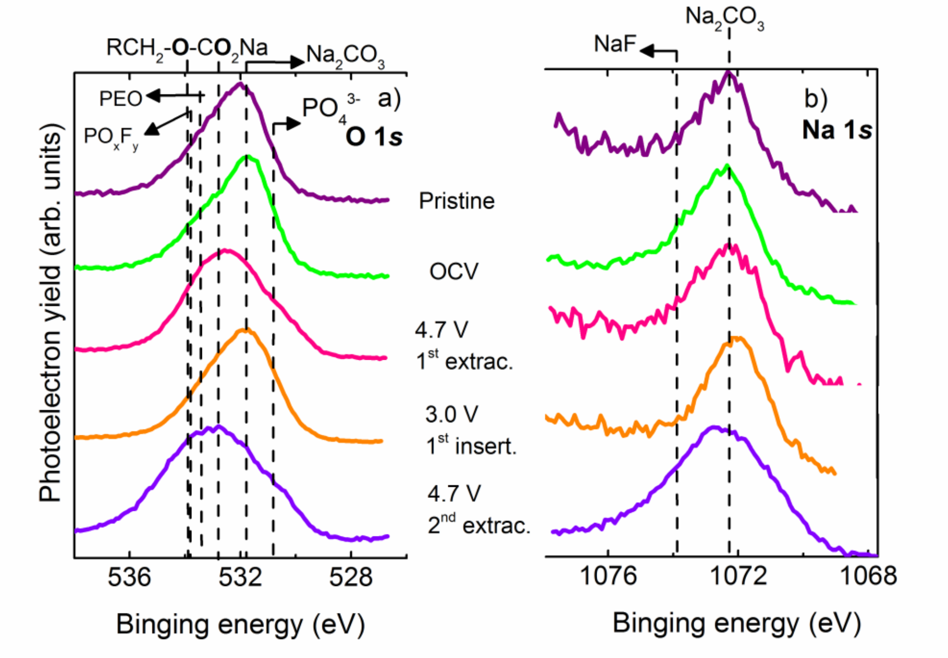

Figure 5.20: a) O 1*s* and **b)** Na 1*s* photoelectron spectra of **NCP-C** electrode before cycling (pristine) and at different oxidation states during Na^+ extraction/insertion curve as indicated in **Figure 5.17**.

The F 1*s* XPS peaks (**Figure 5.21a**) corroborate the behaviour observed in the C 1*s* spectra (**Figure 5.19**). The main F 1*s* component corresponds to the -CF_2 group of PVdF (~ 688.0 eV) [27] which remains almost constant during the electrochemical cycling, verifying the existence of a thin and/or discontinuous SPI layer. However, the F 1*s* signal slightly decreases during Na^+ extraction and increases during the insertion which could be associated to the formation and dissolution/cracking of the SPI layer. The dehydrofluorination reaction of the PVdF in NaF and decomposition of the $NaPF_6$ salt in $NaPF_xO_y$ are expected, as previously reported [15, 21]; however this may occur to a less extent and/or covered by other decomposition products, therefore, there are not significant features in the F 1*s* spectra. The P 2*p* photoelectron lines (**Figure 5.21b**) are investigated in order to verify the possible salt decomposition products. The pristine electrode shows a main peak at 133 - 134 eV from the phosphate/pyrophosphate group of the active material, while the OCV electrode shows additionally some residual $NaPF_6$ at ~ 138.5 eV and fluorophosphates ($NaPF_xO_y$) at 135 eV [33, 34]. Interestingly, due to the high cut-off voltage (4.7 V *vs.* Na^+/Na), the salt of the electrolyte decomposed and at the end of the Na^+ extraction process fluorophosphates ($NaPF_xO_y$) are observed whereas during the Na^+ insertion the main compounds are the

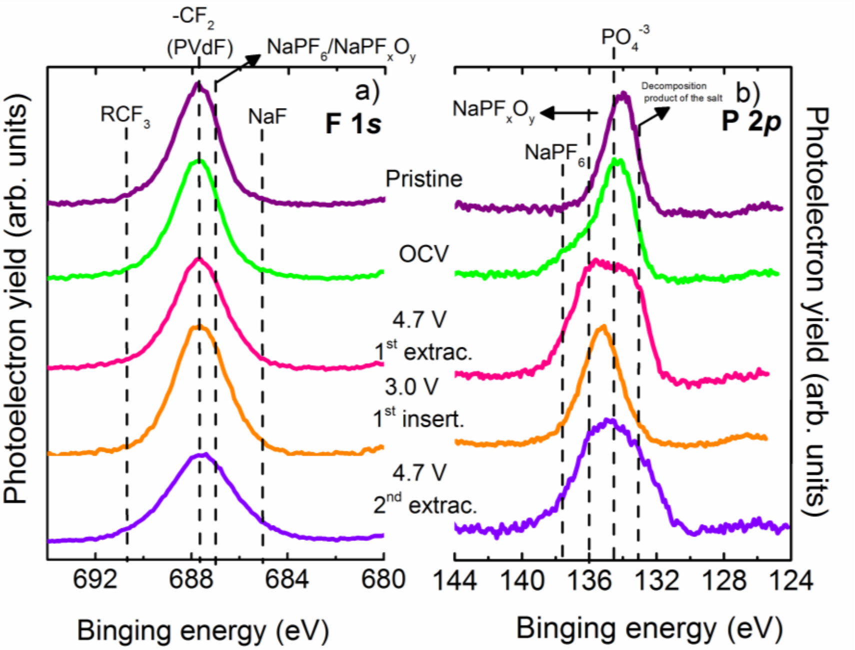

Figure 5.21: a) F 1*s* and **b)** P 2*p* photoelectron spectra of **NCP-C** electrode before cycling (pristine) and at different oxidation states during Na^+ extraction/insertion curve as indicated in **Figure 5.17**.

phosphates; indicating that the decomposition products of the salt depend on the working voltage value. Moreover, the main peak at 133 - 134 eV from the phosphate/pyrophosphate group of the active material is observed in all oxidation state as well as the graphite peak in C 1*s* spectra, hence the SPI layer is very thin, even thinner than in **P2-NFMO-LV** electrodes; since in the latter cathode the active material is covered by decomposition products from the solvents (c.f. **Figure 4.19**).

5.5.2. Depth profiling by Ag L_α source

The composition of the SPI surface layer, around the first 10 nm, has been investigated in **section 5.5.1.**, however, in order to obtain more information and a better understanding of the SPI layer higher photon energy (Ag L_α 2984.3 eV) has been employed to observe what happens at higher depths of the SPI layer. Additionally, with this photon energy it will be possible to observe if NaF has been formed during the electrochemical cycling.

The C 1*s*, O 1*s*, F 1*s*, P 2*p*, Na 1*s* and Co 2*p*, core level spectra have been analysed for the 1st Na^+ extraction and insertion electrodes (**Figure 5.22**) by means of conventional XPS. In general, due to the low resolution and signal/noise ratio when the Ag source is used, significant changes can be only shown in the first 10 nm of depth, except for the O 1*s* spectra.

At the end of the Na^+ extraction and insertion almost the same shape and composition of the SPI layer is observed. The main components of C 1*s* XPS spectra (in both oxidation states) at higher depth than 10 nm are the graphite-like (284.4 eV) and PVdF (290.9 eV $-CF_2$ and 286.2 eV $-CH_2$), which prove that the most of Na_2CO_3, $NaCO_3R$ and PEO are on the outward region of the SPI layer.

From the F 1*s* spectra the same conclusion can be obtained. By using more energetic Ag source, it is possible to see the NaF signal at ~ 685 eV which bear out the decomposition of the $NaPF_6$ salt and/or the spontaneous dehydrofluorination reaction of the PVdF. When Mg source is used, it is not possible to detect NaF since it is covered by decomposition products.

Additionally, from the Na 1*s* spectra it is possible to conclude that the NaF is almost covered by a thin layer of Na_2CO_3. Since the intensity of the Na_2CO_3 peak decreases at 10 nm of depth and the main component is the NaF, as it is expected.

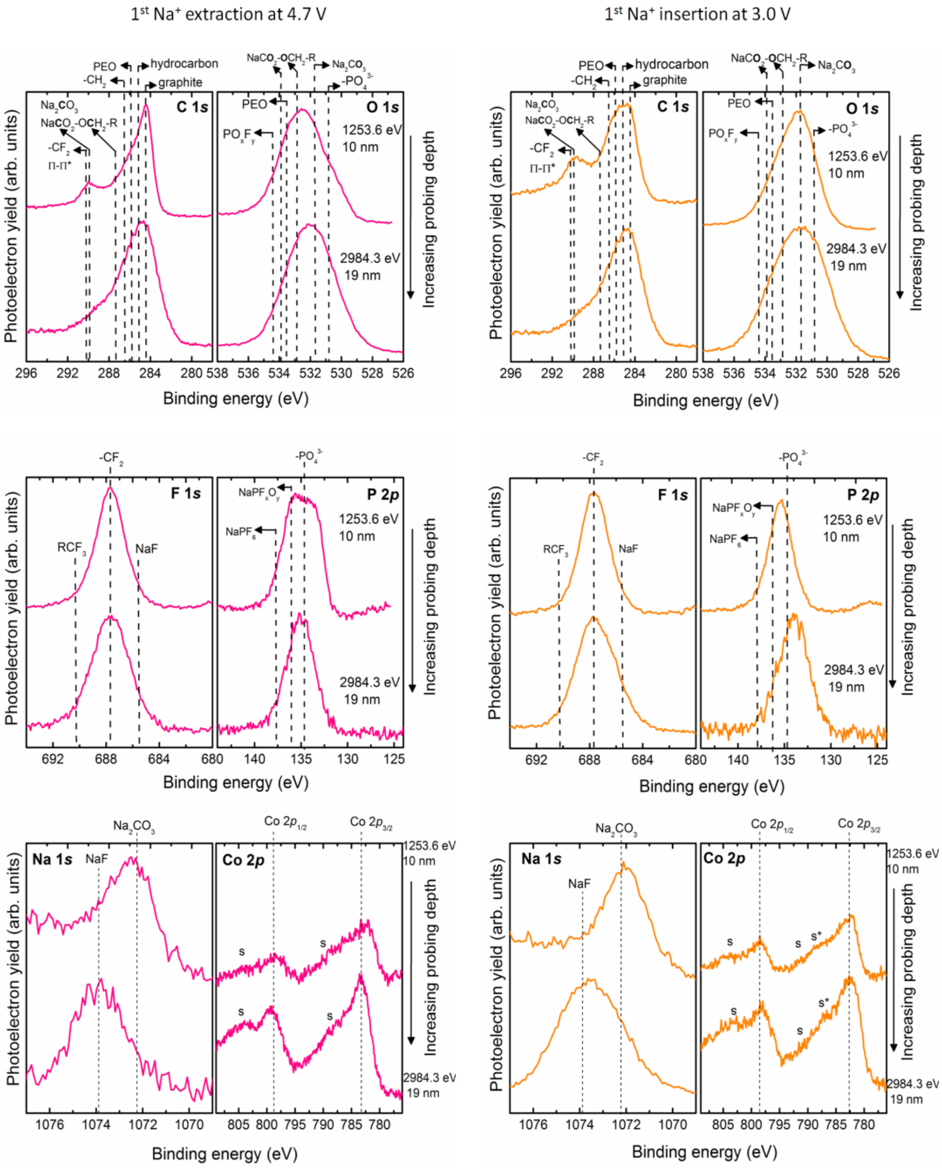
1st Na^+ extraction at 4.7 V

1st Na^+ insertion at 3.0 V

Figure 5.22: C 1*s*, O 1*s*, F 1*s*, P 2*p*, Na 1*s* and Co 2*p* photoelectron spectra of 1st Na^+ extraction at 4.7 V (**left**) 1st Na^+ insertion at 3.0 V (**right**) of **NCP-C** electrodes. (s) Co 2*p* satellite and (s*) extra satellite from Co^{2+} high spin

Moreover, the P 2*p* spectra suggest that in the first 10 nm apart from Na_2CO_3 the layer is formed also by fluorophosphates ($NaPF_xO_y$) and at higher depths the main phosphoric compounds are the phosphates. The source of these phosphates compounds can be the active material and/or some decomposition products of the salt.

Finally, by the fits of all elements and taking into account the cross section of all of them it is possible to determinate the percentage of Co at both depths 10 nm and 19 nm. The obtained values are collected in the **Table 5.7**.

Table 5.7: Percentage of Co on the 1st Na^+ extraction and insertion electrode at different depths.

Oxidation state	Mg K_α-10nm	Ag L_α-19nm
1st Na^+ extrac. at 4.7 V	1.2%	81.8%
1st Na^+ insert. at 3.0 V	2.4%	99.2%

It can be observed that after 10 nm of depth the Co amount is much higher, suggesting that the SPI layer is thinner than 10 nm since after 10 nm the active material is shown.

5.6. Conclusions

The highest voltage mixed polyanion $Na_4Co_3(PO4)_2P_2O_7$ shows poor electrochemical performance when is not or not completely C-coated. However, when CBP is used as carbon precursor some spherical carbon and C-NTs are interconnecting and covering the active particles which increase the electronic conductivity and hence the electrochemical properties, delivering a capacity close to the theoretical one, 112 mAh/g with a very good capacity retention after 100 cycles (94%).

As regards the structural evolution of $Na_4Co_3(PO4)_2P_2O_7$, the preliminary analysis shows that it exhibits a complex reaction mechanism, similar to the one from $Na_4Mn_3(PO_4)_2P_2O_7$, which consist in a triphasic solid solution region and the formation of a fourth phase at the end of the Na^+ extraction which remains during the insertion process between 4.7 - 3.8 V *vs.* Na^+/Na, when the inserted Na amount is close to 1.40.

The EIS experiments carried out in the voltage range of 4.0 - 4.7 *vs.* Na^+/Na show that the R_{CT} increases during the 1st cycle to remain constant during the 2nd cycle. The R_{SPI} exhibits also a similar behaviour, indicating that the SPI layer is quite stable once is formed. However, the obtained impedance data show some inductance problem and hence their fit becomes very difficult. However, from a qualitative analysis it is possible to confirm that during the 2nd cycle an extra process is happening, since a new semicircle is developed at a lower frequency than the charge-transfer (<10 Hz). The reason of this new process is unknown but would be correlated with the changes in the C-coating morphology that ultimately affects the bulk electronic conductivity of the active particles.

Finally, the evolution of the composition, stability and properties of the electrode/electrolyte interphase, SPI layer, have been studied during the Na^+ deintercalation/intercalation by XPS using two different photon energies. The schematic illustration of the SPI layer evolution is shown in **Figure 5.23**.

The pristine electrode shows that the main contribution corresponds to the conductive additive, the carbon from the C-coating and the PVdF. Some intrinsic contamination is shown as C-H compounds and Na_2CO_3 covering the electrode surface. Additionally the Na 1*s* spectrum, when Ag L_α is used as photon source, confirms that NaF is also formed from dehydrofluorination reaction of the PVdF , although it cannot be detected because during cycling it is covered by the electrolyte salt and solvents decomposition products. Once the electrode is

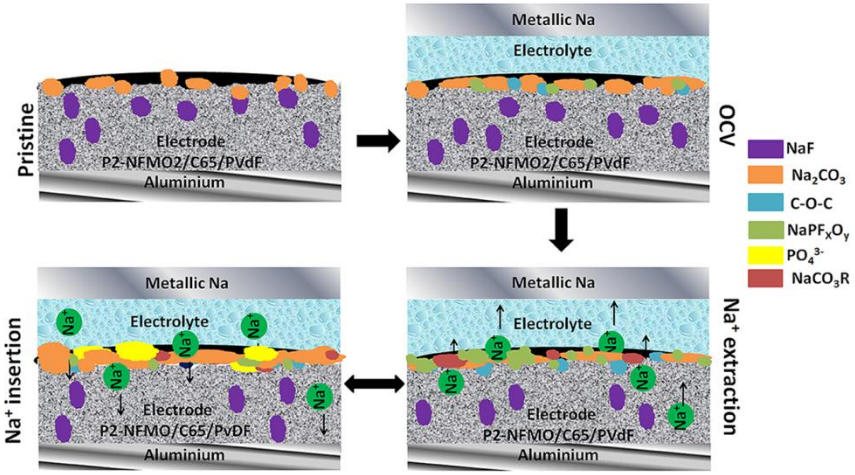

Figure 5.23: Schematic illustration of the SPI layer evolution before and during the electrochemical performance obtained by XPS of **NCP-C** electrodes.

assembled, the $NaPF_6$ salt spontaneously decompose on phosphate compounds, as occurs with other cathode samples P2-$Na_{2/3}[Fe_{1/2}Mn_{1/2}]O_2$ studied; which coexist with PEO, -COOH compounds, $NaCO_3R$ and Na_2CO_3; where the latter specie is the main component of the SPI layer.

During the Na^+ extraction and insertion some of the components (PEO and $Na_{2-x}CO_3R_x$) are dissolved and reformed. However, the SPI layer is almost stable; as suggests the EIS experiments and the XPS spectra. The presence of graphite and active material signals in C 1*s* and P 2*p* spectra, respectively in all electrodes corroborate the low thickness of the SPI layer (<< 5 nm). As regards the salt decomposition products, during the Na^+ extraction the main compounds are the fluorophosphates while during the Na^+ insertion the phosphate compounds which show a dependency with voltage.

As conclusion, the SPI layer formed onto $Na_4Co_3(PO4)_2P_2O_7$ electrode is very thin as it is observed for P2-$Na_{2/3}[Fe_{1/2}Mn_{1/2}]O_2$ cathode but is more homogeneously distributed. The small variations of the SPI layer do not affect the electrochemical properties of the high voltage cathode material $Na_4Co_3(PO4)_2P_2O_7$. In fact, it exhibits a good specific capacity and capacity retention after 100 cycles, becoming a very good candidate to be used as cathode in NIBs.

.

5.7. References

---

[1] M. Nose, H. Nakayama, K. Nobuhara, H. Yamaguchi, S. Nakanishi, H. Iba, $Na_4Co_3(PO_4)_2P_2O_7$: a novel storage material for sodium-ion batteries, J. Power Sources 234 (2013) 175-179.

[2] H. Kim, I. Park, D.H. Seo, S. Lee, S.W Kim, W.J. Kwon, Y.U. Park, C.S. Kim, S. Jeon, K. Kang, New iron-based mixed-polyanion cathodes of lithium and sodium rechargeable batteries: combined first principles calculations and experimental study, J. Am. Chem. Soc. 134 (2012) 10369-10372.

[3] H. Kim, G. Yoon, I. Park, K.Y. Park, B. Lee, J. Kim, Y.U. Park, S.K. Jung, H.D. Lim, D. Ahn, S. Lee, K. Kang, Anomalous Jahn-Teller behavior in a manganese-based mixed-phosphate cathode for sodium ion batteries, Energy Environ. Sci. 8 (2015) 3325-3335.

[4] B. Senthilkumar, G. Ananya, P. Ashok, S. Ramaprabhu, Synthesis of carbon coated nano-$Na_4Ni_3(PO_4)_2P_2O_7$ as a novel cathode material for hybrid supercapacitors, Electrochim. Acta 169 (2015) 447-455.

[5] M. Nose, S. Shiotani, H. Nakayama, K. Nobuhara, S. Nakanishi, H. Iba, $Na_4Co_{2.4}Mn_{0.3}Ni_{0.3}(PO_4)_2P_2O_7$: high potential and high capacity electrode material for sodium-ion batteries, Electrochem. Comun. 34 (2013) 266-269.

[6] H. Pan, Y.S. Hu, L. Chen, Room-temperature stationary sodium-ion batteries for large-scale electric energy storage, Energy Environ. Sci. 6 (2013) 2338-2360.

[7] H. Kim, H. Kim, Z. Ding, M.H Lee, K. Lim, G. Yoon, K. Kang, Recent progress in electrode materials for sodium-ion batteries, Adv. Energy Mater. DOI: 10.1002/aenm.201600943 (2016).

[8] J. Baker, R.J. Heap, N. Roche, C. Tan, R. Sayers, J. Whitley, Y. Liu, The commercialization of high energy density Na-ion battery technology, Faradion Limited, Innovation Centre, 2nd International Symposium on sodium batteries (2015).

[9] H. Moriwake, A. Kuwabara, C.A.J. Fisher, M. Nose, H. Nakayama, S. Nakanishi, H. Iba, Y. Ikuhara, Crystal and electronic structure changes during the charge-discharge process of $Na_4Co_3(PO_4)_2P_2O_7$, J. Power Sources 326 (2016) 220-225.

[10] H. Kim, I. Park, S. Lee, H. Kim, K.Y. Park, Y.U. Park, H. Kim, J. Kim, H.D. Lim, W.S. Yoon, K. Kang, Understanding the electrochemical mechanism of the new iron-based mixed-phosphate $Na_4Fe_3(PO_4)_2(P_2O_7)$ in a Na rechargeable battery, Chem. Mater. 25 (2013) 3614-3622.

[11] J.B. Goodenough, Y Kim, Challenges for rechargeable Li batteries, Chem. Mater. 22 (2010) 587-603.

[12] P. Georén, G. Lindbergh, On the use of voltammetric methods to determine electrochemical stability limits battery electrolytes, J. Power Sources 124 (2003) 213-220.

[13] A. Bhide, J. Hofmann, A.K. Dürr, J. Janek, P. Aldelhem, Electrochemical stability of non-aqueous electrolytes for sodium-ion batteries and their compatibility with $Na_{0.7}CoO_2$, Phys. Chem. Chem. Phys. (2014) 1987-1998.

---

[14] F. Sanz, C. Parada, J.M. Rojo, C. Ruíz-Valero, Synthesis, structural characterization, magnetic properties and ionic conductivity of $Na_4M(II)_3(PO_4)_2P_2O_7$ (M(II)= Mn, Co, Ni), Chem. Mater. 13 (2001) 1334-1340.

[15] M.A. Muñoz-Márquez, M. Zarrabeitia, E. Castillo-Martínez, A. Eguía-Barrio, T. Rojo, M. Casas-Cabanas, Composition and evolution of the Solid-Electrolyte Interphase in $Na_2Ti_3O_7$ electrodes for Na-ion batteries: XPS and Auger parameter analysis, ACS Appl. Mater. Interfaces 7 (2015) 7801-7808.

[16] E. Barsoukov, J.R. Macdonald; Impedance spectroscopy theory, experiment and application, 2nd ed., John Wiley & Sons Inc., Hoboken, New Jersey 2005.

[17] A. Ponrouch, E. Marchante, M. Courty, J.M. Tarascon, M.R. Palacín, In search of an optimized electrolyte for Na-ion batteries, Energy Environ. Sci. 5 (2012) 8572-8583.

[18] B.A. Boukamp, Parametic analysis using impedance spectroscopy: relationship between material properties and battery performance, Solid State Ionics 20 (1986) 31-44.

[19] J. Walton, P. Wincott, N. Fairley, A. Carrick, Peak Fitting with CasaXPS a Casa pocket book, Accolyte Sicence, Knutsford, UK 2010.

[20] N.S. McIntyre, M.G. Cook, X-ray photoelectron studied on some oxides and hydroxides of cobalt, nickel, and cooper, Anal Chem. 47 (1975) 2208-2213.

[21] S. Doubaji, B. Philippe, I. Saadoune, M. Gorgoi, T. Gustafsson, A. Solhy, M. Valvo, H. Rensmo, K. Edtröm, Passivation layer and cathodic redox reactions in sodium-ion batteries probed by HAXPS, Chem. Sus. Chem. 9 (2016) 97-108.

[22] R. Dedryvère, S. Laruelle, S. Grugeon, P. Poizot, D. Gonbeau, J.M. Tarascon, Contribution of X-ray photoelectron spectroscopy to the study of the electrochemical reactivity of CoO toward lithium, Chem. Mater. 16 (2004) 1056-1061.

[23] L. Dahéron, R. Dedryvère, H. Martinez, M. Ménétrier, C. Denage, C. Delmas, D. Gonbeau, Electron transfer mechanisms upon lithium deintercalation from $LiCoO_2$ to CoO_2 investigated by XPS, Chem. Mater. 20 (2008) 583-590.

[24] N. Andreu, D. Flahaut, R. Dedryvère, M. Minvielle, H. Martinez, D. Gonbeau, XPS investigation of surface reactivity of electrode materials: effect of the transition metal. ACS Appl. Mater. Interfaces 7 (2015) 6629-6636.

[25] http://www.xpsfitting.com/search/label/Graphite (acceded in August 2016)

[26] R.I.R. Blyth, H. Buqa, F.P. Netzer, M.G. Ramsey, J.O. Besenhard, P. Golob, M. Winter, XPS studies of graphite electrode materials for lithium ion batteries, Appl. Surf. Sci. 167 (2000) 99-106.

[27] G. Beamson, D. Briggs, High Resolution XPS of Organic Polymers: The Scienta ESCA300 Database, John Wiley & Sons, Chichester, UK 1992.

[28] A.M. Bradshaw, S.L. Cederbaum, W. Domcked, U. Kraus, Plasmon coupling to core hole excitations in carbon, J. Phys. C: Solid State Phys. 7 (1974) 4503-4512.

[29] A.M. Andersson, A. Henningson, H. Siegbahn, U. Jansson, K. Edström, Electrochemically lithiated graphite characterized by photoelectron spectroscopy, J. Power Sources 119-120 (2003) 522-527.

[30] S. Komaba, W. Murata, T. Ishikawa, N. Yabuuchi, T. Ozeki, T. Nakayama, A. Ogata, K. Gotoh, K. Fujiwara, Electrochemical Na insertion and solid electrolyte interphase for hard-carbon electrodes and application to Na-ion batteries, Adv. Func. Mater. 21 (2011) 3859-3867.
[31] L. Vogdanis, W. Heitz, The polymerization of ethylene carbonate, Makromol. Chem., Rapid Commun. 7 (1986) 543-547.
[32] S. Malmgren, K. Ciosek, M. Hahlin, T. Gustafsson, M. Gorgoi, H. Rensmo, K. Edtröm, Comparing anode and cathode electrode/electrolyte interface composition and morphology using soft and hard X-ray photoelectron spectroscopy, Electrochim. Acta 97 (2013) 23-22.
[33] N. Membreno, K. Park, J.B. Goodenough, K.J. Stevenso, Electrode/electrolyte interface of composite #-LiV(PO) cathodes in a non-aqueous electrolyte for lithium ion batteries and the role of the carbon additive, Chem. Mater. 27 (2015) 3332-3340.
[34]. Bodenes, A. Darwiche, L. Monconduit, H. Martinez, The solid electrolyte interphase a key parameter of the high performance of Sb in sodium-ion batteries: comparative X-ray photoelectron spectroscopy study of Sb/Na-ion and Sb/Li-ion batteries, J. Power Sources 273 (2015) 14-24.

6. General conclusions

In this work the low and high voltage stability of three different Na-ion electrode materials has been studied. To do so, when required, the electrochemical properties of these materials have been optimized. Then, transport properties and their evolution with the structural transitions occurring during cycling have been studied by electrochemical impedance spectroscopy (EIS) and have been correlated with the electrochemical performance. The electrode/electrolyte interphase properties have also been studied by X-ray photoelectron spectroscopy (XPS) and correlated with the electrochemical properties. The studied materials were the low operating voltage $Na_2Ti_3O_7$ negative electrode and the high cut-off voltage cathode materials: P2-$Na_{2/3}[Fe_{1/2}Mn_{1/2}]O_2$ (4.25 V *vs*. Na^+/Na) and $Na_4Co_3(PO_4)_2P_2O_7$ (4.7 V *vs*. Na^+/Na).

The electrochemical properties of $Na_2Ti_3O_7$ were enhanced by employing NaOH instead of Na_2CO_3 as Na precursor, and Ar atmosphere instead of air atmosphere during the cooling process since Na_2CO_3 (either from unreacted precursor, either formed by surface corrosion from the interaction between the $Na_2Ti_3O_7$ particles and water and CO_2 of the atmosphere) is highly soluble in the electrolyte and has a direct impact in SEI layer stability. The capacity retention was further increased by C-coating since, in addition to improve the electronic conductive of the material, acts as a protective layer leading to the best capacity retention reported up to date.

The moisture and water stability of $Na_2Ti_3O_7$ was also studied and it was found that a solid solution of the form $Na_{2-X}H_XTi_3O_7$ ($0<x<2$) is spontaneously formed by ion exchange. Two pure compositions were isolated ($Na_{1.3}H_{0.7}Ti_3O_7$ and $Na_{0.6}H_{1.4}Ti_3O_7$) and their exact structure was determined. Both crystallize in a C-centred unit cell with AB $[TiO_6]$ layer stacking sequence (S.G: *C*2/*m*) as $H_2Ti_3O_7$, (instead of the primitive cell of $Na_2Ti_3O_7$ (S.G: $P2_1/m$ and AA $[TiO_6]$ sequence). This transformation was found to revert during the 1st Na^+ insertion process, allowing the possibility to use water-soluble binders for electrode preparation which are more environmentally friendly than the commonly used PVdF, that requires the use of organic solvents. When employing Na-CMC aqueous binder better 1st cycle reversible capacity, Coulombic efficiency and capacity retention were found.

Once optimized, the transport properties of $Na_2Ti_3O_7$ were investigated by EIS. A reversible transition from electronic insulator to conductor during the cycling was revealed close to the Na^+ insertion plateau. It was also found that the C-coated sample exhibited lower and more constant values of charge-transfer and SEI resistances upon electrochemical cycling than the non-coated one since the C-coating protects the active material for the direct interaction with the electrolyte. The SEI layer composition of a non-coated and a coated sample was analysed by XPS combining conventional XPS, Auger parameter analysis and depth profiling. In both samples a thin (~ 5nm, thicker in C-coated sample) SEI layer was found, mainly composed by inorganic compounds from electrolyte reduction. The outward side was formed by $NaCO_3R$, PEO and chemisorbed oxygen, while the inner subregion was mainly formed by Na_2CO_3. Another layer of NaF and NaCl close to the electrode was observed arising from PVdF dehydrofluorination and spontaneous decomposition of $NaClO_4$. The PVdF degradation was observed in both samples, although in the non-coated sample it was already observed during electrode preparation by ^{19}F-ssNMR. The outward layer of both electrodes was partially dissolved and/or cracked upon Na^+ extraction (less pronounced in the coated sample), not forming a stable SEI layer. This instability and the PVdF degradation contribute to capacity fading. Finally, in order to observe the possible influence of metallic Na, when was used as counter electrode, on the SEI layer composition and stability, the C-coated sample was tested using $NaFePO_4$ as counter electrode. Similar composition of the SEI layer was found when it was tested in half- or full-cell. Two main differences were observed: firstly, at OCV charge state the formed SEI layer in a full-cell showed better stability, since the formation of the SEI layer was almost negligible and secondly, the SEI layer thickness was thinner in a full-cell than in a half-cell.

The SPI layer of P2-$Na_{2/3}[Fe_{1/2}Mn_{1/2}]O_2$ was also studied by conventional XPS and, as in the SEI layer of $Na_2Ti_3O_7$, it was found to be mainly formed by inorganic compounds. The P2-$Na_{2/3}[Fe_{1/2}Mn_{1/2}]O_2$ pristine electrode was covered by Na_2CO_3 due to its moisture sensitivity and NaF from the dehydrofluorination reaction of PVdF. Once the cell was assembled decomposition products of the salt appeared ($NaPF_xO_y$ compounds) and at Na^+ extraction state $NaPF_xO_y$, Na_2CO_3 and PEO species were the main contribution of the SPI layer covering completely the NaF. Upon reduction the signals of $NaCO_3R$ and NaF species re-appear and disappear again in the following oxidation process. Although the SPI was not found to be completely stable, the PVdF and graphitic signals were continuously observed, hence SPI layer was very thin (<< 5 nm) and discontinuously distributed which only changed slightly upon cycling. This stability was confirmed by EIS experiments since a constant SPI resistance was shown. In addition, EIS experiments have shown that the poor capacity retention of P2-$Na_{2/3}[Fe_{1/2}Mn_{1/2}]O_2$ cathode material was related with the structural P2 → OP4 transition occurring at 4.0V since the bulk electronic resistance increases drastically. The possible formation of staking faults and/or defects in each transition, corroborated by the broader of the peaks by XRD, most probably causes a progressive capacity loss. Considering that the SPI layer was practically stable but a large increment of the resistance was shown above 4.0 V, it can be concluded that the main contribution to capacity loss is the structural transition from P2 to OP4 at low Na content (x=0.21).

Finally the cathode $Na_4Co_3(PO4)_2P_2O_7$ with the highest Na^+ insertion/extraction voltage was investigated, which exhibited very good electrochemical properties when was prepared with Carbon Black Performance. In the SPI layer during Na^+ extraction, salt and solvents decomposition products (phosphates, fluorophosphates and $Na_{2-x}CO_3R_x$ and PEO) were found covering NaF. During Na^+ insertion more Na_2CO_3 was formed which dissolved in the following Na^+ extraction and $NaCO_3R$ appeared again. However, similar spectra were observed at different oxidation states, being the main components the PVdF and the graphitic signal from the electrode. Hence a very thin and rather stable SPI layer was formed, which is very similar to what is observed at lower voltage for P2-$Na_{2/3}[Fe_{1/2}Mn_{1/2}]O_2$. This SPI layer stability gives the opportunity to use high cut-off voltage materials in NIBs without the risk of a continuous decompose of the electrolyte.

In summary, the structural changes during the cycling influence on the transport properties and in turn on electrochemical performance. The observed transition in $Na_2Ti_3O_7$ from insulator to conductor when Na^+ are inserting promotes the Na^+ insertion/extraction, while the structure change from P2 to OP4 of P2-$Na_{2/3}[Fe_{1/2}Mn_{1/2}]O_2$ at 4.0 V provides a capacity loss. As regards the electrode/electrolyte interphases, contrary to the interphases formed in LIBs which contain more organic species, both SEI and SPI layers formed in NIBs are mainly composed by inorganic products. Moreover the SEI layer in $Na_2Ti_3O_7$ (∼ 5 nm) was found to be much thinner than typical SEI layers found in LIBs (>20 nm thick). The SPI was even thinner and almost stable, with slight changes in composition depending on the electrode/electrolyte configuration that do not seem to be affected by the applied voltage.

A Experimental techniques

A.1. Physicochemical characterization techniques

Physicochemical characterization techniques were used to characterize the structure, morphology and surface and bulk composition of the synthesized materials (see synthesis details in chapters dedicated to each material). Additionally, the X-ray photoelectron spectroscopy (XPS) technique was used to study the electrode/electrolyte interphase of cycled electrodes. The description of the fundamentals and the equipment used for each of these techniques is detailed below.

A.1.1. Diffraction techniques

A.1.1.1. X-ray Diffraction (XRD)

X-ray diffraction (XRD) is probably the most commonly employed method in solid state inorganic chemistry to determine the phase, crystal structure and purity of crystalline solids. This technique is based on the X-ray irradiation of a sample and the interaction of these incident rays with the sample producing constructive interference when Bragg´s law condition takes place. **Figure A.1.1** shows the Bragg condition for the reflection of X-rays by a crystal. Black points represent atoms and the lines joining the dots mark a set of parallel planes with Miller indices *hkl* and interplanar spacing d_{hkl}. A parallel beam of monochromatic X-rays A, D and I is incident to the planes at an angle θ_{hkl}. The ray A is scattered by the B atom and the ray D by F atom. For the reflection beams to emerge as a single beam of reasonable intensity, they must arrive in phase with one another. This is known as constructive interference and to take place, the path lengths of the interfering beams must differ by an integral number of wavelengths [1]. The difference in path length between two atoms, for example E-F and F-G, is given as:

$$difference\ in\ path\ length = 2d_{hkl}\sin\theta_{hkl} \quad (\mathbf{Eq. A.1.1})$$

Since this must be equal to an integral number of wavelengths *n*, and the wavelength of X-rays is λ:

$$n\lambda = 2d_{hkl}sin\theta_{hkl} \qquad (\mathbf{Eq. A.1.2})$$

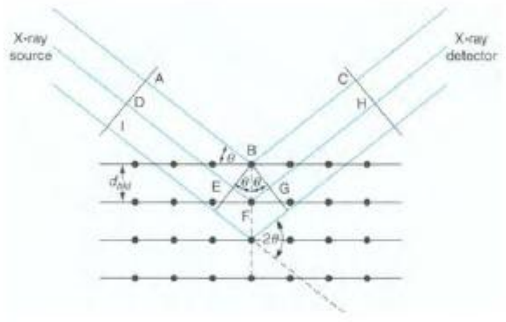

Figure A.1.1: Bragg reflection from a set of crystal planes with a spacing d_{hkl}.

This equation is known as Bragg´s law and it related the spacing between the crystal planes d_{hkl}, to the particular Bragg angle θ_{hkl} at which reflections from these planes are observed [2].

The obtained diffractogram is plotted as the intensity of the diffracted beam as a function of 2 Theta angle. The position and the relative intensity of the peaks allow identifying the phase as well as the crystal structure, since the position of each peak is characteristic distance between atomic planes according to Bragg's law (**Eq. A.1.2**) and the intensity is related to its atomic content.

Powder X-ray Diffraction (PXRD) data were recorded using two different diffractometers with copper radiation, on the one hand, a dichromatic Bruker Advance D8 (λ (CuKα_1) = 1.5406 Å and λ(CuKα_2) = 1.5444 Å) and on the other hand, a monochromatic Bruker D8 Discover (λ(CuKα_1) = 1.54056 Å). *In-situ* measurements were done in the Bruker Advance D8 instrument using a home-made cell based on a 1-inch Swagelok type cell. The 70% of active material $Na_{0.39}H_{1.61}Ti_3O_7$ were mixed with a 30% of carbon Super C65. The electrochemical test was done using Na as counter and 1 M $NaClO_4$ EC:PC as electrolyte. PXRD data were collected every 30 min between 2 Theta = 8 - 35 ^{o} during the 1st Na^+ insertion.

In recent years, synchrotron facilities have become widely used. Synchrotron radiation is emitted by electrons or positrons travelling at near light speed in a circular storage ring. This powerful source is thousands to millions of times more intense than laboratory X-ray tubes. In this work the structural evolution of $Na_4Co_3(PO_4)_2P_2O_7$ sample was measured at the Australian Synchrotron in collaboration with Dr. Neeraj Sharma. The employed cell was a coin cell with a kapton window and the electrode mass loading was 3.3 mg. The $Na_4Co_3(PO_4)_2P_2O_7$ was charged to 4.7 V at 40 mA/g and discharged to 3.0 V at 8 mA/g during the 1st cycle, while in following cycles a current density of 30 mA/g was applied. The

HRXRD data was collected with a wavelength λ = 0.0688077 nm every 20.5 min with an acquisition time of 2.4 min.

A.1.1.2. Neutron Diffraction (ND)

Neutron radiation can also be used instead of X-rays, however ND is a less common technique because few sources of neutron are available since require a nuclear reactor. Nevertheless, for certain structures and to determine the position of some elements ND is advantageous. The main difference between XRD and ND techniques lies in the scattering process: X-rays are scattered by electrons around the nucleus, while neutrons are scattered by the nucleus. Therefore, since the scattering factor for X-rays increases linearly with the number of electrons in the atom, heavy atoms are more effective at scattering than light atoms and light elements like hydrogen are weakly observed. In neutrons, since the atomic nuclei, rather than the extra nuclear electrons, are responsible for the scattering and in fact, hydrogen is a strong scattered of neutrons. Moreover, ND is also used to and allows distinguishing between atoms that have similar X-ray scattering powers, such us Mn and Fe or Co and Ni; as well as to determine the magnetic structure [1, 3].

Powder neutron diffraction (PND) data were recorded at the D1B instrument (ILL, Grenoble, France) at room temperature with a wavelength λ = 1.28 Å. D1B is a high intensity powder diffractometer with a new steady 128 ^{o} position sensitive detector (PSD) covering the angular range 0.8 to 128.8 ^{o} [4].

Both XRD (PXRD either HRXRD) and PND data were analyzed by means of the FullProf analysis software [5]. All diffraction patterns were refined by the Rietveld method using Thompson-Cox-Hastings pseudo-Voigt function to model the peak shape parameters, scale factors, zero point, unit cell constants, atomic positions, isotropic Debye-Waller B factors and atomic occupancies, that were simultaneously refined. The structural models used were obtained from the ICSD database [6]. The GFourier program (included in the FullProf suite) was used to determine the Na^+ and H^+ position of $Na_{2x-}H_xTi_3O_7$ samples from difference Fourier maps since they have opposite neutron scattering length: Na 3.63 fm and H -3.74 fm [5, 7]. The reliability factors of the refined patterns were used as reference for the goodness of the Rietveld method. Finally, the *in-situ* XRD patterns were refined by Le Bail method also using FullProf software in order to determinate symmetry changes and cell parameter evolution during the electrochemical performance. By Le Bail method the cell parameters and space group is determined, although does not provide atomic positions as the Rietveld method, which is possible to solve crystal structure.

A.1.1.3. Electron Diffraction (ED)

ED technique uses the wave properties of electrons because the scattering efficiency of electrons is high and hence a small amount of sample may be used. The results take the form of patterns of spots on photographic films. ED is very useful technique to obtain the unit cell and space group information [3].

A FEI Tecnai G2 transmission electron microscopy (TEM) was used to gather electron diffraction (ED) data. The samples were prepared by previously dispersing them in acetone and placing a drop onto a holey-carbon film. Gold was used to calibrate the length.

A.1.1.4. Laser Diffraction

Laser diffraction technique delivers rapid and accurate particle size distributions for both wet and dry dispersions measuring over the nanometer to millimeter particle size ranges. It works by measuring the intensity of light scattered as a laser beam passes through a dispersed particulate sample. This data is then analyzed to calculate the size of the particles that created the scattering pattern [8].

The information that the laser diffraction gives is the particle size distribution, where the dV90 means that 90% of the particles have at least this size, while dV50 and dV10 correspond to the 50% and 10% of them, respectively. Additionally, the relative standard deviation (RSD%) is given. This factor is standardized measure of dispersion of a probability distribution; expressing the precision and repeatability of the measurement. RSD is the ratio between the standard deviation (σ) and average value (μ) (**Eq. A.3**). The standard deviation is a factor to show how precise is the average, that is, how well the individual numbers agree with each other.

$$RSD\% = \left(\frac{\sigma}{\mu}\right) x\ 100 \quad (\mathbf{Eq.A.1.3})$$

A Mastersizer 3000 laser (Malvern) diffraction particle size analyzer was used to determine the particle size distribution of all studied samples which were previously dispersed in ethanol.

A.1.2. Electron Microscopy techniques

Electron microscopy is widely used in the characterization of solids to study structure, morphology and crystallite size, to examine defects and to determine the distribution of elements. The electron beam is produced by an electron gun and focused by magnetic fields in a high vacuum environment. The very short wavelength of the electron allows an imaging resolution down to 0.1 nm, where the electrons are absorbed or scattered by the object. In this study Scanning Electron Microscopy (SEM) and Transmission Electron Microscopy were used, the latter with a higher resolution as can be observed in **Figure A.1.2** [3].

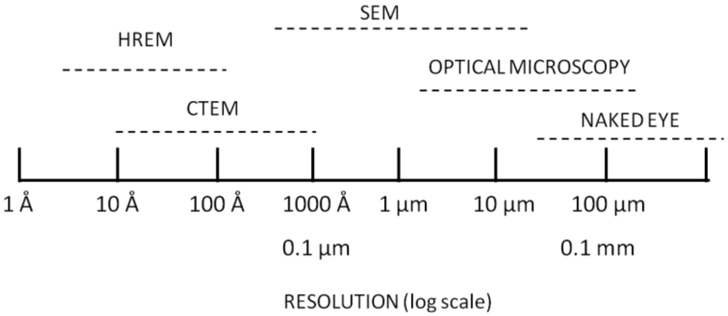

Figure A.1.2: Working range of various microscopy techniques: CTEM = conventional transmission electron microscopy, HREM = high resolution electron microscopy and SEM = scanning electron microscopy.

A.1.2.1. Scanning Electron Microscope (SEM)

The finely focused beam of electrons is rastered across the surface of the sample, those electrons are reflected by the surface of the sample and the emitted secondary electrons (which have higher resolution than other type of signal such as backscattered electrons or X-rays) are detected so a map of the surface topography of the sample can be produced. It is useful for looking at particle size, crystal morphology, magnetic domains and surface defects. A wide range of magnifications can be used and the accelerating voltage is usually between 1 and 30 kV. Moreover, sometimes it is necessary to coat the sample with gold or carbon in order to increase the electronic conductivity and avoid charge accumulation [3].

In this work the morphology and particle size were analysed using a SEM (Quanta 200 FEG-FEI model) operated at 30 kV. $Na_{2-x}H_xTi_3O_7$ samples were coated with gold using a SPI module TM Super Coater.

A.1.2.2. Transmission Electron Microscope (TEM)

In this case, a thin sample is required since a high intensity beam of electrons is used which should pass through the sample and form a two dimensional projection of the sample in the detector. The electrons may be elastically or inelastically scattered. In high resolution instruments (HREM-HTEM), a very high potential field, up to 10^6 V, accelerates the electrons, increasing their momentum to give very short wavelengths. Since the electrons pass through the sample, TEM images are able to detect crystal defects [3].

A high resolution TEM/STEM FEI Tecnai G2 with a 200 kV field emission gun (FEG) was used to obtain high resolution images. A Philips CM 200 TEM from SGIker (Servicios Generales de Investigación from UPV/EHU) was used to study the C-coating on $Na_2Ti_3O_7$ and $Na_4Co_3(PO_4)_2P_2O_7$ samples.

A.1.3. Spectroscopic techniques

There are many different spectroscopy techniques but all work on the same basic principles. That means that under certain conditions, materials are capable of absorbing or emitting energy, normally as electromagnetic radiation, but it also can be sound waves, particles, etc. The electromagnetic spectrum covers a huge range of frequencies and wavelengths, and hence energies. The different spectroscopic techniques operate over different limited frequency ranges depending on the processes and magnitudes of the energy changes that are involved (**Figure A.1.3**).

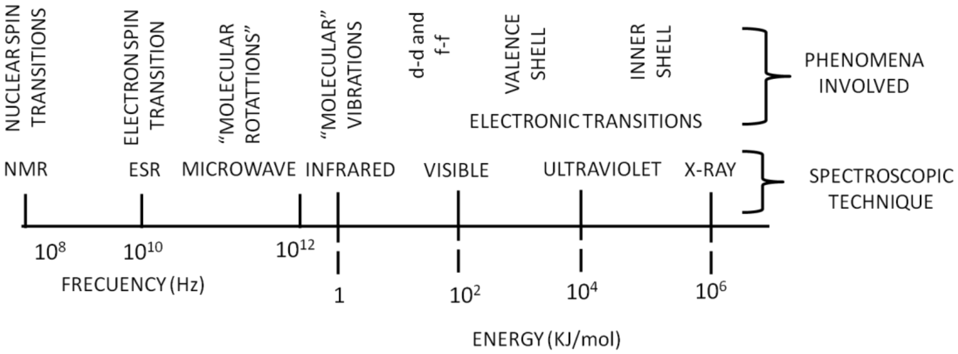

Figure A.1.3: Principal regions of the electromagnetic spectrum and the associated spectroscopic techniques.

A.1.3.1. Fourier Transform Infrared Spectroscopy (FTIR)

FTIR spectroscopy is one of the most useful techniques for identifying the type of bond between two or more atoms. Since vibrational modes, involving pairs or groups of bonded atoms, can be excited to higher energy states by absorption of radiation of appropriate frequency, FTIR is able to identify functional groups. In FTIR the absorption frequency of the incident radiation is varied and the quantity of radiation absorbed or transmitted by the sample is measured. The FTIR spectrum is a plot of intensity of absorption/transmission as a function of frequency or wavelength.

In this work FTIR data were collected in a FTIR Spectrum 400 DTGS (Perkin Elmer) after diluting the sample in KBr, which does not absorb in the measured region. The analysis was carried out in the range 4000 - 500 cm^{-1}.

A.1.3.2. Solid-state Nuclear Magnetic Resonance (ssNMR)

NMR technique involves the magnetic spin energy of atomic nuclei. The magnetic energy levels split into two groups when magnetic field is applied depending on how the nuclear spins are aligned: parallel or antiparallel. The energy difference between these two states is associated with the frequency of absorption, which at the same time depends on the particular element and also on its chemical environment [3]. In liquid NMR the spectrum has a high resolution since dipolar interactions and anisotropic effects are averaged out by the nuclear spin transitions. However, in solid state NMR the peaks trend to broad due to three main effects:
1- Magnetic dipolar interactions
2- Low abundance isotopes have long spin lattice relaxation time and give rise to poor signal/noise ratio.
3- The chemical shift of some atom can vary with the orientation of the molecule to the magnetic field. This effect is called chemical shielding anisotropy.
However, high resolution ssNMR can be used in most isotopes with spin I = 1/2; such as, H^+ [3].

In this work three types of nuclei were measured: ^{23}Na (I = 3/2), ^{1}H (I = 1/2) and ^{19}F (I = 1/2). ^{23}Na Magic Angle Spinning Nuclear Magnetic Resonance (MAS-NMR) spectra were recorded with a WB Bruker Advance III 500 spectrometer working at a frequency ν_o = 132.29 MHz for ^{23}Na. The experiments were performed on powdered samples spun at the magic angle with a 2.5 mm standard probe. The MAS frequency was set to 20 kHz in all cases. ^{23}Na spectra were referenced to a 0.1

M NaCl solution resonating at 0 ppm. The one dimensional ^{23}Na-NMR spectra were recorded using a non-selective π/2 pulse with the duration adjusted to 1.3 µs and a recycling delay of 24 s for all $Na_2Ti_3O_7$ samples while 5 s of delay was used for $Na_{2-x}H_xTi_3O_7$ samples. Moreover, the ^{23}Na multiple quantum magic angle spectra (MQMAS) of $Na_{2-x}H_xTi_3O_7$ samples were recorded using a 3 pulse basic sequence with z-filter [9]. The first two hard pulses were set to 4.6 and 1.4 µs respectively, and the final soft pulse to 19 µs.

The ^{1}H-ssNMR spectra were recorded using rotor synchronized echo experiments with a π/2 pulse of 3 µs and the recycling delay was set to 100 s.

For ^{19}F-ssMMR experiments electrodes were scratched out of the aluminum current collector and the powders were fitted into the rotors inside an Ar-filled glovebox. ^{19}F-ssNMR data were collected on a Bruker 500 MHz spectrometer, at an operating frequency of 470 MHz, with a 1.3 mm probe. Rotors were spun at a magic-angle-spinning (MAS) rate of 50 kHz. A rotor synchronized Hahn echo (90°-τ-180°-τ-acq.) sequence was used with a 90° pulse of 3.6 µs and a delay of 40 s. Spectra are referenced to secondary LiF (−201 ppm) [10]. Approximately 100 000 scans were collected per ^{19}F-ssNMR spectrum.

A.1.3.3. Inductively Coupled Plasma Optical Emission Spectroscopy (ICP-OES)

ICP-OES is an analytical technique for the determination of concentration of elements in a sample. Samples are mainly introduced in the spectrometer as aqueous solution and then by a peristaltic pump to the nebulizer system. There, the liquid is transformed to wet spray by Ar gas. Later, the wet spray is dried and the inductively coupled plasma produces excited atoms and ions that emit electromagnetic radiation. These ions or excited atoms, when go back to the initial state, emit radiation of a wavelength that is characteristic of each element. This radiation crosses an optical system which divides the radiation depending on the wavelength. Then the detector measures the intensity of each radiation which is linked with the concentration of each element in the sample. However, firstly it is necessary to calculate the calibration curve by a standard dissolution [11].

The used equipment was a Horiba-Ultima 2 Sequential ICP-OES. The samples were digested in a concentrated solution of HCl in the Rotative Solid-Phase Microwave Reactor (Roto Synth-Milestone S.R.L) at 150 °C for 1 h. Later the dissolution was diluted before introduced in the spectrometer.

A.1.3.4. Ion Beam Analysis (IBA)

IBA techniques from the *Centro Nacional de Aceleradores* (CNA) in Seville (Spain) were used to obtain a more accurate and complete compositional analysis of $Na_{2-x}H_xTi_3O_7$ samples. At CNA a 3 MV Tandem accelerator is available to deliver H^+ or He^{2+} high energy beams, the beam can be deflected into seven different beamlines devoted to a wide variety of IBA techniques.

The Na, Ti and O content was determined by means of Rutherford backscattering spectrometry (RBS); a beam of 1.5 MeV alpha particles was projected on the samples and the backscattered particles were collected with a Si solid state detector placed at a scattering angle of 165 °. The intensity of backscattered particles was calibrated using a Pt standard ($18x10^{15}$ at/cm^2), therefore the exact concentrations could be determined.

Although RBS can provide a very accurate determination of atomic concentration, it is not suited to determine the H^+ concentration; in this case, elastic recoil detection analysis (ERDA) was performed using 3.0 MeV He^{2+} particles at a scattering angle of 34 °. With this forward scattering configuration the He^{2+} incident ions drag H^+ from the sample, an Al coated Mylar filter is placed between the sample and the detector in such a way that the scattered He^{2+} particles are stopped and only the recoil H^+ go through and are detected. Therefore a signal from the H^+ concentration in the sample is obtained [12].

A.1.3.5. X-ray Photoelectron Spectroscopy (XPS)

XPS technique is one of the best options to study the composition and evolution of the SEI layers. With this method an electron spectrometer is used to measure the energy distribution of photoelectrons and Auger electrons emitted from a surface irradiated by X-ray photons. The X-ray sources commonly used are Al and Mg non-monochromated (Al K_α = 1486.6 eV and Mg K_α = 1253.6 eV), although X-ray sources with other anodes or synchrotron radiation is also available. The basics of this technique are shown in **Figure A.1.4**. The photons interact with the core electrons in the atom creating a hole and then, the core electron ejected to the vacuum level with a given energy. The kinetic energy of the emitted photoelectron is then analysed by the electron spectrometer and the data presented as graph of photoelectron intensity (counts/s) *vs*. photoelectron kinetic energy.

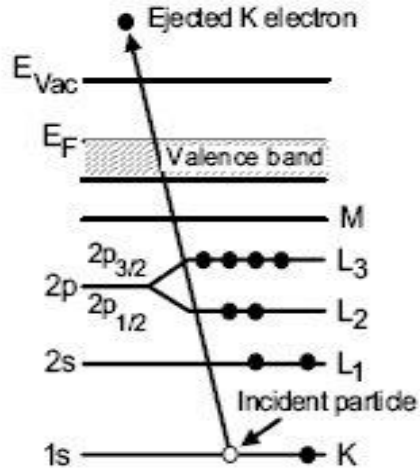

Figure A.1.4: Schematic diagram of the XPS process, showing phtotoionization of atom by the ejection of a 1s electron.

The measured kinetic energy (E_K) is given by the following equation:

$$E_K = h\nu - (E_B + W) \quad (\mathbf{Eq. A. 1. 4})$$

where *hυ* is the photon energy, E_B electron binding energy of the atom and W the spectrometer work function. The E_K of ejected photoelectron depends on the photon energy of the X-ray employed and therefore is not intrinsic of the material while the electron binding energy (E_B) is specific of the measured material. This allows to determine the atomic species on the surface. Moreover, the chemical environment of the atoms produces variations in the binding energies of the electrons, shifting the E_B to higher or lower values being possible not only to determine the atom type but also the chemical environment and oxidation state. However, although the incident photons are able to penetrate about 1 - 10 µm into the material, the emitted photoelectrons that reach the detector only come from the outermost 3 - 10 nm which is the maximum distance that a XPS photoelectron can travel in a solid before losing energy and being trapped. This distance is the so called inelastic mean free path (IMFP) and it depends on the photoelectron kinetic energy; if higher photon energies are used, the kinetic energy of the photoelectrons will be higher and, therefore, the IMFP will be larger (**Figure A.1.5**) [13].

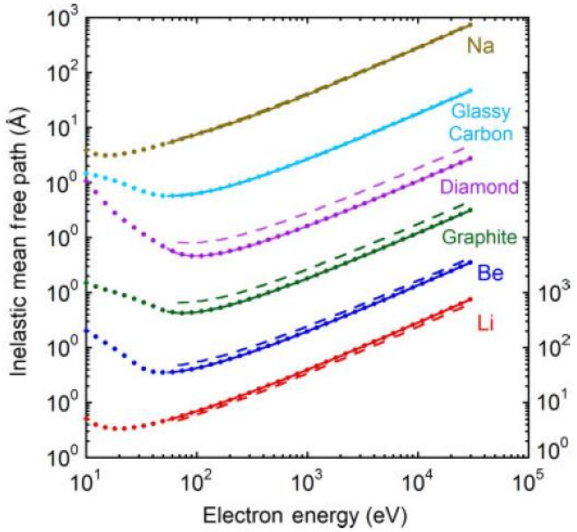

Figure A.1.5: Plots of electron inelastic mean free path (IMFP) as a function of electron energy.

It is worth mentioning that the absolute energy determination relies on having a grounded sample which can easily refill the created holes. If the sample has an insulating character, the hole refill will be hampered and surface charging effects will appear leading to unpredictable shifts and lineshape distortions of the XPS peaks. It is possible to compensate this situation through co-irradiation of the sample surface with a low energy electron beam produced by a flood gun. This excess of electrons is used to produce a uniform negative charge at the surface of the sample which should correct the lack of electrons coming from ground. Finally the photoelectron peaks should be shifted to their correct positions during the data collection [14, 15].

One of the methods that can be used to obtain more information at higher depths is the ion bombardment which gently removes the outermost surface layers by means of an ion beam (typically Ar). The experimental procedure consists in the analysis of the undisturbed surface by XPS. Then the sample undergoes a period of ion etching using ions whose energy is in the range of a few hundred to a few thousands eV. Later the XPS data are collected again with the ion beam switched off. This process is repeated until the required depth is reached. However, this methodology can destroy the sample and induce the formation of undesired compounds. For this reason it has to be used with caution.

Furthermore, in the XPS experiment not only occur the emission of core level photoelectrons, sometimes, depending on the element, Auger electrons are

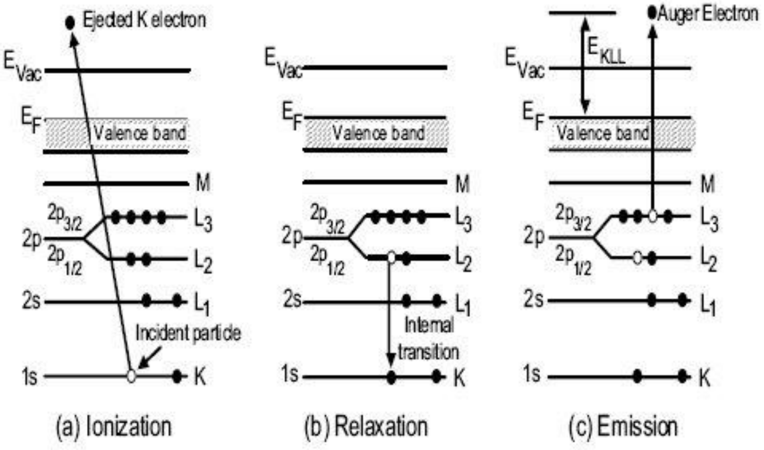

Figure A.1.6: Schematic diagram of the Auger process, showing phtotoionization of atom by the ejection of a 1s electron, relaxation process and Auger electron emission

emitted. The Auger process takes place due to the relaxation of an atom with a vacancy in an inner electron shell. The Auger emission process is illustrated in **Figure A.1.6** and consists on the fall down of an electron from a higher orbital (in this case from 2*p*) to fill the hole originated by the ejected photoelectron (1*s* orbital). Then the excess energy of the excited state ion is removed by the ejection of an Auger electron.
The kinetic energy of the Auger electron (E_{KA}) is given by the following equation:

$$E_{KA} = \left(E_{1s} - E_{2p1/2}\right) - E_{K2p3/2} \ + W\big) \quad (\mathbf{Eq.A.1.5})$$

where E_{1s} is the binding energy of the photoelectron hole in the 1s level, $E_{2p1/2}$ is the binding energy of the electron that falls down to fill the 1*s* hole, $E_{K2p2/3}$ is the kinetic energy of the emitted Auger electron and W the spectrometer work function.

Moreover, taking into account the binding energy of the photoemission and the kinetic energy of Auger lines for the same atom is possible to determine the Auger parameter ($\alpha + h\upsilon$) for the studied atom which provides the identification of surface components. The Auger parameter (α) for a given atom is described by the following equation:

$$\alpha + h\nu = E_K \ + \ E_B \qquad (\mathbf{Eq.A.1.6})$$

This parameter is specific of each species and, due to the nature of the process; it is not affected by surface charging effects. Hence, the analysis of the Auger parameter allows identifying the surface composition without influence from surface charging effects. Typically, the SEI layer which is formed by conducting and non-conducting species, will suffer of surface charging effects which will difficult the absolute binding energy calibration and, therefore, the peak assignment. Hence, the analysis of the Auger parameter will be crucial to go one step further as regards the SEI layer study.

Electrode/electrolyte interphase, SEI layer even SPI layer, was investigated at different charge states using a Phoibos 150 XPS spectrometer and different X-ray sources. For $Na_2Ti_3O_7$ samples, non-monochromatic Mg K_α (hν = 1253.6 eV) was employed while for P2-$Na_{2/3}[Fe_{1/2}Mn_{1/2}]O_2$ sample both Mg K_α and Al K_α source (hν = 1486.6 eV)) were used. The $Na_4Co_3(PO_4)_2P_2O_7$ sample was measured with the Mg K_α and Ag K_α source (hν = 2984.3 eV). This greater energy allows the possibility of enhanced probing depth without the need to use ion etching which is a destructive methodology.

Cycled electrodes were rinsed with PC (for the anode) or DEC (for the cathodes) prior to XPS experiments inside the Ar-filled glove box and inserted into the XPS vacuum chamber using an Ar-filled transfer system, never exposing the samples to air. High resolution scans were acquired at 100 W, 20 eV pass energy and 0.1 eV energy step.

All experiments were carried at low power (100 W) in order to avoid the possibility to damage the sample. At high power energies the X-ray induced decomposition of the PVdF and $NaClO_4$ is expected, hence, the species that will appear in the XPS photoelectron spectra will be the result of radiation effects and not from the electrochemical process.

Depth profiling of un coated $Na_2Ti_3O_7$ sample was done using a focused ion gun for keV Ar^+ with a sputtering rate of 0.2 Å/s, which was determined from measurements in a Ta_2O_5 standard calibrated with laser profilometry and corrected by the relative sputtering cross section of our particular compound. Moreover, reference samples ($Na_2Ti_3O_7$, Na_2CO_3, PVdF and $NaClO_4$) were measured in order to minimize the damage of the sample to X-ray beam and ion beam power.

The flood gun was used in P2-$Na_{2/3}[Fe_{1/2}Mn_{1/2}]O_2$ sample to charge compensate where the energy applied was 1.5 V and the emission 10 µA.

For all samples the binding energy calibrations were done taking into account the graphitic-like carbon peak at 284.4 eV as reference. For the charge states were the graphitic signal was not visible, the same shift measured for the previous charge state was used. Using the graphitic carbon as reference for Na-ion cells is possible since the Na^+ do not insert into graphite [16, 17]. In LIBs this would not be possible because the Li^+ ions insert into the graphite to form Li_xC_6 and the binding energy of the C–C bond would shift to lower binding energies. Moreover, other possible peaks to use as reference is the $-CF_2$ from the PVdF binder, however, the Na^+ can chemically interact with PVdF strongly influencing the fluorine electronic structure and shitting the signal to higher energies [18]. Therefore, selecting the graphite peak as the reference for the binding energy is the best option. However, due to differential surface charging effects, since the electro/electrolyte interphase is composed by conducting and non-conducting microdomains, the calibration procedure is not sufficient for a full determination of the surface layer composition some cases. Hence, the Auger parameters were determinate for non-coated and coated $Na_2Ti_3O_7$ samples by measuring additionally the Na $KL_{23}L_{23}$ peaks and the photoelectron Na 1*s* peak. The positions of those peaks were fitted using the CasaXPS software [19], by Voigt functions. In the case of the studied cathode material the determination of Auger parameter was not possible, probably due to the signal overlapping and the very thin electrode/electrolyte interphase.

A.1.4. Thermal analysis

A.1.4.1.Thermogravimetric analysis (TGA)

TGA experiments are used to monitor the weight of a sample as a function of time as the temperature is increased/decreased at a controlled uniform rate [3]. This method is thus useful for investigation of phase changes, decomposition, loss of water or oxygen, and for constructing phase diagrams.

In our case, a STA 449 F3 system-Netzch was used to quantify the amount of H^+ in $Na_{2-x}H_xTi_3O_7$ samples taking into account the reaction below:

$$Na_{2-x}H_XTi_3O_7 \rightarrow Na_{2-x}H_XTi_3O_7 + {}^{x}/_{2}\, HO_2$$

The carbon amount was also determined by TGA in several samples by heating them at 800 °C under air atmosphere and measuring the weight loss.

A.2. Electrochemical characterization techniques

Three main different electrochemical techniques were used in this work: cyclic voltammetry (CV), galvanostatic measurements and electrochemical impedance spectroscopy (EIS).

A.2.1. Electrode preparation

The active material was mixed in the required ratio with conductive additive Super C65 and binder which was firstly dissolved in NMP when PVdF was used, and in water in the case of Na-CMC. The slurries were casted on battery grade Aluminium foil. Laminates were dried under vacuum overnight at 120 ^{o}C for all samples, except for $Na_{2-x}H_xTi_2O_3$ ($0<x\leq2$) laminates which were dried overnight at 80 ^{o}C, in order to avoid the decomposition of the compound. Disk electrodes were punched at required sizes (11 mm for galvanostatic measurements and 9 mm for EIS experiments) and pressed at 5 tons. Except for $Na_4Co_3(PO_4)_2P_2O_7$ which is stable under atmospheric conditions, all samples were stored and electrodes were prepared in an Ar-filled glove box to avoid any contact with the atmosphere.

A.2.2. Cell preparation

Cells were tested using metallic Na disk as counter and reference electrode and glass fibre (Whattman GF D 55) as separator. Two electrolytes were used for $Na_{2-x}H_xTi_3O_7$ anode 1 M $NaClO_4$ in EC: PC and for both cathode 1 M $NaFP_6$ EC: DEC. All measurements were carried out at room temperature.

A.2.3. Cyclic voltammetry (CV)

CV technique provides the information about the number of redox reactions that are occurring in the cell, as well as the voltage at which they occur and their reversibility. The measure consists on measuring the intensity of the working electrode when a voltage scan is applied with a constant scan rate [20].

CV was carried out in two electrode Swagelok cells using a VMP3 potentiostat (Bio-Logic) in the same voltage range applied in the galvanostatic measurements for each sample. CVs were performed at 0.40 mV/s.

A.2.4. Galvanostatic experiments

A galvanostatic experiment consists in measuring the change of voltage over time, ion insertion or capacity under a constant current density and in a selected voltage range. When a half-cell configuration is used in other word, when the intercalation material is tested *vs*. metallic Na, the measured voltage corresponds to the working electrode (WE), with is the electrode that is under study. While in a full-cell, both the WE and the counter electrode (CE) are Na^+ intercalation materials and hence the voltage before electrochemical cycling starts is the differential voltage between both electrodes. For example in the case of $Na_2Ti_3O_7$ *vs*. $NaFePO_4$ the voltage was close to 0 V. The applied constant current for the galvanostatic tests was calculated as a function of the theoretical capacity (C_{theo}) of the studied active material, which is expressed as:

$$C_{theo}\left(\frac{mAh}{g}\right) = \frac{nF}{3600\ PM} \quad (\mathbf{Eq. A.2.7})$$

where *n* is the number of electrons in the reaction, *F* is the Faraday constant (96,485.33289(59) C/mol) and corresponds to the magnitude of electric charge per mole of electrons, and PM is the molecular weight of the material expressed in kg/mol.

Galvanostatic measurements of all studied samples were carried out using coin cells tested in a VMP3 potentiostat (Bio-Logic) or a Maccor battery tester. The $Na_{2-x}H_xTi_3O_7$ ($0<x\leq2$) was tested at 0.1C in the voltage window of 0.05 - 1.6 V *vs.* Na^+/Na, while $H_2Ti_3O_7$ at 0.1C but at 0.9 - 2.2 V *vs.* Na^+/Na. Meanwhile the P2-$Na_{2/3}[Fe_{1/2}Mn_{1/2}]O_2$ and $Na_4Co_3(PO_4)_2P_2O_7$ at 0.05C in the working voltage of 1.5 - 4.25 V or 2.0 - 4.0 V and at 0.2C in the voltage range of 3.0- 4.7 V *vs.* Na^+/Na, respectively.

A.2.5. Electrochemical Impedance Spectroscopy (EIS)

Electrochemical impedance spectroscopy (EIS) can give accurate information of the transport properties. For this reason, EIS is becoming a powerful tool in the battery field. Alternating current (AC) impedance analysis is an electrochemical method to observe the current response during the electrochemical process under AC voltage in order to obtain values for resistance (R), capacitance (C) and inductance (I). AC voltage changes periodically over time and a phase difference exits with the current:

$$V(t) = Vm\sin(\varpi t) \quad (\mathbf{Eq. A.2.8})$$

where Vm is the maximum voltage and ω the angular frequency.

The current has a phase difference of θ with respect to AC voltage:

$$I(t) = Im \sin(\varpi t - \theta) \quad (\mathbf{Eq. A. 2. 9})$$

And the impedance is defined as the ratio of the voltage and the current:

$$Z(w) = \frac{Vm}{Im} \quad (\mathbf{Eq. A. 2. 10})$$

The impedance has two parts: the real part (Z´) and the imaginary part (Z”). The real part (Z´) is the resistance, while the imaginary part (Z”) corresponds to the capacitance and inductance elements.

$$Z\ (w) = Z' + j\, Z" \quad (\mathbf{Eq. A. 2. 11})$$

The impedance is plotted as the real part (Z´ = Re) on the X-axis and the imaginary part (Z” = -Im) on the Y-axis, obtaining the graph named as Nyquist Plot (**Figure A.2.7a**). Notice that the Z” (Y-axis) is negative and that each point on the Nyquist Plot is the impedance at one frequency where the low frequency data are on the right side of the plot and higher frequencies are on the left. EIS data are commonly analyzed by fitting to an equivalent circuit model where the common elements are the resistor, capacitor, and inductor. The Nyquist Plot of **Figure A.2.7a** can be fitted with the electrical circuit model of **Figure A.2.7b**.

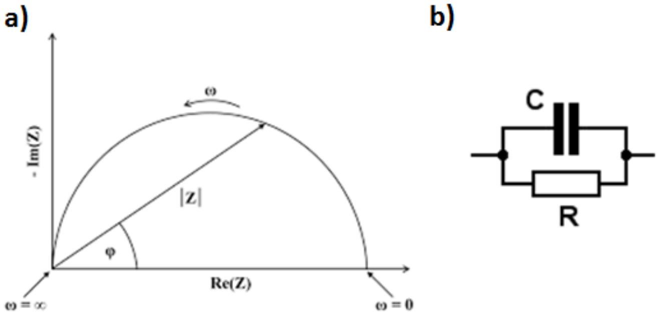

Figure A.2.7: a) Schematic of the Nyquits plot and **b)** corresponds equivalent circuit.

The electrochemical impedance plot of an intercalation material contains several semicircles and usually only a portion of a semicircle is seen since, the overlapping of semicircles occurs. Since several process take place, the EIS model of an intercalation material consists of a number of elements in a series. The most common elements observed in intercalation materials that are frequency dependent are shown in **Figure A.2.8**. In the following list, the most common processes and their circuit equivalent at different frequencies are detailed [21]:

1.- At high-frequency (HF):

1.1.- Electrolyte resistance (R_{sol}): corresponds to the ion when travels across the electrolyte.

1.2.- Electrode/electrolyte resistance (R_{SEI}) and capacitance (C_{SEI}): are originated by the resistance experienced by the ions when they cross the interphase and by the double layer that is formed on the surface of the interphase, respectively.

2.- At medium-frequency (MF):

2.1.- Charge-transfer resistance (R_{CT}) and double layer capacitance (C_{DL}): these processes occur on the surface of the particles when the ions go into the particles. On the surface of the particles the negative and positive charges are accumulated behaving as a capacitor.

3.- At low-frequency (LF):

3.1.-Warburg diffusion (Z_W): related to the solid-state diffusion of the ions inside the crystal.

3.2.- Intercalation capacity (C_i): linked to the charge accumulation. This process occurs in intercalation electrodes, known also as blocking electrode since at certain voltage the electrode material is not able to insert the ions and hence the charge will accumulate on the surface of the particle.

Moreover, the surface of the particles and interphases are not ideal in the intercalation materials and in order to take into account any inhomogeneity, roughness or degree of polycrystallinity the capacitances and Z_w were substituted by constant phase elements (CPEs), which is expresed as:

$$C_i = \frac{Q_t \Delta_x(E)}{\Delta E} \quad (PITT) \quad (\mathbf{Eq. A. 2. 12})$$

$$C_i = -\frac{1}{Z''_{\varpi \to 0}} \quad (\mathbf{Eq. A. 2. 13})$$

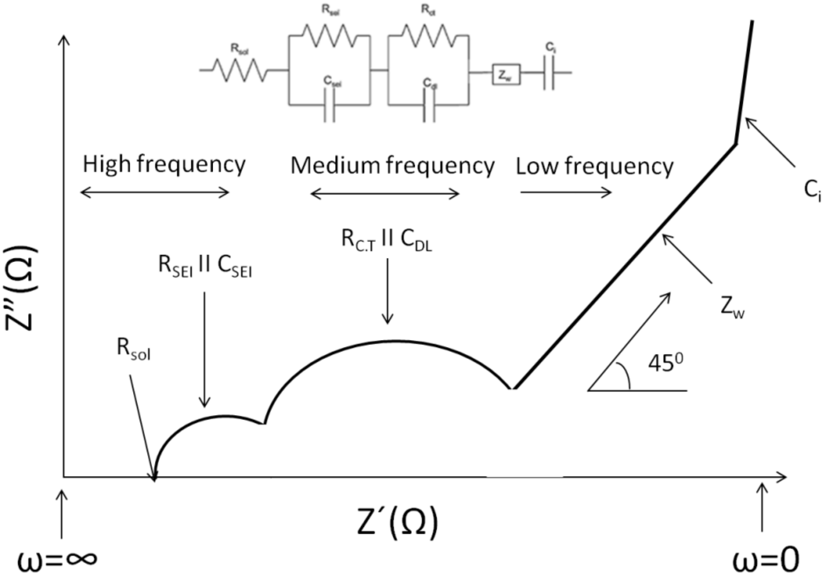

Figure A.2.8: A typical Nyquits plot of an intercalation material and the equivalent circuit.

EIS were carried out in two and three electrode Swagelok cells using a VMP3 potentiostat (Bio-Logic) in the same voltage range and current density applied in the galvanostatic measurements. EIS experiments were performed by controlling the electrode potential through PITT (potentiostatic intermittent titration technique) intercalation and deintercalation scans with steps of 25 mV for $Na_2Ti_3O_7$ samples while for the studied cathodes the voltage step was 45 mV. Sinusoidal perturbations of 5 mV, in the frequency range 5 mHz-100 kHz, were superimposed to the bias potentials. In order to reach an equilibrium condition, 4 hour equilibration time at constant potential was allowed before recording each impedance spectra. Boukamp´s Equivalent Circuit software was used to fit all EIS data [22].

A.3. References

[1] L.E. Smart, E.A. Moore, Solid state chemistry, An introduction, 3rd ed, Taylor & Francis Group Boca Raton 2005.
[2] J.P. Glusker, K.N. Trueblood, Crystal structure analysis: A premier, Oxford Universitypress, New York 1985.
[3] A.R, West, Solid state chemistry and its applications, John Wiley & Sons Ltd. 1990.
[4] https://www.ill.eu/en/html/instruments-support/instruments-groups/instruments/d1b/description/instrument-layout/ (accessed in July 2016).
[5] J. Rodríguez-Carvajal, Recent advances in magnetic structure determination by neutron powder diffraction, Physica B: Condensed Matter 192 (1993) 55-69
[6] https://icsd.fiz-karlsruhe.de/search/basic.xhtml (acceded in July 2016).
[7] https://www.ncnr.nist.gov/resources/n-lengths/ (acceded in July 2016).
[8] http://www.malvern.com/en/products/product-range/mastersizer-range/mastersizer-3000/ (acceded in July 2016).
[9] J.P. Amoureux, C. Fernandez, S. Steuernagel, Z Filtering in MQMAS NMR, J. Magn. Reson. A 123 (1996) 116-118.
[10] U. GroB, S. Rüdiger, A.R. Grimmer, E. Kemnitz, ^{19}F-NMR solid state investigations of monovalent alkali metal fluorides and tetra-alkylammonium fluorides; J. Fluorine Chem. 115 (2002) 193-199.
[11] Horiba Scientific, ICP user manual ultima 2 family, Horiba Jobin Yvon S.A.S, Longjumeau (Reference 31 088 486).
[12] http://acdc.sav.us.es/cna/ (accessed in July 2016).
[13] S. Tanuma, C.J. Powell, D.R. Peen, Calculations of electron inelastic mean free paths. IX. Data for 41 elemental solids over the 50 eV to 30 keV range, Surface Interface Ana. 43 (2011) 689-713.
[14] J.F. Watts, J. Wolstenholme, An introduction to surface analysis by XPS and AES, John Wyley & Sons, Ltd., England 2003.
[15] P. Van der Heide, X-ray photoelectron spectroscopy. An introduction to principles practices, John Wiley & Sons, INC. Hoboken, New Jersey 2012.
[16] M.M. Doeff, Y. Ma, S.J. Visco, L.C. De Jonghe, Electrochemical insertion of sodium into carbon, J. Electrochem. Soc. 140 (1993) L169-L170.
[17] S. Komaba, W. Murata, T. Ishikawa, N. Yabuuchi, T. Ozeki, T. Nakayama, A. Ogata, K. Gotoh, K. Fujiwara, Electrochemical Na insertion and solid electrolyte interphase for hard-carbon electrodes and application to Na-ion batteries, Adv. Funct. Mater. 21 (2011) 3859-3867.
[18] B. Xu, J. Choi, C.N. Borca, P.A. Dowben, Comparison of aluminum and sodium doped poly(vinylidene fluoride-trifluoroethylene) copolymers by X-ray photoemission spectroscopy, Appl. Phys. Lett. 78 (2001) 448-450.
[19] J. Walton, P. Wincott, N. Fairley, A. Carrick, Peak Fitting with CasaXPS a Casa pocket book, Accolyte Sicence, Knutsford, UK 2010.
[20] J.K. Park, Principles and applications of lithium secondary batteries, Wiley-VCH Verlag & Co, KGaA, Weinheim, Germany 2012.

---

[21] E. Barsoukov, J.R. Macdonald; Batteries, in: Impedance spectroscopy theory, experiment and application; 2nd ed., John Wiley & Sons Inc., Hoboken, New Jersey, 2005, pp 444-469.

[22] B. A. Boukamp, A nonlinear least squares fit procedure for analysis of immittance data of electrochemical systems, Solid State Ionics 20 (1986) 31-44.

A.4. List of abbreviations

B_{ove}	Overall isotropic displacement parameter
B_{iso}	Isotropic displacement parameter
C_{elec}	Accumulation of charge at the surface o intraparticles
C_{DL}	Double layer capacitance
C_i	Intercalation capacity
CPE	Constant phase element
C_{SEI}	SEI layer capacitance
CV	Cyclic voltammetry
DEC	Diethyl carbonate
DFT	Density functional theory
DI	Bond-length distortion parameter
DMC	Dimethyl carbonate
E_B	Binding energy
EC	Ethylene carbonate
ED	Electron Diffraction
EES	Electrical energy storage
EIS	Electrochemical Impedance Spectroscopy
E_K	Kinetic energy
ERDA	Elastic recoil detection analysis
ESW	Electrolyte stability window
ssNMR	Solid state Nuclear Magnetic Resonance
FEC	Fluoroethylene carbonate
FTIR	Fourier Transform Infrared Spectroscopy
HAXPES	Hard Energy X-ray Photoelectron Spectroscopy
HC	Hard Carbon
HEV	Hybrid electric vehicle
HF	High frequency
HOMO	Highest occupied molecular orbital
IBA	Ion Beam Analysis
LF	Low frequency
LIBs	Lithium-ion batteries
LUMO	Lowest unoccupied molecular orbital
MF	Medium frequency
MQMAS	Multiple Quantum Magic Angle Spinning
Na-CMC	Sodium carboxymethyl cellulose
PND	Powder Neutron Diffraction
NIBs	Sodium-ion batteries
PC	Propylene carbonate

PEO	Poly(ethylene oxide)
Ph	Phthalocyanine
PVdF	Polyvinylidene fluoride
PXRD	Powder X-ray Diffraction
R_{CT}	Charge-transfer resistance
R_{elec}	Bulk electronic resistance
R_{SEI}	SEI layer resistance
R_{sol}	Electrolyte resistance
RBS	Rutherford Backscattering Spectrometry
RDS	Relative standard deviation
SEI	Solid Electrolyte Interphase
SEM	Scanning Electron Microscopy
S.G	Space group
SHE	Standard hydrogen electrode
SOF	Site occupancy factors
SPI	Solid Permeable Interphase
T_M	Transition metal
TEM	Transmission Electron Microscopy
TGA	Thermogravimetric analysis
UPS	Uninterruptible power supply
X^2	Pearson distribution
XPS	X-ray photoelectron spectroscopy
Z_w	Warburg diffusion

A.5. Powder Neutron Diffraction .pcr files

Files A.5.1: PND .pcr file of NHTO-H_2O sample.

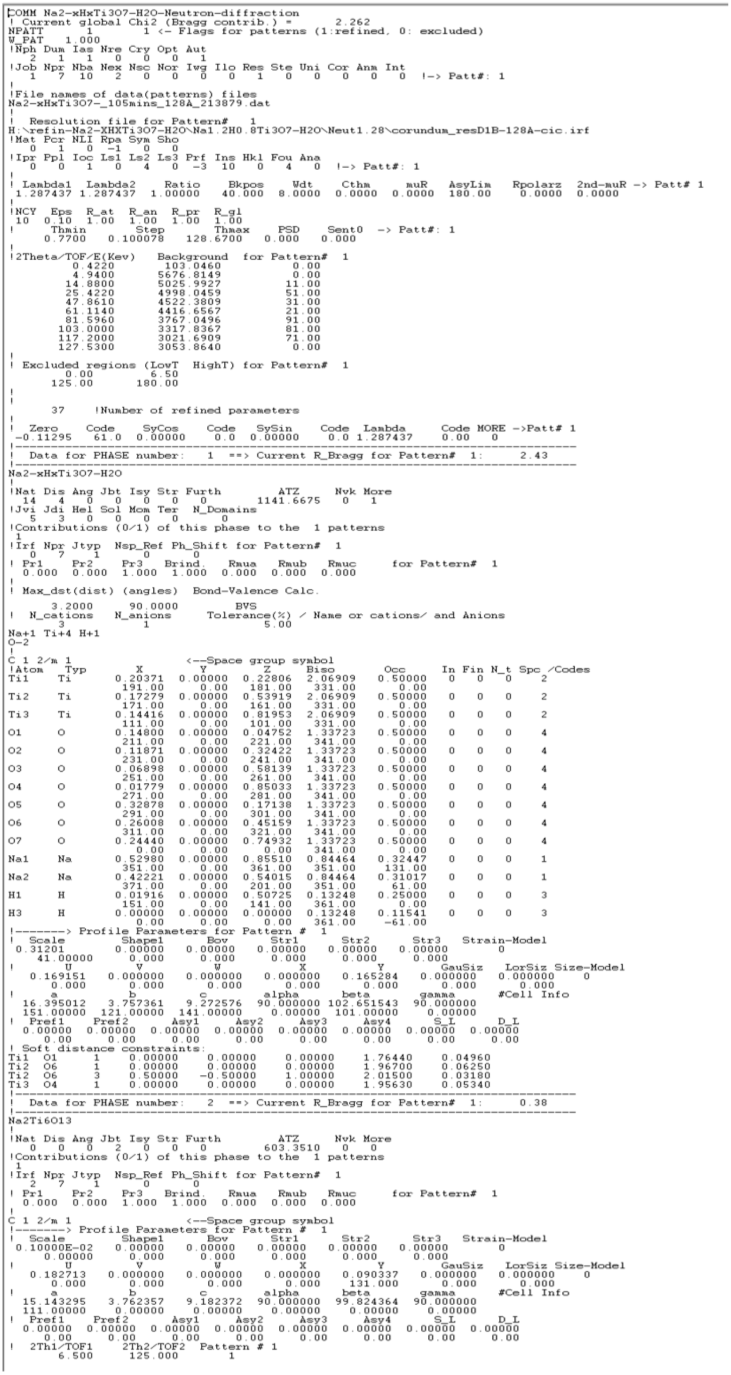

```
COMM Na2-xHxTi3O7-H2O-Neutron-diffraction
! Current global Chi2 (Bragg contrib.) =        2.262
NPATT      1         1 <- Flags for patterns (1:refined, 0: excluded)
W_PAT    1.000
!Nph Dum Ias Nre Cry Opt Aut
   2   1   1   0   0   0   1
!Job Npr Nba Nex Nsc Nor Iwg Ilo Res Ste Uni Cor Anm Int
   1   7  10   2   0   0   0   0   1   0   0   0   0   0   !-> Patt#: 1
!
!File names of data(patterns) files
Na2-xHxTi3O7-_105mins_128A_213879.dat
!
!  Resolution file for Pattern#   1
H:\refin-Na2-XHXTi3O7-H2O\Na1.2H0.8Ti3O7-H2O\Neut1.28\corundum_resD1B-128A-cic.irf
!Mat Pcr NLI Rpa Sym Sho
   0   1   0  -1   0   0
!Ipr Ppl Ioc Ls1 Ls2 Ls3 Prf Ins Hkl Fou Ana
   0   0   1   0   4   0  -3  10   0   4   0   !-> Patt#: 1
!
! Lambda1  Lambda2    Ratio    Bkpos     Wdt    Cthm     muR   AsyLim   Rpolarz  2nd-muR -> Patt# 1
 1.287437 1.287437  1.00000   40.000  8.0000  0.0000  0.0000  180.00    0.0000  0.0000
!
!NCY  Eps  R_at  R_an  R_pr  R_gl
 10  0.10  1.00  1.00  1.00  1.00
!     Thmin       Step       Thmax    PSD    Sent0  -> Patt#: 1
     0.7700    0.100078   128.6700   0.000   0.000
!
!2Theta/TOF/E(Kev)   Background  for Pattern#  1
         0.4220       103.0460          0.00
         4.9400      5676.8149          0.00
        14.8800      5025.9927         11.00
        25.4220      4998.0459         51.00
        47.8610      4522.3809         31.00
        61.1140      4416.6567         21.00
        81.5960      3767.0496         91.00
       103.0000      3317.8367         81.00
       117.2000      3021.6909         71.00
       127.5300      3053.8640          0.00
!
! Excluded regions (LowT  HighT) for Pattern#  1
       0.00          6.50
     125.00        180.00
!
!
     37    !Number of refined parameters
!
!  Zero    Code    SyCos    Code   SySin    Code  Lambda     Code MORE ->Patt# 1
 -0.11295   61.0  0.00000    0.0  0.00000    0.0 1.287437    0.00   0
!-------------------------------------------------------------------------------
!  Data for PHASE number:   1  ==> Current R_Bragg for Pattern#  1:     2.43
!-------------------------------------------------------------------------------
Na2-xHxTi3O7-H2O
!
!Nat Dis Ang Jbt Isy Str Furth        ATZ     Nvk More
  14   4   0   0   0   0   0       1141.6675   0   1
!Jvi Jdi Hel Sol Mom Ter  N_Domains
   5   3   0   0   0   0       0
!Contributions (0/1) of this phase to the  1 patterns
 1
!Irf Npr Jtyp  Nsp_Ref Ph_Shift for Pattern#  1
   0   7    1       0       0
! Pr1    Pr2    Pr3   Brind.   Rmua   Rmub   Rmuc     for Pattern#  1
  0.000  0.000  1.000  1.000  0.000  0.000  0.000
!
! Max_dst(dist) (angles)  Bond-Valence Calc.

     3.2000     90.0000         BVS
!  N_cations   N_anions     Tolerance(%) / Name or cations/ and Anions
       3           1                5.00
Na+1 Ti+4 H+1
O-2
!
C 1 2/m 1                <--Space group symbol
!Atom   Typ       X        Y        Z       Biso       Occ      In Fin N_t Spc /Codes
Ti1     Ti      0.20371  0.00000  0.22806  2.06909   0.50000    0   0   0    2
                 191.00     0.00   181.00   331.00      0.00
Ti2     Ti      0.17279  0.00000  0.53919  2.06909   0.50000    0   0   0    2
                 171.00     0.00   161.00   331.00      0.00
Ti3     Ti      0.14416  0.00000  0.81953  2.06909   0.50000    0   0   0    2
                 111.00     0.00   101.00   331.00      0.00
O1      O       0.14800  0.00000  0.04752  1.33723   0.50000    0   0   0    4
                 211.00     0.00   221.00   341.00      0.00
O2      O       0.11871  0.00000  0.32422  1.33723   0.50000    0   0   0    4
                 231.00     0.00   241.00   341.00      0.00
O3      O       0.06898  0.00000  0.58139  1.33723   0.50000    0   0   0    4
                 251.00     0.00   261.00   341.00      0.00
O4      O       0.01779  0.00000  0.85033  1.33723   0.50000    0   0   0    4
                 271.00     0.00   281.00   341.00      0.00
O5      O       0.32878  0.00000  0.17138  1.33723   0.50000    0   0   0    4
                 291.00     0.00   301.00   341.00      0.00
O6      O       0.26008  0.00000  0.45159  1.33723   0.50000    0   0   0    4
                 311.00     0.00   321.00   341.00      0.00
O7      O       0.24440  0.00000  0.74932  1.33723   0.50000    0   0   0    4
                   0.00     0.00     0.00   341.00      0.00
Na1     Na      0.52980  0.00000  0.85510  0.84464   0.32447    0   0   0    1
                 351.00     0.00   361.00   351.00    131.00
Na2     Na      0.42221  0.00000  0.54015  0.84464   0.31017    0   0   0    1
                 371.00     0.00   201.00   351.00     61.00
H1      H       0.01916  0.00000  0.50725  0.13248   0.25000    0   0   0    3
                 151.00     0.00   141.00   361.00      0.00
H3      H       0.00000  0.00000  0.00000  0.13248   0.11541    0   0   0    3
                   0.00     0.00     0.00   361.00    -61.00
!-------> Profile Parameters for Pattern #  1
!  Scale        Shape1      Bov       Str1      Str2      Str3   Strain-Model
 0.31201      0.00000    0.00000   0.00000   0.00000   0.00000       0
    41.00000    0.000      0.000     0.000     0.000     0.000
!       U          V          W          X          Y        GauSiz   LorSiz Size-Model
   0.169151   0.000000   0.000000   0.000000   0.165284   0.000000   0.000000    0
      0.000      0.000      0.000      0.000      0.000      0.000      0.000
!     a          b         c        alpha      beta       gamma      #Cell Info
  16.395012   3.757361   9.272576  90.000000 102.651543  90.000000
  151.00000  121.00000  141.00000    0.00000  101.00000    0.00000
!  Pref1    Pref2    Asy1     Asy2     Asy3     Asy4      S_L      D_L
  0.00000  0.00000  0.00000  0.00000  0.00000  0.00000  0.00000  0.00000
     0.00     0.00     0.00     0.00     0.00     0.00     0.00     0.00
! Soft distance constraints:
Ti1  O1     1    0.00000    0.00000    0.00000    1.76440    0.04960
Ti2  O6     1    0.00000    0.00000    0.00000    1.96700    0.06250
Ti2  O6     3    0.50000   -0.50000    1.00000    2.01500    0.03180
Ti3  O4     1    0.00000    0.00000    0.00000    1.95630    0.05340
!-------------------------------------------------------------------------------
!  Data for PHASE number:   2  ==> Current R_Bragg for Pattern#  1:     0.38
!-------------------------------------------------------------------------------
Na2Ti6O13
!
!Nat Dis Ang Jbt Isy Str Furth        ATZ     Nvk More
   0   0   0   2   0   0   0       603.3510    0   0
!Contributions (0/1) of this phase to the  1 patterns
 1
!Irf Npr Jtyp  Nsp_Ref Ph_Shift for Pattern#  1
   2   7    1       0       0
! Pr1    Pr2    Pr3   Brind.   Rmua   Rmub   Rmuc     for Pattern#  1
  0.000  0.000  1.000  1.000  0.000  0.000  0.000
!
C 1 2/m 1                <--Space group symbol
!-------> Profile Parameters for Pattern #  1
!  Scale        Shape1      Bov       Str1      Str2      Str3   Strain-Model
 0.10000E-02  0.00000    0.00000   0.00000   0.00000   0.00000       0
    0.00000     0.000      0.000     0.000     0.000     0.000
!       U          V          W          X          Y        GauSiz   LorSiz Size-Model
   0.182713   0.000000   0.000000   0.000000   0.090337   0.000000   0.000000    0
      0.000      0.000      0.000      0.000    131.000      0.000      0.000
!     a          b         c        alpha      beta       gamma      #Cell Info
  15.143295   3.762357   9.182372  90.000000  99.824364  90.000000
  111.00000    0.00000    0.00000    0.00000    0.00000    0.00000
!  Pref1    Pref2    Asy1     Asy2     Asy3     Asy4      S_L      D_L
  0.00000  0.00000  0.00000  0.00000  0.00000  0.00000  0.00000  0.00000
     0.00     0.00     0.00     0.00     0.00     0.00     0.00     0.00
!  2Th1/TOF1    2Th2/TOF2  Pattern # 1
       6.500      125.000       1
```

Files A.5.2: PND .pcr file of **NHTO-HCl** sample.

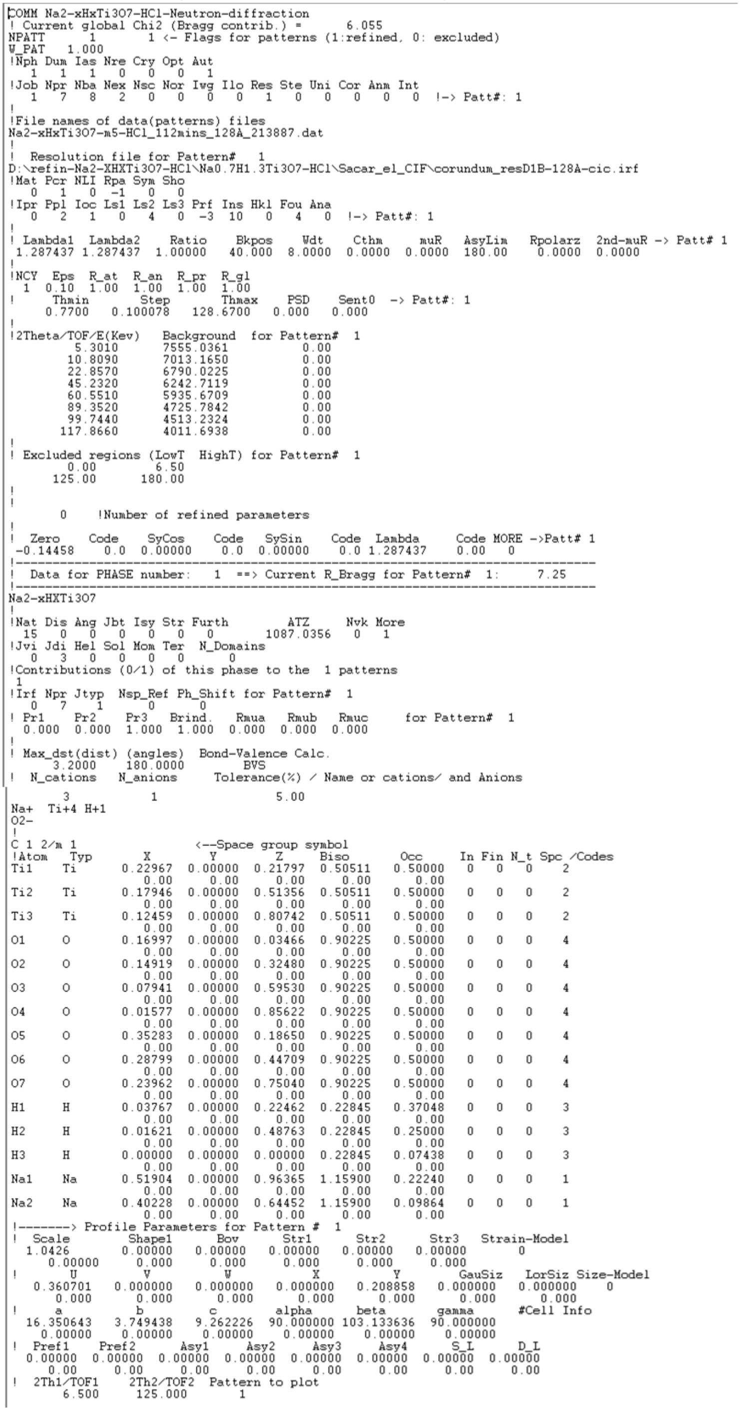

```
COMM Na2-xHxTi3O7-HCl-Neutron-diffraction
! Current global Chi2 (Bragg contrib.) =      6.055
NPATT      1       1 <- Flags for patterns (1:refined, 0: excluded)
W_PAT   1.000
!Nph Dum Ias Nre Cry Opt Aut
   1   1   1   0   0   0   1
!Job Npr Nba Nex Nsc Nor Iwg Ilo Res Ste Uni Cor Anm Int
   1   7   8   2   0   0   0   0   1   0   0   0   0   0  !-> Patt#: 1
!
!File names of data(patterns) files
Na2-xHxTi3O7-m5-HCl_112mins_128A_213887.dat
!
!  Resolution file for Pattern#   1
D:\refin-Na2-XHXTi3O7-HCl\Na0.7H1.3Ti3O7-HCl\Sacar_el_CIF\corundum_resD1B-128A-cic.irf
!Mat Pcr NLI Rpa Sym Sho
   0   1   0  -1   0   0
!Ipr Ppl Ioc Ls1 Ls2 Ls3 Prf Ins Hkl Fou Ana
   0   2   1   0   4   0  -3  10   0   4   0  !-> Patt#: 1
!
! Lambda1  Lambda2    Ratio    Bkpos    Wdt    Cthm     muR   AsyLim   Rpolarz  2nd-muR -> Patt# 1
 1.287437 1.287437  1.00000   40.000  8.0000  0.0000  0.0000  180.00    0.0000  0.0000
!
!NCY  Eps  R_at  R_an  R_pr  R_gl
  1  0.10  1.00  1.00  1.00  1.00
!     Thmin       Step       Thmax    PSD    Sent0  -> Patt#: 1
     0.7700   0.100078   128.6700   0.000   0.000
!
!2Theta/TOF/E(Kev)   Background  for Pattern#  1
         5.3010      7555.0361          0.00
        10.8090      7013.1650          0.00
        22.8570      6790.0225          0.00
        45.2320      6242.7119          0.00
        60.5510      5935.6709          0.00
        89.3520      4725.7842          0.00
        99.7440      4513.2324          0.00
       117.8660      4011.6938          0.00
!
! Excluded regions (LowT  HighT) for Pattern#  1
        0.00          6.50
      125.00        180.00
!
!
       0    !Number of refined parameters
!
!  Zero    Code    SyCos    Code   SySin    Code  Lambda     Code MORE ->Patt# 1
 -0.14458    0.0  0.00000    0.0  0.00000    0.0 1.287437    0.00    0
!-------------------------------------------------------------------------------
!  Data for PHASE number:   1  ==> Current R_Bragg for Pattern#  1:     7.25
!-------------------------------------------------------------------------------
Na2-xHXTi3O7
!
!Nat Dis Ang Jbt Isy Str Furth        ATZ     Nvk More
  15   0   0   0   0   0   0       1087.0356   0   1
!Jvi Jdi Hel Sol Mom Ter  N_Domains
   0   3   0   0   0   0       0
!Contributions (0/1) of this phase to the  1 patterns
 1
!Irf Npr Jtyp  Nsp_Ref Ph_Shift for Pattern#  1
   0   7    1      0       0
! Pr1    Pr2    Pr3   Brind.   Rmua   Rmub   Rmuc     for Pattern#  1
  0.000  0.000  1.000  1.000  0.000  0.000  0.000
!
! Max_dst(dist) (angles)  Bond-Valence Calc.
      3.2000    180.0000        BVS
!  N_cations   N_anions     Tolerance(%) / Name or cations/ and Anions
       3           1                5.00
Na+  Ti+4 H+1
O2-
!
C 1 2/m 1                  <--Space group symbol
!Atom   Typ       X        Y        Z     Biso       Occ     In Fin N_t Spc /Codes
Ti1    Ti      0.22967  0.00000  0.21797  0.50511   0.50000   0   0   0    2
                  0.00     0.00     0.00     0.00      0.00
Ti2    Ti      0.17946  0.00000  0.51356  0.50511   0.50000   0   0   0    2
                  0.00     0.00     0.00     0.00      0.00
Ti3    Ti      0.12459  0.00000  0.80742  0.50511   0.50000   0   0   0    2
                  0.00     0.00     0.00     0.00      0.00
O1     O       0.16997  0.00000  0.03466  0.90225   0.50000   0   0   0    4
                  0.00     0.00     0.00     0.00      0.00
O2     O       0.14919  0.00000  0.32480  0.90225   0.50000   0   0   0    4
                  0.00     0.00     0.00     0.00      0.00
O3     O       0.07941  0.00000  0.59530  0.90225   0.50000   0   0   0    4
                  0.00     0.00     0.00     0.00      0.00
O4     O       0.01577  0.00000  0.85622  0.90225   0.50000   0   0   0    4
                  0.00     0.00     0.00     0.00      0.00
O5     O       0.35283  0.00000  0.18650  0.90225   0.50000   0   0   0    4
                  0.00     0.00     0.00     0.00      0.00
O6     O       0.28799  0.00000  0.44709  0.90225   0.50000   0   0   0    4
                  0.00     0.00     0.00     0.00      0.00
O7     O       0.23962  0.00000  0.75040  0.90225   0.50000   0   0   0    4
                  0.00     0.00     0.00     0.00      0.00
H1     H       0.03767  0.00000  0.22462  0.22845   0.37048   0   0   0    3
                  0.00     0.00     0.00     0.00      0.00
H2     H       0.01621  0.00000  0.48763  0.22845   0.25000   0   0   0    3
                  0.00     0.00     0.00     0.00      0.00
H3     H       0.00000  0.00000  0.00000  0.22845   0.07438   0   0   0    3
                  0.00     0.00     0.00     0.00      0.00
Na1    Na      0.51904  0.00000  0.96365  1.15900   0.22240   0   0   0    1
                  0.00     0.00     0.00     0.00      0.00
Na2    Na      0.40228  0.00000  0.64452  1.15900   0.09864   0   0   0    1
                  0.00     0.00     0.00     0.00      0.00
!-------> Profile Parameters for Pattern #  1
!  Scale        Shape1      Bov      Str1      Str2      Str3   Strain-Model
  1.0426       0.00000   0.00000   0.00000   0.00000   0.00000       0
     0.00000     0.000     0.000     0.000     0.000     0.000
!       U          V          W          X          Y        GauSiz   LorSiz Size-Model
   0.360701   0.000000   0.000000   0.000000   0.208858   0.000000   0.000000    0
      0.000      0.000      0.000      0.000      0.000      0.000      0.000
!     a          b          c        alpha      beta       gamma      #Cell Info
  16.350643   3.749438   9.262226  90.000000 103.133636  90.000000
    0.00000    0.00000    0.00000    0.00000    0.00000    0.00000
!  Pref1    Pref2      Asy1     Asy2     Asy3     Asy4      S_L      D_L
  0.00000  0.00000  0.00000  0.00000  0.00000  0.00000  0.00000  0.00000
     0.00     0.00     0.00     0.00     0.00     0.00     0.00     0.00
!  2Th1/TOF1    2Th2/TOF2  Pattern to plot
       6.500      125.000       1
```

A.6. Values of the impedance data fits

Table A.6.1: The values of resistance, capacitance, α, and X^2 of **NTO-CO-Air** obtained from fitting the impedance spectra of the 1st Na^+ insertion using the equivalent circuit of **Figure 3.5b** of the manuscript.

E_{we} (V)	R_{sol} (Ω/mg)	R_{SEI} (Ω/mg)	C_{SEI} ($F/cm^2s^{\alpha-1}$)	α_{SEI}	R_{CT} (Ω/mg)	$C_{D.L}$ ($F/cm^2s^{\alpha-1}$)	α_{DL}	R_{elec} (Ω/mg)	C_{elec} ($F/cm^2s^{\alpha-1}$)	α_{elec}	D	α_D	C_i	X^2
1.0	9.39	11.28	$9.84\cdot10^{-05}$	0.64	34.79	$3.64\cdot10^{-05}$	0.89	170626.83	$8.84\cdot10^{-04}$	0.80	0.006	0.84	--	$4.39\cdot10^{-04}$
0.88	8.43	13.23	$7.66\cdot10^{-05}$	0.63	42.59	$3.00\cdot10^{-05}$	0.92581	723.41	$1.86\cdot10^{-03}$	0.86	0.001	0.65	--	$5.94\cdot10^{-04}$
0.70	8.87	14.00	$2.54\cdot10^{-05}$	0.72	49.95	$3.38\cdot10^{-05}$	0.90	10496.23	$8.39\cdot10^{-04}$	0.69	0.003	0.72	--	$1.02\cdot10^{-03}$
0.68	8.87	13.98	$2.52\cdot10^{-05}$	0.72	50.01	$3.39\cdot10^{-05}$	0.90	10394.41	$8.43\cdot10^{-04}$	0.69	0.003	0.72	--	$1.00\cdot10^{-03}$
0.65	9.11	12.80	$1.59\cdot10^{-05}$	0.76	60.33	$4.45\cdot10^{-05}$	0.86	7312.66	$7.55\cdot10^{-04}$	0.71	0.006	0.69	--	$6.08\cdot10^{-04}$
0.62	9.21	12.40	$1.31\cdot10^{-05}$	0.78	64.20	$4.83\cdot10^{-05}$	0.84	5272.40	$7.63\cdot10^{-04}$	0.72	0.006	0.66	--	$4.47\cdot10^{-04}$
0.60	7.57	12.30	$1.17\cdot10^{-05}$	0.78	74.86	$5.10\cdot10^{-05}$	0.84	1412.66	$7.77\cdot10^{-04}$	0.72	0.007	0.62	--	$3.21\cdot10^{-04}$
0.48	9.43	12.03	$8.43\cdot10^{-06}$	0.81	70.92	$5.87\cdot10^{-05}$	0.82	1026.78	$8.28\cdot10^{-04}$	0.72	0.01	0.50	0.08	$7.85\cdot10^{-05}$
0.45	9.22	12.29	$8.75\cdot10^{-06}$	0.81	65.52	$5.54\cdot10^{-05}$	0.82	763.41	$8.61\cdot10^{-04}$	0.71	0.02	0.50	0.07	$6.37\cdot10^{-05}$
0.40	9.39	12.30	$8.01\cdot10^{-06}$	0.82	69.13	$5.73\cdot10^{-05}$	0.82	536.70	$9.01\cdot10^{-04}$	0.69	0.02	0.50	0.07	$6.01\cdot10^{-05}$
0.35	9.48	12.04	$8.08\cdot10^{-06}$	0.82	71.04	$5.70\cdot10^{-05}$	0.82	370.13	$9.43\cdot10^{-04}$	0.67	0.03	0.46	0.07	$5.37\cdot10^{-05}$
0.30	9.24	11.88	$8.11\cdot10^{-06}$	0.82	64.81	$5.89\cdot10^{-05}$	0.81	205.09	$9.38\cdot10^{-04}$	0.69	0.04	0.46	0.08	$4.90\cdot10^{-05}$
0.18	8.93	8.98	$1.01\cdot10^{-05}$	0.80	72.12	$6.71\cdot10^{-05}$	0.79	109.94	$9.55\cdot10^{-04}$	0.69	0.05	0.83	--	$3.07\cdot10^{-05}$
0.05	8.77	6.48	$8.18\cdot10^{-06}$	0.82	92.07	$7.22\cdot10^{-05}$	0.77	34.39	$9.84\cdot10^{-04}$	0.81	0.07	0.59	0.14	$2.60\cdot10^{-05}$

Table A.6.2: The values of resistance, capacitance, α, and X^2 of **NTO-OH-Ar-C** obtained from fitting the impedance spectra of the 1st Na^+ insertion using the equivalent circuit of **Figure 3.10** of the manuscript.

E_{we} (V)	R_{sol} (Ω/mg)	R_{SEI} (Ω/mg)	C_{SEI} ($F/cm^2s^{\alpha-1}$)	α_{SEI}	R_{CT} (Ω/mg)	$C_{D.L}$ ($F/cm^2s^{\alpha-1}$)	α_{DL}	R_{Ccot} (Ω/mg)	C_{Ccot} ($F/cm^2s^{\alpha-1}$)	α_{Ccot}	R_{elec} (Ω/mg)	C_{elec} ($F/cm^2s^{\alpha-1}$)	α_{elec}	D	α_D	C_i	X^2
1.0	3.99	3.67	$9.58\cdot10^{-05}$	0.73	54.01	$4.64\cdot10^{-05}$	0.86	308.78	$4.68\cdot10^{-03}$	0.78	7.341.31	$8.13\cdot10^{-03}$	0.85	0.006	0.76	--	$9.72\cdot10^{-05}$
0.88	3.89	5.22	$7.48\cdot10^{-05}$	0.72	67.04	$4.14\cdot10^{-05}$	0.90	216.34	$3.16\cdot10^{-03}$	0.82	1335.26	$4.03\cdot10^{-02}$	0.99	0.003	0.65	0.17	$1.14\cdot10^{-04}$
0.70	3.96	5.06	$3.52\cdot10^{-05}$	0.78	63.82	$4.11\cdot10^{-05}$	0.91	189.33	$2.03\cdot10^{-03}$	0.87	1921.99	$2.07\cdot10^{-02}$	0.89	0.004	0.54	0.14	$6.23\cdot10^{-05}$
0.68	4.07	4.15	$1.87\cdot10^{-05}$	0.85	61.17	$3.88\cdot10^{-05}$	0.92	150.73	$2.03\cdot10^{-03}$	0.91	1880.73	$1.73\cdot10^{-02}$	0.86	0.005	0.49	0.12	$6.92\cdot10^{-05}$
0.65	4.01	3.90	$1.77\cdot10^{-05}$	0.85	60.93	$3.83\cdot10^{-05}$	0.93	136.76	$1.96\cdot10^{-03}$	0.91	1897.89	$1.73\cdot10^{-02}$	0.82	0.006	0.47	0.14	$6.78\cdot10^{-05}$
0.62	3.86	3.23	$1.37\cdot10^{-05}$	0.89	57.73	$3.66\cdot10^{-05}$	0.94	112.27	$1.98\cdot10^{-03}$	0.93	1528.89	$1.43\cdot10^{-02}$	0.80	0.01	0.43	0.13	$6.04\cdot10^{-05}$
0.48	3.84	3.41	$1.20\cdot10^{-05}$	0.89	58.25	$3.77\cdot10^{-05}$	0.91	63.42	$1.60\cdot10^{-03}$	0.85	263.61	$1.35\cdot10^{-02}$	0.73	0.01	0.37	0.12	$5.58\cdot10^{-05}$
0.45	3.70	3.20	$1.13\cdot10^{-05}$	0.90	53.48	$3.81\cdot10^{-05}$	0.91	53.36	$1.63\cdot10^{-03}$	0.84	150.70	$1.50\cdot10^{-02}$	0.86	0.02	0.35	0.12	$6.12\cdot10^{-05}$
0.40	3.63	2.93	$1.13\cdot10^{-05}$	0.90	54.77	$3.57\cdot10^{-05}$	0.91	49.45	$1.60\cdot10^{-03}$	0.82	96.21	$1.82\cdot10^{-02}$	0.78	0.02	0.32	0.12	$4.78\cdot10^{-05}$
0.35	3.58	2.71	$1.20\cdot10^{-05}$	0.90	56.33	$3.36\cdot10^{-05}$	0.92	44.28	$1.58\cdot10^{-03}$	0.80	60.00	$1.97\cdot10^{-02}$	0.80	0.02	0.30	0.12	$3.40\cdot10^{-05}$
0.30	3.73	3.16	$1.41\cdot10^{-05}$	0.87	51.75	$3.71\cdot10^{-05}$	0.89	32.05	$1.54\cdot10^{-03}$	0.81	36.42	$2.20\cdot10^{-02}$	0.79	0.03	0.30	0.12	$3.16\cdot10^{-05}$
0.18	4.00	3.77	$4.81\cdot10^{-04}$	0.84	51.97	$3.81\cdot10^{-05}$	0.88	26.14	$1.78\cdot10^{-03}$	0.74	28.62	$1.69\cdot10^{-02}$	0.73	0.09	0.84	--	$2.97\cdot10^{-05}$
0.05	3.47	3.65	$2.89\cdot10^{-04}$	0.88	43.21	$3.05\cdot10^{-05}$	0.92	20.85	$2.32\cdot10^{-03}$	0.62	25.13	$2.80\cdot10^{-02}$	0.69	0.19	0.80	0.37	$3.69\cdot10^{-05}$

Table A.6.3: The obtained values from the fits by Boukamp´s software of the impedance data collected at 3.69 V, 4.15 V, 2.42 V and 1.50 V, of **P2-NMFO-LV** sample.

	1st Na^{+} deintercalation		**1s^{t} Na^{+} intercalation**	
	3.69 V	4.15 V	2.42 V	1.50 V
R_{SPI} (Ω/mg)	24.39	25.60	20.42	20.35
C_{SPI} (F/cm^{2}s$^{\alpha-1}$)	$3.6{\cdot}10^{-7}$	$3.9{\cdot}10^{-7}$	$4.1{\cdot}10^{-7}$	$3.8{\cdot}10^{-7}$
α_{SPI}	1.0	1.0	1.0	1.0
$R_{C.T}$ (Ω/mg)	59.42	79.52	60.90	162.51
$C_{D.L}$ (F/cm^{2}s$^{\alpha-1}$)	$1.1{\cdot}10^{-5}$	$2.0{\cdot}10^{-5}$	$1.3{\cdot}10^{-5}$	$2.3{\cdot}10^{-5}$
$\alpha_{D.L}$	0.93	0.85	0.96	0.92
R_{elec} (Ω/mg)	83.58	3205.66	244.71	10398.32
C_{elec} (F/cm^{2}s$^{\alpha-1}$)	$1.40{\cdot}10^{-3}$	$2.6{\cdot}10^{-3}$	$1.2{\cdot}10^{-3}$	$6.38{\cdot}10^{-4}$
α_{elec}	0.93	0.86	0.83	0.73
CPE (F/cm^{2}s$^{\alpha-1}$)	0.077	0.009	0.045	0.081
X^{2}	$6.5{\cdot}10^{-4}$	$6.0{\cdot}10^{-4}$	$7.2{\cdot}10^{-4}$	$1.8{\cdot}10^{-3}$

Table A.6.4: The obtained values from the fits by Boukamp´s software of the impedance data collected at 3.71 V, 4.00 V during the extraction and at 2.44 V and 2.00 V during the Na^+ insertion of **P2-NMFO-SV** sample.

	1^{st} Na^+ deintercalation		**$1s^t$ Na^+ intercalation**	
	3.71 V	4.00 V	2.44 V	2.22 V
R_{SPI} (Ω/mg)	9.94	15.13	21.78	19.78
C_{SPI} ($F/cm^2s^{\alpha-1}$)	$3.5\cdot10^{-6}$	$4.9\cdot10^{-5}$	$4.4\cdot10^{-5}$	$4.1\cdot10^{-5}$
α_{SPI}	0.74	0.70	0.72	0.74
R_{CT} (Ω/mg)	33.27	19.76	48.39	56.04
C_{DL} ($F/cm^2s^{\alpha-1}$)	$2.4\cdot10^{-4}$	$8.9\cdot10^{-5}$	$1.6\cdot10^{-4}$	$1.4\cdot10^{-4}$
α_{DL}	0.90	1.0	0.80	0.74
R_{elec} (Ω/mg)	143.59	64.35	168.98	284.59
C_{elec} ($F/cm^2s^{\alpha-1}$)	$3.72\cdot10^{-3}$	$5.6\cdot10^{-3}$	$2.3\cdot10^{-3}$	$2.0\cdot10^{-4}$
α_{elec}	1.0	0.94	0.83	0.94
CPE ($F/cm^2s^{\alpha-1}$)	0.091	0.090	0.071	0.014
X^2	$2.5\cdot10^{-3}$	$4.7\cdot10^{-4}$	$1.4\cdot10^{-4}$	$3.2\cdot10^{-4}$

A.7. Auger parameters

Table A.7.5: Experimental Auger parameters of the Na-based compounds of the SEI layer at different oxidation states of **NTO-CO-Air** electrodes

Oxidation state	Na 1*s* position (eV)	Na $KL_{23}L_{23}$ position (eV)	Auger parameter*	Compound
Pristine	1072.72	989.28	2062.0	$Na_2Ti_3O_7$
Soaked	1072.69	989.07	2061.8	NaCl
0.81 V	1072.77	988.51	2061.3	Na_2CO_3
0.18 V	1072.83	988.29	2061.1	Na_2CO_3 + $NaCO_3R$
1st Na^+ insert.	1072.88	988.20	2061.1	Na_2CO_3 + $NaCO_3R$
1st Na^+ extrac.	1072.90	988.36	2061.3	Na_2CO_3
2nd Na^+ insert.	1072.78	988.29	2061.1	Na_2CO_3 + $NaCO_3R$
3rd Na^+ extrac.	1072.72	988.48	2061.2	Na_2CO_3 + $NaCO_3R$

*Value corresponding to the modified Auger parameter: $\alpha + h\nu = E_K (KL_{23}L_{23}) + E_B (1_s)$

Table A.7.6: Experimental Auger parameter of the Na-based compounds of the SEI layer at different oxidation states of **NTO-OH-Ar-C**.

Oxidation state	Na 1*s* position (eV)	Na $KL_{23}L_{23}$ position (eV)	Auger parameter*	Compound
Pristine	1072.6	988.6	2061.2	Na_2CO_3
Soaked	1072.8	988.0	2060.8	$NaCO_3R$
OCV	1072.9	987.9	2060.8	$NaCO_3R$
1st Na^+ insert.	1074.1	986.8	2060.9	Na_2CO_3 + $NaCO_3R$
1st Na^+ extrac.	1072.6	988.4	2061.0	Na_2CO_3 + $NaCO_3R$
2nd Na^+ insert.	1074.2	986.7	2060.9	Na_2CO_3 + $NaCO_3R$
3rd Na^+ extrac.	1072.7	988.1	2060.8	$NaCO_3R$

*Value corresponding to the modified Auger parameter: $\alpha + h\nu = E_K (KL_{23}L_{23}) + E_B (1_s)$

Table A.7.7: Experimental Auger parameter of the Na-based compounds of the SEI layer at different oxidation states of **NTO-OH-Ar-C-FC**.

Oxidation state	Na 1*s* position (eV)	Na $KL_{23}L_{23}$ position (eV)	Auger parameter*	Compound
OCV	1072.0	989.3	2061.3	$NaCO_3R$
1st Na^+ insert.	1071.7	989.7	2061.5	$NaCO_3R$
1st Na^+ extrac.	1070.9	990.3	2061.2	$NaCO_3R$

*Value corresponding to the modified Auger parameter: $\alpha + h\nu = E_K (KL_{23}L_{23}) + E_B (1_s)$

A.8. List of contributions

A.8.1. Publications

- Maider Zarrabeitia, Francesco Nobili, Miguel Ángel Muñoz-Márquez, Teófilo Rojo, Montse Casas-Cabanas, Direct observation of electronic conductivity transitions and solid electrolyte interphase stability of $Na_2Ti_3O_7$ electrodes for Na-ion batteries, J. Power Sources 330 (2016) 78-83.

- Maider Zarrabeitia, Elizabeth Castillo-Martínez, Juan Miguel López Del Amo, Aitor Eguia-Barrio, Miguel Ángel Muñoz-Márquez, Teófilo Rojo, Montse Casas-Cabanas, Towards environmentally friendly Na-ion batteries: Moisture and water stability of $Na_2Ti_3O_7$, J. Power Sources 324 (2016) 378-387.

- Maider Zarrabeitia, Elizabeth Castillo-Martínez, Juan Miguel López Del Amo, Aitor Eguia-Barrio, Miguel Ángel Muñoz-Márquez, Teófilo Rojo, Montse Casas-Cabanas, Identification of the critical synthesis parameters for enhanced cycling stability of Na-ion anode material $Na_2Ti_3O_7$, Acta Mater. 104 (2016) 125-130.

- Miguel Ángel Muñoz-Márquez, Maider Zarrabeitia, Elizabeth Castillo-Martínez, Aitor Eguia-Barrio, Teófilo Rojo, Montse Casas-Cabanas, Composition and evolution of the Solid-Electrolyte Interphase in $Na_2Ti_3O_7$ electrodes for Na-ion batteries: XPS and Auger Parameter analysis, ACS Appl.Mater Interfaces 7 (2015) 7801-7808.

- Aitor Eguia-Barrio, Elizabeth Castillo-Martínez, Maider Zarrabeitia, Miguel Ángel Muñoz-Márquez, Montse Casas-Cabanas, Teófilo Rojo, Structure of $H_2Ti_3O_7$ and its evolution during sodium insertion as anode for NA ion batteries, Phys. Chem. Chem. Phys. 17 (2015) 6988-6994.

A.8.2. Conferences

- Maider Zarrabeitia, Miguel Ángel Muñoz-Márquez, Francesco Nobili, Elizabeth Castillo-Martínez, Teófilo Rojo, Montse Casas-Cabanas, SEI layer stability and kinetics of $Na_2Ti_3O_7$ as anode for Na ion batteries, e-MRS, September 19-22, 2016, Warsaw, Poland (Oral).

- Maider Zarrabeitia, Miguel Angel Muñoz-Márquez, Elizabeth Castillo-Matínez, Aitor Eguía, Juan Miguel López Del Amo, Teófilo Rojo, Montse Casas-Cabanas, Strucutral characterization of $Na_{2-x}H_xTi_3O_7$, $0<x<2$ negative sodium-ion electrode material, VIII Reunión de la Sociedad Española de Técnicas Neutrónicas, June 26-29, 2016, Bilbao, Spain (Oral).

- Maider Zarrabeitia, Miguel Ángel Muñoz-Márquez, Elizabeth Castillo-Martínez, Aitor Eguía-Barrio, Teófilo Rojo, Montse Casas-Cabanas, Influences of synthesis parameters on the SEI layer of $Na_2Ti_3O_7$ as anode for Na-ion batteries, 8th International Conference on Advanced Lithium Batteries for Automobile Applications, October 30-02, 2015, Bilbao, Spain (Poster).

- Maider Zarrabeitia, Miguel Ángel Muñoz-Márquez, Elizabeth Castillo-Martínez, Aitor Eguía-Barrio, Juan Miguel López Del Amo, Teófilo Rojo, Montse Casas-Cabanas, Influences of synthesis parameters on the electrochemical and interfacial properties of $Na_2Ti_3O_7$ as anode for Na ion batteries, ECS Conference on Electrochemical Energy Conversion & Storage with SOFC-XIV, July-August 26-02, Glasgow, United Kingdom (Oral).

- Maider Zarrabeitia, Elizabeth Castillo-Martínez, Aitor Eguía-Barrio, Miguel Ángel Muñoz-Márquez, Juan Miguel López Del Amo, Teófilo Rojo, Montse Casas-Cabanas, $Na_2Ti_3O_7$ as Na ion anode material: air stability and decomposition products, Power our future 2014, April 01-04, 2014, Vitoria-Gasteiz, Spain (Poster).

- Maider Zarrabeitia, Miguel Ángel Muñoz-Márquez, Elizabeth Castillo-Martínez, Aitor Eguía-Barrio, Teófilo Rojo, Montse Casas-Cabanas, $Na_2Ti_3O_7$ as negative electrode for sodium-ion batteries: study of the material and its interface with electrolyte, 1st Symposium on Na Batteries, October 16-17, 2013, Vitoria-Gasteiz, Spain (Poster).

- Maider Zarrabeitia, Miguel Ángel Muñoz-Márquez, Elizabeth Castillo-Martínez, Aitor Eguía-Barrio, Teófilo Rojo, Montse Casas-Cabanas, Surface studies of eledtrode materials for rechargeable sodium-ion batteries, XXXIV Reunión Bienal de la Sociedad Española de Química, September 15-18, 2013, Santader, Spain (Oral).